A COMBINED EXPERIMENTAL AND THEORETICAL STUDIES ON SOME ZEOLITE -Y ENCAPSULATED TRANSITION METAL COMPLEXES

A THESIS SUBMITTED IN PARTIAL FULFILLMENT OF THE
REQUIREMENTS FOR THE DEGREE OF

DOCTOR OF PHILOSOPHY

By

Kusum Kr. Bania

Registration No. 029 of 2010

Department of Chemical Sciences

Tezpur University,

Napaam, Tezpur – 784028

Assam, India

March, 2013

Dedicated to My Parents
And Brothers

ABSTRACT

Over the last decade, the encapsulation of transition metal co-ordination complexes and organometallics within the voids of microporous zeolite has attracted attention since it provides a simple way of coupling the reactivity of the metal complex with the robustness and stereochemistry of the host zeolite. Rapid progress is being made in developing encapsulated base catalysts as they are found to have wide application in heterogeneous and homogeneous catalytic processes. There are number of well documented examples in which catalytic activity of the encapsulated complex is either enhanced or more selective as compared to the same complex in solution.

Living systems have found a way to frustrate irreversible dimerization and destruction of ligands by encapsulation of active site in protein mantle. These protein mantle impose steric constrain around a metal complex leading to its distortion and splits the d-orbitals resulting in alteration of redox potential of metal complex. Similarly, the ship in a bottle complexes do suffer space constraints imposed by zeolite as well as specific interaction with the zeolite framework and undergoes structural change as compared to its unencapsulated analogue. The distortion of the metal complexes within the voids of the zeolite matrix leads to the change in the electronic, electrochemical and chemical behaviours from that of the neat complex. So in addition to the application of these hybrid materials in catalytic reactions, they are now being well studied to mimic the bio-system. Metal complexes of oxygen and nitrogen containing chelating ligands (such as porphyrin, salens) encapsultated in zeolite framework are being studied as model system to understand the role of metal complex in nature. Metal complexes encapsulated in zeolites can mimic metalloenzymes and therefore they are being termed as zeozymes.

The thesis consist of seven chapters, a brief overview of which are given below

Chapter 1. Introduction

This chapter briefly explains the structure of zeolite and its composition followed by the features of zeolite -Y to act as host material for transition metal complexes. A brief overview of the zeolite -Y encapsulated transition metal complexes, their methods of synthesis and their catalytic application in various organic transformations including the asymmetric synthesis has been elucidated. Furthermore,

the application of density functional theory (DFT) on the zeolite-Y encapsulated transition metal complexes is also included.

Chapter 2. Experimental and Theoretical Methods

This chapter includes the materials used in the synthesis of Schiff base ligands, neat and zeolite -Y encapsulated complexes and also the materials used in catalytic reactions. The procedures used for the synthesis of Schiff base ligands, metal exchanged zeolites, neat and zeolite -Y encapsulated complexes are explained in detail. The methods used for the catalytic oxidation of phenol and 2-napthol and for asymmetric Henry reaction are also incorporated in this chapter. The details of the analytical techniques and theoretical methods with a brief introduction to density functional theory are covered under this chapter.

Chapter 3. Encapsulation and Tethering of Tris(1,10-phenanthroline) Complexes of Fe (II), Cu(II) and Zn(II) Inside Zeolite-Y

This chapter deals with the synthesis of tris(1, 10-phenanthroline) complexes of iron (II), copper(II) and zinc (II) within the supercage of zeolite-Y and their characterization by elemental analysis (EDX), SEM, powder XRD, FTIR, UV-vis/DRS, cyclic voltammetry and EPR techniques. TDDFT calculations are carried out on the neat phenanthroline complexes in order to allow an accurate characterization and assignment of experimental UV-vis absorption spectra. Density functional theory has been used to calculate a range of DFT-based descriptors such as global hardness, local softness and Fukui functions in order to investigate the change in the reactivity values of the metal complexes upon encapsulation.

Chapter 4. Encapsulation of Bis(Picolinato) Complexes of Co(II), Ni(II) and Cu(II) Inside Zeolite-Y and Their Application in Selective Oxidation of Phenol

In this chapter both experimental and theoretical studies have been performed on the selective oxidation of phenol to catechol by bis(picolinate) complexes of cobalt, nickel and copper prepared in solution and encapsulated in zeolite-Y. The catalytic activities of the homogeneous and heterogeneous catalysts are compared in the light of the experimental and theoretical results. The catalytic oxidation of phenol has been carried out under microwave irradiation in presence H_2O_2 as mild oxidant. EPR, cyclic voltammetry study along with the density functional theory calculations are implemented to reveal the existence of *cis* → *trans* isomerization in case of Cu(II) complex. A plausible mechanism for the oxidation reaction mediated by the synthesized complexes has been provided by means of DFT calculations along with the energetics involved in all the transformations.

Chapter 5. Effect of Alkali Metal Cations on Electronic, Redox and Catalytic Properties of Fe(III) Schiff Base Complexes Encapsulated in Zeolite -Y

This chapter describes the synthesis and characterization of iron (III) Schiff-base complex of general formula $[Fe(L)_2Cl].2H_2O$, where L= *N,N′*-bis(salicylidene) ethylenediamine and *N,N′*-disalicylidene-1,2-phenylenediamine encapsulated within various alkali exchanged zeolites *viz.* LiY, NaY and KY by flexible ligand method. The catalytic activity of the two complexes towards the selective oxidation of 2-napthol to BINOL has been studied. The effect of alkali metal cations on the electronic, redox properties and their role in asymmetric induction in the selective oxidation of 2-napthol to BINOL by the two synthesized iron Schiff base complexes has been carried out using various spectrochemical and electrochemical studies. Density functional calculation has been carried out on both the neat Fe-Salen and Fe-Salophen complexes and those encapsulated in NaY zeolite to investigate change in structural parameters, energies of the HOMO and LUMO, global hardness and softness. Fukui functions, as local descriptor are used to analyze the hard-hard interaction at a particular site of the complexes.

Chapter 6. Asymmetric Henry Reaction by Chiral Cu(II) Schiff Base Complexes Encapsulated in Zeolite-Y

This chapter deals with synthesis, characterization and catalytic study of two chiral Schiff-base complexes of Cu(II) encapsulated inside the cavity of zeolite-Y. The two heterogeneous chiral Cu(II) Schiff base complexes prepared via "*ship in a bottle*" synthesis method are tested for asymmetric Henry reactions and their catalytic activities are compared with their homogeneous counterpart. The effect of solvent and temperature on the catalytic activity of the complexes has been studied. Density functional theory calculation has been implemented to understand the effect of zeolite matrix on structural, electronic and reactivity of the synthesized complexes. The mechanism of Henry reaction is studied using DFT calculation involving the probable reaction intermediate and transition states.

Chapter 7. Conclusion and Future Scope

This chapter outlines the concluding remarks, highlights of the findings followed by future scope of the present investigation.

DECLARATION BY THE CANDIDATE

I hereby declare that the thesis entitled "*A Combined Experimental and Theoretical Studies on Some Zeolite -Y Encapsulated Transition Metal Complexes*" being submitted to the Department of Chemical Sciences, Tezpur University, is a record of original research work carried out by me under the guidance of Prof. R. C. Deka. Any text, figures, results or design that are not of own devising are appropriately referred in order to give credit to the original authors(s). All sources of assistance have been duly acknowledged. I also declare that no part of this thesis has been submitted elsewhere for award of any other degree.

Date: 28\02\13
Place: Tezpur

K. Bania
(Kusum Kr. Bania)
Department of Chemical Sciences
Tezpur University
Assam, India

TEZPUR UNIVERSITY
(A Central University established by an Act of Parliament)
NAPAAM, TEZPUR -784028
DISTRICT: SONITPUR: ASSAM: INDIA

Ph: 03712-267008
03712-267009

Fax: 03712-267005
03712-267006

email: ramesh@tezu.ernet.in

Prof. Ramesh Ch. Deka
Department of Chemical Sciences
Tezpur University

This is to certify that the thesis entitled ***"A Combined Experimental and Theoretical Studies on Some Zeolite -Y Encapsulated Transition Metal Complexes"*** submitted by **Kusum Kr. Bania** to Tezpur University for the award of the degree of Doctor of Philosophy is a bonafide record of research work carried out by him under my supervision. He has been duly registered, completed his Ph.D. course work and the thesis presented is worthy being considered for the Ph.D. degree. The contents of this thesis, in full or in parts, have not been submitted to any other University for the award of any degree or diploma.

Date: 1/3/2013

Place: Tezpur

RDeka
Signature of the Supervisor

Acknowledgement

This thesis would not have been possible without the guidance and the help of several individuals who in one way or another contributed and extended their valuable assistance in the preparation and completion of this study.

First and foremost, I express my utmost gratitude to my research guide Prof Ramesh. Ch. Deka, Department of Chemical Sciences, Tezpur University for his constant guidance and encouragement. Prof. Deka stands as my inspiration as I hurdle all the obstacles in the completion this research work.

I am thankful to Prof N. Karak, present Head of the Department of Chemical Sciences, for his kind concern and consideration during my research work. Prof. S. K. Dolui and Prof. N. S. Islam, my research committee members for their unselfish, unfailing support and steadfast encouragement to complete this study.

I would like to thank Dr. G.V. Karunakar, IICT, Hyderabad, Dr. Kula Kamal Senapati, IIT, Guwahati, Pradyumya Goswami and Hema Prabha Saikia of Gauhati University for their unaffordable help. I shall also remain grateful to Ratan Baruah, Dept of Physics, Tezpur University, Sankur Phukan, Arup Chakrabarty and Biraj Jyoti Borah, Dept of Chemical Sciences, Tezpur University, for their exorbitant help.

I am also greatly indebted to my colleagues (Pankaj da, Nayan, Bipul da, Ashwini da and Ashim da & Ranjeet), all my lab mates and all the technical staffs for their invariable support in carrying out my entire research work. It gives me great pleasure to thank all my near and dear friends, especially Amar, Ankur and Murshid, who shared all kinds of moments with me.

I am thankful to Honble' Vice Chancellor of Tezpur University, Prof. M. K. Chaudhuri for his instant support and inspiring words. I would also like to thank the Administrators of the School of Science, Tezpur University for their untiring effort in encouraging the teaching staff to pursue professional growth. Likewise the staff of the Dean's Office for their relaying every communication sent in my behalf.

Last but not the least, my family and the one above all of us, the omnipresent God, for answering my prayers for giving me the strength to plod on despite my constitution wanting to give up and throw in the towel, thank you so much Dear Lord.

Kusum Kr. Bania

Contents

Chapter 2. Experimental and Theoretical Methods 33-54

List of Abbreviations and Symbols

Å	Angstron
A^-	Anions
a.u.	Atomic Unit
B3LYP	Becke Lee, Yang and Parr
BBU	Basic Building Units
BINOL	1,1′-Binapthol
byp	Bipyridyl
CCSD(T)	Coupled Cluster Single, Double (Triple) excitations
CI	Configuration Interaction
CISD	CI, Single and Double excitations
COD	1,5-Cyclooctadiene
C-PCM	Conductor-like Polarizable Continuum Model
$[Co(Pic)_2]$	Bis(Picolinato) Co(II) neat complex
$[Co(Pic)_2]Y$	$[Co(Pic)_2]$ encapsulated in NaY
$[Cu(Phen)_3]^{2+}$	Tris (phenanthroline)Cu(II) neat complex
$[Cu(Pic)_2]$	Bis(Picolinato) Cu(II) neat complex
$[Cu(Pic)_2]Y$	$[Cu(Pic)_2]$encapsulated in NaY
$[Cu(L_1)_2]$	Bis[2, 2′-(1, 2-Diphenylethane-1,2-diyl) Bis(Azan-1-yl-1-ylidene) Bis(Mthan-1-yl-1-ylidene)diphenol] Cu(II) neat complex
$Cu(L_1)_2$-Y	$[Cu(L_1)_2]$ encapsulated in NaY
$[Cu(L_2)_2]$	Bis[6, 6′-(1, 2-Diphenylethane-1,2-diyl)Bis(Azan-1-yl-ylidene) Bis(Methan-1-yl-1-ylidene)Bis(3-Methoxyphenol)] Cu(II) neat complex
$Cu(L_2)_2$-Y	$[Cu(L_2)_2]$encapsulated in NaY
Cu-PhenY/$[Cu(Phen)_3\text{-}Y]^{2+}$	Tris (phenanthroline)Cu(II) encapsulated in NaY
CV	Cyclic Voltammetry
Cyt	Cytochrome
°C	Degree centigrade

DCM	Dichloromethane
DFT	Density Functional Theory
DN	Double Numeric
DRS	Diffuse Reflectance Spectroscopy
EA	Electron Affinity
ECP	Effective Core Potential
EDX	Energy Dispersive X-ray
EMT	Elf (or Ecole Supérieure) Mulhouse Chimie - two
en	ethylene diamine
ESR	Electron Spin Resonance
eV	Electron Volt
$[Fe(Phen)_3]^{2+}$	Tris (phenanthroline)Fe(II) neat complex
Fe-PhenY/$[Fe(Phen)_3\text{-}Y]^{2+}$	Tris (phenanthroline)Fe(II) encapsulated in NaY
Fe-Salen	Fe(III) [bis(salicylidene) ethylenediamine] neat complex
Fe-Salen-KY	Fe-Salen encapsulated in KY
Fe-Salen-LiY	Fe-Salen encapsulated in LiY
Fe-Salen-NaY	Fe-Salen encapsulated in NaY
Fe-Salophen	Fe(III) [bis(*N*, *N′*-disalicylidene-1,2-phenylendiamine)] neat complex
Fe-Salophen-KY	Fe-Salophen encapsulated in KY
Fe-Salophen-LiY	Fe-Salophen encapsulated in LiY
Fe-Salophen-NaY	Fe-Salophen encapsulated in NaY
FFs, f_K^+ and f_k^-	Fukui Functions
FTIR	Fourier Transform Infrared
GEA	Gradient Expansion Approximation
GGA	Generalized Gradient Approximation
HMOT	Hückel Molecular Orbital Theory
HOMO	Highest Occupied Molecular Orbital
HPA	Hirshfeld Population Analysis
HPLC	High Performance Liquid Chromatography
Im	Imidazole
IP	Ionization Potential

KM	Kubelka-Munk
L	lignand
L1	2, 2′-(1, 2-Diphenylethane-1,2-diyl) Bis(Azan-1-yl-1-ylidene) Bis(Mthan-1-yl-1-ylidene)diphenol
L2	6, 6′-(1, 2-Diphenylethane-1,2-diyl)Bis(Azan-1-yl-ylidene) Bis(Methan-1-yl-1-ylidene)Bis(3-Methoxyphenol)
LDA	Local Density Approximation
LMCT	Ligand to Metal charge Transfer
LUMO	Lowest Unoccupied Molecular Orbital
MCM-41	Mobil Crystalline Material No 41
MD	Molecular Dynamics
mg	Milli gram
MHP	Maximum Hardness Principle
ml	Millilitre
MLCT	Metal to Ligand Charge Transfer
mmol	Millimole
MP 2	Møller–Plesset
NaY	Sodium Y zeolite
NMR	Nuclear Magnetic Resonance
[Ni(Pic)$_2$]	Bis(Picolinato) Ni(II) neat complex
[Ni(Pic)$_2$]Y	[Ni(Pic)$_2$] encapsulated in NaY
Oxd^n	Oxidation
Phen	1,10 phenanthroline
Pic	Picolinate
PPh$_3$	Triphenyl phosphine
Pr	Propionate
QM	Quantum Mechanics
Qn	8-hydroxyquinoline
Red^n	Reduction
S	Softness
Salen	Salicylidene ethylenediamine
salnptn(4-OH)$_2$	*N*,*N*′-bis(2,4-dihydroxyacetophenone)-

	2,2dimethyl-propandiimine
Salophen	*N, N'*-disalicylidene-1,2-phenylendiamine
SDD	Stuttgart/Dresden
SEM	Scanning Electron Microscopy
SFCH	Salicylaldehyde Furoic-2-Carboxylic Hydrazone
SIB	Ship In a Bottle
STCH	Salicylaldehyde Thiophene-2-Carboxylic Hydrazone
STCH	Salicylaldehyde Thiophene-2-carboxylic Hydrazone
T	Tetrahedral species (Si, Al, P etc)
TBAP	Tetrabutyl Ammonium Phosphate
t-butyl	Tertiary butyl
TDDFT	Time Dependent Density Functional Theory
TGA	Thermogravimetry Analysis
TLC	Thin Layer Chromatography
TON	Turn Over Number
USY	Ultra Stable-Y
UV-vis	Ultra Violet -visible
V	Volt
VPI-5	Virginia Polytechnic Institute - five
VWN	Vosko-Wilk-Nusair
X_2- haacac	X = H, Cl, CH_3 and NO_2), haacac =2-hydroxyanilacetylacetone
XRD	X-Ray Diffraction
$[Zn(Phen)_3]^2$	Tris (phenanthroline)Zn(II) neat complex
Zn-PhenY/$[Zn(Phen)_3\text{-}Y]^2$	Tris (phenanthroline)Zn(II) encapsulated in NaY
μ	Chemical potential
η	Hardness
ω	Electrophilicity Index

List of Tables

Chapter 2

Chapter 3

Chapter 4

Chapter 5

Chapter 6

List of Figures and Schemes

Chapter 1

Chapter 3

Chapter 4

Chapter 5

Chapter 6

Schemes

Chapter 1

Introduction

1.1. General Aspects

Science is a pyramidal endeavour, each layer of discovery arising out of the previous ideas and research.[1] The discovery of synthetic zeolite by Barrer and Milton[2] in the mid of 19th century is recognized as one of those venture that has added a new dimension in material science and appeared as one of the fascinating material of the modern periods. Zeolites owe their importance as they are thermally stable, chemically robust and can be regenerated by calcination. Because of these significant characteristics these types of materials have found wide application in various catalytic reactions and large scale petrochemical processes.[3-5] And after the promising success of gas phase reaction in zeolites, intense research has been devoted towards the development of zeolites as acid-base and redox catalysts for the production of chemicals and fine chemicals.[6,7] Success has been achieved in heterogeneous catalysis of organic reactions by zeolites and is also considered as environmentally benign catalyst.

In addition to the importance of zeolites in heterogeneous catalysis, these solids have found broad application in heteogenization of homogeneous transition and organometallic complexes.[8-10] Transition metal and organometallic complexes, those are accessible in various oxidation states, exhibits good catalytic activity for various organic transformations.[11-13] However, they have certain snags because of their homogeneous nature. [14,15] They are difficult to separate from reaction mixture, have less thermal stability and also fail in terms of reusability.[16] Furthermore, many of the transition metal complexes are expensive to purchase and prepare. The current interest is now therefore to synthesize catalysts that do not get deactivated and can be recovered with 100% efficiency. And the search for efficient catalytic processes having high activity and selectivity is presently becoming perennial importance. In this respect, heterogenization of transition metal and organometallic complexes on various porous supports provides a viable alternative path for achieving some of these goals, particularly in terms of reducing waste, increasing the efficiency and selectivity in various significant catalytic processes.[17-20] Choosing an appropriate spatial-confinement support and tuning of the active site for enhancing the catalytic ability and selectivity is vital as per selective transformations are concerned.

One method for heterogenization of homogeneous catalyst is to encapsulate them into zeolite pores.[21] Over the last decade, the encapsulation of transition metal and organometallic complexes within the voids of microporus zeolite has attracted attention, since it provides a simple way of coupling the reactivity of the metal complex with the robustness and stereochemistry of the host zeolite.[22] The steric and space constrain imposed by the walls of the zeolite matrix changes the electronic, magnetic and redox behaviour of the encapsulated complexes.[23] These in turn influence the chemical properties of the metal complexes in comparison to their homogeneous counterparts. And these result in another aspect of heterogenization of homogeneous catalysts. Besides these changes, these host-guest complexes provide a simple extraction procedure as well as recycling, ensuring commercial advantages in addition to ease of manipulation.[24-26] In recent times rapid progress has been made in developing encapsulated base catalysts as they are found to have wide applications in various organic transformations.[27] In addition to the application of these hybrid materials in catalytic reactions, they are now being well studied to mimic the bio-system.[22] Metal complexes similar to those present in metalloenzyme when encapsulated in zeolites can mimic metalloenzymes and therefore they are being termed as zeozymes.[28,29]

In the present scenario of encapsulated transition metal complexes, active research is being carried out in the following aspects to develop new catalytic systems

- Spectroscopic and physicochemical characterization of hybrid materials
- Catalytic application of zeolite supported transition metal complexes
- Density Functional Theory calculation on zeolite embedded complexes
- Heterogenization of biologically active molecule to mimic the biosystem

1.2. Zeolites

1.2.1. Structure and Composition

Zeolites are tridimensional crystalline aluminosilicates of natural or synthetic origin with highly ordered structures. They consist of SiO_4^{4-} or AlO_4^{5-} tetrahedra, which are called primary or basic building units (BBU).[30] In the centre of the tetrahedra are atoms with relatively low electronegativities (Si^{IV}, Al^{III}, P^{V}, Zn^{II}, etc.) and in the corners are oxygen anions (O^{2-}). These combinations can be depicted as [SiO_4], [AlO_4], [PO_4], etc and are commonly designate as TO_4 unit where T stands for any tetrahedral species. The tetrahedra in zeolite materials are somewhat rigid.[31] In general, the O-T-O angle is close to the "ideal" value of 109°28′ for a geometrically perfect tetrahedron and deviations of more than a few degrees are not frequent.[32] All zeolite frameworks can be built by linking the tetrahedral units in a periodic pattern. To build the zeolite framework these building blocks are linked through common oxygen atoms (T-O-T) producing a three dimensional network containing channels and cavities of molecular dimensions, named micropores. The T-O-T bond angle ranges from 140 to 165°, Figure 1.1. The interior of the channels characteristics of zeolites contains water molecules and exchangeable alkali cations. When an Al atom replaces a Si atom isomorphically in the framework, the alkali cations compensate the negative charge produce in the framework. One interesting problem in zeolite chemistry is the distribution of silicon and aluminium atoms among the T sites. According to *Löwenstein rule*,[33] Al-O-Al linkages in zeolitic frameworks are forbidden. As a result, all aluminate tetrahedra must be linked to four silicate tetrahedra, and in general this is proved to be the case, but recent investigations have also shown non-Löwenstein distributions in aluminosilicate cluster.[34]

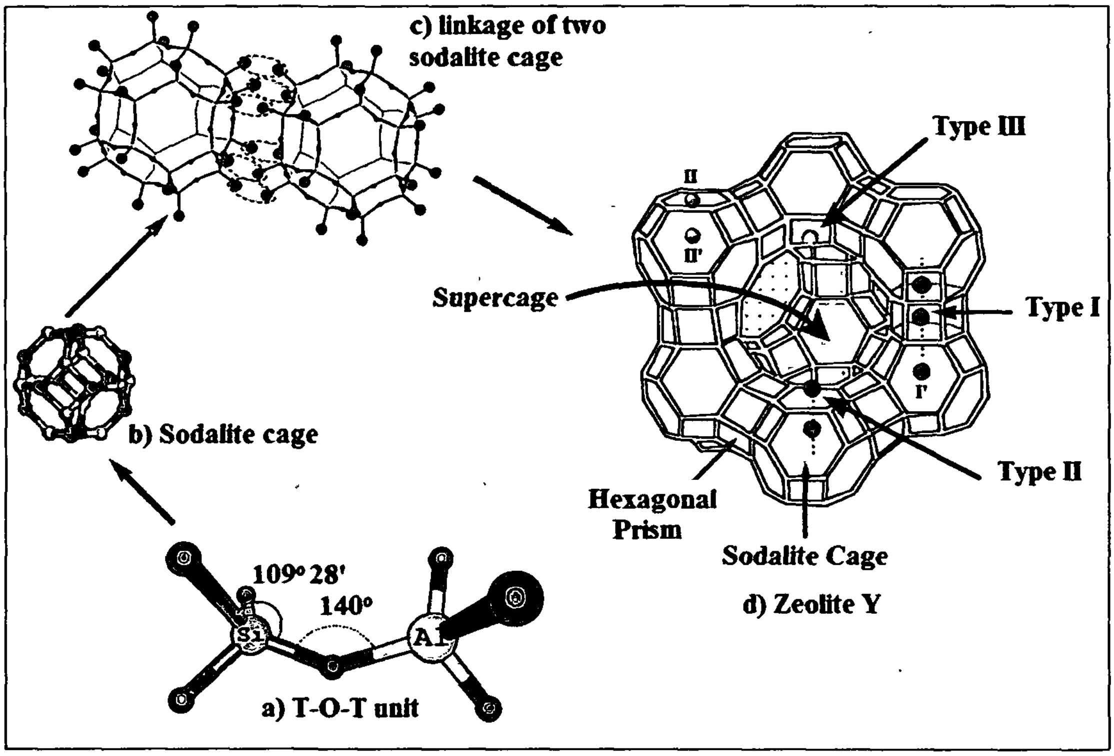

Figure 1.1. a) T-O-T unit b) sodalite cage c) linkage between two sodalite cages d) structure of zeolite-Y showing the cation sites (I, II, III, I', II').

The size of the channels and the cavities of these kinds of microporous materials depend on the composition, the zeolite type and the cation. Based on the number of oxygen or T-O-T atoms they are defined as ultralarge, large and medium or small pore material.[35] The smallest structural units or the primary building units can be linked to generate 16 possible secondary blocks (polygons).[36] When these secondary blocks are interconnected, they form hollow three dimensional structures. There are also various type of zeolites which are composed of polyhedra as tertiary units. These include truncated octahedra (sodalite or β cage, Figure 1.1), composed of 4 and 6 rings and the α-cage from by the linking of eight such truncated octahedra. The α-cage are larger in size than the β-cages.

Out of the various types of zeolite form by connection of tertiary units, zeolite-Y is the one having the high pore dimension. It is the synthetic form of faujasite and has a Si/Al ratio between 2 and 5. The zeolite-Y belong to the space group *Fd3m* (å = 24.7 Å). A unit cell contains eight large cavities (supercages), 8 sodalite cages, and 16 double 6-ring units. The diameter of the unit cell is about 13Å. The 12-ring windows, with a free diameter of 7.4 Å, are perpendicular to the (111) directions, but because of the tetrahedral symmetry of the cavity there are no straight channels along this direction.[37] Each supercage is connected to four other supercages through a 12-membered ring window and forms a three-dimensional network. The charge-compensating cations in zeolite-Y can occupy three positions (site I, II and III, Figure 1.1).[38] The first type, site I and I′, is located on the hexagonal prism faces between the sodalite units. The second type, site II′ and II, is positioned in the open hexagonal faces. The third type, site III, is sited on the walls of the supercage.

1.2.2. *Zeolite as Host Material*

Zeolite consists of empty channels and cavities of regular diameter called micropores.[39, 40] These micropores allow mass transfer from the exterior to the interior of the zeolite matrix, provided that the size of the diffusing molecule is smaller than the dimensions of the micropores.[22a,41] The existence of these accessible micropores ranks zeolites at the top of the list of solids exhibiting large specific surface areas. Because of this, these types of materials have been extensively used as suitable host for trapping various organic substances.[42,43] One of the important characteristics of zeolite is that they possess high transition state and product selectivity and so they are used as catalyst in various selective organic transformations.[44-49] Further, these kinds of materials can be reused, easy to separate from reaction mixture and is environmentally benign and hence are considered as green catalyst.[50-52] All these features together culminate zeolite as a good scavenger for the organic molecules. The application of these materials has not been restricted only to encapsulation of organic molecules. During the last few decades it has been proved that these molecular systems with channels and cages not only serve as host for the organic substrates but too can be used widely in encompassing the transition and organometallic complexes.[53-55]

Although there are natural zeolites, most of the over 176 zeolites known are synthetic. The first synthesis of zeolite-Y by Barrer in the 1948 has been widely recognized as one of the most advances in the chemistry of the last century.[56] This faujasite type zeolite has not only been used as greener catalyst but has played an important role in the field of heterogenization of homogeneous transition metal complexes.[23,57-60] Due to the high pore dimension, zeolite -Y is now considered to be one of the suitable host for entrapping transition or organometallic complexes. Besides the size of the zeolite cavity, another aspect of importance regarding the micropore system of zeolites is the geometry of the pores. In this regard zeolites can be classified as uni-, bi- and tridirectional zeolites, depending on whether the channel system is arranged along one, two or the three cartesian axes.[61] The directionality of the zeolite pore system is relevant with respect to the ability of zeolites to include guests inside the micropores. In the case of tridirectional zeolites having a pore geometry formed by large cavities interconnected by smaller windows, a situation can be envisioned in which a guest can be accommodated inside the zeolite cavity. Once the complex is formed inside the cage it will retained in the interior cavity of the zeolite. The guest complex can not diffuse out of the cavity because it is too large to cross the corresponding cavity opening due to its bulkiness relative to the pore dimensions.

1.3. Zeolite-Y Encapsulated Transition Metal Complexes: A Brief Overview

During the last two decades, substantial progress has been achieved in generating newer types of inclusion compounds based on porous substances.[62-65] Out of the various zeolite inclusion compounds, zeolite-Y containing transition-metal complexes occupies a special place amongst inclusion compounds based on porous substances. They are probably the most convenient materials for encapsulation of transition metal complexes. One can vary the central ion and ligands widely and can synthesize various transition metal complexes. Romanovsky and co-workers were probably the first to report the synthesis of metallophthalocyanines inside the supercage of zeolite NaY in 1977. Due to similarities in the structure and chemical properties between metallophthalocyanines and metalloporphyrins, the latter[67,68] have often been used as substitutes, for mimicking the catalytic function of cytochrome P450 enzymes, Figure 1.2. Researchers from DuPont [69-72] are among the early pioneers to exploit the chemistry of natural enzymes. They adopted strategies for the encapsulation of transition-metal complexes within porous hosts, and apply them to the rational design of zeolite-based catalysts for industrial application and to mimic the natural enzymes. Followed by their work various researchers established that a range of metal complexes could be successfully immobilised within the internal cavities of a zeolitic framework and demonstrated the viability of a supramolecular system. [73-81]

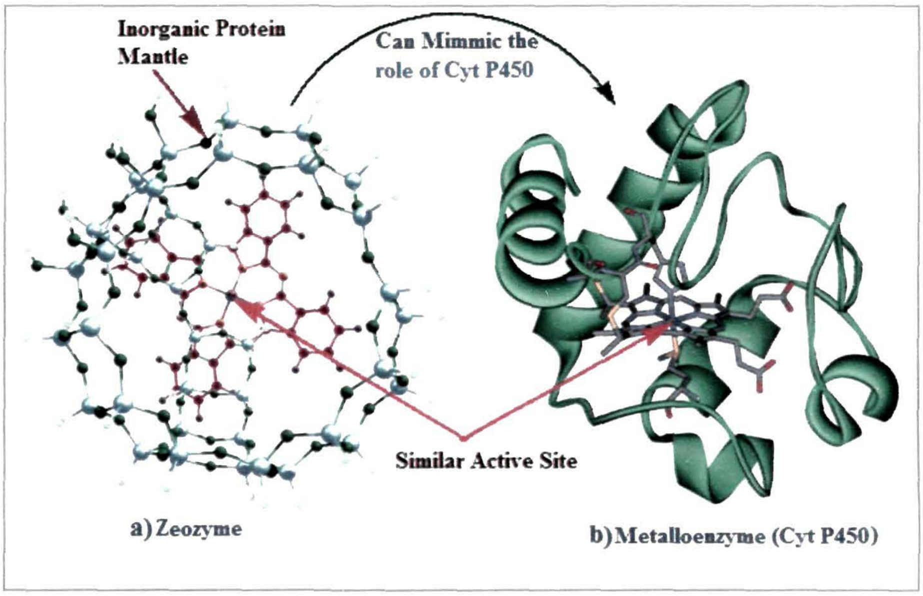

Figure 1.2. a) Metal phthalocyanine complex inside zeolite-Y (zeozyme) b) Cytochrome P450 enzymes.

The transition metal complexes that are formed inside the cavity of zeolite-Y have different molecular properties in comparison to the complex in solution phase.[82] The topology of the voids has an immense influence on the structural, electronic and catalytic behaviour of the intrazeolite transition metal complexes. The electronic confinement or "boxing effect"[83] that basically arises due to the space constrain imposed by the micropore system of zeolite-Y restricts the motion of the guest molecule. Once assembled, these complexes cannot be removed without destroying the lattice. Because of the steric impartment, the guest molecules are strained to undergo structural distortion in order to fit inside the cavity of zeolite-Y. Besides the confinement effect there may be Coulombic effect that are produced inside the zeolite cavity by the partial charge distribution along the framework.[84] Due to these two effects, there occurs change in the molecular properties of the confined guest complexes. The most visible manifestations of such alternation are in the electronic, magnetic properties, redox behaviour, reactivity and catalytic properties.[23] One of the earliest, and perhaps the most dramatic, of such changes was reported by Mizuno and Lunsford.[85] They observe a temperature driven interconversion between a low-spin state and a high-spin state in cobalt(II) tris(bipyridyl) complex ion, $[Co(bpy)_3]^{2+}$, encapsulated in the supercage of zeolite-Y. The observation is interesting because normally the $[Co(bpy)_3]^{2+}$ complex ion retains a high-spin ground state, both in solution and in the solid state, irrespective of the temperature or the nature of the counter ion.[86]

1.4. Design of Intra-Zeolite Complexes

A number of routes[87] *viz* ion exchange, flexible ligand approach, zeolite synthesis, ligand adsorption and ship-in-bottle methods are known for preparation of metal complexes inside zeolites. These are portrayed in Figure 1.3. In the Figure 1.3 the zeolite source is assumed to be NaY zeolite.

1.4.1. Ion Exchange Method

In the ion exchange strategy, sodium exchange zeolite is treated with a solution containing other cations thereby facilitating the exchange of the sodium ions. This method has been used for encapsulating metal–amino acid complexes inside a zeolite structure. An example of this is the zeolite-Y entrapped Cu–histidine complex.[88-] During the synthesis, the NaY zeolite enriched with sodium is treated with Cu-Histidine solution at pH 7.3. The pH of the reaction, the charge and stablity of the metal complex influences capability of the copper complex to undergo ion-exchange process. At lower pH (=2) or at highly acidic medium, less than 1% of the Cu^{2+} is coordinated to the histidine ligand. On increasing the pH to 3, Cu^{2+} forms mono-histidine complexes and within a pH range of 6-10, bis complexes are formed. The four nitrogen atoms from the imidazole and amine group of each molecule as well as the carboxylate can coordinate to Cu-centre leading to square-planar bis(Histidine) Cu(II) complex.

1.4.2. Flexible Ligand Method

This methodology is the most common and widely used for flexible ligand systems such as Schiff base lignads which have approximates size equivalent to that of the zeolite cavity. The ligands employed in this method should have thermal stability so that it does not get decomposed during the adsorption on the metal exchanged zeolites. The principle involved in this method is the diffusion of ligands into an already metal exchanged zeolite pores. The details of experimental procedure are given shown in Figure 1.3. First the respective metal salts are ion exchanged with calcined NaY zeolite by stirring the zeolite in a metal salt solution at around 303 K for 24 hours. The zeolite are then filtered and dried at around 390 K. The formation of the host-guest complex depends on the metal exchange. Therefore, to achieve a better metal exchange zeolite-Y, the process can be repeated for 2 to 3 times. The metal exchanged zeolite is then heated and evacuated to around a pressure of 10^{-5} Torr. The metal exchanged zeolite is then treated with ligand dissolve in a suitable solvent most often in water. The resultant mixture is subjected to heating in an inert atmosphere for 48h. Depending upon the ligand, the heating temperature will vary from 363-523 K. The excess ligand and metal complexes present on the external surface are removed by Soxhlet extraction with various solvents. The resultant product is then filtered and dried under vacuum for further characterization and application.

1.4.3. Ship-in-bottle (SIB) Synthesis Method

This method is basically applied when the ligand's molecular dimensions exceed the pore size and hence they cannot diffuse into the pores of zeolites. In such cases, ligand itself is constructed inside the zeolite matrix. The term SIB was probably coined by Herron, who reported the synthesis of several types of metallic complexes (including achiral salen-metal complex) encapsulated within zeolites.[73] According to this concept the zeolite encapsulated complex can be thought of like the artistic bottle containing a ship larger than the bottle neck. The SIB approach considers the host-guest interaction to be physical rather than chemical (neither ionic nor covalent bonding).[89] It reflects the fact that immobilization cause by the fact that the size impedes the guest from exiting through the host pores, like a large piece of furniture in a small room.[90] Stoddart coined the term *mechanical immobilization* to represent such situation.[91]

As in the previous case first the metal salts are exchanged with zeolite matrix. The metal exchanged zeolite is evacuated to a pressure of 10^{-5} Torr. The molecules that constitute the ligand species (ligand precursors) are then adsorbed into the zeolite matrix in an inert atmosphere. The atoms from the ligands of interest complexes with the metals present in the zeolite. The excess ligand precursors, the ligand present on the external surface and the complex present on the external surface are removed usually by Soxhlet extraction. The synthesis of metallic phthalocyanines inside faujasite X and Y by reacting *o*-phthalodinitrile with a transition metal exchanged faujasite indepentdently by Schulz-Ekloff and Romanovskii is one of the examples of such synthesis.[92-94]

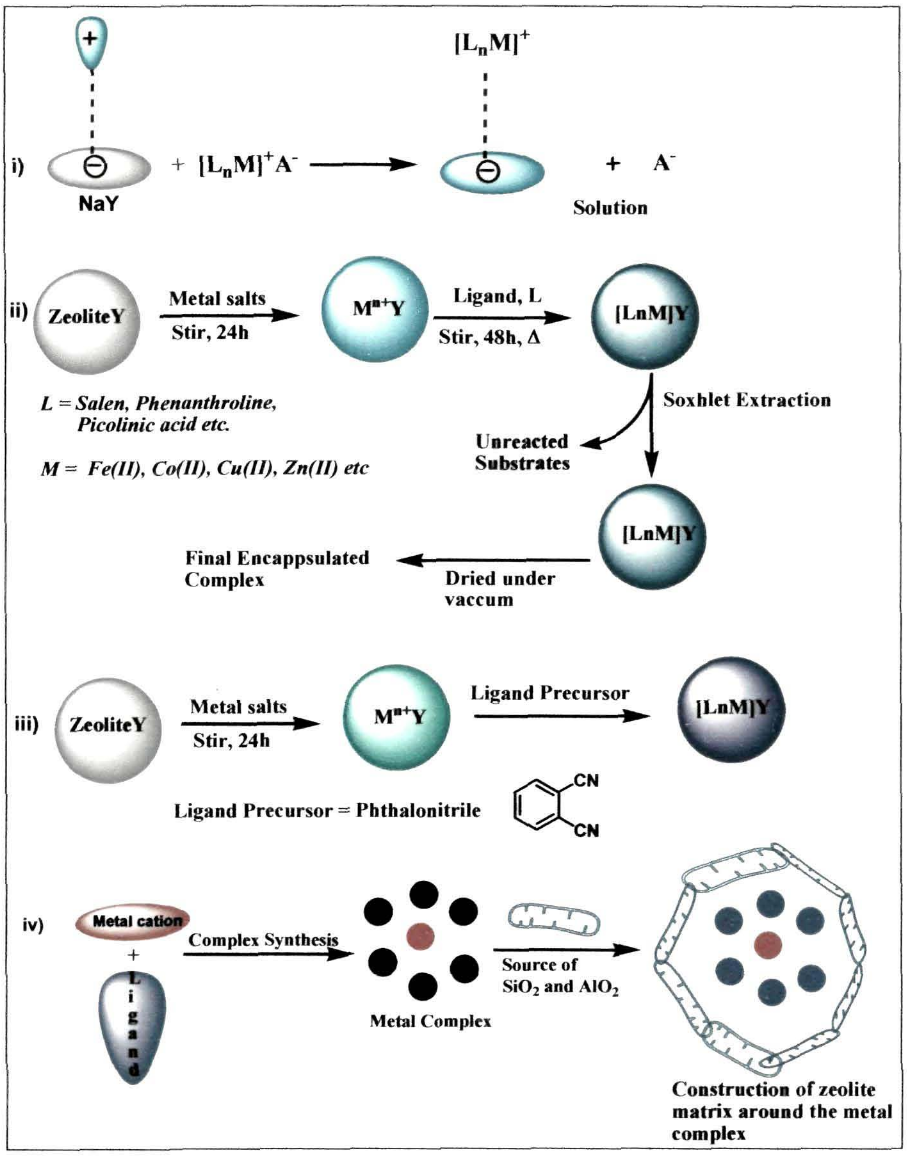

Figure 1.3. Methods of encapsulating metal complexes within zeolite-Y cavity. i) Ion exchange ii) Flexible ligand iii) Ship in a bottle synthesis and iv) Zeolite synthesis method.

1.4.4. Zeolite Synthesis Method

The zeolite synthesis method follows a kind of templeted approach. The metal complex which is to be incorporated into zeolite cavity is added during the period of zeolite crystallization. The zeolite is formed around the metal complex as a sort of template and thereby encapsulating it. The silica source is dissolved in NaOH. To that solution, metal complex is added and stirred for 30 minutes. Aluminium isopropoxide, which is dissolved in NaOH, is added and the resulting gel is autoclaved at 363 K for 24 hours and then Soxhelt extracted. There are certain conditions to be satisfied for the complexes to be encapsulated during zeolite synthesis. The metal complexes should have appreciable solubility in zeolite synthesis medium. The pH is maintained around 11-12 during zeolite synthesis. The complex should not get decomposed at this pH and also at hydrothermal conditions. The presence of complex should not alter the synthesis window. This method allows for the encapsulation of well defined metal complexes without contamination by excess ligands or uncomplexed metal ions. Metal phthalocyanines, porphyrins and amino acids are examples of such entrapped complexes.

1.5. Application of Zeolite Encapsulated Complexes

Zeolite encapsulated complexes have found wide application in mimicking the metalloenzyme and as catalyst for various organic transformation. In recent years they are also used as molecular switches and sensors, Figure 1.4. Herein we shall mainly focus on the applicaton of zeolite-Y encapsulated complexes as zeozymes and some of the important catalytic reaction mediated by such hybrid complexes.

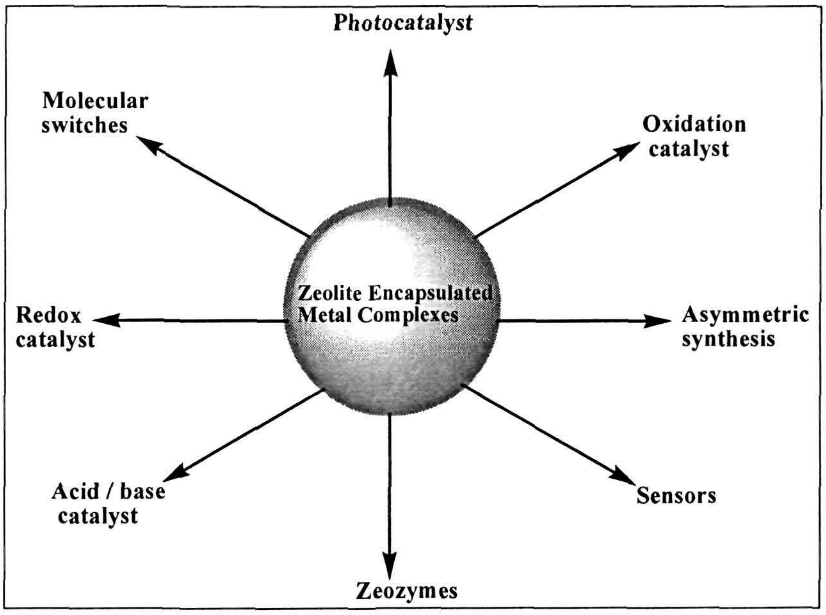

Figure 1.4. Various application of zeolite encapsulated complexes.

1.5.1. Zeolite Encapsulated Complexes as Zeozymes

There are various enzymes which contain transition metal complex and hence are known as metalloenzymes. In the metalloenzymes, the metallic complex acts as the active site and the protein mantle protect this active site from reaction such as self destruction of metal complex and regulate the access of the substrate to their active site. As proposed by Herron[95] zeolite can act as substitutes to the protein scaffold and can create a spatial environment similar to that of the natural enzymes. Therefore, it is possible to imagine an analogous system similar to that of metalloenzymes by embedding a catalytically active metallic complex within an inorganic matrix. These types of analogical organizations are termed as zeozymes. The term zeozymes combines words zeolite and enzymes and refers to the latter posibilbilty.[96, 97] Thus it is relevant to consider that this "ship in bottle complexes" will help in understanding the nature and the co-ordination sphere of the active metal centre in a metalloenzyme. And will also provide a valuable insight for developing heterogenized bio-inspired catalyst for chemical transformation.

In this context, Herron[74] first synthesized Co^{2+}-salen [salen= bis(salicylidene) ethylenediamine] complex, Figure 1.5a, by adsorbing flexible salen ligand into a Co^{2+}-ion exchanged zeolite-Y, to mimic the reversible binding of oxygen by haemoglobin and myoglobin. The encapsulated Co^{2+}-salen complex, Figure 1.5b, forms 1:1 adduct

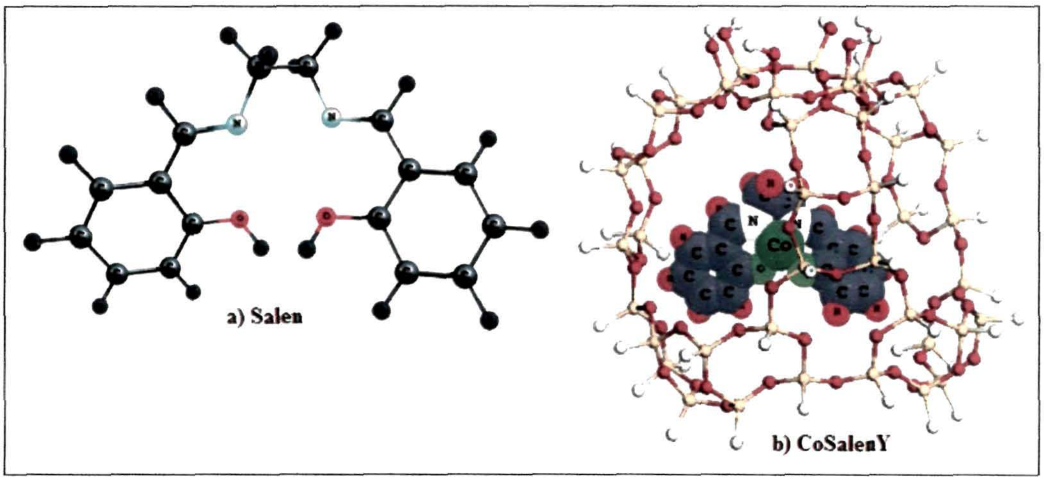

Figure 1.5. a) Salen ligand and b) CoSalen complex inside zeolite-Y as model system for dioxygen binding.

with dioxygen but exhibits a somewhat lower binding equilibrium than in solution. However, it has an excellent resistance to undergo autooxidation even at elevated temperatures.[74] This system resembles to that of hemoglobin in the sense that the Co^{2+}-salen acts as a prosthetic group binding oxygen reversibly and the zeolite behaves as an ''inorganic'' protein mantle. This example developed by bioinspiration is the origin of the word zeozymes. The significant achievement of such kind of encapsulation lies in the suppression of the dimerization of such metal complexes that lead to the formation of the inactive μ-oxo and peroxo-complexes of cobalt. Inspired by the importance of mimicking of dioxygen binding, Li et al.[98] also synthesized cobalt tetramethylporphyrin complex inside zeolite-Y and studied its dioxygen binding property. Progressively, many other transition-metal-salen complexes of iron,[99] vanadium[100] and ruthenium[101] are encapsulated in zeolite-Y as heterogeneous analogue of metalloenzymes, which reversibly bind to dioxygen.

Metalloporphyrins are one of the important classes of metalloenzymes which plays vital role in various catalytic reactions in the living organisms. Therefore, the designing of zeozymes analogues to metalloporphyrins would certainly put light on understanding the active role of such systems. Metallocyanines, due to its similar structural and chemical properties have been well studied by incorporating them into voids of zeolite-Y matrix. The molecular size of phthalocyanine macrocycle (14 Å) is large enough to diffuse into zeolite-Y cavity. So they are synthesized by a "ship in a bottle" synthesis starting from o-pthalodinitrile and transition metal exchanged zeolite or by a build-the bottle-around-the ship strategy. Herron, who coined the term" ship-in-a-bottle" synthesis, has prepared iron-phthalocyanine inside faujasites X and Y by thermal tetramerisation of o-phthalodinitrile templated by iron ions.[73] Balkus, Jr. has made significant contributions in this area and has written several reviews on the preparation and catalytic activity of encapsulated metallophthalocyanines.[102] They also reported for synthesise of Ru^{II}perchloro and perfluorophthalocyanine [103] inside zeolite X by build the bottle around the ship methodology. In similar attempt to prepare analogs of cytochrome P-450, copper (Figure 1.6a) and iron-phthalocyanine have been encapsulated in zeolite-Y by Jacobs and co-worker.[104] Ichikawa et al. in an interesting report account for the synthesis of much bulkier iron-tetra-tert-butylphthalocyanine (estimated diameter of 19Å) inside NaY.[105]

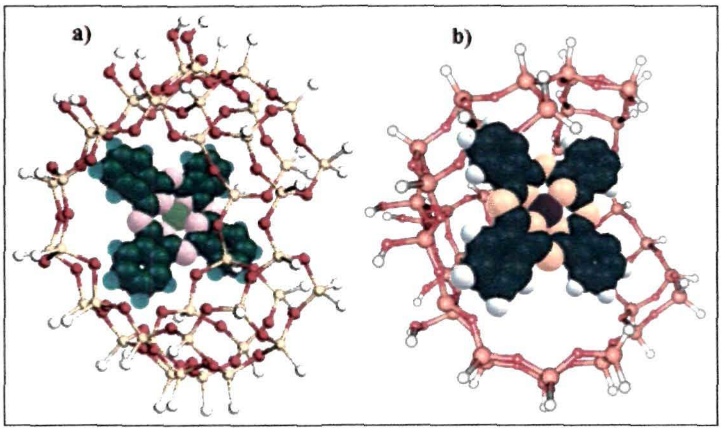

Figure 1.6. Molecular models showing a) Cu phthalocyanine and b) Co phthalocyanine complexes encapsulated in zeolite-Y.

Due to large size of the phthalocyanine ligands, the heteroatomic macrocycle once synthesized inside the cavities suffers from steric compression because of the space constrain imposed by zeolite walls. As a result these types of ligands maintain a roof like structure rather than flat conformation inside zeolite-Y. Ray et al.[23] reported that Co^{2+} phthalocyanines synthesized inside zeolite-Y is forced to adopt a distorted geometry, Figure 1.6b. The extent of loss of planarity has been identified via spectroscopic and molecular modelling study. In an approach to avoid such steric compression of phthalocyanine, various other zeotype materials with larger pore size has been attempted and success has been obtained in zeolite EMT and VPI-5. Zhan et al. [106] reported that metalloporphyrins can be encapsulated within faujasite by using the build-the-bottle around- the-ship approach, crystallising the zeolite gel around the porphyrin. However, metallic complex which are chemically robust, have high thermal resistance and highly soluble in water are only fit for such methodology. One such example is the preparation of the metallotetrakis (*N, N, N*-trimethylanilinium) porphyrin cation entrapped in faujasite Y which is used as catalyst for oxidation of cyclohexane.[109]

1.5.2. Zeolite Encapsulated Complexes as Catalyst

Zeolite encapsulated complexes due to their various advantages over their homogeneous counterparts have found profound application in various catalytic transformation. Starting from the synthesis of ship in bottle complexes to the present time, various transition metal complexes have been encapsulated, tethered or immobilized over zeolite-Y and has applied in heterogeneous catalyst. There are various organic transformations where such hybrid materials have been used as catalysis.[22,62] Based on their structural, chemical and redox behaviour, they are being either used as acid catalyst, base catalyst and redox or electro-catalyst.[107-109] In recent times much interest has been focussed on application of these encapsulated complexes in asymmetric catalysis,[62] photocatalysis[110] and as molecular switches.[111] Since, it is not possible to cover all the catalytic applications of such zeolite embedded metal complexes, in this chapter the discussion has been restricted to oxidation and asymmetric catalytic processes.

1.5.2.1. Oxidation Catalyst

The oxidation of alcohols, phenols, ketones, alkenes and carboxylic acids are pivotal reaction in organic synthesis.[112,113] Traditionally, such reactions have been performed with inorganic oxidants containing chromium and manganese reagents or by strong inorganic acids.[114] The emphasis in recent times is on developing recyclable catalysts to bring about oxidation reactions using clean oxidants such as oxygen and hydrogen peroxide, under mild conditions compared to classical oxidations. Metal complexes have attracted attention as dioxygen activating catalysts. But these homogeneous systems have several drawbacks, as they show a tendency for self degradation, and there is difficulty in reusing them. One means of overcoming these problems is to encapsulate them in zeolite pores. In recent times zeolite encapsulated complexes have been found to be catalytically active towards various oxidation reaction viz oxidation of alkanes, alkenes and alcohols. The encapsulated complexes are also reported to give high yield, high selectivity and most importantly they can be reused for several times.

Jacobs and co-workers reported the selective oxidation of alkanes and alkene by *cis*-$[Mn(bpy)_2]^{2+}$ complex (a) encapsulated in zeolite-Y (Scheme 1.1).[115] The selective epoxidation of alkenes using this encapsulated complex was achieved without complications from competing processes such as self-oxidation or catalyst activity. The zeolite encapsulated copper Schiff base and oxo-vanadium complexes are also well explored for oxidation of alkenes, styrenes and ethyl benzene.[101,116] The most important application of Schiff base complexes is as asymmetric catalysts for the enantioselective epoxidation of alkenes using zeolite-Y encapsulated manganese complex of bis(2,4-di-tert-butylsalicylidene)-1,2-cyclohexanediamine that is commonly known as the Katsuki-Jacobsen catalyst.[117,118] Very recently Katkar et al.[119] accounted for the green epoxidation of 1-hexene using [hydrazine-N-salicylidene-N_9-salicyloyl-]-

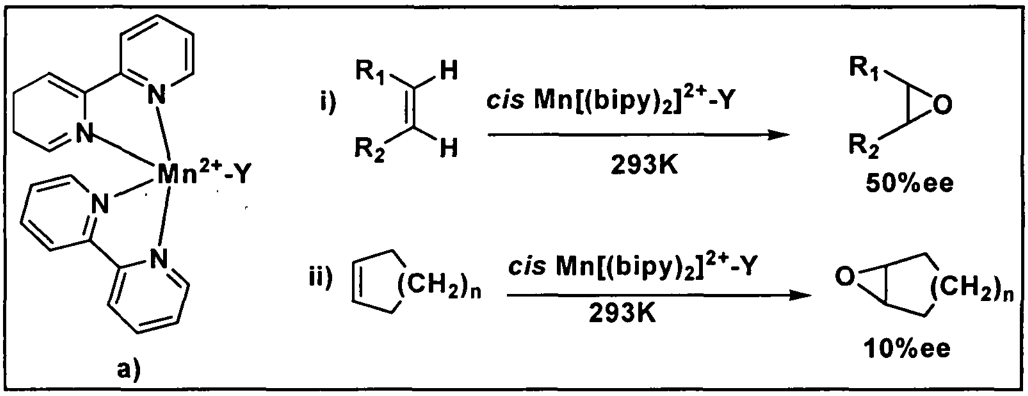

Scheme 1.1. Epoxidation of alkenes by *cis*-$[Mn(bpy)_2]^{2+}$ complex encapsulated in zeolite-Y.

cis dioxomolybdenum(VI) and its zeolite-Y composite as catalyst in DMF in the presence of molecular oxygen as oxidant and in the temperature range of 333-363 K.

The oxidation of alkanes catalyzed by metal complexes is often hampered by oxidative degradation of the catalyst and/or deactivation by irreversible dimerization of the complexes. To avoid this, Balkus Jr. et al.[105] employed an alternative strategy to enhance the lifetime and activity of such catalysts. They used zeolite X and Y encapsulated iron and ruthenium(II) perfluorinated phthalocyanines complexes as the halogen substitute phthalocyanines are less susceptible to electrophilic attack. These intrazeolite complexes exhibited high catalytic activity as much as 3 orders of magnitude greater than that of the homogeneous catalysts and appeared as promising catalysts for the oxidation of alkanes. In continuation with this, Bein et al. achieved success in olefin metathesis using rhenium oxo complexes encapsulated in zeolite-Y.[120] Ledney and Dutta succeeded in perfoming the oxidation of water to dioxygen by $[Ru(bpy)_3]^{2+}$ entrapped within the supercages of zeolite-Y.[121] Barton et al. used zeolite encapsulated Fe(III) picolinate complex for successful oxidation of cyclohexane by hydrogen peroxide.[122] García and co-workers reported the encapsulation of iron picolinate inside a series of zeolites and found that the zeolites containing encapsulated picolinate complex are efficient and reusable heterogeneous catalysts for the oxidation of cyclohexane to cyclohexyl hydroperoxide, cyclohexanol and cyclohexanone.[123] Analogously, vanadyl picolinate encapsulated within NaY was also found active for the oxidation of alkanes, alcohols and benzene with hydrogen peroxide.[124] Jacobs and coworker reported that the ship in a bottle synthesis of an iron complex of a tetradentate N_4 ligand derived from 2-pyridinecarboxamide is able to effect the oxidation of cyclohexane to cyclohexyl hydroperoxide as well as cyclohexanol and cyclohexanone.[125] Schiff-base and phthalocyanine complexes of transition metals are also established to be active catalyst for such oxidation processes. Kervinen et al.[126] stabilized a mononuclear copper (II) complex with one MIm_2Pr ligand [MIm_2Pr) 3, 3-bis(1-methylimidazol-2-yl)propionate] in the supercages of zeolite-Y and the resulting materials were tested for the catalytic oxidation of benzyl alcohol. Benzaldehyde was obtained above 90% and the encapsulated complex was found to have high turn over number (TON) in comparison to the neat complex. Güne et al.[127] for the first time reported for the oxidation of carvocol using Schiff base complexes of Cr(III), Fe(III), Bi(III), Ni(II), and Zn(II) in presence of hydrogen peroxide. The iron complex was found to produce high amount (22%) of thymoquinone without any by-products.

Selective oxidation of phenol to catechol is one of the important oxidation reactions. Catechol and hydroquinone are two of the many phenolic derivatives of high value. They are widely used, as photographic chemicals, antioxidants, and polymerization inhibitors and are also used in pesticides, flavouring agents, and medicine.[128] Some of the transition metal framework-substituted zeolites have been reported to exhibit attractive catalytic conversion, selectivity and stability in phenol hydroxylation.[129] However, difficulties lie in their synthesis and are not economically viable. In recent times, a lot of attention has been devoted by researchers in search of an alternative source for selective hydroxylation of phenol. As part of an alternative approach for direct synthesis of phenol to catechol, zeolite encapsulated organometallic compounds and transition metal complexes are used because of their high selectivity and efficient catalytic activity, Scheme 1.2. Raja et al.[130] performed selective oxidation of phenol using Cu-salenY complexes. Maurya and his group also designed various metal complexes inside zeolite-Y cavity for selective oxidation of phenol.[131]

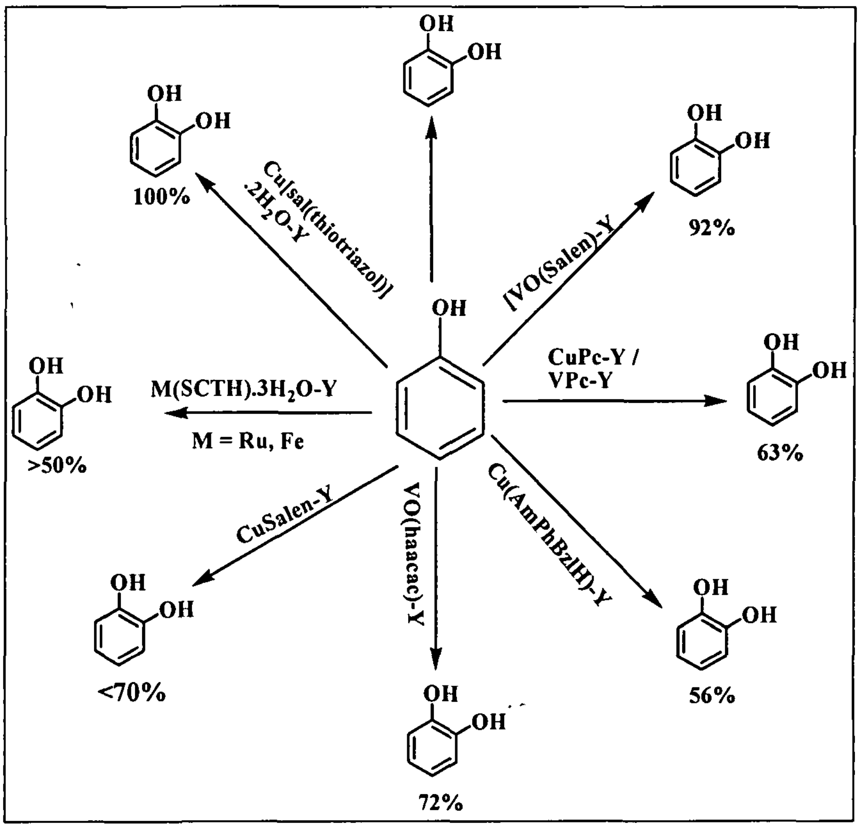

Scheme 1.2. Oxidation of phenol to catechol using different zeolite-Y encapsulated transition metal complexes.

Seelan et al. and Zsigmond et al.[132] used metal phthalocyanine complexes for oxidation of phenol in presence of peroxide. Oxovanadium(IV) tetradentate Schiff-base complexes, [VO(X_2-haacac)] (X = H, Cl, CH_3 and NO_2), X_2-haacac = substituted bis(2-hydroxyanil) acetylacetone, encapsulated zeolite NaY, [VO(X_2-haacac)]-NaY, was used by Salavati-Niasari et al. for oxidation of phenol.[133] Nethravathi et al. used zeolite-encapsulated 2-(*o*-aminophenyl) benzimidazole complexes for phenol oxidation in presence of 30% peroxide. High to moderate yield of catechol was obtained.[134] Abbo et al. reported for high selective oxidation of phenol to catechol using zeolite-Y encapsulated thio Schiff base complexes of Cu(II), Fe(III) and Bi(III).[135] Very recently, Modi and Trivedi designed zeolite-Y based nanohybrid materials with general formulae [M(STCH)·$3H_2O$]-Y and [M(SFCH)·$3H_2O$]-Y [where, M = Ru(III) and Fe(III), STCH = salicylaldehyde thiophene-2-carboxylic hydrazone, SFCH = salicylaldehyde furoic-2-carboxylic hydrazone] for selective hydroxylation of phenol.[136]

1.5.2.2. Asymmetric Catalyst

Due to high application of chiral molecules in pharmaceutical markets, drug designing and production of natural compounds, asymmetric catalysis have always been given the higher priority compared to other catalysis.[137-139]..The award of Nobel Prize for chemistry in 2001 by William S. Knowles and Ryoji Noyori "for their work on "*chirally catalysed hydrogenation reactions*" and K. Barry Sharpless "for his work on "*chirally catalysed oxidation reactions*" the homogeneous asymmetric catalysis has made big progress during the last decades.[140] However, the difficulties in the catalyst separation and recycling of homogeneous catalysts often make the practical application difficult.[141] Heterogeneous catalysis supplies the opportunity for easy separation and recycle of catalyst, easy purification of product, and, possibly, continuous or multiple processing of chiral compounds.[142] Although heterogeneous asymmetric catalysis has potential advantages over the homogeneous ones, still much intense research interest has not focussed on heterogenization of homogeneous chiral catalyst. The probable reason might be i) upon immobilization or encapsulation onto solid support the catalyst might get distorted due to confinement effect or various other effects discussed previously. And once it suffers the distortion, the substrate may find it difficult to access the active site thereby decreasing the catalytic performance. ii) Leaching of the catalyst on immobilization may cause severe damage to activity of the chiral catalyst. These difficulties limit the heterogeneous asymmetric catalysis to only few successful examples, and, therefore, hinder the heterogeneous asymmetric catalysis from fast development.

The current progress in the designing of chiral heterogeneous catalyst has demonstrated the possibility of preparing the robust heterogeneous chiral catalysts retaining the chirality. Some heterogeneous catalysts have been found to have higher stability and shows the catalytic performance as good as homogeneous catalysts or even higher than their corresponding homogeneous catalysts. J. M. Thomas and R. Raja have well documented in their review article about the application of the mesoporous and microporous materials in designing of chiral heterogeneous catalyst and their application in their asymmetric catalysis.[143] C. Li also well described the synthesis of chiral catalyst on solid supports.[144] A closer look into various other literatures suggest that these types of catalysts are widely studied extremely over mesoporous MCM-41 and silica.[61,145] However, less has been done on the zeolite-Y encapsulated complexes. Corma et al. first performed hydrogenation of *N*-acylphenylalanine derivatives using zeolite supported transition metal chiral catalysts.[146] The heterogeneous catalyst (3a-3d) obtained by tethering of proline-derived amide 1a chelated metal complex of [Rh(I), Ru(II), Co(II), or Ni(II)] on modified Y zeolite (USY) (Scheme 1.3) found to show high enantioselectivity (99%) in comparison to the unbound catalyst (2a-2d, 87%). These results emphasize the role of the micropores of the zeolite in stereoselective induction of the catalyzed reaction. Taylor et al.[147] reported that chiral Cu(II) bis(oxazoline) complex confined in zeolite-Y shows superior enantioselectivity (ee of 93%) compared with 57% for the homogeneous catalyst in the reaction of methylenecyclopentane with ethyl glyoxalate. The $[Rh(COD)L]^+$ complexes (L= L-prolinamide or N-tert-butyl-L-prolinamide) encapsulated in NaY zeolite[148] are also reported to catalysed the enantioselective hydrogenation of (*Z*)-methyl-α-acetamidocinnamate and trans-2-

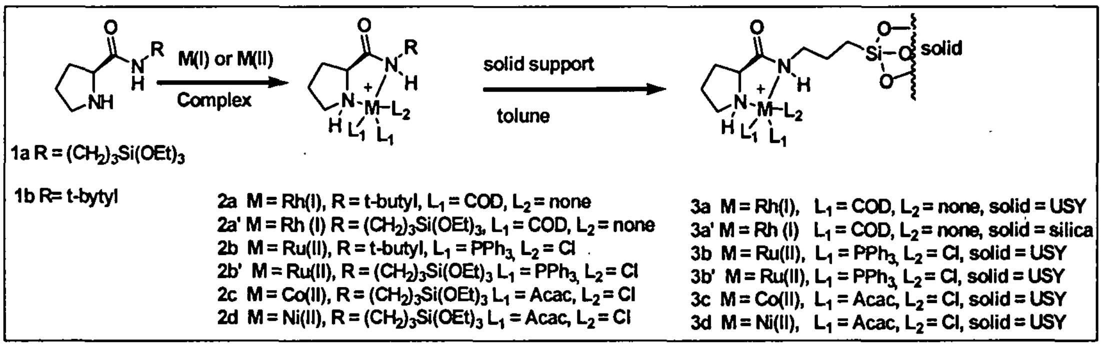

Scheme 1.3. Hydogenation of *N*-acylphenylalanine derivatives by zeolite supported complexes.

methylpent-2-enoic acid. This catalyst was found to exhibit higher activity and enantioselectivity than the homogeneous rhodium complex.

Among the various transition metals chiral catalysts, the chiral Schiff-base complexes are well studied over the microporous support. The first successful preparation of a Mn-based chiral salen complex encapsulated into the supercages of a large pore zeolite has been accomplished, approximately simultaneously, by Sabatier using the zeolite-Y[149] and by Ogunwumi and Bein using the EMT zeolite.[150] The zeolite encapsulated Mn(III) complex found to be suitable catalyst for epoxidation of alkenes. Other salen-metal complexes, such as those of cobalt[151] and chromium[152] have also been encapsulated inside the zeolite cages. The salen-cobalt complex entrapped inside the ultrastable zeolite-Y (USY) is used as asymmetric heterogeneous catalyst for the transhydrogenation of acetophenone. Zeolites-Y and EMT are used as hosts to immobilize salen-chromium complexes, which are employed for the asymmetric ring opening of epoxides (namely, cyclohexane oxide and cyclopentane oxide). However, these complexes give less enantioselectivity and low recyclability in comparison to the homogeneous complexes. The reason for this low catalytic ability of these heterogeneous complexes was due to steric constrained imposed by the zeolite walls and leaching of the metal complex. Hölderich and co-workers solved this problem of moderate enantiomeric excesses in the SIB (ship in a bottle) strategy by introducing a post-synthetic zeolite modification prior to complex encapsulation to generate some mesoporosity in the zeolite particles.[153,154] The chiral salen-metal complexes

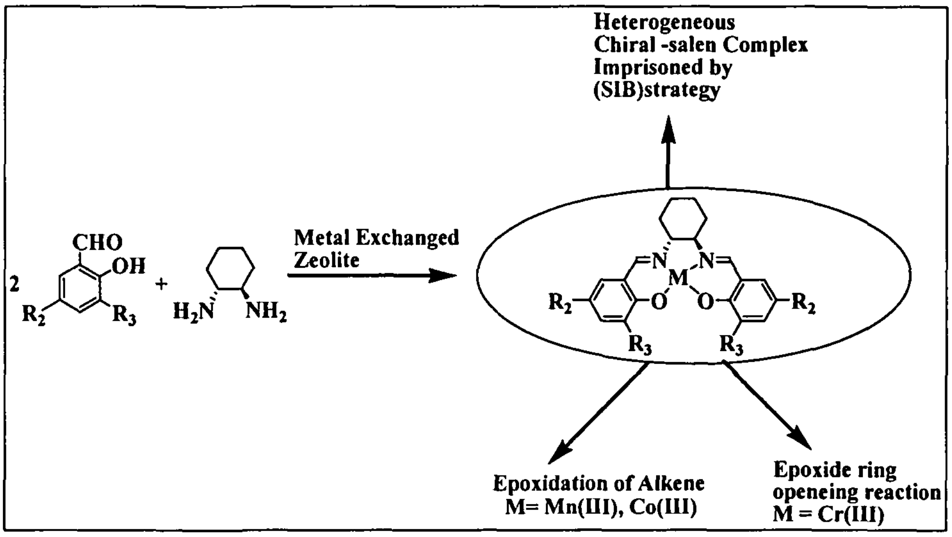

Scheme 1.4. "*Ship in a bottle*" synthesis of chiral Schiff base complexes inside zeolite-Y and their apllication in epoxidation recations.

encapsulated in these new materials are those of cobalt and manganese, using trans-1,2-diphenylethylene-1,2-diamine as the chiral diamine to form the salen complex, Scheme 1.4.[155] These heterogeneous salen-metal catalysts are used for the asymmetric epoxidation of olefins (limonene and α-pinene). Compared with the homogeneous analogues, the zeolite encapsulated chiral salen complexes result in higher reactions rates and ee values without loss of the chemoselectivity.

Enantioselective Henry reaction and C-C coupling of 2-napthol are two very important outcome of asymmetric catalysis. The products of Henry reaction are essential starting material for various important organic and bio-molecules. The significant success in nitro-aldol condensation has been achieved by Shibasaki and Trost using dinuclear metal complexes.[156-159] Subsequently, Evans's and Palomo's chiral catalyst are both found to be effective towards enatioselective nitro-aldol condensation.[160,161] The oxidative coupling of 2-napthol is a representative reaction mode for direct synthesis of 1,1′-binapthol (BINOL) whose optically pure derivatives are regarded as versatile chiral auxiliaries and ligands in asymmetric synthesis. However, these substances remain largely unstudied because of their difficulties in synthesis. Most of the recently published highly enantioselective syntheses of BINOL and its derivatives are based on naphthol coupling catalyzed by chiral complexes containing one or two metal centre(s) viz., vanadium, iron or copper.[162-166] The formation of a self dimerized chiral assembly of vanadium complexes on a SiO_2 surface is also reported to promote the enantioselective naphthol coupling.[167] However, zeolite encapsulated metal complexes are less explored to bring out both the C-C bond formation reaction. Hence, there remains a lot of scope in designing newer catalyst inside the pore of zeolite-Y for asymmetric version of Henry reaction and C2-symmetric BINOL and its derivatives.

1.6. Density Functional Theory (DFT) Studies on Zeolite Encapsulated Complexes

Various spectrochemical and physicochemical techniques such EDX, SEM, XRD, FTIR, XPS, EPR, UV-vis/DRS and CV studies are implemented to locate the presence of transition metal complexes in the internal voids of zeolite. However, the experimental studies give very little information regarding the type of interaction that may occur in the supramolecular host-guest system and about the influence of the zeolite matrix on the structure and electronic properties of the inclusion compounds.

Therefore, it is equally imperative to understand the effect of confinement on the properties of zeolite embedded complexes. Quantum chemical calculation can play a vital role in understanding the fundamental aspects of the inclusion compounds. Zicovich-Wilson et al.[85] based on Hückel Molecular Orbital Theory (HMOT) well explained the effect of confinement on the molecular orbital energy levels and the catalytic activity of ethylene molecule when trapped into a microscopic cavity. Quantum chemical calculations have also proven that Si-O bonds in zeolites have covalent character.[168] Valence electrons in zeolites are distributed all over the framework atoms as a partially delocalized electronic cloud. At relatively short distances between the complex molecule and the walls of the zeolite cavities, the electron-electron repulsions will be operative, which will influence the structural and electronic behaviour of the zeolite embedded complexes.

So far, most of the initial quantum chemical studies carried-out to study the complex formation are the Møller–Plesset perturbation theory (MP2, MP3 or MP4), molecular dynamics (MD)[169], semi-empirical quantum mechanics (QM)[170] methods and Hartree-Fock method.[171] The semi-empirical methods give only qualitatively correct conclusions, whereas the non-empirical methods give semi-quantitative to quantitative results depending on the basis set used and the degree of inclusion of correlation energy. The transition from semi-empirical to non-empirical method is accompanied by a sharp increase in the computation time. *Ab initio* methods are the most rigorous methods. Most of the calculations are carried out using the STO-3G basis set.[171] Increase in the quality of basis set or size of the cluster and inclusion of heavy atoms increase the computation time sharply. Quantum chemical calculations based on density functional theory (DFT) offer a good compromise between the need for rigorous calculations and the problems of computing time. In recent years, DFT calculation has been explicitly used as strong tool in understanding the mechanism of various organic transformations mediated by various homogeneous transition metal and organometallic complexes.[172] DFT calculation has also been applied to predict the basicity of zeolites, in gas adsorption study, spectroscopic analysis, reactivity and catalytic study of various zeolites.[173-177] Besides these applications, this theory has also gain importance in understanding the structural parameter, complex formation, host-guest interaction and different allied properties like hardness (η), softness (S) and binding energy etc. of the encapsulated complexes. The transition metal complex when encapsulated undergoes a constrain chemistry due to the space restriction imposed by the walls of zeolite cavity. This changes their redox behaviour, electronic and magnetic behaviour and hence, thereby modifies the catalytic activity the encapsulated complexes. The reduction and the oxidation potential of a given species are often interrelated to the energies of the frontier orbitals ($Oxd^n = E_{HOMO}$ and $red^n = E_{LUMO}$). Therefore, by calculation of the energies of the HOMO and LUMO energies of the zeolite embedded complexes one can easily explain the change in the redox behaviour of the encapsulated complexes. To understand the nature of change in redox behaviour of zeolite-Y encapsulated bis-(ethylenediamine)Cu(II), (Cu-en) and bis-(8-hydroxyquinoline) Mn(II), (Mn-Qn) complexes, Viswanathan and his co-workers [178] performed DFT calculation on both the neat and encapsulated Cu-en and Mn–Qn complexes in 10- and 12-membered ring clusters. In both the cases, DFT calculation envisaged that the two complexes suffer distortion from the square planar geometry due to the influence of the zeolite walls and changes their geometrical parameters (the bond length and bond angle). This in turn also changes the HOMO and the LUMO energies of encapsulated complexes in comparison to the neat complexes and changes the redox behaviour of the two complexes. In both the encapsulated complexes, the HOMO and the LUMO energies are found to increase in comparison to the neat complexes.

A good number of global and local reactivity descriptors are available in DFT which can be explicitly used to understand the effect of zeolite matrix on the structure, electronic properties and reactivity of intrazeolite complex. The global reactivity descriptors such as chemical potential (μ), global hardness (η), and global softness (S) can be established within the purview of density functional theory. Recently, Jafarian et al.[179] performed DFT-calculation on zeolite-Y encapsulated Ni(II)-(N,N'-bis(2,4-dihydroxyacetophenone)-2,2dimethyl-propandiimine, Ni(II)(salnptn(4-OH)$_2$} complex to investigate changes in structural parameters, energies of the HOMO and LUMO, and absolute hardness and softness in comparison to the neat complex. They observed that upon encapsulation the HOMO and LUMO orbitals of the Ni(II) complex gets lifted up with a decrease in the HOMO-LUMO gap, (Figure 1.7) which in turn changes the global hardness and softness of the encapsulated complex.

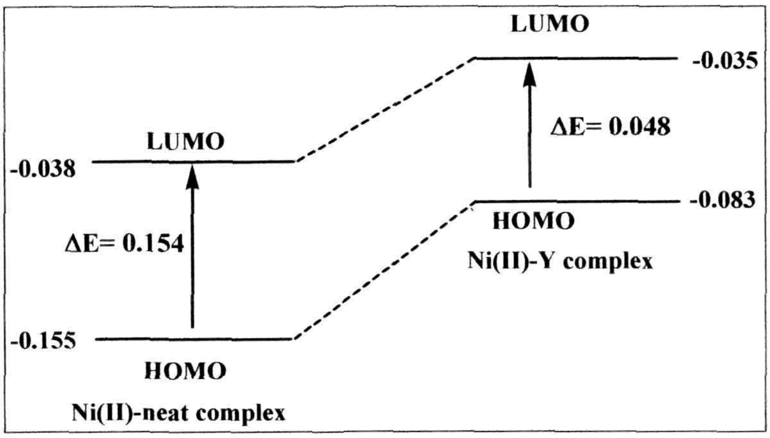

Figure 1.7. Change in HOMO and LUMO energies (in a.u.) in the neat and the encapsulated {Ni(II)(salnptn(4-OH)$_2$}complex.

Corrêa et al.[180] used DFT calculation in order to elucidate the position and geometry of Fe and Mn Salen (Salen = N,N'-(salicylaldehyde)ethylenediamine) complexes inside the Y zeolite. It was observed that both Fe and Mn(Salen) complexes occupy two cages of Y zeolite instead of only one cavity, Figure 1.8. Further due to interaction with zeolite walls the two complexes are found to deviate from square planar geometry.

Modi et al.[181] performed DFT calculation on some Schiff base complexes of general formula [M(STCH).xH$_2$O]-Y [where M = Mn(II), Fe(II), Co(II), Ni(II), (x = 3) and Cu(II), (x = 1), STCH = salicylaldehyde thiophene-2-carboxylic hydrazone]. They also observed change in the HOMO and LUMO energies of the encapsulated complexes as the complexes gets distorted inside the zeolite cavity.

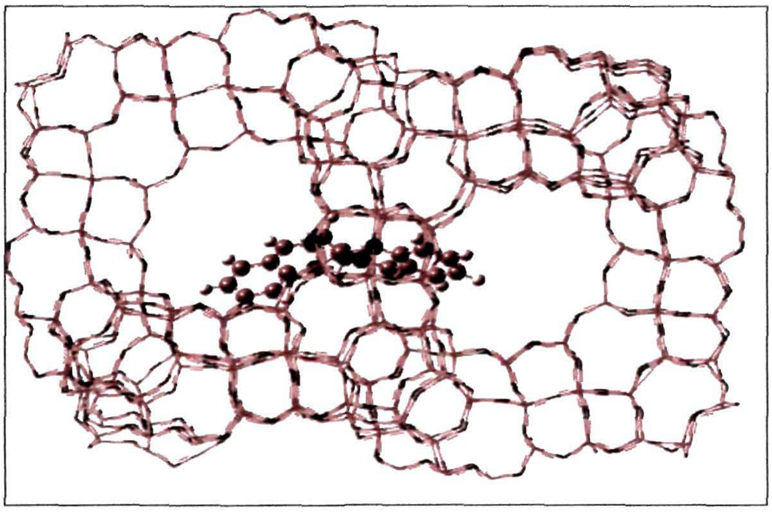

Figure 1.8. Mn(Salen) complex occupying two different cavities inside zeolite-Y.

Vargas et al.[182] applied density functional theory within a supramolecular approach to study the guest-host interactions in $[Fe(bpy)_3]^{2+}$Y(Figure 1.9) and their influence on the structural, energetic and ^{57}Fe Mössbauer spectroscopy properties of the encapsulated $[Fe(bpy)_3]^{2+}$ complex in the low- and high-spin states. They observed that in either spin state, the structure of $[Fe(bpy)_3]^{2+}$ shrinks and distorts upon encapsulation. Based on their calculations they also proposed that the bonding between the complex and the supercage is more electrostatic than covalent. The calculated quadrupole splitting of ^{57}Fe values are found to be in good agreement with the experimental one.

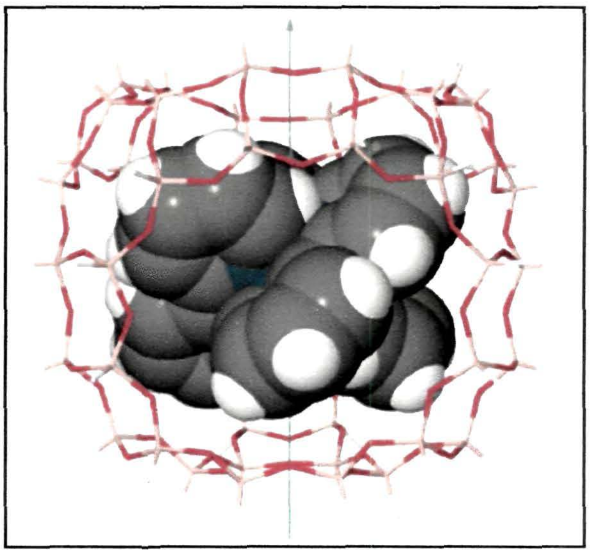

Figure 1.9. Molecular modelling of $[Fe(bpy)_3]^{2+}$ complex inside zeolite-Y.

1.7. Objective of the Present Work

The intrazeolite complexes due to heterogeneous nature possess great advantages over the homogeneous counterparts. Because of which in present days they have gained wide interest both in industry and academics. The synthesizing of inorganic complexes inside the cavity of zeolite-Y not only provides a viable path for rationalizing the catalytic activity of transition metal complexes but also enables one in designing of newer supramolecular host-guest system which can be helpfull in mimicking the biosystem, devising molecular switches and sensors. Till now a large number of researchers have made significant contribution in designing intrazeolite complexes and their application in various fields. However, there remains a lot of scope in synthesis, characterization and catalytic study of newer heterogeneous systems. Especially a very little success has been achieved in asymmetric catalysis using these heterogeneous systems. Moreover, despite the growing interest in the field of computational chemistry, DFT calculations has not been implemented to great extent to understand the structural, electronic and reactivity behaviours of encapsulated complexes. So keeping all these features in mind the present work has been designed based on the following objectives

- Encapsulation of transition metal complexes of Fe, Cu, Ni, Co and Zn inside zeolite-Y.
- Characterization of the intrazeolite complexes using various spectrochemical and physicochemical techniques.
- Making a comparative study between the neat and zeolite encapsulated complexes.
- Examining the effect of the zeolite framework on the structure, electronic and reactivity of the complex using density functional theory (DFT) calculation.
- Assessing the catalytic behaviour of the neat and encapsulated complexes and to study the reaction mechanism using DFT calculation.

References

[1] Jeffey, G. A. *An Introduction to Hydrogen Bonding*, Oxford University Press, New York, 1997.

[2] a) Barrer, R.M. *Zeolites* **1**(3), 130-140, 1981 b) Milton, R. M. *Molecular Sieves Adsorbents*. **U.S. Patent 2, 882, 244,** April 14, 1959.

[3] Wojciechowski, B. W., & Corma, A. *Catalytic Cracking, Catalysts Kinetics and Mechanisms*, Marcel Dekker, New York, 1984.

[4] Thomas, J. M. *Angew. Chem. Int. Ed. Engl.* **27**(12), 1673-1691, 1988.

[5] Venuto, P. B. *Microporous Mater.* **2**(5), 297-411, 1994.

[6] a) Guisnet, M. *Heterogeneous Catalysis and Fine Chemicals* II Elsevier, Amsterdam, 1991, b) Guisnet, M. *Heterogeneous Catalysis and Fine Chemicals* III, Elsevier, Amsterdam, 1993.

[7] a) Corma, A., & García, H. *Chem. Rev.* **102**(10), 3837-3892, 2002, b) Corma, A. & García, H. *Chem. Rev.* **103**(11), 4307-4365, 2003.

[8] Alcón, M. J., et al. *J. Organomet. Chem.* **655**(1-2) 134-145, 2002.

[9] Chaudhari, R. V. *Platinum Metals Rev.* **55**(3), 180-185, 2011.

[10] Blaser, H. U., et al. *Heterogeneous Catalysis and Fine Chemicals,* 4th ed., Elsevier Science Ltd, Amsterdam, 1997.

[11] Parshall, G. W., & Ittel, S. D. *Homogeneous Catalysis,* 2nd ed., Wiley, New York, 1996.

[12] Elschenbroich,Ch., & Salzer, A. *Organometallics,* 2nd ed., VCH, Weinheim,1992.

[13] Marciniec, B. *Coord. Chem. Rev.* **249**(21-22), 2374-2390, 2005.

[14] Fadhel, A. Z., et al. *Molecules* **15**(11), 8400-8424, 2010.

[15] McMorn, P., & Hutchings, G. J. *Chem. Soc. Rev.* **33**, 108-122, 2004.

[16] Cole, H. D. J. *Science* **299**(5613), 1702-1706, 2003.

[17] Skinner, K. J. *Chem. Eng. News* **55**(6), 18-19, 1977.

[18] George, S. M. *Chem. Rev.* **95**(3), 475-476, 1995.

[19] Fryzuk, M. *J. Am. Chem. Soc.* **122**(21), 5233-5234, 2000.

[20] Ding, K., & Uozumi, Y. *Handbook of Asymmetric Heterogeneous Catalysis,* Wiley-VCH, Weinheim, 2008.

[21] Collis, A. E. C., & Horváth, I. T. *Catal. Sci. Technol.* **1**, 912-919, 2011.

[22] a) Corma , A., & García, H. *Eur. J. Inorg. Chem.* **2004**(6) 1143-1164, 2004, b) Xuereb, D. J., & Raja, R. *Catal. Sci. Technol.* **1**, 517-534, 2011.

[23] Ray, S., & Vasudevan, S. *Inorg. Chem.* **42**(5), 1711-1719, 2003.

[24] Chen, P., et al. *Catal. Commun.* **7**(12), 969-973, 2006.

[25] Ebitani, K., et al. *Chem. Commun.* 869-870, 2000.

[26] Mirkhani , V., et al. *Appl. Catal. A: General* **321**(1) 49-57, 2007.

[27] Pietrzyk, P., et al. *J. Am. Chem. Soc.* **133**(49), 19931-19943, 2011.

[28] Jacob, C. R., et al. *Appl. Catal. A* **182**(1), 91-96, 1999.

[29] Jacob, C. R., et al. *Micropor. Mesopor. Mat.* **22**(1), 465-474, 1998.

[30] van Bekkum, H., et al. *Introduction to Zeolite Science and Practice* Elsevier, Amsterdam, 1991.

[31] Hammonds, K. D., et al. *J. Phys. Chem. B* **102**(10), 1759-1767, 1998.

[32] Depmeier, W. *In: Molecular Sieves: Science and Technology,* Springer-Verlag, Berlin, 2001.

[33] Bell, R. G., et al. *Zeolites* **12**(7) 870 - 871, 1992.

[34] Yang, C. S., et al. *J. Phys. Chem. C* **115**(49), 24102-24114, 2011.

[35] Corma, A. *Chem. Rev.* **95**(3), 559-614, 1995.

[36] Hagen, J. *Industrial Catalysis A Practical Approach* Wiley-VCH Verlag GmbH & Co. KGaA, Weinheim, Germany, 2006.

[37] Scott, M. A., et al. *Handbook of Zeolite Science and Technology*, Marcel-Dekker, New York, 2003.

[38] Jiang, X. J., et al. *J. Phys. Chem. B* **108**(40), 15728-15734, 2004.

[39]Ma, Y., et al. *Micropor. Mesopor.Mat.* **37**(1-2), 243-252,

2000.

[40] van Donk, S., et al. *Catal. Rev.* **45**(2), 297-319, 2003.

[41] Gabuda, S. P., et al. *Appl. Magn. Reson.*, **41**, 431-437, 2011.

[42] García, H., & Roth, H. D. *Chem. Rev.* **102**(11), 3947-4007, 2002.

[43] Yoon, K. B. *Chem. Rev.* **93**(1), 321-339, 1993.

[44] a) Xing, G.W., et al. *Tetrahedron* **56**(22), 3517-3522, 2000, b) Shailaja, J., et al. *Tetrahedron* **56**(36), 6927-6943, 2000.

[45] Lalitha, A., et al. *Tetrahedron* **57**(20), 4455-4459, 2001.

[46] Schuster, C., et al. *Catal. Lett.* **74**(1-2), 69-75, 2001.

[47] Rees, L.V.C. *Nature* **309**, 583-583, 1984.

[48] Bhan, A., & Iglesia, E. *Acc. Chem. Res.* **41**(4), 559-567, 2008.

[49] Smit, B., & Maesen, T. L. M. *Nature* **451**, 671, 2008.

[50] Clark, L. A., et al. *J. Am. Chem. Soc.* **126**(3), 936-947, 2004.

[51] Nishina, Y., & Takami, K. *Green Chem.* **14**, 2380-2383, 2012.

[52] Nasrollahzadeh, M., et al. *Tetrahedron* **65**(51) 10715-10719, 2009.

[53] Gortsov, Yu. G. *Theo. Exp. Chem.* **35**(4), 183-197, 1999.

[54] Incavo, J. A., & Dutta, P. K. *J. Phys. Chem.* **94**(7), 3075-3081, 1990.

[55] Pokhrel, M. R., et al. *J. Phys. Chem. C* **113**(11), 4560-4565, 2009.

[56] Barrer, R. M. *Mol. Seieves Pap.Conf.* 39-46, 1968.

[57] Alco'na, M. J., et al. *J. Organomet. Chem.* **655**(1-2), 134-145, 2002.

[58] Joseph, T., et al. *J. Mol. Catal. A: Chemical* **184**(1-2) 289-299, 2002.

[59] Silva, A. R., et al. *Ind. Eng. Chem. Res.* **50**(20), 11495-11501, 2011.

[60] a) Mukhopadhyay, K., et al. *Chem. Mater.* **15**(9), 1766-1777, 2003, b) Huang, T. N., & Schwartz, J. *J. Am. Chem. Soc.* **104**(19), 5244-52451, 1982.

[61] Baleizão, C., & Garcia, H. *Chem. Rev.* **106**(9), 3987-4043, 2006.

[62] Teixeira, C., et al. *New J. Chem.* **32**, 2263-2269, 2008.

[63] Mori, K., et al. *Phys. Chem. C* **112**(7), 2593-2600, 2008.

[64] Park, Y. S., et al. *J. Am. Chem. Soc.* **121**(13), 3193-3200, 1999.

[65] Park, Y. S., et al. *J. Am. Chem. Soc.* **124**(24), 7123-7135, 2002.

[66] Zakharov, A. N., & Romanovsky, B. V. *Incl. Phenom.* **3**(18), 385-389, 1985.

[67] Lyons, J. E., et al. *J. Catal.* **155**(1), 59-73, 1995.

[68] Ellis Jr. P. E., & Lyons, J. E. *Coord. Chem. Rev.* **105**(1), 181-193, 1990.

[69] Herron, N., & Tolman, C. A. *J. Am. Chem. Soc.* **109**(9), 2837-2839, 1987.

[70] Herron, N. *Inorg. Chem.* **25**(26), 4714-4717, 1986.

[71] Corbin, D. R., & Herron, N. *J. Mol. Catal.* **86**(1-3), 343-369, 1994.

[72] Herron, N. *J. Coord. Chem.* **19**(1-3), 25-38, 1988.

[73] Howe, R. F., & Lunsford, J. H., *J. Phys. Chem.* **79**(17), 1836-1842, 1975.

[74] Srinivas, D., & Sivasanker, S. *Catal. Surv. Asia* **7**(2-3), 121-132, 2003.

[75] PBez-Mozo, E., et al. *J. Phys. Chem.* **97**(49), 12819-12827, 1993.

[76] Corma, A., et al. *Chem. Mater.* **16**(7), 1170-1176, 2004.

[77] Kumar, S., et al. *J. Mol. Catal. A: Chemical* **154**(1-2), 115-120, 2000.

[78] Kozlov, A., et al. *J. Chem. Soc. Faraday Trans.* **94**(6), 809-816, 1998.

[79] Groen, J. C., et al. *Micropor. Mesopor. Mater.* **87**(2), 153-161, 2005.

[80] Weckhuysen, B. M., et al. *Angew. Chem. Int. Ed. Engl.* **34**(23-24), 2652-2654, 1995.

[81] Grommen, R., et al. *J. Am. Chem. Soc.* **122**(46), 11488, 2000.

[82] Scaiano, J. C., & García, H. *Acc. Chem. Res.* **32**(9), 783-793, 1999.

[83] Zicovich-Wilson, C. M., & Corma, A. *J. Phys.Chem.* **98**(42), 10863-10870, 1994.

[84] (a) Rabo, J. A., & Gajda, G. J. *In Guidelines for Mastering The Properties of Molecular Sieves,* NATO AS1 Series, Plenum, New York, 1990, (b) Mirodatos, C., & Barthomeuf, D. *J. Catal.* **93**(2) 246-255, 1985, (d) Uytterhoeven, L., et al. *J. Chem. Soc. Faraday Trans.* **88**(18), 2753-2760, 1992, (d) Barrer, R. N. *In Zeolites and Clay Minerals,* Academic Press, London, 1978, (e) Teunissen, E. H., et al. *J. Phys. Chem.* **97**(1), 203-210, 1993, f) Teunissen, E. H., et al. *J. Phys. Chem.* **96**(1), 366-371, 1993, (g) Derouane, E. *In Guidelines for Mastering The Properties of Molecular Sieves,* NATO AS1 Series, Plenum, New York, 1990.

[85] Mizuno, K., & Lunsford, J. H. *Inorg. Chem.* **22**(23), 3484-3486, 1983.

[86] Figgis, B. N., et al. *J Chem. Soc. A* 2086, 1968.

[87] Xuereb, D., et al. *Catalysis by Metal Complexes: Heterogenized Homogeneous Catalysts for Fine Chemical Production*, Springer, Dordrecht, 2010.

[88] Mesu, J. G., et al. *Chem.Eur. J.* **12**(27) 7167-7177, 2006.

[89] Corma, A., & García, H. *Eur. J. Inorg. Chem.* **2004**(6), 1143-1164, 2004.

[90] Cantrill, S. J., et al. *Acc. Chem. Res.* **38**(1), 1-9, 2005.

[91] Stoddart, J. F., *Acc. Chem. Res.* **34**(6), 410-411, 2001.

[92] Shpiro, E. S., et al. *Stud. Surf. Sci. Catal.* **18**(1), 31-39, 1984.

[93] Meyer, G., et al. *Zeolites* **4**(1), 30-34, 1984.

[94] Zakharov, V. Y., et al. *React. Kinet. Catal. Lett.*, **6**, 133-137, 1977.

[95] Herron, N. *Biocatalysis and Biomimetics, ACS Symposium Series*, Chapter 11, 1989,141-154,

[96] Weitkamp, J., et al. *Zeolites and Related Microporous Materials: State of the Art*, Elsevier, Amsterdam, 1994.

[97] Weitkamp, J. *Proceedings of the 9th International Zeolite Conference*, Montreal, 1992.

[98] Li, G. Q., & Govind, R. *Inorg. Chim. Acta.* **217**(1-2), 135-140, 1994.

[99] Balkus Jr., et al. *Appl. Catal. A* **143**(1), 159-173, 1996.

[100] Bedioui, F., et al. *Electrochem. Soc.* **141**(11), 3049-3052, 1994.

[101] a) Balkus Jr., K. J., et al. *Zeolites* **10**(8), 722-729, 1990, b) Balkus Jr., K. J., et al. *J. Incl. Phenom. Mol. Recog.* **10**(1), 141-151, 1991.

[102] Balkus Jr., K. J. " *Zeolite Encapsulated Metallophthalocyanines", in Phthalocyanines*, Lever, A.B.P. & Leznoff, C. C. eds., VCH Publishers, 1996.

[103] Balkus Jr., K. J., et al. *J. Am. Chem. Soc.* **117**(43), 10753-10754, 1995.

[104] Parton, R. F., et al. *Nature* **370**, 541, 1994.

[105] Ichikawa, M., et al. *Stud. Surf. Sci. Catal.* **60**(1-2), 335-342, 1991.

[106] Zhan, B. Z., & Li, X. Y. *Chem. Commun.* 349-350, 1998.

[107] Sulikowski, B., et al. *Catal. Lett.*, **39**(1-2), 27-31, 1996.

[108] Dutta, P. K., & Incavo, J. A. *J. Phys. Chem.* **91**(17), 4443-4446, 1987.

[109] Cojocaru, B., et al. *Langmuir* **24**(9), 4478-4481, 2008.

[110] Shimizu, K., et al. *J. Phys. Chem. C* **111**(17), 6440-6446, 2007.

[111] a)Alvaro, M. B., et al. *J. Phys. Chem. B* **106**(26), 6815-6820, 2002, b) Alvaro, M. B., et al. *Chem. Commun.* 2106-2107, 2001.

[112] Hudlicky, M. *Oxidations in Organic Chemistry*, American Chemical Society, Washington DC, 1990.

[113] Sheldon, R. A., et al. *Acc. Chem. Res.* **35**(9) 774-781, 2002.

[114] Smith, M. B., & March, J. *March's Advanced Organic Chemistry*, 6th ed., Willey, London, 2007.

[115] Knops-Gerrits, P. P., et al. *Nature* **369**, 543 - 546, 1994.

[116] a) Maurya, M. R., et al. *J. Mol.Catal. A: Chemical* **278**(1-2), 12-21, 2007, b) Maurya, M. R., et al. *Eur. J. Inorg. Chem.* **2007**(36), 5720-5734, 2007, c) Zsigmond, A., et al. *J. Mol.Catal. A: Chemical* **171**(1-2) 95-102, 2001, d) Saha, P. K., et al. *J. Mol. Catal. A: Chemical* **203**(1-2) 173-178, 2003, e) Sabater, M. J., et al. *Chem. Comm.* 1285-1286, 1997, f) Joseph, T., et al. *J. Mol.Catal. A: Chemical* **184**(1-2) 289-299, 2002, g) Mauryaa, M. R., et al. *J. Mol. Catal. A: Chemical* **274**(1-2), 192-201, 2007.

[117] Hosoya, N., et al. *Tetrahedron* **50**(15), 4311-4322, 1994.

[118] Potvin, P. G., & Branchet, S. *J. Org. Chem.* **57**, 629-6635, 1992.

[119] Katkar, M. A., et al. *RSC. Adv.* **2**, 8071-8078, 2012.

[120] Bein, T., et al. *Chem. Mater.* **9**(11), 2252-2254, 1997.

[121] Ledney, M., & Dutta, P. K. *J. Am. Chem.* Soc. **117**(29), 7687-7695, 1995.

[122] Barton, D. H. R., & Doller, D. *Acc. Chem. Res.* **25**(11), 504-512, 1992.

[123] Alvaro, M., et al. *Tetrahedron* **55**(40), 11895-11902, 1999.

[124] Kozlov, A., et al. *Chem. Lett.* **26**(4), 313-314, 1997.

[125] Knops-Gerrits, P. P., et al. *Stud. Surf. Sci. Catal.* **101**, 811-820, 1996.

[126] Kervinen, K., et al. *J. Am. Chem. Soc.* **128**(10), 3208-3217, 2006.

[127] Güneş, A., et al. *Ind. Eng. Chem. Res.* **45**(1), 54-61, 2006.

[128] a) Korkina, L. G., et al. *Curr.Med. Chem.* **16**(30), 3943-65, 2009, and references cited therein, b) Nemoto, H., et al. *Org. Lett.* **13**(10), 2714-2717, 2011, c) Abraham, I., et al. *J. Braz. Chem. Soc.* **22**(3), 385-421, 2011, d) Nohl, H., et al. *Adv. Free Radical Biol.& Med.* **2**(1), 211-279, 1986.

[129] a) Deshpande, S., et al. *J.Catal.* **188**(2), 261-269, 1999, b). Maurya, M.R., et al. *J. Mol. Catal. A*: *Chemica*l **180**(1-2), 201-209, 2002, c) Maurya, M.R., et al. *J. Mol. Catal. A*: *Chemica*l **214**(2), 257-264, 2004.

[130] Raja, R., & Ratnasamy, P. *Appl. Catal. A: General* **143**(1), 145-158, 1996.

[131] Maurya, M. R., et al. *Catal. Lett.* **86**(1-3), 97-105, 2003.

[132] a) Seelan, S., & Sinha, A. K. *Appl. Catal. A: General* **238**(2), 201-209, 2003, b) Zsigmonda, A., et al. *Catal. Lett.* **65**(1-3), 135-139, 2000.

[133] Salavati-Niasar, M., et al. *J. Porous. Mater.* **14**(4), 423-432, 2007.

[134] Nethravathi, B. P. et al. *J. Porous. Mater.* **18**(2), 389-397, 2011.

[135] Abbo, H. S., & Titinchi, S. J. J. *Top. Catal.* **53**(3-4), 254-264, 2010.

[136] a) Modi, C. K., & Trivedi, P. M. *Micropor. Mesopor. Mater.* **155**(1), 227-232, 2012, b) Modi, C. K., & Trivedi, P. M. *Adv. Mat. Lett.* **3**(2), 149-153, 2012.

[137] Collins, A. N., et al. *Chirality in Industry: The Commercial Manufacture and Applications of Optically Active Compounds*, John Wiley & Sons, Ltd , Chichester, 1992.

[138] Collins, A. N., et al. *Chirality in Industry II: Developments in the Commercial Manufacture and Applications of Optically Active Compounds*, John Wiley & Sons, Ltd , Chichester, 1997.

[139] Sheldon, R. A. *Chirotechnology: Industrial Synthesis of Optically Active Compounds*, Dekker, New York, 1993.

[140] http://nobelprize.org/nobel-prizes/chemistry/laureates/2001/index.html.

[141] Fraile, J. M., et al. *Chem. Rev.* **109**(2), 360-417, 2009.

[142] a) Davis, M. E. *Acc. Chem. Res.* **26**(3), 111-115, 1993, b) Zhang, L., et al. *Catal. Sci. Technol.* **1**, 507-516, 2011, c) Hutchings, G. J. *Annu. Rev. Mater. Res.* **35**(1), 143-66, 2005.

[143] Thomas, J. M., & Raja, R. *Acc. Chem. Res.* **41**(6), 708-720, 2008.

[144] Li, C. *Catal. Rev.* **46**(3-4), 419-492, 2004.

[145] Fraile, J. M., et al. *Chem. Soc. Rev.* **38**, 695-706, 2009.

[146] Corma, A., et al. *J. Organomet. Chem.* **431**(2), 233-246, 1992.

[147] Taylor, S., et al. *J. Chem. Soc. Perkin Trans.* **2**, 1714-1723, 2001.

[148] Zsigmond, A., et al. *J. Catal.* **213**(1), 103-108, 2003.

[149] Sabatier, M. J., et al. *Chem. Commun.* 1285-1286, 1997.

[150] Ogunwumi, S. B., & Bein, T. *Chem. Commun.* 901-903, 1997.

[151] Kahlen, W., et al. *Catal. Lett.* **54**(1), 85-89, 1998.

[152] Gigante, B., et al. *Catal. Lett.* **68**(1-2), 113-119, 2000.

[153] Heinrichs, C., & Hölderich, W. F. *Catal. Lett.* **58**(2-3), 75-80, 1999.

[154] Schuster, C., & Hölderich, W. F. *Catal. Today* **60**(3), 193-207, 2000.

[155] Schuster, C., et al. *Catal. Lett.* **74**(1-2), 69-75, 2001.

[156] (a) Sasai, H., et al. *J. Am. Chem. Soc.* **114**(11), 4418-4420, 1992, (b) Shibasaki, M., & Yoshikawa, N. *Chem. Rev.* **102**(6), 2187-2210, 2002, and references therein.

[157] (a) Trost, B., & Yeh, V. S. C. *Angew. Chem. Int. Ed.* **41**(5), 861-863, 2002. (b) Trost, B., et al. *Org. Lett.* **4**(16), 2621-2623, 2002.

[158] (a) Christensen, C., et al. *Chem. Commun.* 2222-2223, 2001, (b) Christensen, C., et al. *J. Org. Chem.* **67**(14), 4875-4881, 2002, (c) Risgaard, T., et al. *Org. Biomol. Chem.* **1**(1), 153- 156. 2003.

[159] (a) Ooi, T., et al. *J. Am. Chem. Soc.* **125**(8), 2054-2055, 2003, (b) Corey, E. J., & Zhang, F. Y. *Angew. Chem. Int. Ed.* **38**(13-14), 1931-1934, 1999.

[160] Evans, D. A., et al. *J. Am. Chem. Soc.* **125**(42), 12692-12693, 2003.

[161] Palomo, C., et al. *Angew. Chem. Int. Ed.* **44**(25), 3881 -3884, 2005.

[162] Egami, H., & Katsuki, T. *J. Am. Chem. Soc.* **131**(17), 6082-6083, 2009.

[163] Egami, H., et al. *J. Am. Chem. Soc.* **132**(39), 13633-13635, 2010.

[164] (a) Luo, Z., et al. *Angew. Chem. Int. Ed.* **41**(24), 4532-4535, 2002, b) Guo, Q. X., et al. *J. Am. Chem. Soc.* **129**(45), 13927-13938, 2007.

[165] Somei, H., et al. *Tetrahedron Lett.* **45**(9), 1841-1844, 2004.

[166] Gao, J., et al. *Angew. Chem. Int. Ed.* **42**(48), 6008-6012. 2003.

[167] Tada, M., et al. *Chem. Commun.* **22**, 2542-2543. 2004.

[168] Sauer, J. *Chem. Rev.* **89**(1), 199-255, 1989.

[169] Alvaro, M., et al.. *J. Phys. Chem. B* **106**(26), 6815-6820, 2002.

[170] Zhou, H.W., et al. *J. Comput. Aided Mol. Des.*, **23**(3), 153-162, 2009.

[171] Anconi, C. P. A., et al. *J. Phys. Chem. A* **111**(48), 12127-12135, 2007.

[172] a) Helen, K., & Bayer, A. *Organometallics* **30**(9), 2483-2497, 2011, b) Jiří V. J., et al. *Organometallics* **30**(18), 4822-4829, 2011.

[173] Esteves, P. M., et al. *J. Phys. Chem. B* **103**(47), 10417-10420, 1999.

[174] Li, J., & Li, S. *J. Phys. Chem. C* **112**(43), 16938-16944, 2008.

[175] Mignon, P., et al. *J. Phys. Chem. B* **110**(49), 24947-24954. 2006.

[176] Pereira, M. S., & Nascimento, M. A. C. *J. Phys. Chem. B* **110**(7), 3231-3238, 2006.

[177] Simperler, A., et al. *J. Phys. Chem. B* **108**(22), 7152-7161, 2004.

[178] a) Ganesan, R. & Viswanathan, B. *J. Phys. Chem. B* **108**(22), 7102-7114, 2004. b) Ganesan, R., & Viswanathan, B. *J. Mol. Catal. A: Chemical* **223**(1-2), 21-29, 2004.

[179] Jafarian, M., et al. *J. Phys. Chem. C* **116**(34), 18518–18532, 2012.

[180] Corrêa, R. J., et al. *Appl. Catal. A: General* **336**(1-2) 35-39, 2008.

[181] Modi, C. K., et al. *J. Incl. Phenom.Macrocycl. Chem.* **74**(1-4)117-127, 2012.

[182] Vargas, A., et al. *J. Chem. Theory Comput.* **5**(1), 97-115, 2009.

Chapter 2

Experimental and Theoretical Methods

This chapter deals with the materials, methodologies and characterization techniques employed for the synthesis of various neat and encapsulated transition metal complexes. The various physicochemical and spectrochemical techniques *viz.* scanning electron microscope (SEM), EDX, X-ray diffraction (XRD), thermo gravimetric analysis (TGA), Fourier transform infrared (FTIR) spectroscopy, UV-visible/ diffuse reflectance spectroscopy(UV-vis/DRS), X-ray photoelectron spectroscopy (XPS), electron spin resonance (ESR) spectroscopy and cyclic voltammetry (CV) used for the characterization of the synthesized complexes are highlighted with necessary theoretical background. The details of the computational methodologies use to study the structure, electronic and reactivity of the intrazeolite complexes and the mechanism of the catalytic reaction are discussed along with a brief introduction to density functional theory (DFT).

2.1. Materials Used

Table 2.1. The chemicals used in this study along with the manufacturers are listed below

Chemicals	Suppliers
i) Sodium Y zeolite (NaY zeolite)	High Tech India. Ltd. Bomabay, India
ii) Ferrous Chloride, $FeCl_2.2H_2O$	E-Merck, India
iii) Zinc Chloride, $ZnCl_2.2H_2O$	do
iv) anhydrous $CuCl_2$	do
v) anhydrous Ferric Chloride, $FeCl_3$	Otto Chemicals, Mumbai, India
vi) Salicylaldehyde and its derivatives	Alfa Aesar, India
vii) *Ortho*-phenylenediamine	CDH (Central Drug House)
viii) Ethylenediamine	Merck
ix) Lithium Chloride	RANKEM, India
x) Potassium Nitrate	do
xi) 2-naphthol (analytical grade (AR),	G.S Chemical Testing Lab & Allied Industries, Bombay
xii) Tetrabutyl Ammonium Phosphate (TBAP)	E-Merck
xiii) Cobalt Chloride Hexahydrate, $CoCl_2.6H_2O$, and	RANKEM, India
xiv) Nickel Chloride Hexahydrate, $NiCl_2.6H_2O$,	do
xv) Copper Chloride Dihydrate, $CuCl_2.2H_2O$	do
xvi) Phenol (analytical grade (AR),	G.S Chemical Testing Lab & Allied Industries, Bombay
xvii) Picolinic Acid	Sigma-Aldrich, India
xviii) Chiral 1,2 diamine	do

Besides these the solvents used are of analytical grade (AR) and HPLC grade.

2.2. Experimental Methods

2.2.1. Synthesis of N, N'-bis(salicylidene)ethylenediamine (Salen)

To a 40 mmol salicylaldehyde (4.17 ml), 20 mmol ethylenediamine (1.33 ml) is added under cold condition. A yellow crystalline product so obtained after few minutes is further recrystallized in toluene. The purity and structure of the compound is analyzed by NMR, FT-IR and UV-vis techniques.

2.2.2. Synthesis of N,N'-disalicylidene-1,2-phenylendiamine (Salophen)

To a well stirred solution of 10 mmol o-phenylenediamine (1.08 g) in ethanol, 20 mmol salicylaldehyde (2.1 ml) is added. The mixture is stirred under reflux at 50 °C for 2h. A yellowish orange crystalline product is obtained which is further recrystallized in toluene and analyzed by NMR, FT-IR and UV-vis techniques.

2.2.3. Synthesis of 2,2'-(1,2-Diphenylethane-1,2-diyl)Bis(Azan-1-yl-1-ylidene) Bis(Mthan-1-yl-1-ylidene)diphenol (L1)

The ligand L1 is synthesized according to Scheme 2.1. In a typical procedure a solution of (*1R, 2R*)-(+)-1,2-Diphenylethylenediamine (424mg, 2 mmol) and 2-hydroxybenzaldehyde (488mg, 0.426mL, 4mmol) in EtOH are stirred at room temperature for 18 h under nitrogen atmosphere. After completion of reaction, the reaction mixture is diluted with EtOAc and water. The organic layer is then separated and washed sequentially with brine and dried over Na_2SO_4. The solvent is removed in vacuum and the resulting residue is purified by chromatography. TLC is performed in 10% EtOAc and Hexane. The title compound is eluted at 6% EtOAc in Hexane. $R_f = 0.4$.

2.2.4. Synthesis of 6,6'-(1,2-Diphenylethane-1,2-diyl)Bis(Azan-1-yl- ylidene) Bis(Methan-1-yl-1-ylidene)Bis(3-Methoxyphenol) (L2)

A solution of (*1R,2R*)-(+)-1,2-diphenylethylene- diamine (424mg, 2mmol) and 2-hydroxy-4-methoxy benzaldehyde (608mg, 4mmol) in EtOH is stirred at room temperature for 18 h under nitrogen atmosphere. After completion of reaction the reaction mixture is diluted with EtOAc and water. The organic layer is then separated and washed sequentially with brine and dried over Na_2SO_4. The solvent is removed in vacuum and the resulting residue is purified by chromatography. TLC is run in 10% EtOAc and Hexane. The title compound is eluted at 6% EtOAc in Hexane. R_f*=0.4.*

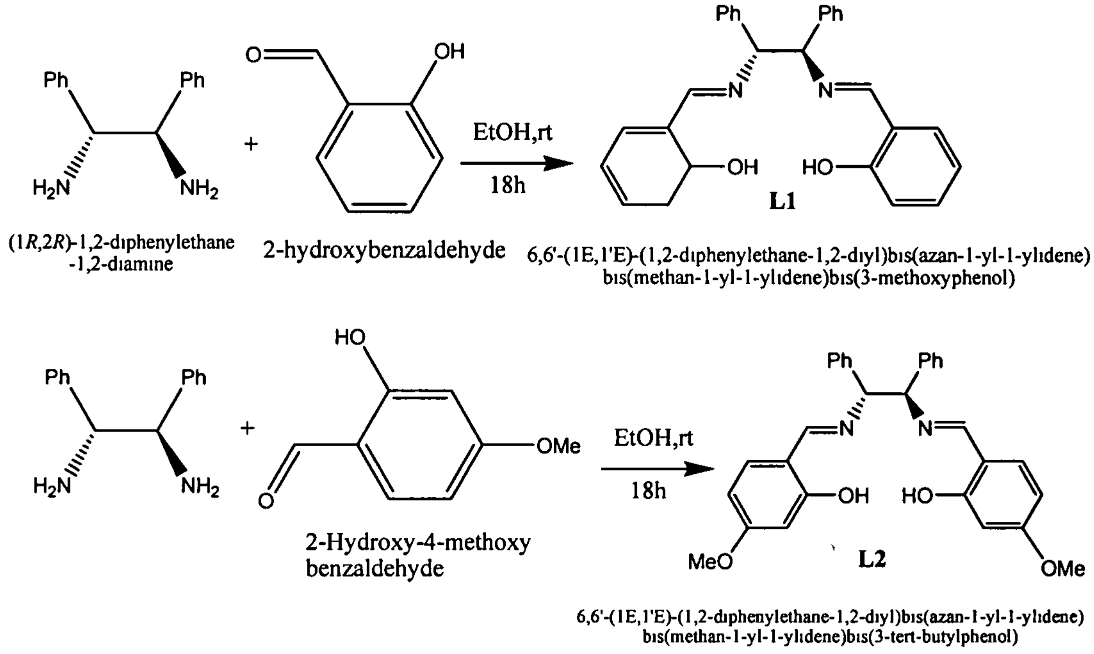

Scheme 2. 1. Synthesis of Chiral Schiff base Ligand L1 and L2

2.2.5. Preparation of the Tris (1, 10 phenanthroline) M (II) complex, where M = Fe, Cu and Zn, $[M(C_{12}H_8N_2)_3]Cl_2.2H_2O$ (M-Phen or $[M(Phen)_3]^{2+}$

To a well stirred solution of 1,10 phenanthroline (0.595g, 3 mmol) in methanol (10ml) taken in a round bottom flask (50ml), a solution of $FeCl_2.2H_2O$ (1mmol, 0.162g) in methanol (5 ml) is added. The resulting homogeneous solution is stirred at room temperature for 4 h. The solution is filtered and the filtrate on standing led to crystallization of the product. The black crystal so obtained is washed with ethanol followed by diethyl ether and dried at room temperature. The light greenish-blue crystal of copper and dirty white crystal of zinc are obtained following the same procedure using 0.135g (1mmol) anhydrous $CuCl_2$ and 0.136g (1mmol) $ZnCl_2.2H_2O$ in case of copper and zinc complexes, respectively in methanol.

2.2.6. Synthesis of Fe (III) Salen complex

To a well stirred solution of 1 mmol of *N,N'*-bis(salicylidene)ethylenediamine (0.268 g) in DMF (dimethylformamide), 1 mmol of anhydrous $FeCl_3$ (0.162 g) is added. The homogeneous solution is stirred for 6 h and kept for crystallization. The black crystal so obtained is washed with ethanol and diethyl ether and finally dried at room temperature.

2.2.7. *Synthesis of Fe (III) Salophen complex*

Same procedure is carried out for the synthesis of this complex. The only difference is in the use of the ligand *N,N'*-disalicylidene-1, 2-phenylendiamine instead of *N, N'*-bis(salicylidene)ethylenediamine.

2.2.8. *Synthesis of Bis(Picolinato) M(II) [M= Co, Ni and Cu] complexes*

The bis(Picolinato) complexes [$M^{II}(Pic)_2$] are prepared according to the reported procedure.[13] An aqueous solution of the free ligand is prepared by dissolving the free acid (picolonic acid) in a slight excess of dilute sodium hydroxide solution and adjusting the pH to 6-7 with dilute acid. The filtered ligand solution is then added to an aqueous solution of $MCl_2.xH_2O$ in a 2: 1 ligand-metal mole ratio. The dark green compound is washed with acetone, ethanol and finally dried in vacuum. The purple and sky-blue complexes of cobalt and nickel, respectively are prepared using the same procedure.

2.2.9. *Preparation of $Cu(L1)_2$ and $Cu(L2)_2$ complex*

To a well stirred solution in acetonitrile (10 ml) taken in a round bottom flask (50 ml), a solution of the corresponding ligand (L1 or L2) dissolve in minimum volume of acetronitile is added and stirred for 3h at 4 °C. The resultant solution after three days gives greenish violet powders which are soluble in water.

2.2.10. *Preparation of alkali metal exchanged zeolites*

For the preparation of the alkali exchanged zeolite the NaY zeolite is used as precursor. The Na form of zeolite Y is treated with aqueous 1M NaCl solution once again and subsequently washed with distilled water until the silver ion test for chloride is negative. A mixture of 2.0 g NaY and 1 mmol (0.423 g) LiCl in demineralized water is then stirred under reflux at 60 °C for 24h. The slurry is then filtered and washed with distilled water and dried overnight in oven to get Li-exchanged zeolite (Li-Y). The K-Y is obtained by exchanging NaY with 1 mmol (0.101 g) of KNO_3.

2.2.11. *Preparation of Fe (III) exchanged zeolites*

A mixture of 1 g of the alkali metal exchanged zeolites (LiY, NaY and KY) and 1 mmol (0.162 g) of anhydrous $FeCl_3$ solution in water are stirred under reflux at 60 °C for 24h. The pH of the solution is maintained within 3-3.5 using buffer tablets order to prevent the precipitation ferric ion as $Fe(OH)_3$. The slurry is then filtered and washed with distilled water and dried overnight in an oven at 80 °C to get Fe-exchanged LiY, NaY and KY as pale brown powders.

2.2.12. Preparation of metal exchanged zeolites M^{2+}(M= Fe, Co, Ni Cu, Zn) and Encapsulated Complexes

The various encapsulated transition metal complexes are synthesized by following the general "*flexible ligand*" and *ship in a bottle synthesis*, shown in Table 2. The transition metal exchanged zeolites (Fe^{2+}-Y, Co^{2+}-Y , Ni^{2+}-Y, Cu^{2+}-Y and Zn^{2+} -Y) are first prepared by stirring a mixture of NaY (2.0g) and 1mmol of individual metal chlorides [$FeCl_2.2H_2O$ = 0.162g) $CoCl_2.6H_2O$ = 0.237g, $NiCl_2.6H_2O$ = 0.237g $CuCl_2.2H_2O$ = 0.170g and $ZnCl_2.2H_2O$ = 0.136g] in 50 ml of water at 60 °C for 24h under refluxing condition. The pH of the solutions are maintained within 3-5 using buffer tablets in order to prevent the precipitation of metal hydroxides. The mixtures so obtained are washed with deionized water until the filtrate gives no white precipitate with $AgNO_3$ solution. Except Cu(II) Schiff base complexes all other encapsulated complexes are prepared via flexible ligand method. In a general flexible ligand method, the metal exchanged zeolites, dried at 100 °C are then treated individually with stoichiometric excess of the respective ligands to get zeolite encapsulated transition metal complexes. The powders obtained after 48 hours of stirring the mixtures in

Table 2.2. List of various zeoliteY encapsulated transition metal complexes along with their representation and colour.

Complexes	Representation	Colour
i) Tris(1,10,Phenanthroline) complexes of Fe(II), Cu(II) and Zn(II)	Fe-PhenY/$[Fe(Phen)_3\text{-}Y]^{2+}$ Cu-PhenY/$[Cu(Phen)_3\text{-}Y]^{2+}$ Zn-PhenY/$[Zn(Phen)_3\text{-}Y]^{2+}$	dark brown light greenish pale white
ii) Schiff Base complexes of Fe(III)	Fe-Salen-NaY, Fe-Salophen-NaY, Fe-Salen-LiY, Fe-Salophen-LiY Fe-Salen-KY, Fe-Salophen-KY	Reddish-brown
iii) Picolinato Complexes of Co(II), Ni(II) and Cu(II)	$[Co(Pic)_2]Y$ $[Ni(Pic)_2]Y$ $[Cu(Pic)_2]Y$	dark brown sky blue blue-violet
iv) Chiral Schiff Base complex of Cu(II)	$Cu(L1)_2$-Y $Cu(L2)_2$-Y	dark greenish

water-methanol solution refluxing at 60 °C are subjected to Soxhlet extraction for several hours using methanol and diethyl ether as solvents. The powders are then dried under vacuum and kept for 32h in a oven at 80 °C for further characterization.

The encapsulated transition metal complexes of copper here represented as $Cu(L_1)_2$-Y and $Cu(L_2)_2$-Y are synthesized following the general "*Ship in a bottle* " synthesis method, Scheme 2.2. The copper exchanged zeolite is first prepared by stirring a mixture of NaY (2.0g) and 0.01mmol of anhydrous $CuCl_2$ in 50 ml of water at 60 °C for 24h under refluxing condition. The pH of the solutions is maintained within 3-5 using buffer tablets in order to prevent the precipitation of metal hydroxides. The mixture so obtained is washed with deionized water until the filtrate gives no white precipitate with $AgNO_3$ solution. The copper exchanged zeolite is then dried at 100 °C. To the copper exchanged zeolite, (*1R,2R*)-(+)-1,2-diphenylethylene-diamine and 2-hydroxybenzaldehyde or its dervative dissolved in EtOH is added in stoichiometric amount and reflux at 40 °C fo 18h. The dark greenish powders obtained after 18 hours of stirring the mixtures are subjected to Soxhlet extraction for several hours using acetonitrile, ethanol and diethyl ether as solvents. The color of the samples remained same after Soxhlet extraction indicating the formation of metal complexes inside zeolite-Y. The powders are then dried under vacuum and kept for 32h in a desicator for further characterization.

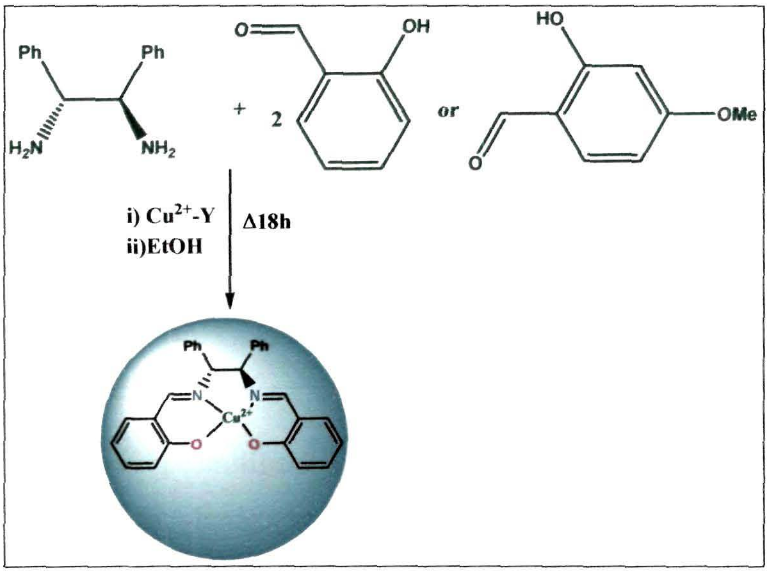

Scheme 2.2. Ship in a bottle synthesis of Cu-Schiff-base complex.

2.2.13. Catalytic Oxidation of 2-napthol

The oxidation of 2-napthol with air is carried out in a batch reactor. In a typical run, 5 mmol of 2-napthol along with 10 ml of toluene, 10 mg of catalyst is added into a 100 ml two-necked flask equipped with a condenser and an air pump. The reaction is started by bubbling the dry air with a stable flow rate of 80 ml /min controlled by a flowmeter into the bottom of reactor at reaction temperature. The progress of the reaction is monitored by thin layer chromatography and after the completion of the reaction; the catalyst is filtered, washed with toluene and dried at 100 °C overnight. The amount of iron content in 10 mg of the catalyst is determined according to Vogels method.[1] The turn over number is determined by following the equation, TON = [BINOL (mmol)/ Fe-atoms on catalyst (mmol)].

2.2.14. Catalytic Oxidation of Phenol

To a carry out the catalytic oxidation of phenol, the catalyst (15mg) is first treated with stoichiometric amount of 30% H_2O_2 and stirred for 10 min in nitrogen atmosphere. To this a solution of stoichiometric amount of phenol prepared in acetonitrile is added and the whole reaction mixture is subjected to microwave irradiation (280 watt). The progress of the reaction is monitored by TLC and UV-vis spectroscopy after an interval of 10 min. The solid catalyst is extracted by filtration and crude reaction mixture is quenched with saturated aqueous NH_4Cl and extracted with diethyl ether (3-20 mL), and the combined organic phases are dried over Na_2SO_4. A sample is taken for HPLC analysis, and the remaining mixture is evaporated and purified by column chromatography (EtOAc/petroleum ether 1:3) to afford catechol.

2.2.15. General Procedure for Asymmetric Henry Reaction

Asymmetric nitroaldol reactions are carried out in magnetically stirred glass reactor. Neat, Zeolite encapsulated chiral copper (II) complexes and Cu-exchanged zeoliteY(10mg) in either case is taken in ethanol (1 ml) and the resulting slurry is cooled to 0 °C. To the cold slurry, an appropriate aldehyde (1 mmol) is added with stirring and after a lag of 15 min; nitromethane (0.6 ml) is added through a syringe. The resulting suspension is stirred for 30 h at 0 °C. Reactions are monitored by TLC analysis using Merck Silica Gel 60 F-254 thin layer plates. After completion of the reaction, the reaction mixture is purified by column chromatography on silica-gel column (20% ethyl acetate in *n*-hexane) to give the desired nitro-aldol adduct.

Enantiomeric excesses are determined by HPLC analysis using chiral columns (φ 4.6 mm × 250 mm, DAICEL CHIRALCEL OD-H or CHIRALPAK AD-H). NMR spectra are recorded on JEOL spectrometers in $CDCl_3$.

2.3. Methods of Characterization

The various characterization techniques that we have used during our study are shown below:

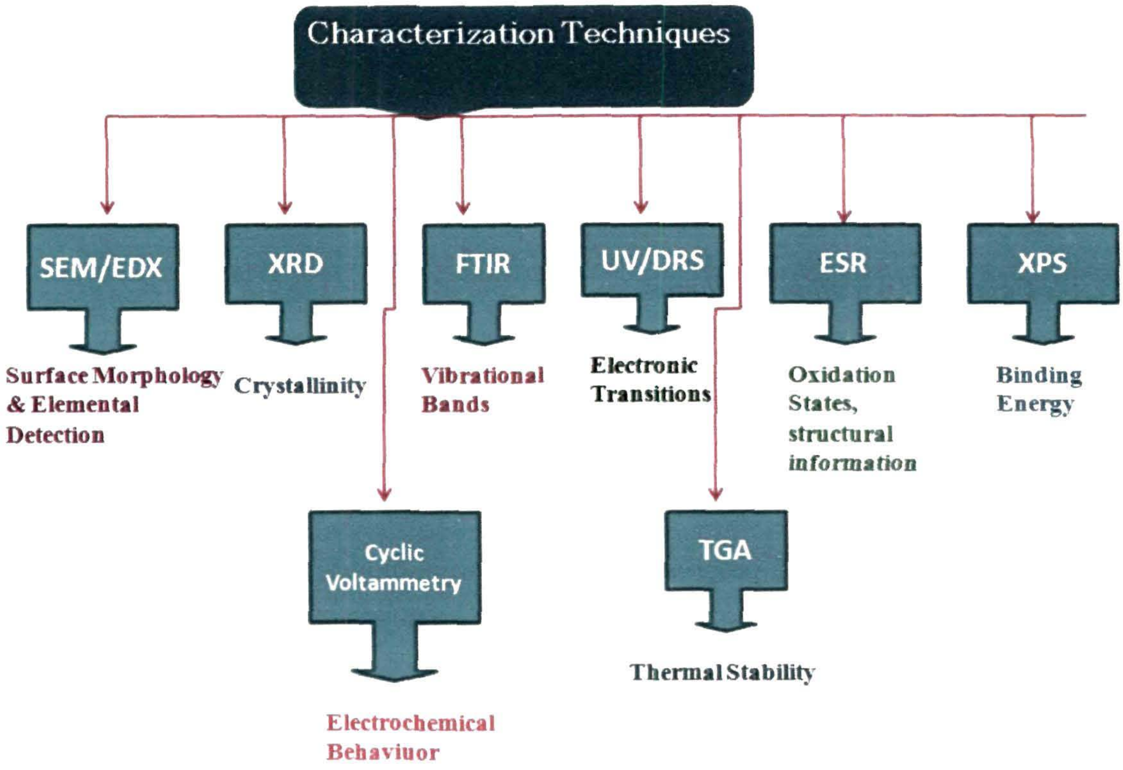

Scheme 2.3. Schematic representation of the overall characterization techniques.

2.3.1. X-ray Diffraction (XRD)

Powder X-ray diffraction (XRD) patterns are recorded on a Shimadzu XD-D1 powder X-ray diffractometer using Cu Kα radiation ($\lambda = 1.542$ Å). XRD patterns are recorded in the 2θ range of 5-50° at a scanning rate of 2°/min.

2.3.2. Fourier Transform Infra Red (FTIR) Spectroscopy

The infrared spectra in the range of 450-4000 cm^{-1} are recorded on a Perkin-Elmer Spectrum 2000 FTIR spectrometer using a DRIFT accessory. The spectra of the neat and the zeolite-encapsulated complexes are recorded as KBr pellets by mixing the samples well with KBr.

2.3.3. *Scanning Electron Microscopy (SEM)*

The scanning electron microscope is often the preferred starting tool for analytic microscopy as it can provide a wide range of information. In SEM, a focused beam of high-energy electrons is scanned over the surface of a material. The electron beam interacts with the material, causing a variety of signals; secondary electrons, backscattered electrons, X-rays, photons, etc. each of which may be used to characterize a material with respect to specific properties. To study the surface topography and to assess the presence various elemets, the SEM and elemental chemical analyses are performed by using JEOL JSM-6390 LV at an acceleration voltage of 5-15 kV. The samples are deposited on a brass holder and sputtered with platinum.

2.3.4. *Ultra Violet visible/ Diffuse Reflectance Spectroscopy (UV-vis/DRS)*

The absorption bands occurring in the visible and near-UV regions are used to obtain information on the electronic structure of catalyst. Most heterogeneous catalysts are opaque powdered samples from which light is reflected and not transmitted. The radiation reflected from a powdered crystalline surface consists of two specular component that is reflected from the surface without transmission (mirror reflection) and the diffuse component that is absorbed into the material and reappears at the surface after multiple scattering.

The electronic absorption spectra are recorded using a Hitachi U-3400 spectrophotometer with a diffuse reflectance attachment equipped with an integrating sphere of 60 mm inner diameter. Mono-chromatic light was used in the whole spectral region in order to minimize the effect of fluorescence. The UV-vis spectra of the neat complexes and the ligands are recorded in solution mode and those of the metal exchanged zeolites and zeolite encapsulated metal complexes are recorded as the powdered samples. For recording absorption spectra of the powdered samples, the samples are placed in a black absorbing hole (10mm, in diameter and 3 mm deep) of a sample holder, and the surface is smoothen. The layer can be regarded as infinitely thick, as required by the Kubelka-Munk theory. The optical spectra are then recorded in the reflectance mode. A Kubelka-Munk (KM) analysis[2] is performed on the reflectance data. The KM factor, $F(R)$, is given by $F(R) = (1-R)^2/2R = k/s$ where R is the diffuse reflectance of the sample as compared to $BaSO_4$, k is the molar absorption coefficient, and s is the scattering coefficient of the sample.

2.3.5. Electron Spin Resonance (ESR) Spectroscopy

ESR spectra of neat complexes are recorded in appropriate solvents with Varian E–112 spectrometer at liquid nitrogen temperature (77 K). For encapsulated systems, the spectra are taken in solid state by taking 50 mg of the sample in a quartz tube.

2.3.6. Cyclic Voltammetry

The cyclic voltammograms of neat and encapsulated complexes are recorded on a Wenking potentioscan (model POS73) with a digital recorder, and 0.1 M TBAP is used as the supporting electrolyte. The working electrode is prepared by taking a 1:1 weight ratio of neat or encapsulated metal complexes in 1 ml of DCM. This suspension is ultrasonicated for 15 min. 10μL of this dispersion is coated on glassy carbon electrode and 5 μL of 5% styrene (as binder from Aldrich) is added on these coating and dried. The glassy carbon electrode is used as the working electrode and Ag/AgCl/KCl (saturated) is used as reference electrode. The cyclic voltammogram of neat complex is taken in solution mode, using 0.01M of the metal complexes in a 0.1M tetra butyl ammonium phosphate (TBAP). Cyclic voltammograms of all the catalysts are taken in 10 ml of DCM using 0.1M TBAP as supporting electrolyte.

2.3.7. Thermogravimetric Analysis (TGA)

Thermo-gravimetric and differential thermal analysis are performed on simultaneous TG-DTA thermo analyzer, Mettler Toledo, with a Pt crucible, Pt/Pt-Rh 13% thermocouples and flow rate of the controlling gas (air) of 20 mL/min.

2.3.8. X-ray Photoelectron Spectroscopy (XPS)

X-ray photoelectron spectroscopy (XPS) is a well-known surface analytical technique widely used for investigating the chemical composition of solid surfaces with its attenuation depth of 20 Å. XPS is accompanied by irradiating a sample with monoenergetic soft X-rays and energy analysing the electrons emitted. Mg Kα (1253.6 eV) or Al Kα (1486.6 eV) X-rays are ordinarily used. These photons have limited penetrating power in a solid, of the order of 1-10 micrometers. They interact with atoms in this surface region by the photoelectric effect, causing electrons to be emitted. The emitted electrons have kinetic energy (KE) given by

$$KE = h\upsilon - BE - \varphi_s$$

where, hυ is the energy of photon, BE is the binding energy of atomic orbital from which the electron originates, φ_s is the spectrometer work function

The binding energy may be regarded as ionization energy of the atom for the particular shell involved. Since there are a variety of possible ions from each type of atom, there is a corresponding variety of kinetic energies of the emitted electrons.

The XP spectra of neat and encapsulated picolinato complexes and metal exchanged zeolites viz, $Cu^{2+}Y$, $Co^{2+}Y$ and $Ni^{2+}Y$ are made on a KRATOS (ESCA AXIS 165) spectrometer by using Mg Kα (1253.6 eV) radiation as the excitation source. Charging of catalyst samples are corrected by setting the binding energy of the adventitious carbon (C_{1s}) at 284.6 eV. The finely ground oven-dried samples are dusted on a double stick graphite sheet and mounted on the standard sample holder. The sample holder is then transferred to the analysis chamber, which can house 10 samples at a time, through a rod attached to it. The samples are out gassed in a vacuum oven overnight before XPS measurements.

2.4. Density Functional Theory (DFT) Calculation

Density functional theory (DFT) calculations are performed on the neat and the zeolite Y encapsulated complexes to understand the effect of zeolite matrix on the structure, electronic and reactivity of the transition metal complexes. Further, DFT calculations are also performed to study mechanism of phenol oxidation by metal picolinato complexes and the Henry reaction catalysed by chiral Cu-Schiff base complexes. So herein we provide a brief account of density functional theory before describing the methodologies employed for such calculations.

2.4.1. Density Functional Theory

The ground state energy of a collection of atoms may be computed by solving the Schrödinger equation – the time independent and non relativistic form of which is given by,[3]

$$\hat{H}\psi(\mathbf{r}_1, \mathbf{r}_2, \ldots, \mathbf{r}_N) = E\psi(\mathbf{r}_1, \mathbf{r}_2, \ldots, \mathbf{r}_N) \qquad (1)$$

The Hamiltonian operator, $\hat{H}$, is the summation of kinetic energy, the interaction with the external potential (V_{ext}) and the electron-electron interaction (V_{ee}), i. e.,

$$\hat{H} = -\frac{1}{2}\sum_{i}^{N}\nabla_i^2 + \hat{V}_{ee} + \sum_{i<j}^{N}\frac{1}{|\mathbf{r}_i - \mathbf{r}_j|} \qquad (2)$$

In general, the external potential of interest is simply the interactions of electrons with the atomic nuclei;

$$\hat{V}_{ext} = -\sum_{\alpha}^{N_{at}} \frac{Z_\alpha}{|\mathbf{r}_i - \mathbf{R}_\alpha|} \tag{3}$$

where $\mathbf{r}_i$ and $\mathbf{R}_\alpha$ are the coordinate of electron *i* and nucleus α respectively, and Z_α is the charge on the nucleus. For simplification, the spin part is omitted here and from further discussions on DFT. Equation 1 is solved for a set of ψ with the antisymmetric constraint. The lowest eigenvalue, E_0, is the ground state energy and the probability density of finding an electron with any particular set of coordinates $\{\mathbf{r}_i\}$ is $|\psi_0|^2$. The average value of a state for a particular ψ is the expectation value of H, i. e.,

$$E[\psi] = \int \psi^* \hat{H}\psi \, d\mathbf{r} \equiv \langle\psi|\hat{H}|\psi\rangle \tag{4}$$

The notation $E[\psi]$ indicates that energy is a *functional* of the wavefunction. The variational theorem states that the energy so obtained is higher than that of the ground state energy (E_0) unless ψ corresponds to ψ_0.

$$E[\psi] \geq E_0 \tag{5}$$

The ground state wavefunction and the energy may be evaluated by looking for all possible wavefunctions and finding the one that minimizes the total energy. One such procedure is Hartree-Fock theory where the total wavefunction is assumed to be the antisymmetric product of functions (φ_i) each of which is dependent on the coordinates of one electron, i. e.,

$$\psi_{HF} = \frac{1}{\sqrt{N!}} \det\,[\varphi_1\varphi_2\varphi_3 \cdots \varphi_N] \tag{6}$$

where 'det' indicates a matrix determinant. Substitution of ψ into Schrödinger equation results in Hartree-Fock expression for energy;

$$\begin{aligned} E_{HF} = &\int \varphi_i^*(r)\left(-\frac{1}{2}\sum_i^N \nabla_i^2 + V_{ext}\right)\varphi_i\,(\mathbf{r})d\mathbf{r} \\ &+ \frac{1}{2}\sum_{i,j}^N \int \frac{\varphi_i^*\,(\mathbf{r}_1)\varphi_i(\mathbf{r}_1)\varphi_j^*(\mathbf{r}_2)\varphi_j(\mathbf{r}_2)}{|\mathbf{r}_i - \mathbf{r}_j|}\, d\mathbf{r}_1 d\mathbf{r}_2 \\ &- \frac{1}{2}\sum_{i,j}^N \int \frac{\varphi_i^*\,(\mathbf{r}_1)\varphi_j(\mathbf{r}_1)\varphi_i(\mathbf{r}_2)\varphi_j^*(\mathbf{r}_2)}{|\mathbf{r}_i - \mathbf{r}_j|}\, d\mathbf{r}_1 d\mathbf{r}_2 \end{aligned} \tag{7}$$

The second term in eqn. 7 is the classical coulomb energy and the third term is the exchange energy written in terms of the orbitals. Applying variation theorem to the energy expression within the constraint that orbitals are orthonormal yields the ground state energy and lead to the Hartree-Fock equations,

$$[-\frac{1}{2}\nabla^2 + V_{ext}(\mathbf{r}) + \int\frac{\rho(\mathbf{r}')}{|\mathbf{r}-\mathbf{r}'|}d\mathbf{r}']\,\varphi_i(\mathbf{r}) + \int V_X(\mathbf{r},\mathbf{r}')\,\varphi_i(\mathbf{r}')d\mathbf{r}' = \varepsilon_i\varphi_i(\mathbf{r}) \qquad (8)$$

where V_X is the non-local exchange potential and is such that

$$\int V_X(\mathbf{r},\mathbf{r}')\varphi_i(\mathbf{r}')d\mathbf{r}' = -\sum_j^N \int \frac{\varphi_j(\mathbf{r})\varphi_j^*(\mathbf{r}')}{|\mathbf{r}-\mathbf{r}'|}\varphi_i(\mathbf{r}')d\mathbf{r}' \qquad (9)$$

Thus, the Hartree-Fock equations describe non-interacting electrons under the influence of a mean potential field consisting of the classical coulomb potential and a non-local exchange potential. From this point onwards, better approximation (correlated methods) for ψ and E_0 are readily obtained. However, the cost of such computation is very high. Many correlated methods are now available such as MP2, MP3, MP4, CISD, CCSD and CCSD(T) which formally scales with the number of electrons raised to the power of 5,6,7,6,6 and 7, respectively. In most cases, the accuracy of CCSD(T) calculations are sufficient enough for determination of chemical properties. However, the accuracy of such calculations comes at very high cost thereby limiting their use in real systems. Thus, it appears that solution of Schrödinger's equations for realistic system is very cumbersome. This gave rise to the development of a new theory called the density functional theory.

The Hamiltonian operator (eqn. 2) involves the coordinates of one and two electrons only. For the computation of total energy, knowledge of two-particle probability density,

i. e., probability of finding an electron at $\mathbf{r}_1$ and another at $\mathbf{r}_2$ is sufficient. This implies that the total energy can be computed without the proper knowledge of 3N dimensional wave function.

The second order density matrix, a quantity of great use in analyzing the energy expression, is given by,

$$P_2(\mathbf{r}_1',\mathbf{r}_2';\mathbf{r}_1,\mathbf{r}_2) = \frac{N(N-1)}{2}\int \psi^*(\mathbf{r}_1',\mathbf{r}_2',\ldots,\mathbf{r}_N')\psi(\mathbf{r}_1,\mathbf{r}_2,\ldots,\mathbf{r}_N)d\mathbf{r}_3 d\mathbf{r}_4..d\mathbf{r}_N \qquad (10)$$

The diagonal elements of P_2, referred to as two-particle density matrix or pair density, are given by,

$$P_2(\mathbf{r}_1,\mathbf{r}_2) = P_2(\mathbf{r}_1,\mathbf{r}_2;\mathbf{r}_1,\mathbf{r}_2)$$

This is the required two electron probability function which determines all two particle operators. The first order density matrix, P_1, may be defined in a similar way and can be written in terms of P_2 as,

$$P_1(\mathbf{r}_1'; \mathbf{r}_1) = \frac{2}{N-1}\int P_2(\mathbf{r}_1', \mathbf{r}_2'; \mathbf{r}_1, \mathbf{r}_2)\,d\mathbf{r}_2 \qquad (11)$$

Knowing P_1 and P_2, the total energy can be determined exactly,

$$\mathrm{E}= \int \left[\left(-\frac{1}{2}\nabla_1^2 - \sum_{\alpha}^{\mathrm{N_{at}}} \frac{\mathrm{Z}_\alpha}{|\mathrm{r}_1-\mathrm{R}_\alpha|}\right)\mathrm{P}_1(\mathrm{r}_1',\mathrm{r}_1)\right]_{\mathrm{r}_1=\mathrm{r}_1'} d\mathrm{r}_1 + \int \frac{1}{|\mathrm{r}_1-\mathrm{r}_2|}\mathrm{P}_2(\mathrm{r}_1,\mathrm{r}_2)\,d\mathrm{r}_1,d\mathrm{r}_2 \qquad (12)$$

The diagonal elements of the first and second order density matrices completely determine the total energy. This vastly simplifies the task. The solution of full Schrödinger equation for ψ is not required – it is sufficient to determine P_1 and P_2 – and the problem in 3N coordinates space has been reduced to a problem in a 6 dimensional space.

Direct minimization of $E(P_1,P_2)$ suffers from specific problems as the density matrices should be constructed from an antisymmetric ψ. This is non trivial and currently an unsolved problem.[4] Thus, it appears that eqn. 12 does not lead immediately to a reliable method for computing the total energy without calculating the many body wavefunction. However, the fact that boosts the density functional theory is the diagonal elements of the first order density matrix, i. e., the charge density, can completely determine the ground state energy.

2.4.2. The Hohenburg-Kohn Theorems

In 1964, Hohenburg and Kohn provided two theorems[5] which simplified the task in hand. The first theorem may be stated as:

The electron density determines the external potential (to within an additive constant).

As the external potential is used to specify the Hamiltonian operator (eqn. 2), thus, in principle, the Hamiltonian operator can be uniquely determined by the charge density and all the wavefunction of all the states can be computed. The second theorem establishes a variational theorem for a system of N electrons:

For any positive definite trial density, ρ_t, such that $\int\rho_t(\mathbf{r})\,d\mathbf{r} = N$, then $E[\rho_t] \geq E_0$.

The two theorems lead to the fundamental statement of density functional theory:

$$\delta\left[E[\rho] - \mu\left(\int \rho(\mathbf{r})d\mathbf{r} - N\right)\right] = 0 \qquad (13)$$

where μ is the chemical potential or the Lagrange multiplier of the constraint that the density contains the correct number of electrons. Thus, it appears that there is a *universal* functional $E[\rho]$ (i. e., it is independent of the external potential) which, if we know its form, can be inserted into the above equation and minimized to obtain the exact ground state density and energy.

2.4.3. The Energy Functional

The energy functional contains three terms – the kinetic energy, the interaction with external potential and the electron-electron interaction;

$$E[\rho] = T[\rho] + V_{\text{ext}}[\rho] + V_{\text{ee}}[\rho]$$

The interaction with external potential is given by,

$$V_{ext}[\rho] = \int \hat{V}_{ext}\, \rho(\mathbf{r}) d\mathbf{r}$$

The kinetic and electron-electron functionals are not known. Direct minimization of the energy would be possible if good approximation to these functionals could be found. This possibility is a matter of recent research.[6]

Kohn and Sham proposed the following for approximating the kinetic and electron-electron functionals.[7] They introduced a system of N non-interacting electrons to be described by a single determinant wave function in N "orbitals" ϕ_i. In this system, the kinetic energy and electron density are known exactly from the orbitals,

$$T_s[\rho] = -\frac{1}{2}\sum_{i}^{N} \langle \phi_i | \nabla^2 | \phi_i \rangle$$

The true ground state density can be expressed in terms of ϕ_i as,

$$\rho\,(\mathrm{r}) = \sum_{i}^{N} |\phi_i|^2 \qquad (14)$$

The construction of density from a set of orbitals ensures that it is legal and can be constructed from an asymmetric wavefunction.

If one considers that classical Coulomb interaction or the Hartree energy represents a significant component of electron-electron interaction, then the second term in eqn. 7 written in terms of density will be,

$$V_H[\rho] = \frac{1}{2}\int \frac{\rho(\mathbf{r}_1)\rho(\mathbf{r}_2)}{|\mathbf{r}_1 - \mathbf{r}_2|} d\mathbf{r}_1 d\mathbf{r}_2$$

The energy functional can be rearranged as,

$$E[\rho] = T_s[\rho] + V_{\text{ext}}[\rho] + V_{\text{H}}[\rho] + E_{\text{xc}}[\rho] \qquad (15)$$

where $E_{\text{xc}}[\rho]$ is the *exchange-correlation functional* which can be expressed as,

$$E_{xc}[\rho] = (T[\rho] - T_s[\rho]) + (V_{ee}[\rho] - V_H[\rho])$$

E_{xc} is simply the sum of error in using a non-interacting kinetic energy and the error in treating the electron-electron interaction classically. Writing the functional (eqn. 15) explicitly in terms of the density obtained from non-interacting orbitals (eqn. 14) and applying the variational theorem (eqn. 13), one finds that the orbitals which minimize the energy satisfy the following set of equation,

$$[-\frac{1}{2}\nabla^2 + V_{ext}(\mathbf{r}) + \int \frac{\rho(\mathbf{r}')}{|\mathbf{r}-\mathbf{r}'|} d\mathbf{r}' + V_{xc}(\mathbf{r})]\, \phi_i(\mathbf{r}) = \varepsilon_i \phi_i(\mathbf{r}) \qquad (16)$$

where the local multiplicative potential is the functional derivative of exchange correlation energy with respect to the density,

$$V_{xc}(\mathbf{r}) = \frac{\delta E_{xc}[\rho]}{\delta \rho} \qquad (17)$$

This set of non-linear equations (the Kohn-Sham) describes the behaviuor of non-interacting electrons under the influence of an effective local potential. Thus, for the exact functional and exact local potential, the orbitals yield the exact ground state density and energy via eqn. 14 and 15, respectively. These Kohn-Sham equations are similar to the Hartree-Fock equations (eqn. 8) where the non-local exchange potential has been replaced by the local exchange-correlation potential, V_{xc}. However, the exact functional and its associated potential are not known. But, in principle, it is possible to solve the Schrödinger equations for a particular system and determine the energy functional and its associated potential. This of course needs greater effort. Nevertheless, the ability to determine the universal functional in a number of systems allows excellent approximations to the functional to be made. The approximations are discussed below in brief.

For calculations in which energy is the quantity of primary interest, DFT provides excellent and highly accurate alternative to the costly wavefunction based methods. However, the utility of this theory (DFT) is dependent on the approximation used for $E_{xc}[\rho]$.

2.4.4. The Local Density Approximation for E_{xc} [ρ]

The generation of approximations for E_{xc} has initiated a rapidly expanding field of research. Different functional are now available which are more or less appropriate for any particular study. The early model that led to a practical utility of density functional theory was that of homogeneous electron gas for which exact results could be obtained. In this model, the electrons are subjected to a constant external potential and hence, the charge density is constant. The system can be specified by a single number – the value of the constant electron density, ρ=N/V.

The homogeneous electron gas was studied by Thomas and Fermi in 1920's[8] considering the plane wave orbitals of the system. If the electron-electron interaction is approximated by classical Hartree potential (i. e., neglecting exchange and correlation effects), then the total energy functional can be readily obtained.[8] Under these conditions, the kinetic and exchange energy (eqn. 7) can be expressed in terms of *local* functions of density. Application of the kinetic and exchange energy densities of the non-interacting homogeneous electron gas leads to following eqns,

$$T[\rho] = 2.87 \int \rho^{\frac{5}{3}}(\mathbf{r})d\mathbf{r}\,;\text{ and, } E_x[\rho] = 0.74 \int \rho^{\frac{4}{3}}\,(\mathbf{r})d\mathbf{r} \qquad (18)$$

The local exchange correlation energy per electron may be approximated as,

$$E_{xc}[\rho] \approx \int \rho(r)\varepsilon_{xc}(\rho(r))dr \qquad (19)$$

where $\varepsilon_{xc}(\rho)$ is the local charge density which by choice is approximated to be the exchange and correlation energy density of the homogeneous electron gas of density ρ. This is the *local density approximation* (LDA). Within LDA, $\varepsilon_{xc}(\rho)$ can be separated into exchange and correlation contributions,

$$\varepsilon_{xc} = \varepsilon_x(\rho) + \varepsilon_c(\rho) \qquad (20)$$

The Dirac form[9] of ε_x can be written as,

$$\varepsilon_x(\rho) = -C\rho^{1/3} \qquad (21)$$

where C is a constant introduced rather than that determined for a homogeneous electron gas. The functional form of the correlation energy density $\varepsilon_c(\rho)$ is unknown and can be obtained by numerical Monte Carlo calculations on homogeneous electron gas which yield exact results.[10]

LDA has been a fruitful approximation by the fact that it reduces the energy functional to a simple local function of the density. It provides reliable results of many properties such as structure, vibrational frequencies etc. However, in computing energy difference between rather different structures, energy barriers in diffusion or chemical reactions, LDA has proven to be not so reliable. Thus, the modification of the approximation is required and as such is now available.

One of the obvious extensions of the LDA is to recognize that the exchange contribution to the energy is dominant over the correlation energy for many systems. Thus, computation of the non-local exchange potential exactly as in Hartree Fock theory (eqn 7) and approximating the correlation potential within the LDA would yield a functional of the form,

$$E_{xc} \approx E_{Fock} + E_c^{LDA} \tag{22}$$

2.4.5. *The Generalized Gradient Approximation*

The LDA can be considered as the zeroth order approximation to the semi-classical expansion of the density matrix in terms of the density and its derivative. A natural strategy is to adopt the gradient expansion approximation (GEA) in which the first order gradient terms in the expansion is included.

In the generalized gradient approximation (GGA), a functional form is implemented which ensures the normalization condition and leads to an energy functional that depends on both density and its gradient. However, the analytical properties of the exchange correlation hole within LDA are retained. The typical form for a GGA functional is,

$$E_{xc} \approx \int \rho\,(\mathbf{r})\varepsilon_{xc}(\rho, \nabla\rho)d\mathbf{r} \tag{23}$$

2.4.6. *Meta-GGA Functionals*

Recently, functionals that depend on the Laplacian of the spin density or of the local kinetic energy density have been developed.[11] Such functionals are referred to as meta-GGA functionals.

The typical form of such a functional is,

$$E_{xc} \approx \int \rho\,(r)\varepsilon_{xc}(\rho, |\nabla\rho|, \nabla^2\rho, \tau)d\mathbf{r} \tag{24}$$

where the kinetic energy density is

$$\tau = \frac{1}{2}\sum_i |\nabla\varphi_i|^2 \tag{25}$$

Significant advances in approximations for $E_{xc}[\rho]$ have made DFT a practical, efficient and unbiased tool for computing various properties of molecules.

2.5. Theoretical Methods

An overview of the DFT calculation implemented during our study is represented schematically in Scheme 2.3. All DFT calculations are carried out using the DMol^3 program[15] with VWN correlation functional and double numeric (DN) basis set. We performed all electron calculations for the neat phenanthroline complexes of iron, copper and zinc and for those encapsulated inside the framework of zeolite. The zeolite

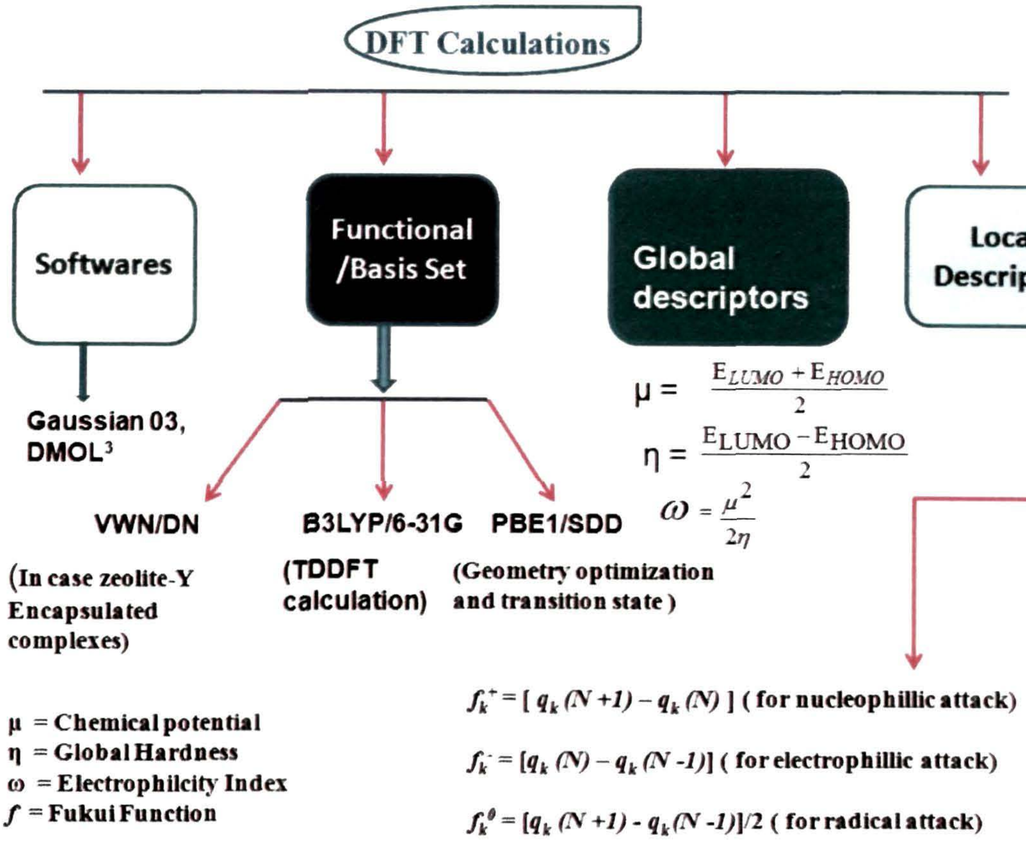

Scheme 2.4. Overall representation of DFT calculations implemented in the present work.

clusters generated by taking 40 tetrahedral units (40T) of faujasite structure around the supercage, saturating them with hydrogen atoms. Initially, the framework Si and O atoms of the clusters are held fixed at their crystallographic positions and all the terminal H atoms are optimized. Following Löwenstein's rule depending on the overall charge of the complexes, silicon atoms of the six-member ring are replaced with aluminium atoms. For example in case of doubly charged complexes two silicon atoms are replaced by two aluminium atoms. The gas phase optimized complexes are then encapsulated inside the supercage at several orientations. The two negative charges generated in the cluster are compensated by two positive charges of the complexes. While optimizing the clusters, terminated hydrogen atoms are held fixed at their initially optimized positions.

Following the Koopmans theorem,[12] the chemical potential (μ) and global hardness (η) can be expressed as

$$\mu = \frac{E_{LUMO} + E_{HOMO}}{2} \qquad (26)$$

$$\eta = \frac{E_{LUMO} - E_{HOMO}}{2} \tag{27}$$

where, E_{LUMO} is the energy of the lowest unoccupied molecular orbital and E_{HOMO} is the energy of the highest occupied molecular orbital.

However, the finite difference approximation defines the above quantities in terms of ionization potential (IP) and electron affinity (EA) of the system.[13]

$$\mathrm{IP} = E_{N-1} - E_N \tag{28}$$

$$\mathrm{EA} = E_N - E_{N+1} \tag{29}$$

where E_N, E_{N-1} and E_{N+1} are energies of N, N-1 and N + 1 electron system.

In most numerical applications, chemical potential (μ) and chemical hardness (η) are calculated using finite difference approximation in terms of IP and EA and therefore, μ and η, given below, can be used as a working formula

$$\mu = -\frac{(IP + EA)}{2} \tag{30}$$

$$\eta = \frac{(IP - EA)}{2} \tag{31}$$

The global electrophilicity as introduced by Parr et al.[14] can be defined as

$$\omega = \frac{\mu^2}{2\eta} \tag{32}$$

The global softness S is defined as the inverse of the global hardness η,

$$S = \frac{1}{2\eta} \tag{33}$$

In a finite difference approximation, the condensed Fukui function[15] of an atom, k, in a molecule with N electron is defined as

$f_k^+ = [\, q_k(N+1) - q_k(N)\,]$ (for nucleophillic attack) (34)

$f_k^- = [q_k(N) - q_k(N-1)]$ (for electrophillic attack) (35)

$f_k^0 = [q_k(N+1) - q_k(N-1)]/2$ (for radical attack) (36)

where $q_k(N)$, $q_k(N+1)$ and $q_k(N-1)$ are the charges of the k^{th} atom for N, $N+1$ and $N-1$ electron systems, respectively.

The global reactivity descriptors, chemical potential, hardness, electrophilicity index and softness are calculated using equations (27)-(33), respectively. The Hirshfeld population analysis (HPA) is used to calculate the Fukui functions. The Fukui functions (FFs, f_{κ}^{+} and f_{k}^{-}) are calculated using equations (34) and (35).

TDDFT calculation have been performed in methanol solution using the B3LYP exchange correlations functional[16] and 6-31G basis set[17] as implemented in the Gaussian03 program package.[18] Solvation effects are included by means of the conductor-like polarizable continuum model (C-PCM).[19] In case of $Fe(Phen)_3^{2+}$ complex, 100 excitation energies and in case of Cu and Zn analogues 150 excitation energies are computed. The simulation of the absorption spectra are performed by a convolution of Gaussian function centered at the calculated excitation energies for all excitation.

To study the *cis-trans* isomerization process and the mechanism of phenol oxidation. The PBE1 functional, is used (as provided in Gaussian 03 program)[18] since it performs exceedingly well for the evaluation of energetics of a reaction as well as many other properties.[20] The relativistic small-core effective core potential (ECP) of Stuttgart/Dresden (SDD) for the transition metals are used. As stated by Bühl et al, the combination of PBE1 and SDD can safely be used for studying transition metal complexes.[20] Frequency calculations are performed at the same level of theory to characterize the nature of the stationary points. All the ground state structures are verified as being at an energy minimum by confirming that their respective Hessian (matrix of analytically determined second order derivative of energy) led to all real valued frequencies while the transition states are characterized as stationary points with one imaginary frequency.

References

[1] Vogel, A. I. *Textbook* of *Quantitative Chemical Analysis*, 6th edn, Pearson Education Asia, 2002.

[2] Hecht, H. G. *In Modern Aspect of Reflectance Spectroscopy*, Wendlandt, W. W. Ed., Plenum Press, New York, 1968.

[3] Schrödinger, E. *Phys. Rev.* **28** (6), 1049-1070, 1926.

[4] (a) Coleman, J. *Calculation of the first- and second-order density matrices, in, The Force Concept in Chemistry*, Ed. Deb, B. M. (Van Nostrand Reinhold, New York, 1981). (b) Erdahl, R., & Smith Jr., V. H. Eds. *Density matrices and Density Functionals*, (Reidel, Dordrecht 1987).

[5] Hohenberg, P., & Kohn, W. *Phys. Rev.* **136** (3B), B864-B871, 1964.

[6] Foley, M., & Madden, P. A. *Phys. Rev.* B **53** (16), 10589-10598, 1996.

[7] Kohn, W., & Sham, L. J. *Phys. Rev. A* **140** (4A), 1133-1138, 1965.

[8] (a) Fermi, E. *Z. Phys.* **48**, 73-79, 1928. (b) Thomas, L. H. *Proc. Camb. Phil. Soc.* **23** (5), 542-548, 1927.

[9] Dirac, P. A. M. *Proc. Camb. Phil. Soc.* **26** (3), 376-385, 1930.

[10] Ceperley, D. M., & Alder, B. J. *Phys. Rev. Lett.* **45** (7), 566-569, 1980.

[11] (a) Tschinke, V., & Zieglar, T. *Can. J. Chem.* **67**, 460-472, 1989. (b) Neumann, R., & Handy, N. C. *Chem. Phys. Lett.* **266** (1-2), 16-22, 1997. (c) Perdew, J. P., et al. *Phys. Rev. Lett.* **82** (12), 2544-2547, 1999.

[12] Koopmans, T. A. *Physica.* **1**(1-6), 104-113,1933.

[13] Parr, R. G., & Yang, W *Density Functional Theory of Atoms and Molecules*, Oxford University Press: New York 1989.

[14] Parr, R. G., et al. *J. Am. Chem. Soc.* **121**(9), 1922-1924, 1999.

[15] Yang, W., & Mortier, W. J. *J. Am. Chem. Soc.* **108**(19), 5708-5711, 1986.

[16] Becke, A. D. *J. Chem. Phys.* **98**(7), 5648-5652, 1993.

[17] Binkley, J. S., et al. *J. Am. Chem. Soc.* **102**(3), 939-947, 1980.

[18] Gaussian 03, Revision B.05, Frisch, M. J., et al. Gaussian, Inc., Pittsburgh PA, 2003.

[19] a) Barone, V., & Cossi, M. *J. Phys. Chem. A* **102**(11), 1995-2001, 1998. (b) Cossi, M., et al. *J. Comput. Chem.* **24**(6), 669-681, 2003.

[20] Bühl, M., et al. *J. Chem. Theory Comput.* **4**(9),1449-1459, 2008.

Chapter 3

Encapsulation and Tethering of Tris(1,10 Phenanthroline) Complexes of Fe(II), Cu(II) and Zn(II) Inside Zeolite-Y.

3.1. Introduction

The tris and bis(1,10-phenanthroline) complexes of transition metals, especially of iron, copper, cobalt, zinc and ruthenium are well known examples to interact with DNA and proteins.[1-5] These metal complexes under the influence of the protein mantle undergo a change in their redox behavior and selectivity is induced by virtue of the alternation of redox potential of the metal complexes. Similar environment can be generated upon encapsulation of such complexes into zeolite framework and hence may mimic the biological systems. However, the redox chemistry of encapsulated transition metal complexes is not clear in the literature and is still a matter of debate. Keeping this in mind, in this chapter we have performed the encapsulation of tris(phenanthroline) complexes of iron, copper and zinc in NaY zeolite and their physicochemical as well as redox behaviors are studied using various techniques viz EDX, SEM, powder XRD, FTIR, UV-vis/DRS, cyclic voltammetry and ESR.

So far there are many experimental studies to monitor the properties of such intrazeolite complexes, but little theoretical effort has been paid to understand the structure and reactivity of such complexes.[6,7] Here in, density functional theory (DFT) calculations are performed to determine the structures of encapsulated complexes. Time-dependent density functional theory (TDDFT) calculations are carried out to simulate the experimentally observed electronic transitions in the UV-vis spectra. The global and local reactivities of the neat and encapsulated complexes are predicted using DFT based descriptors.

3.2. Results and Discussion

3.2.1. Experimental Section

3.2.1.1. Elemental Analysis

The results of the elemental analyses given in Table 3.1 gives Si/Al ratio of 2.64 which corresponds to a unit cell formula Na_{54} $[(AlO_2)_{54}(SiO_2)_{138}]$ for parent NaY zeolite. The Si/Al ratio is almost constant in all the metal exchanged zeolites indicating the absence of dealumination during exchange process. The amounts of metal content in the encapsulated complexes are less compared to the ion-exchanged zeolites. This decrease in the metal content in the intrazeolite complexes can be attributed to the participation of metal ion in the formation of co-ordination complexes inside the cavities of zeolite-Y or it may so happen that some of the metal cation leaches out during complex formation. It can be seen from the Table 3.1 that the ligand to metal

Table 3.1. Elemental data analysis (in % by weight).

Sample	Si	Al	Na	M	C	N	H	Unit Cell Formula
NaY	22.70	8.57	7.55	-	-	-		$Na_{54}[(AlO_2)_{54}(SiO_2)_{138}]$
Fe^{2+}-Y	20.48	8.20	6.30	3.67	-	-		$Fe_{19.8}Na_{34.2}[(AlO_2)_{54}(SiO_2)_{138}]$
Fe-PhenY	20.45	8.85	4.80	1.78	4.10	1.28	0.42	
Cu^{2+}-Y	22.96	8.44	5.44	3.76	-	-		$Cu_{15.6}Na_{38.4}[(AlO_2)_{54}(SiO_2)_{138}]$
Cu-PhenY	21.80	8.20	3.65	1.72	3.86	0.68	0.50	
Zn^{2+}-Y	21.76	8.34	5.64	3.50	-	-		$Zn_{20.7}Na_{33.3}[(AlO_2)_{54}(SiO_2)_{138}]$
Zn-PhenY	20.40	8.80	3.35	1.68	3.60	0.76	0.61	

ratio in each case is almost 3:1 suggesting octahedral co-ordination around the central metal cation.

3.2.1.2. SEM Study

While synthesizing metal complexes in zeolites the complexes may form inside the cavities or on the surface. SEM technique gives an insight whether the complexes are present on the surface of zeolite. Some representative SEM pictures are shown in Figure 3.1. Figure 3.1b represents a typical morphology of the zeolite surface for all the considered systems before Soxhlet extraction and it show the deposition of complexes or the uncomplexed species on the external surface. The SEM photograph taken after Soxhlet extraction for several times with different organic solvents *viz* ethanol and acetone for Fe-PhenY and Cu-PhenY systems is shown in Figure 3.1c. It is clear from Figure 3.1c that the external surface is totally washed out giving an indication for complete removal of unbound ligand or other extraneous particles. Further it is revealed from the SEM analysis that the particle size before and after encapsulation of iron or copper phenanthroline complex has remained unchanged suggesting that encapsulation has not led to the destruction of zeolite morphology. In case of the zinc phenanthroline

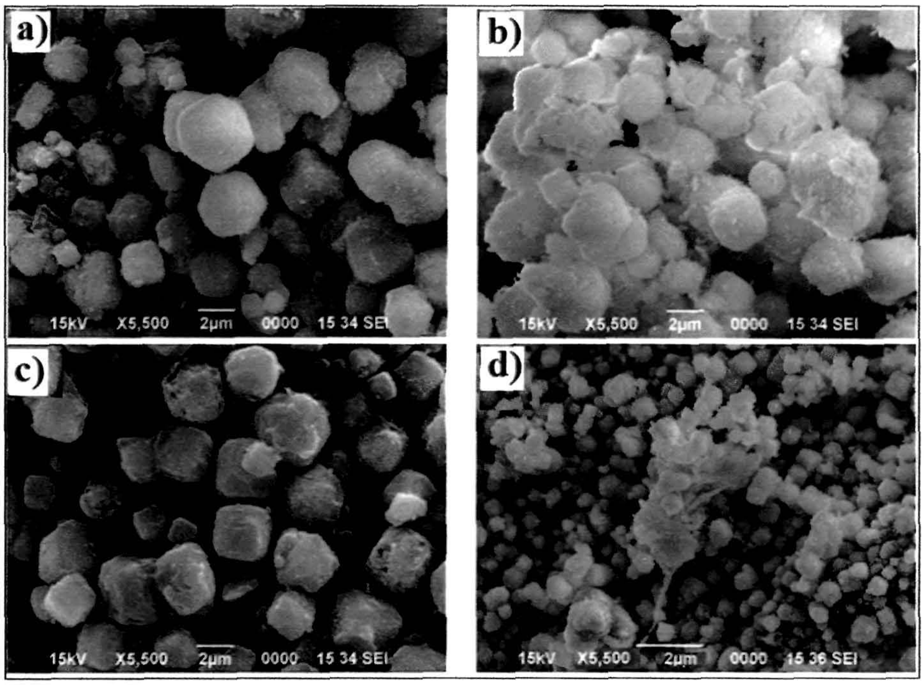

Figure 3.1. a) SEM of NaY zeolite b) Typical SE micrographs of Fe-PhenY, Cu-PhenY and Zn-PhenY complexes before Soxhlet extraction. c) Typical SEM of Fe-PhenY and Cu-PhenY after Soxhlet extraction and d) SEM of Zn-PhenY after Soxhlet extraction indicating the encapsulation of Fe^{2+} and Cu^{2+} complexes and surface adsorption of Zn^{2+} complex.

complex, the SEM picture as shown in Figure 3.1d bares the presence of complex on the external surfaces even after Soxhlet extraction and the particle size about remains same in comparison to the parent zeolite. This suggests that the complex has not diffused into cavities rather it is situated on the surface. This is much clear from the surface plot (Figure 3.2) obtained from SEM analysis. The surface plots, Figure 3.2b and 3.2c for the encapsulated iron and copper complexes, respectively are different from that of the zinc complex (Figure 3.2d), where the white surface area gives a clear indication of the formation of zinc complex on the external surface of NaY.

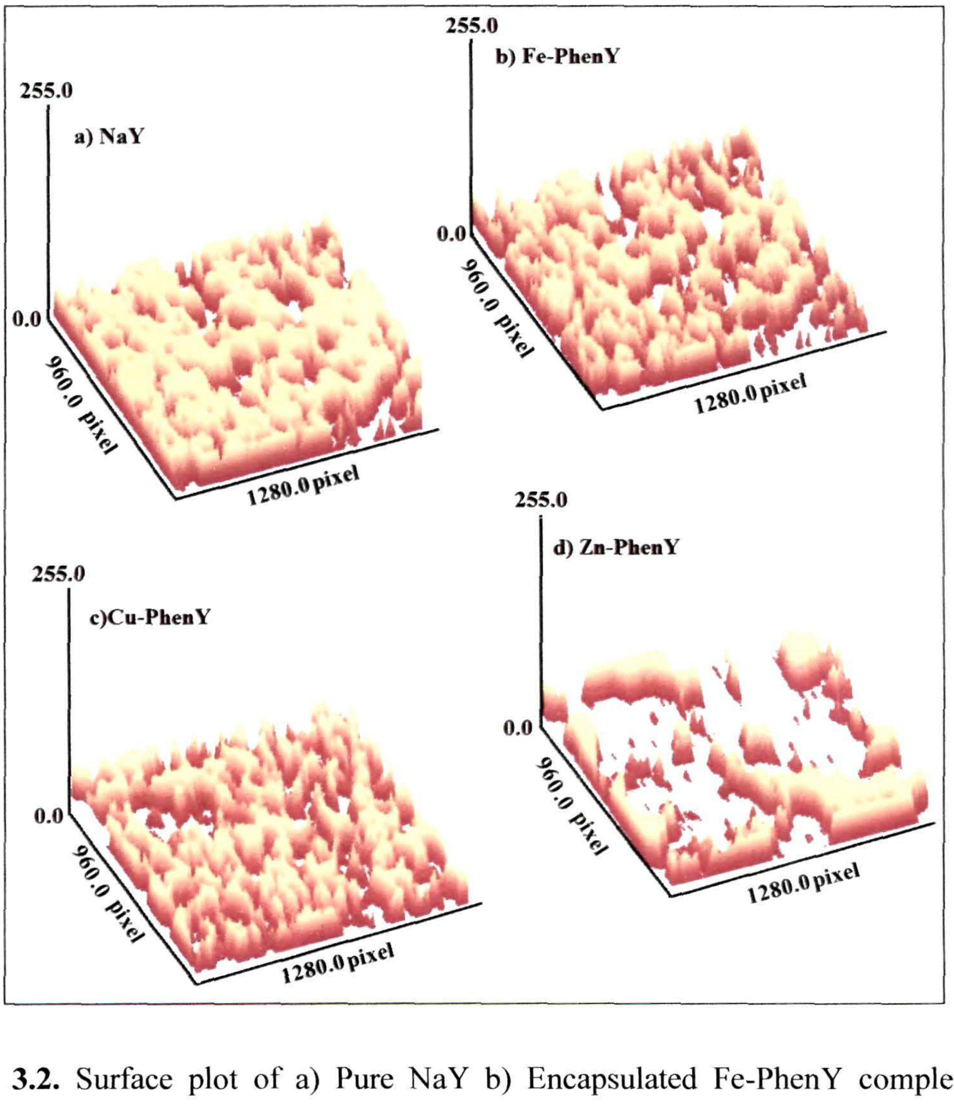

Figure 3.2. Surface plot of a) Pure NaY b) Encapsulated Fe-PhenY complex after Soxhlet extraction c) Encapsulated Cu-PhenY complex after Soxhlet extraction d) Zn-PhenY after Soxhlet extraction. The white portion represents the formation of Zn-Phen complex on zeolite surface. X and Y axis represents width and height, respectively.

3.2.1.3. FTIR Study

The FTIR spectra of NaY, M^{2+}-Y (M= Fe, Cu and Zn) and encapsulated M-PhenY complexes are shown in Figure 3.3. FTIR spectra of NaY zeolite and metal exchanged zeolites show strong zeolite bands in the region 500-1200 cm^{-1}. The strong band and broad band in the region 1000-1100 cm^{-1} can be attributed to the asymmetric stretching vibration of (Si/Al) O_4 units. The broad band at the region 1650 and 3500 cm^{-1} are due to lattice water molecules and surface hydroxylic group, respectively. In Figure 3.3a, the parent NaY zeolite shows the characteristics bands at 560, 686, 1010 and 1652 cm^{-1} and are attributed to T-O bending mode, symmetric stretching and antisymmetric vibrations, respectively.[8] These bands are not modified on ion exchange with M^{2+} ions or by supporting the metal complexes (curve c, d and e), which further implies that the zeolite framework has remained unchanged upon encapsulation of complexes. The FTIR bands of all encapsulated complexes are weak due to their low concentration in the zeolite cage and thus can only absorb in the region 1200 to 1600 cm^{-1} where the zeolite matrix does not absorb. Figure 3f represents the typical IR-spectra of the neat complexes. The FTIR spectrum of the neat $[M(Phen)_3]^{2+}$complex shows major bands at 1632 (C=C), 1514, 1419 (C=N), 845 (C-H benzene ring) and 723 cm^{-1} (C-H pyridine ring) for the coordinated phenanthroline ligand. Similar frequencies are also observed in the case of all encapsulated complexes, M-PhenY (M = Fe, Cu and Zn) with a little shifting of the bands at 1514 and 1419 cm^{-1} to higher wavenumber (1543-1547 and1431-1464 cm^{-1}, respectively) in case of Fe and Cu-complexes indicating nitrogen coordination inside the cavity of zeolite framework. The FTIR of encapsulated complexes shows bands similar to that of the neat complexes. The result gives an indication for the location of the phenanthroline complexes of iron and copper inside zeolite-Y and adsorption of zinc complex on the surface of the zeolite.

The FTIR spectrum of the parent NaY sample activated at 550 °C displays three bands in the OH stretching region, at 3744, 3724, and 3610 cm^{-1} (Figure 3.4c). According to the literature,[9] the band at 3744 cm^{-1} corresponds to external silanols, and that at 3607 cm^{-1} corresponds to bridging acidic OH groups. The weak band at 3724 cm^{-1} is attributed to internal silanols.[10,11] On metal exchange and encapsulation of the metal complexes the band at 3607 cm^{-1} appears with reduced intensity (Figure 3.4a and 3.4b) and is attributed to exchange of part of the acidic zeolite protons with metal cations . However, two new bands at 3647 and 3565 cm^{-1} appears in the FTIR spectrum

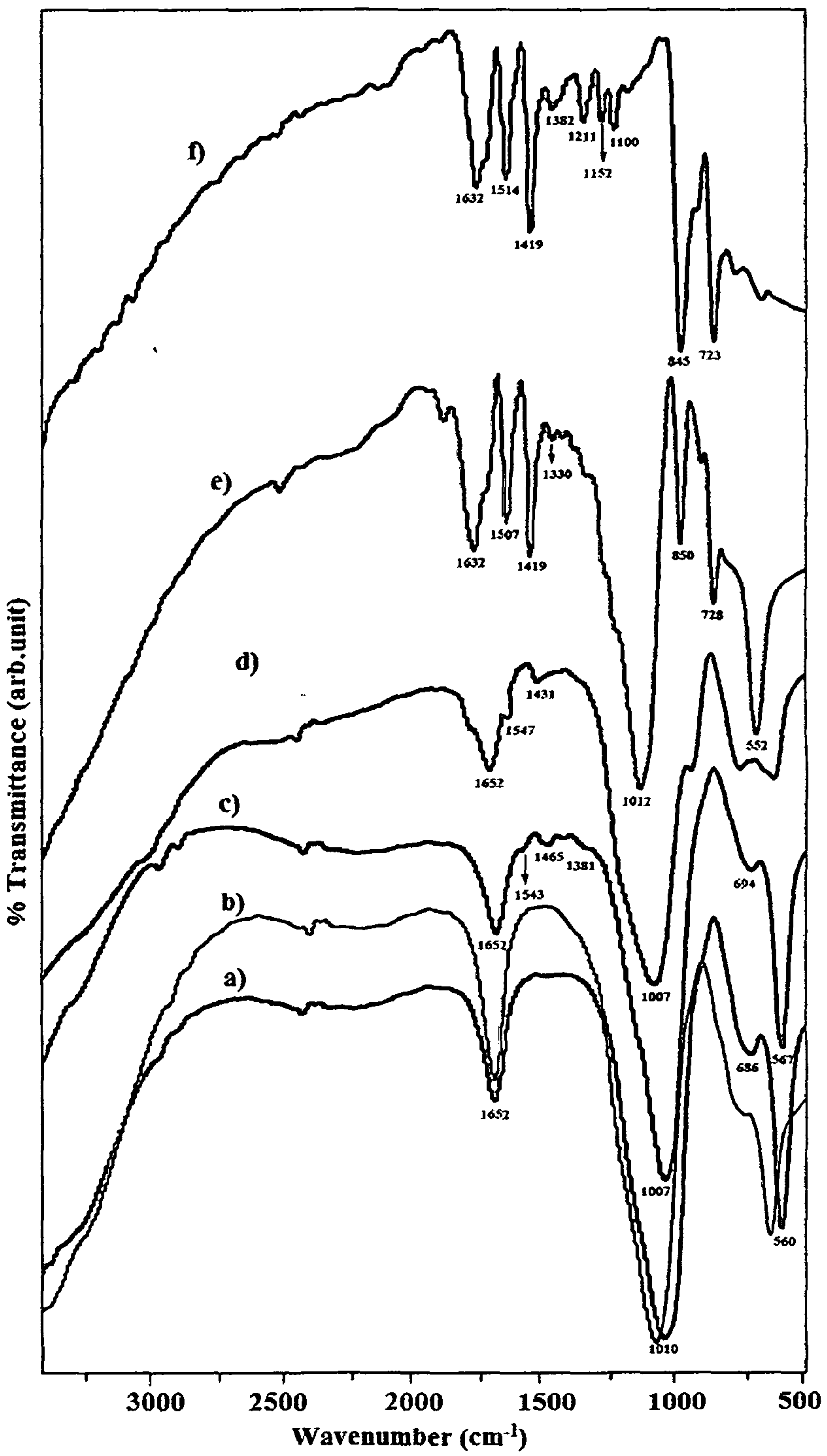

Figure 3.3. FTIR spectra of a) NaY b) M^{2+}-Y c) Fe-PhenY d) Cu-PhenY e) Zn-PhenY f) typical FTIR spectra of $[M(Phen)_3]^{2+}$ complexes (M= Fe, Cu and Zn).

of Zn-PhenY complex, shown in Figure 3.4b. Compared to the neat zeolite-Y and the other encapsulated complexes, the complexation of $[Zn(Phen)_3]^{2+}$ leads to a red shift of the symmetric O-H stretching of the silanol and bridging OH-group by approximately

97 and 47 cm^{-1}, respectively. This indicates the involvement of external silanol oxygen in hydrogen bond formation with the H-atom of coordinated phenanthroline ligand. This further gives information that $[Zn(Phen)_3]^{2+}$ complex is not located on the interior of the zeolite cavity rather it is tethered by silanol group of zeolite-Y to form a host-guest complex via H-bonding interaction.

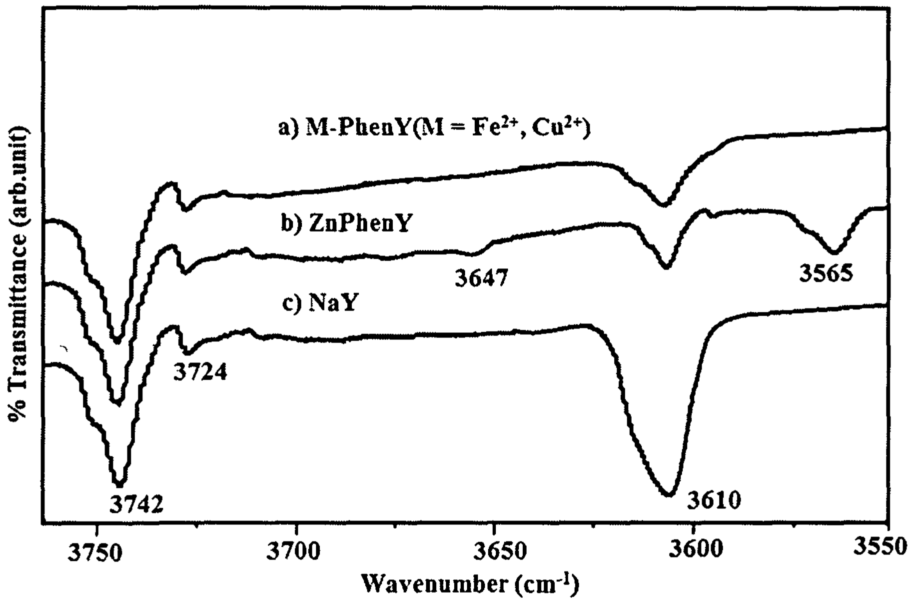

Figure 3.4. FTIR spectra of a) encapsulated Fe-PhenY and Cu-PhenY b) Zn-PhenY c) pure zeolite-Y in the region of 3750-3550cm^{-1}. The appearance of new peak at 3647 and 3565 cm^{-1} indicates the formation of H-bonding between H-atom of phenanthroline ligand of Zn-complex and silanol oxygen of zeolite-Y.

3.2.1.4. UV-vis/DRS Study

The UV-vis spectra of the neat phenanthroline complexes of Fe, Cu and Zn taken in methanol are discussed in combination with the TDDFT study in the theoretical section. Herein, the diffuse reflectance study of the metal-exchanged zeolite-Y and those of the encapsulated complexes are discussed. The UV-vis spectrum of the dried Fe^{2+}-Y zeolite sample (Figure 3.5 a) shows a weak band at 315, 346, 380 nm and low intense shoulder at 480 nm. The second derivative (shown in the inset, Figure 3.5a) suggests the shoulder at 380 nm consists of several components. The peak at 480 nm can be attributed ligand to metal charge transfer transition, in the present case from the oxygen ligand to a tetracoordinated Fe^{2+} ion. The peaks between 300 and 400 nm are usually assigned to small oligonuclear clusters. These results indicate that, in the dried sample, iron is mainly in the form of Fe^{2+} ions. The main part of the Fe^{2+} ions are in the form of isolated ions but some amount of oligonuclear species and iron oxide clusters are also formed. The dehydrated Cu^{2+}-Y sample exhibits absorption bands at 636 and 710 nm, characteristic of the $e \rightarrow t_2$ and $e \rightarrow a_1$ transition of the Cu(II) ($3d^9$) ion in the trigonal site, respectively (Figure 3.5b). The intense UV absorption component is attributed to charge transfer excitation. The band at 253 nm is assigned to the ($3d^{10}$) $^1S_0 \rightarrow$ ($3d^9$ $4s^1$) $^2D_{5/2}$ configurational transition or may be due to interaction of Cu^{2+} ion with the oxygen atoms of zeolite. The second derivative of the peak gives absorption at 253 nm which occurs as a shoulder in the DRS spectrum. This spectral behaviour of the

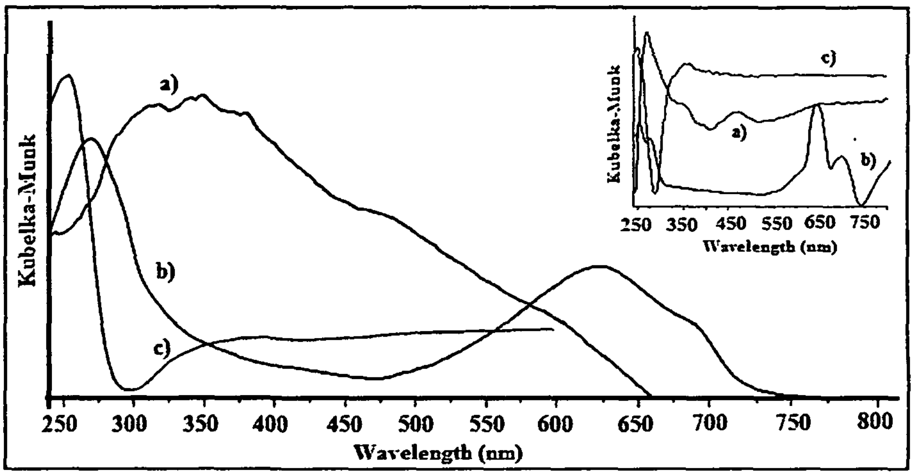

Figure 3.5. Diffuse reflectance spectra of a) Fe^{2+}-Y b) Cu^{2+}-Y c) Zn^{2+}-Y. The inset shows the second derivative of the respective spectrum.

Cu^{2+} exchanged zeolite-Y indicates that Cu^{2+} ion maintains a pseudo-tetrahedral geometry of the type $(O_1)_3$-Cu^{2+}-L (where O= oxygen of the supercage of zeolite-Y).[12] The Zn^{2+}-Y show a sharp peak at 252 nm and a broad peak at 342 nm (consisting of large number of components) which may be attributed to the interaction of Zn^{2+} ion with the zeolite framework.

The optical spectra of the encapsulated Fe-PhenY complex shown in Figure 3.6a consist of four peaks. The two highly intense peak at 215 and 276 nm are due to intraligand π→π* and n→π* transitions, respectively and the peaks at 427 and 498 nm are attributed to metal to ligand charge transfer (dπ→pπ*) transition. On encapsulation, these peaks are shifted to higher wavelength in comparison to the neat complex which may be due to the influence of the zeolite matrix on the electronic and structural properties of the encapsulated complex. The diffuse reflectance spectrum of Cu-PhenY complex shown in Figure 3.6b possesses two very narrowly spaced bands at 207 and 214 nm due to π→π* and two broad bands at 362 and 454 nm due to transition from an admixture of metal based *d* orbitals and ligand based π molecular orbitals to the ligand based π* orbitals. The UV-vis spectra of the copper complex encapsulated in zeolite-Y shows a vast difference in comparison to the optical spectra of the neat complex in methanol. Particularly, the higher energy bands are blue shifted whereas the lower energy bands are red shifted. These changes in the spectral behavior of Cu-complex on encapsulation suggest that Cu-PhenY undergoes a Jahn-Teller distortion under the steric constrain impose by the zeolite matrix. The pattern of the diffuse reflectance spectra of surface bound Zn-PhenY complex shown in Figure 3.6c is similar to that of the neat complex in solution. However, the electronic transition involving the ligand based π and π* gets shifted to higher wavelength due to the interaction of the zeolite framework i.e due to the supramolecular host guest interaction. This also gives an interpretation that due to the interaction of zeolite matrix with incoming guest ($(Zn(Phen)_3]^{2+}$ complex) via the formation of H-bond causes a high red shift of the intra-ligand electronic transitions.

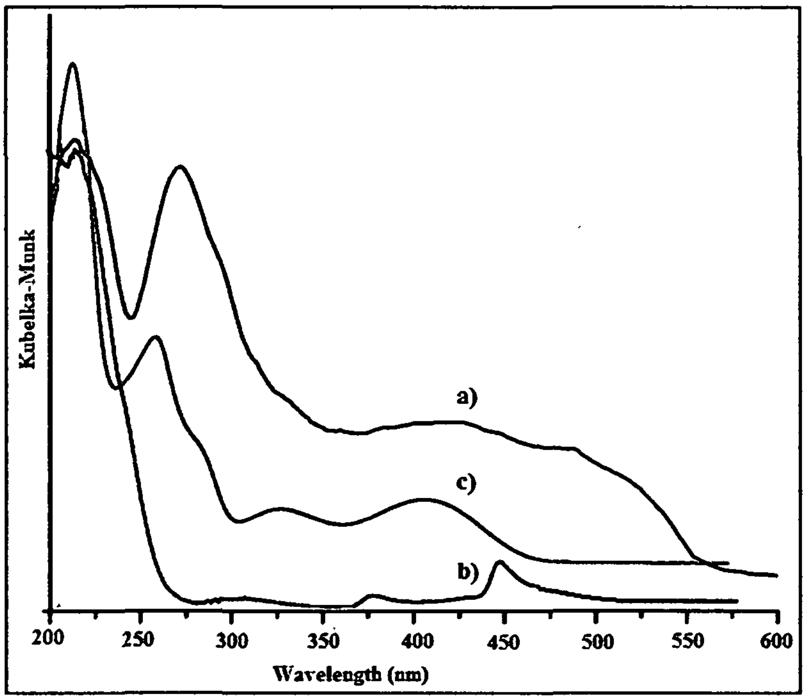

Figure 3.6. UV-vis/DRS spectra of a) Fe-PhenY b) Cu-PhenY c) Zn-PhenY.

3.2.1.5. XRD Study

Although EDX, FTIR and UV-vis studies suggest the M-PhenY [M = Fe^{2+}, Cu^{2+}] complexes to be in the supercage of zeolite-Y, there is still possibility that these complexes are formed on the external surfaces. Quayle et al.[13] reported that the formation of a large transition-metal complex ion in the supercage of zeolite-Y could be confirmed with the alternation of the relative peak intensities of 220 and 311 reflections in the XRD pattern as $I_{220} > I_{311}$ for zeolite-Y and $I_{220} < I_{311}$ for the zeolite including the large complex ion. This empirical relationship among the XRD intensities may be related to the distribution of non coordinated free cations in zeolite-Y.

XRD patterns of NaY, M^{2+}-Y (M = Fe, Cu and Zn) exchanged zeolite and the encapsulated M-PhenY complexes are shown in Figure 3.7. Similar diffraction patterns are noticed in the encapsulated M-PhenY and NaY, except the zeolite with encapsulated complexes have slightly weaker intensities. These observations indicate that the crystallinity of the zeolite is maintained before and after encapsulation. There are, however, differences in the relative peak intensities of the 220 and 311 reflections appearing at $2\theta = 10$ and 12°, respectively. For pure zeolite-Y and for M^{2+}-exchanged zeolite-Y it is found that $I_{220} > I_{311}$, but for the encapsulated complex $I_{311} > I_{220}$. This reversal in intensities has been observed in encapsulated complexes of iron and copper but not in the case of zinc complex. The above observation therefore gives an evidence for the successful encapsulation of Fe and Cu phenanthroline complexes within the supercage of zeolite-Y.

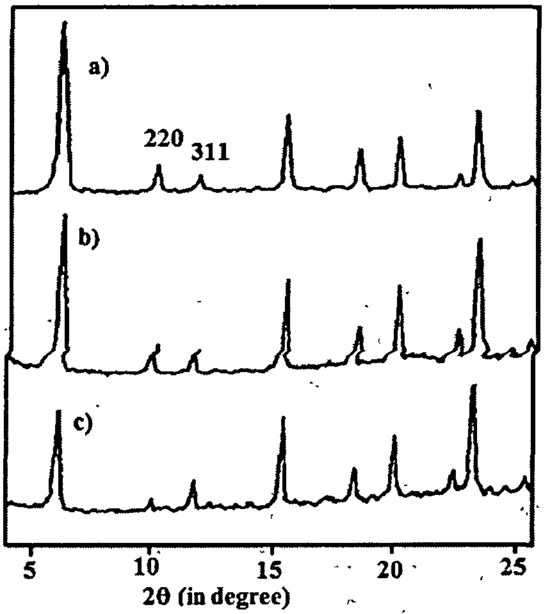

Figure 3.7. XRD pattern of a) Pure zeolite-Y, b) metal exchanged zeolite-Y, c) M-PhenY complexes (M = Fe^{2+} and Cu^{2+}).

3.2.1.6. ESR Study

Zn^{2+} ion is ESR silent and with X-band ESR spectroscopy, Fe^{2+} cations usually remain silent due to the relatively high magnitude of zero-field splitting and the shorter spin-spin relaxation time. So ESR signals are not observed for these metal exchanged zeolites as well as for the neat and the encapsulated complexes. The absence of the ESR signal even at 77 K indicates that in both the iron exchanged zeolite and encapsulated complex, iron is in +2 oxidation state and there occurs no oxidation of Fe(II) to Fe(III) on calcination. This reveals that no spin state conversion occurs as the complexes diffuse into the cavities of zeolite-Y. ESR spectra of the Cu^{2+} exchanged zeolite; neat and the encapsulated Cu-PhenY complex are shown in Figure 3.8. The ESR spectrum for the neat complex as polycrystals is characterized by an axial *g* tensor. Hyperfine features for copper (*S = 1/2 and I = 3/2*) are observed at 77 K due to intermolecular spin–spin coupling for both the neat and the encapsulated complexes.

Table 3.2. ESR spectral parameter data of Cu^{2+} exchanged zeolite, $[Cu(Phen)_3]^{2+}$ and Cu-PhenY.

Samples	g_{II}	$g_{\perp}$	A_{II} (in mT)
Cu^{2+}-Y hydrated	2.39	2.09	150
Cu^{2+}-Y dehydrated	2.44	2.10	200
$[Cu(Phen)_3]^{2+}$	2.40	2.17	140
Cu-PhenY	2.47	2.15	120

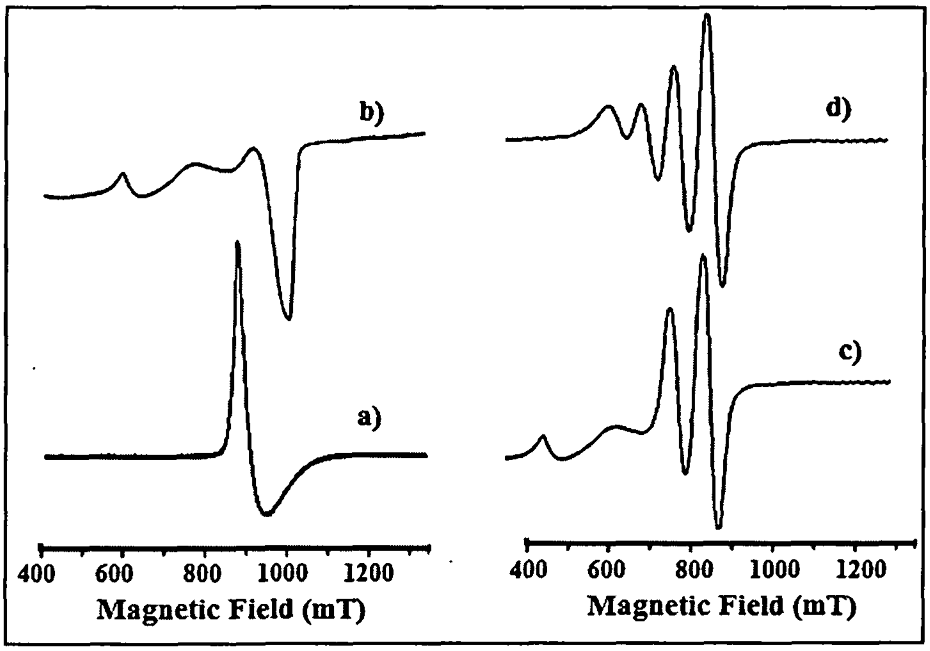

Figure 3.8. Powder ESR spectra of a) Cu^{2+}-Y before calcinations b) Cu^{2+}-Y after calcinations c) encapsulated Cu-PhenY complex and d) neat $[Cu(Phen)_3]^{2+}$complex.

The ESR spectrum of hydrated copper-exchanged zeolite (Figure 3.8a) taken in a glycerine-water mixture in N_2 atmosphere without preactivation shows a broad spectrum with *g* values g_{II} =2.39 and $g_{\perp}$= 2.09. The hyperfine spectrum characteristics of the Cu nucleus with I = 3/2 are not resolved. This result is in accordance with our observe UV-vis/DRS spectrum and also with the reported *g* values obtained from theoretical ESR calculation for tetra co-ordinated Cu^{2+} exchanged zeolite.[14] When the sample is pre-treated by heating to 120 °C under vacuum, the room-temperature ESR spectrum (Figure 3.8b) exhibited resolved copper hyperfine structure. Flentge et al.[15,16] reported that without preactivation of a mixture copper salts with zeolites for an equilibration time of 16 h, all $[Cu(H_2O)_6]^{2+}$ units are preferentially held in the super cages in copper-exchanged zeolite-Y. On activation, Cu^{2+} ions migrated to the sodalite cages. The parameters observed (see Table 3.2) in this study for Cu^{2+} exchanged zeolite-Y correspond to hexa aqua copper ions present in the super cages. The spectrum of neat $[Cu(Phen)_3]^{2+}$complex recorded at 77K (Figure 3.8c) shows hyperfine structure with two *g*-values (shown in Table 3.2) that are characteristic of normal octahedral copper complex undergoing *Jahn-Teller* distortion. The ESR spectrum of encapsulated Cu-PhenY complex (Figure 3.8d) exhibits the characteristic structure of Cu^{2+} complexes that results from hyperfine coupling between the unpaired electron and the copper *(I* = 3/2) nuclear spin. This coupling causes a 4-fold splitting of the ESR line. For an orientationally disordered solid assuming axial symmetry, *g* anisotropy produces a powder pattern in which the sharp features are referred to as parallel and perpendicular edges. Since the copper system has both *g* and hyperfine anisotropy, the overall spectrum is composed of four overlapping powder patterns in which the resolved low-field features are the parallel and perpendicular edges of the four powder patterns. The *g*-values agree well with literature[17] values for octahedral copper complexes observed in zeolites where the surrounding ligands are thought to be water and/or hydroxyl groups. This results predict that the octahedral $Cu(Phen)_3{}^{2+}$ complex is believed to be located in the supercage where it would have the most free space for motion.

3.2.1.7. Cyclic Voltammetric Study

Cyclic voltammetry provides information on the nature of intrazeolite complexes that may not be readily apparent from spectroscopic studies. Two possible mechanisms for electron transfer to redox species associated with zeolites, E_z^{m+} were first proposed by Shaw et al.[18]

Intrazeolite mechanism

$$E_z^{m+} + ne^- + nC_{(s)}^+ \leftrightarrow E_z^{(m-n)+} + nC_{(z)}^+$$

Extrazeolite mechanism

$$E_z^{m+} + \mathrm{m}C_{(s)}^{+} \leftrightarrow E_{(s)}^{m+} + \mathrm{m}C_{(z)}^{+}$$

$$E_{(s)}^{m+} + \mathrm{ne}^{-} \leftrightarrow E_{(s)}^{(m-n)+}$$

(where E^{m+} = electroactive probe z = zeolite, s = solution phase, and C^+ = an electrolyte cation). The intrazeolite mechanism requires that supercage entrapped complexes undergo electron transfer in the interior of the zeolite, but it does not specify the means whereby they do so. Since zeolites are electronic insulators and are comprised of a negatively charged lattice, the means for intrazeolite electron transfer are of considerable interest and debate.

In a number of papers,[19-25] the intrazeolite electron-transfer mechanism has been discussed for the zeolite-encapsulated metal complexes and metal ion exchanged zeolites. The electron transfer to the metal complexes can be achieved only if the metal complexes are present on the electrode surface or in the vicinity of the electrode surface. The complexes which are nearer to the electrode surface should be electroactive even if any one of the electron transfer mechanisms is operating.

The phenanthroline ligand itself is an electroactive species. In general, the electrochemical behavior is strongly dependent on whether an aprotic solvent or an aqueous solvent is employed. In our case we used dichloromethane (DCM) as the solvent and 0.1M TBAP as supporting electrolyte and phenanthroline shows only a single, one electron, and one proton reduction electrochemical wave at 0.061V, Figure 3.9. The redox potential values for all the systems are provided in Table 3.3.

Table 3.3. Oxidation and reduction peak potential values (in V) for neat and the encapsulated M-PhenY (M = Fe^{2+}, Cu^{2+} and Zn^{2+}) complexes, $E_{1/2} = (E_{oxd}+E_{red})/2$

Samples	E_{red}	E_{oxd}	$E_{1/2}$
Fe^{2+}-Y	-0.464	-0.238	-0.351
$[Fe(Phen)_3]^{2+}$	0.588	0.980	0.784
Fe-PhenY	0.921	0.965	0.943
Cu^{2+}-Y	-0.236	-0.095	-0.165
$[Cu(Phen)_3]^{2+}$	-0.264	-0.536	-0.400
Cu-PhenY	-0.515	-0.0563	-0.285
Zn^{2+}-Y	-	-0.69	-0.345
$[Zn(Phen)_3]^{2+}$	-0.295	-0.426	-0.360
Zn-PhenY	-0.265	-0.614	-0.440

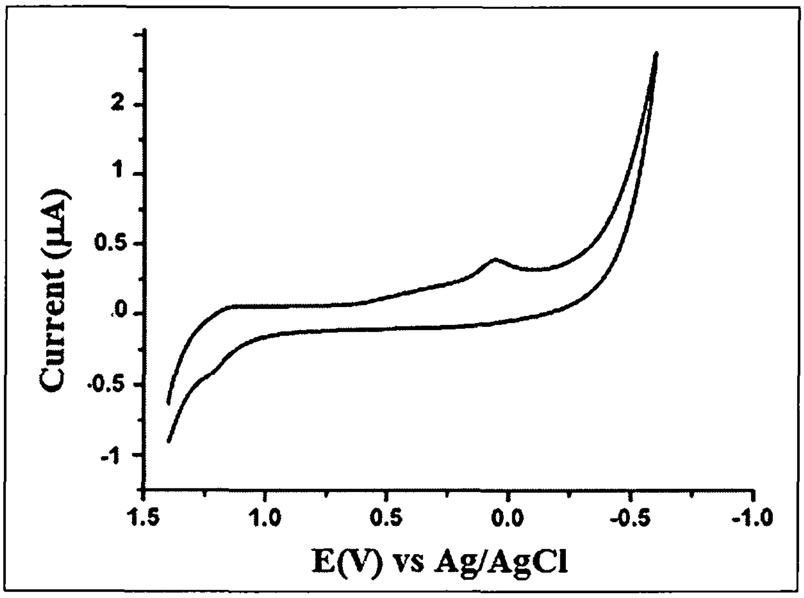

Figure 3.9. Cyclic Voltammogram of 1,10 phenanthroline ligand.

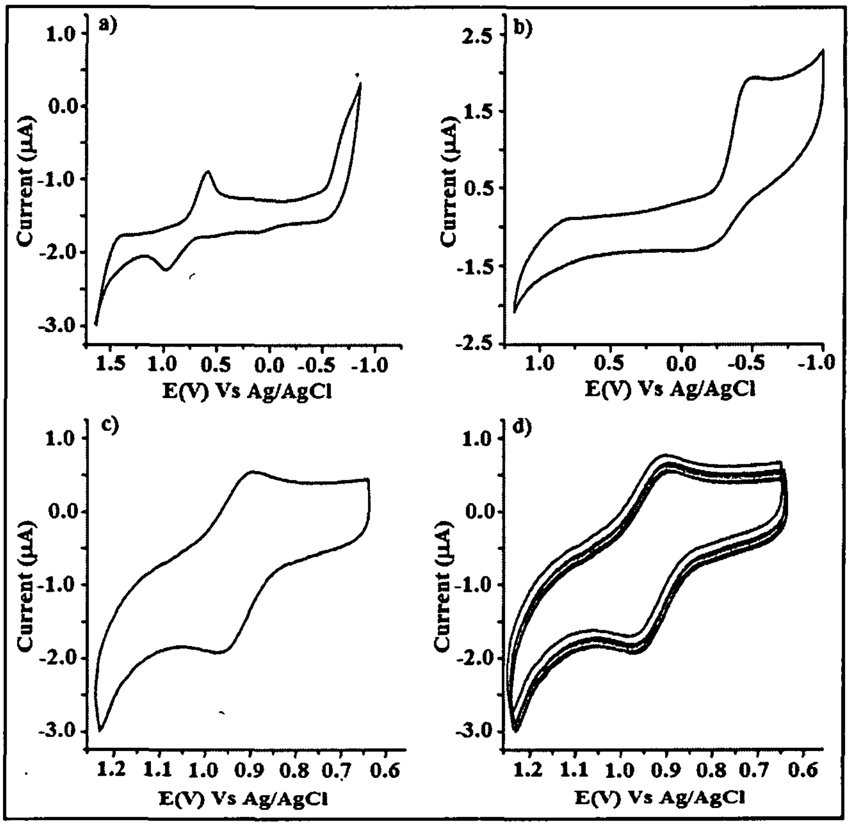

Figure 3.10. Cyclic voltamoogram of a) neat $[Fe(Phen)_3]^{2+}$ b) Fe^{2+}-Y c) Fe-PhenY d) the stability of Fe-PhenY complex upto 50-cycles at scan rate of 0.1V. The voltammograms from a)-d) are taken as ZME in DCM using 0.1M TBAP as supporting electrolyte.

The voltammogram of a neat $[Fe(Phen)_3]^{2+}$ complex in solution mode at a scan rate of 0.1V is shown in Figure 3.10a. It shows a redox couple with values of E_{pc} = 0.588V and E_{pa} = 0.980 V, $E_{1/2}$ = 0.784V. These values of the redox process indicate that the redox process is quasi reversible and is in consistent with the reported values for the $[Fe(Phen)_3]^{2+}$.[26] This redox process, when associated with a cathodic peak, is the reduction of Fe^{3+} to Fe^{2+} and when associated with an anodic peak, is the oxidation of Fe^{2+} to Fe^{3+}. Upon encapsulation in NaY, the reversibility of the electron transfer is maintained but the $E_{1/2}$ = 0.943V (E_{pc} = 0.921V and E_{pa} = 0.965 V) is shifted to more positive values, the peaks are broadened and are stable upto number of cycles, Figures 3.10c and 3.10d. The positive shift in $E_{1/2}$ suggests a difference in the interaction properties of Fe (II) and Fe (III) species with zeolite matrix and indicates the stabilization of Fe^{2+} oxidation state in zeolite cages. The shifting of the peak potential may also be due to the axial interaction of the metal complex with different type of oxygen atoms of the zeolite matrix for which the metal complex does not maintain the same geometry as that in the neat complex but undergoes distortion inside zeolite matrix. To ascertain whether different electrochemical responses are due to uncomplexed Fe^{2+} cations or iron complexes present on the external surfaces, a cyclic voltammogram is recorded for iron-exchanged NaY (Figure 3.10b). The redox couple (E_{pc} = -0.464V and E_{pa} = -0.238 V) is totally different from the iron phenanthroline complex encapsulated in zeolite-Y. This indicates the formation $[Fe(Phen)_3]^{2+}$ complex inside zeolite and not present on the external surface and it follows the intrazeolite electron transfer mechanism.

The cyclic voltammogram of the neat copper complex recorded at room temperature under the similar condition as in the case of iron-phenanthroline complex shows irreversible peak for the Cu(I)→Cu(II) couple at -0.536 V with a direct cathodic peak for Cu(II)→Cu(I) at -0.264V and it also shows one additional irreversible peak in anodic region (Figure 3.11a). The occurrence of an additional irreversible couple may be attributed to isomers of the $[Cu(Phen)_3]^{2+}$ complex, and containing partially associated phenanthroline, ligand-bridged complexes. The cyclic voltammogram of copper phenanthroline complex encapsulated in NaY is shown in Figure 3.11c. Several interesting differences are apparent on comparing the cyclic voltammetry of $[Cu(Phen)_3]^{2+}$ neat complex with that of Cu-PhenY as a component of zeolite modified electrode. Notably the peak potential are broadened and shifted to more negative values. The shifting of the E° values at zeolite modified electrode (ZME) from those of redox couple of the $[Cu(Phen)_3]^{2+}$ complex in solution may be due to an environmental difference. The redox information obtained with ZME for the encapsulated transition metal complexes is somewhat complicated because the electrode binders may have instability in the solvent or the modification of the electrode may impart some mechanical work to the zeolite lattice. Several other groups have observed that the zeolite modified electrode yields a drastic decrease in peak currents over minutes if the electron transfer occurs via an extrazeolite mechanism.[35-37] However, in our case we observed that the peak currents obtained at ZME are stable upto several hours (Figure 3.11d) and it does not vanish upto number of cycles. This behavior of cyclic voltammogram suggest for an intrazeolite redox mechanism.

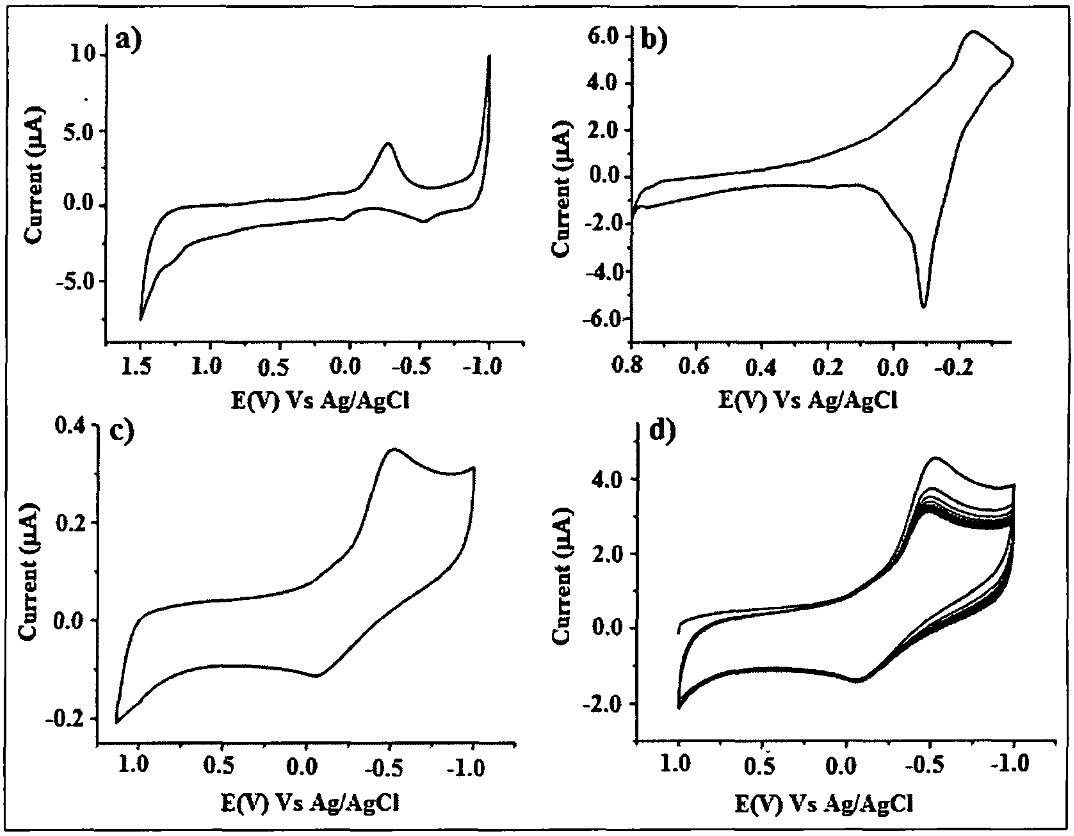

Figure 3.11. Cyclic voltamoogram of a) neat $[Cu(Phen)_3]^{2+}$ b) Cu^{2+}-Y c) encapsulated Cu-PhenY d) the stability of Cu-PhenY complex upto 50-cycles at scan rate of 0.1V. The voltammograms from a)-d) are taken as ZME in DCM using 0.1M TBAP as supporting electrolyte.

The cyclic voltammogram of the neat $[Zn(Phen)_3]^{2+}$ complex in solution shows a redox couple at E_{pc} = -0.295V and E_{pa}= -0.426 ($E_{1/2}$ = -0.360), Figure 3.12 a. The cyclic voltammogram of Zn-PhenY coated electrode do not show redox behavior in 0.1M TBAP supporting electrolyte solution. This shows that interior molecules of Zn-PhenY are voltametrically inaccessible in 0.1M TBAP solution. However, after addition of 2 ml of 0.05M H_2SO_4 in presence of H_2SO_4 the encapsulated Zn-PhenY

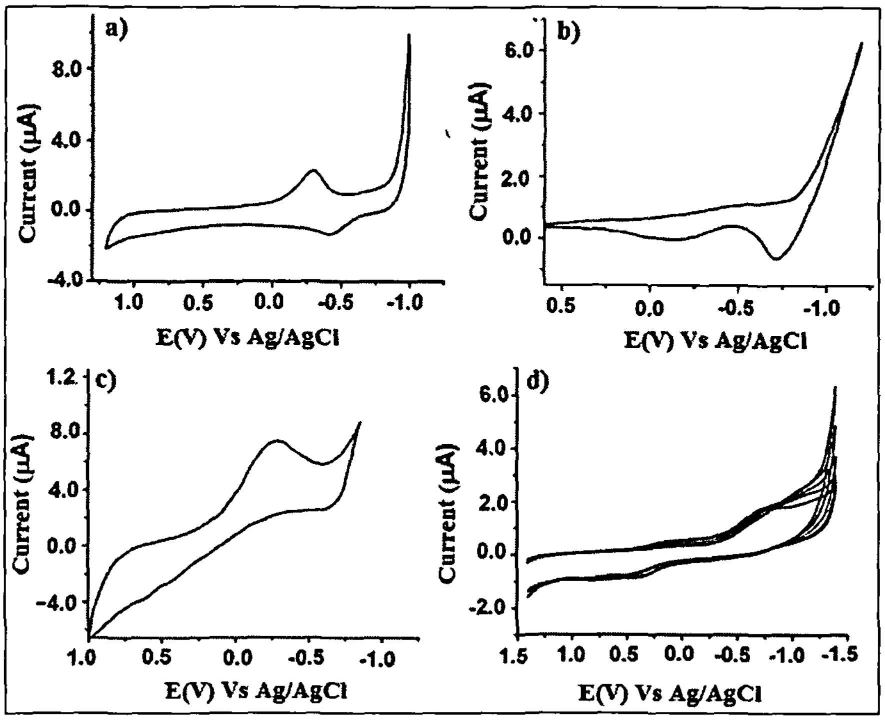

Figure 3.12. Cyclic voltamoogram of a) neat $[Zn(Phen)_3]^{2+}$ b) Zn^{2+}-Y c) Zn-PhenY d) the fluxional behavior in the redox potential of Zn-PhenY complex taken as zeolite modified electrode (ZME) using 0.05M H_2SO_4 as supporting electrode.

complex shows a cathodic wave at -0.265 V due to the reduction of Zn(II) to Zn(0) and the corresponding oxidation potential at -0.614V ($E_{1/2}$= -0.439V), (Figure 3.12c). The cyclic voltammogram observed after addition of 2ml of 0.05 H_2SO_4 solutions is stable up to a limited period of time (30-40min) and vanishes after 1h. The alternation of peak peak potential towards more negative value suggests the stabilization of Zn^{2+} in zeolite supercage. The observed change in the E° values provides the evidence that the actual electroactive species must be related to a boundary associated species on the zeolite. The presence of electrochemical response of the zeolite encapsulated complex in presence of H^+ ion further confirms that the metal complex leach out or get dissociated from the supercage of the zeolite in presence of 0.05M H_2SO_4 and are randomly distributed in the zeolite coating. Ganesan and Ramaraj[27] also reported that polypyridyl metal complexes ($[Ru(bpy)_3]^{2+}$ synthesized inside the supercages of zeolite-Y shows electrochemical behavior in 0.05M H_2SO_4 but are electrochemically inactive in 0.1M Na_2SO_4 or in other supporting electrolyte such as $LiNO_3$ or $CsNO_3$. And they suggest for extrazeolite electron transfer mechanism for the metal complexes adsorbed on the zeolite surface. Thus the appearance of cyclic voltammogram in presence of H^+ ion supports that Zn-Phen complex is formed on the external surface of zeolite-Y and it follows an extrazeolite electron transfer path. The crystallinity of the zeolite-Y is maintained after and before the encapsulation of Zn-phenanthroline complex. However, after acid treatment crystallinity of the NaY is lost as evident from XRD (Figure 3.13). This further indicates the disintegration of zeolite-Y in presence of H_2SO_4 leads to random distribution of zinc complex in the zeolite film.

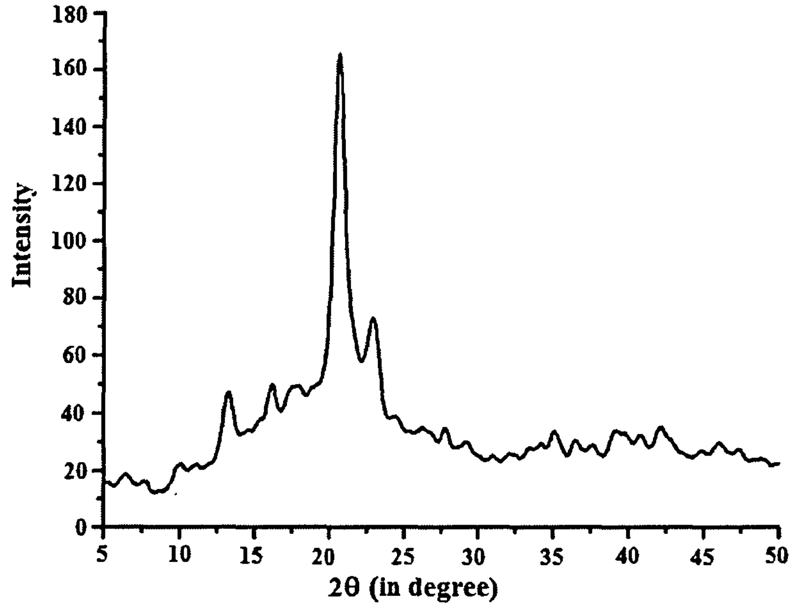

Figure 3.13. XRD pattern of Zn-PhenY after treatment with H_2SO_4.

3.2.1.8. TGA Study

The thermograms of metal exchange zeolite (M^{2+}-Y), M-PhenY and neat $[M(Phen)_3]^{2+}$ (M = Fe^{2+} and Cu^{2+}) are displayed in Figure 3.14. The comparison of TGA profiles for $[M(Phen)_3]^{2+}$ and M-PhenY show that neat complex has four weight loss steps at about 100, 280, 410 and 610 °C. On the basis of the weight changes, the first weight loss step corresponds to the loss of water molecule as an endothermic phenomenon; the second weight loss step may be related to the loss of Cl_2. There is a sharp weight change at 410 ^{0}C which is attributed to loss of phenanthroline groups. The weak peak at 610 ^{0}C may be attributed to sublimation of a part of MC_2. The pattern of thermogravimetric curve for the surface adsorbed zinc phenanthroline complex is found to be the same as that of the neat complex except a little enhancement in the thermal stability. However, for the corresponding encapsulated complexes of iron and copper, is found to show higher thermal stability, which indicates that the thermal stability is greatly enhanced on encapsulation. Furthermore, in the encapsulated systems there occurs no peak at 100-120 ^{0}C indicating the absence of water of crystallization. This gives another piece of strong evidence for the inclusion of $[M(Phen)_3]^{2+}$ complexes in NaY. On the basis of thermal analysis data, it can be concluded that zeolite encapsulated M-PhenY complexes may be treated thermally without any significant decomposition.

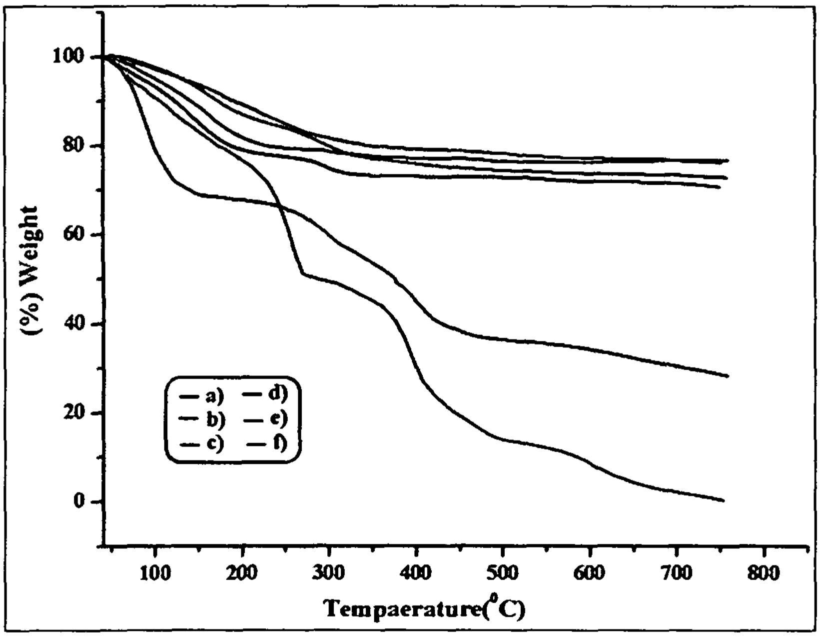

Figure 3.14. Thermogravimetric analysis (TGA) results for a) Na-Y b) M^{2+}-Y c) Fe-PhenY d) Cu-PhenY e) Zn-PhenY, f) $[M(Phen)_3]^{2+}$ neat complex (M= Fe^{2+}, Cu^{2+}, Zn^{2+})

3.2.2. Theoretical Calculation

3.2.2.1. Geometries

The geometrical parameters obtained from VWN/DN level calculations for the neat and the encapsulated complexes are provided in Table 3.4. The geometrical parameters such as bond length and bond angles have been compared with the available crystal structures for tris(phenanthroline) complexes of iron (II), copper (II) and zinc (II)[28-30] and are found to be in good agreement. When these tris chelated metal complexes with D_3 propeller geometry being encapsulated (in case of Fe and Cu) into the zeolite cavity or tethered over zeolite surface (in case of Zn), the bond length and the bond angle between the metal and the ligand molecule slightly changes in comparison to those of the corresponding neat complexes. Quantum chemical calculations have proven that Si-O bonds in zeolites have covalent character.[31] Valence electrons in zeolites are distributed all over the framework as a partially delocalized electronic cloud. At relatively short distances between the complex molecule and the walls of the zeolite cavities, the electron-electron repulsions will be operative, which

Table 3.4. Selected bond distance (in Å) and bond angles (in degree) of the optimized neat complexes, $[M(Phen)_3]^{2+}$and zeolite encapsulated phenanthroline complexes, M-PhenY ($M = Fe^{2+}$, Cu^{2+} and Zn^{2+}).

Bonds	$[Fe(Phen)_3]^{2}$	FePhen Y	$[Cu(Phen)_3]^{2+}$	CuPhen Y	$[Zn(Phen)_3]^{2+}$	ZnPhen Y
$M-N_1$	1.93	1.96	2.04	2.03	2.13	2.19
$M-N_2$	1.93	1.92	2.18	1.98	2.12	2.24
$M-N_3$	1.93	1.94	2.05	2.33	2.12	2.18
$M-N_4$	1.92	1.92	2.17	1.94	2.12	2.14
$M-N_5$	1.94	1.89	2.05	2.21	2.13	2.08
$M-N_6$	1.92	1.91	2.04	2.01	2.12	1.89
<u>Angles</u>						
$\angle N_1-M-N_2$	83.90	83.90	79.50	83.67	78.92	80.28
$\angle N_1-M-N_3$	90.22	87.34	90.81	85.38	93.31	89.42
$\angle N_1-M-N_4$	92.91	88.56	96.42	89.57	94.09	92.14
$\angle N_1-M-N_5$	91.93	94.92	94.34	96.72	94.14	96.41
$\angle N_1-M-N_6$	174.32	178.26	170.82	173.78'	170.31	175.14
$\angle N_2-M-N_3$	83.92	88.07	95.66	85.29	94.35	81.95
$\angle N_2-M-N_4$	175.73	169.81	173.51	164.36	170.04	164.24
$\angle N_2-M-N_5$	88.84	94.20	91.35	96.20	93.84	103.25
$\angle N_2-M-N_6$	92.20	94.52	92.50	101.59	94.71	96.96
$\angle N_3-M-N_4$	83.9	84.93	79.34	79.78	78.84	75.97
$\angle N_3-M-N_5$	177.33	177.12	172.0	177.82	170.03	165.61
$\angle N_3-M-N_6$	94.1	93.42	94.40	101.95	94.46	94.60
$\angle N_4-M-N_5$	94.23	93.22	94.12	98.57	94.02	90.62
$\angle N_4-M-N_6$	91.24	93.25	92.08	86.28	93.07	91.46
$\angle N_5-M-N_6$	84.05	84.50	81.46	79.30	78.84	80.29

will cause the bond length between the metal ion and the ligand molecule to change. The optimized geometry of the zeolite adsorbed zinc complex is shown in Figure 3.15. It can be seen from Figure 3.15 that the bond distances between the oxygen atom of silanol hydroxyl group and hydrogen atom of phenanthroline moiety ranges from 1.97 to 2.5 Å. These distances are smaller than the sum of the van der Waals radii (2.6 Å) of

T-atoms of zeolite and hydrogen atom of phenanthroline ligand. These results indicate the existence of Si-O...H-C hydrogen bond which is in accordance with our experimental FTIR and UV-visible studies. The occurrence of H-bond indicates the possibility of tethering of the metal complex over zeolite surface leading to the formation of a supramolecular host-guest complex.

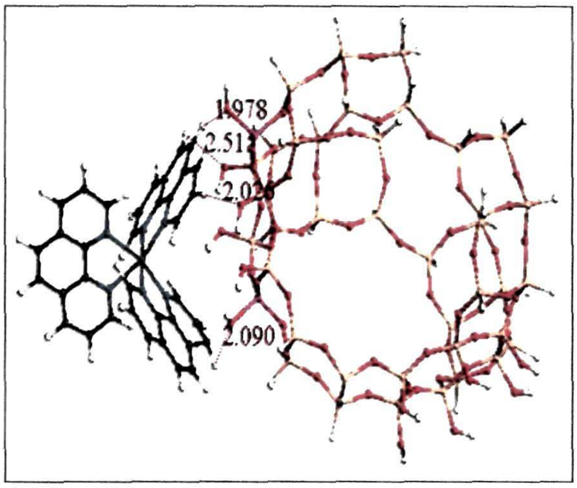

Figure 3.15. The possible supramolecular host-guest interaction between the H-atom of phenanthroline ligand of Zn-complex and silanol oxygen of zeolite moiety via H-bonding.

3.2.2.2. Electronic Structure, Ionization Potential, Electron Affinity and Binding Energy

The HOMO and LUMO orbitals corresponding to those of the neat and the encapsulated complexes are shown in Figure 3.16. For all the complexes, the pattern of the occupied and the unoccupied orbitals are qualitatively similar. Both spin restricted and spin unrestricted calculations are performed on all the systems. As iron and zinc possess close shell d^6 and d^{10} configurations, respectively, the energies of the frontier orbitals corresponding to spin up and spin down states are found to be approximately same in both the calculations. In case of Cu(II) systems with open shell d^9 configuration, the energies of the frontier orbitals in spin restricted and unrestricted are found to be different. Furthermore, the energies of the HOMO and the LUMO orbitals (obtained by spin unrestricted calculation) corresponding to spin up and spin down state are not same as in the case of iron and zinc complexes. The *d*-orbitals of transition metal complexes lie very close in energy, so the first ionization potential (IP) and electron affinity (EA) values for all the complexes are also calculated. To calculate the ionization potential and electron affinities spin unrestricted calculation are performed for the Fe and Zn complexes. Since both Fe and Zn are closed shell systems, either removal or addition of electron will lead to open shell systems with spin multiplicity of doublet. In case of copper (II) complexes with d^9 configuration, two cases are possible. One, after removal of an electron, the electrons in e_{2g} orbitals remain paired due to *Jahn-Teller* distortion. In that case the total spin multiplicity of the system will be 1 with S=0. However, if one ignore the *Jahn-Teller* distortion and assume the two e_{2g}-orbitals to be degenerate, the total spin multiplicity of the system will be 3 with S=1. Considering both the situation spin restricted calculation for S=0 and spin unrestricted calculation for S=1 are carried out to calculate the ionization potential of the Cu-complexes. The IP-value obtained by spin restricted calculation is found to be less than spin unrestricted calculation. For example in case of Cu-PhenY the IP value obtained by spin restricted calculation (6.044 eV) is found to be less than the spin unrestricted calculation (6.118eV) by ~0.074eV. In case of neat $[Cu(Phen)_3]^{2+}$ complex this difference is found to be 0.018eV. This indicates that the Cu(II)-complex undergoes *Jahn-Teller* distortion to lower the energy. In Table 3.5 the IP value for the most stable state are presented. On addition of an extra electron however, will convert the total system to a closed shell system with d^{10} configuration (S=0). For this reason, in case of the copper complexes only spin restricted calculation is done to obtain the EA values. The energy values for the frontier orbitals of all the six systems are given in Table 3.5. It can be seen from Table 3.5 that among the doubly charged neat complexes the frontier orbitals of $[Cu(Phen)_3]^{2+}$ lies higher in energy compared to the other two complexes. The HOMO energies are in the order of $[Zn(Phen)_3]^{2+}$ < $[Fe(Phen)_3]^{2+}$ < $[Cu(Phen)_3]^{2+}$ and that of LUMOs are in the order of $[Fe(Phen)_3]^{2+}$ < $[Cu(Phen)_3]^{2+}$ < $[Zn(Phen)_3]^{2+}$. In case of the neutral M-PhenY complexes, the zeoliteY (possessing two charge compensating Al-atoms in six member ring) act as a counter ion. The order of HOMO energies in these complexes is similar to that of the neat charged complexes and LUMO energies are found to be in the order of Zn-PhenY < Fe-PhenY < Cu-PhenY. Further, it is observed from Table 3.5 that among the charged $[M(Phen)_3]^{2+}$ complexes and the neutral M-PhenY complexes, ionization potential (IP) of encapsulated copper complex is less than the corresponding iron and zinc complexes whereas the surface adsorbed zinc complex has less electron affinity (EA) value. This indicates that Cu-PhenY will act as better oxidizing agent whereas Zn-PhenY will act as a better reducing agent. The change in the energies of the LUMO can be attributed to the influence of the zeolite-Y serving as counter ion. In general, encapsulation accounts for effect of both confinement as well as the counter ion. In order to have a better understanding of the effect of zeolite matrix on the electronic properties of ship in bottle complexes, DFT calculation are executed at the same level of theory by incorporating the charged complex inside the neutral zeolite-Y (modeled by replacing the two Al atoms with two Si atoms).The HOMO and LUMO orbitals corresponding to the three charged complexes, $[M(Phen)_3\text{-}Y]^{2+}$ [M = Fe, Cu and Zn] are shown in Figure 3.17. The energies of the frontier orbitals for these charged complexes are given in Table 3.6. It can be observed from Table 3.6 that the HOMO and the LUMO energies of these complexes become destabilized in comparison to the neat complexes. Moreover, the HOMO-LUMO gap is found to decrease in the zeolite encapsulated complexes. Thus the results of the theoretical studies suggest that on encapsulation of the metal complexes, the energies of the frontier orbital gets lifted up leading to small HOMO-LUMO gap. The change in the energies of the frontier orbitals may be either due to the effect of the counter ion, here zeolite-Y or due to the steric constrain impart by the zeolite matrix. The types of interaction normally considered when a guest molecule is confined inside the zeolite are due to Coulombic effects, coordination effects, and van der Waals interactions.[32] Coulombic effects are produced by the charge distribution along the framework, because of the partial ionic character of the zeolite lattice. This charge distribution generates a strong Coulombic field in the cavities, which might alter the energy level of the transition-metal complexes. Coordination effects are produced by Lewis acid-base-type interactions among the transition-metal complexes and certain sites of the zeolite framework. Weak electronic interactions account for the forces of the van der Waals type. This type of long range effects is not included in the standard DFT exchange-correlation functionals and hence is not incorporated in our discussions. However, such interaction will be very much similar in case of the encapsulated Fe and Cu complexes and will stabilize them in comparison to the surface adsorbed Zn-complex.

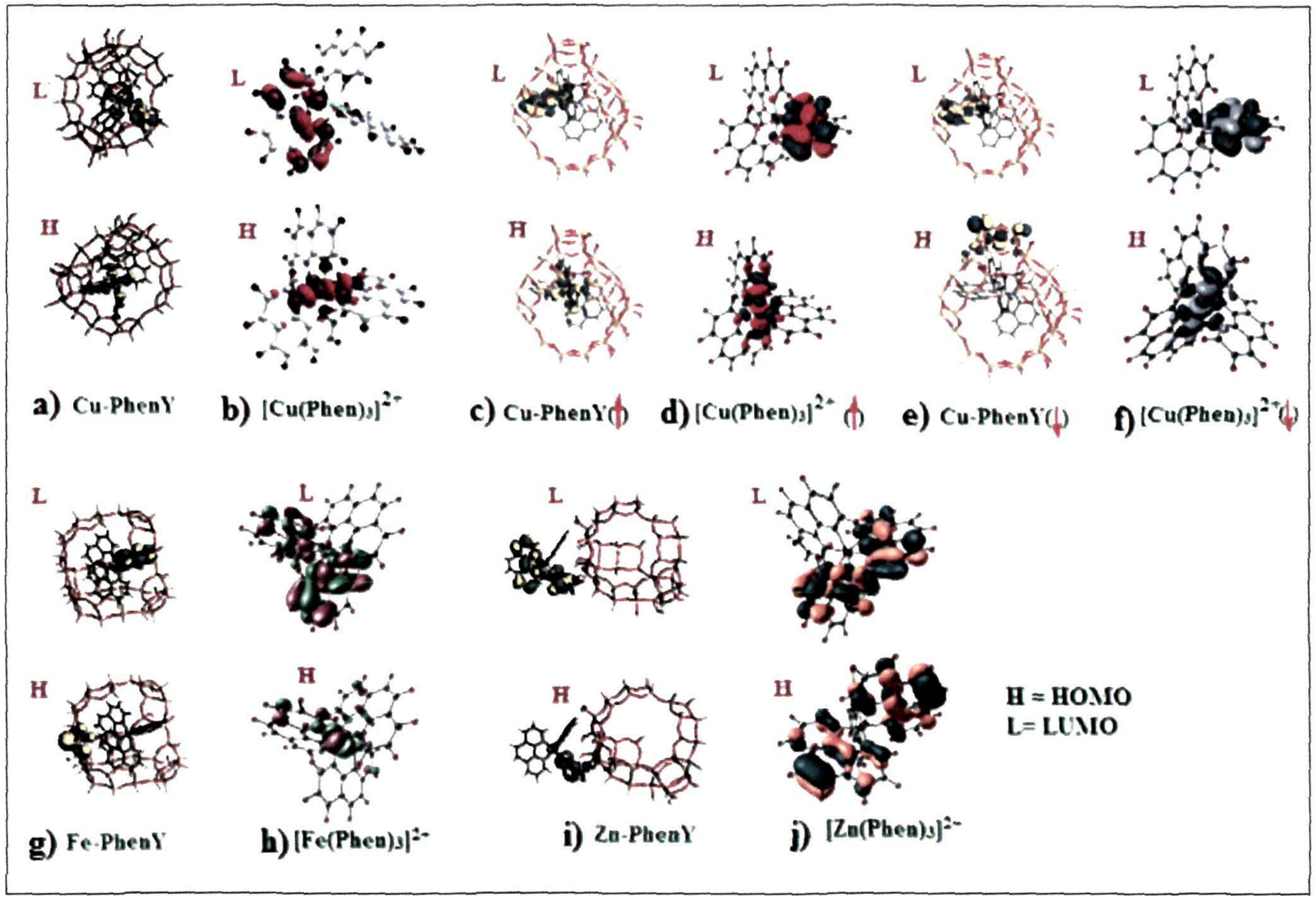

Figure 3.16. Schematic representation of the HOMO and LUMO orbitals of the neat, encapsulated and surface adsorbed phenanthroline complexes. a) Cu-PhenY b) $[Cu(Phen)_3]^{2+}$ c) and d) HOMO and LUMO orbital corresponding to spin up state in Cu-PhenY and $[Cu(Phen)_3]^{2+}$ complexes, respectively. e) and f) corresponds to HOMO and LUMO orbital for the spin down state in Cu-PhenY and $[Cu(Phen)_3]^{2+}$ complexes, respectively. g) Fe-PhenY h) $[Fe(Phen)_3]^{2+}$ i) Zn-PhenY and j) $[Zn(Phen)_3]^{2+}$.

Table 3.5. Calculated first ionization potential (IP in eV), electron affinity (EA in eV) energy of HOMO and LUMO (in eV), hardness (η, in ev), chemical potential (μ, in eV), electrophilicity index (ω in eV) and global softness (S, in eV) of the neat and encapsulated complexes. The values in the parenthesis are obtained using finite difference approximation.

Complexes	IP	EA	E_{HOMO}	E_{LUMO}	μ	η	ω	S
$[Fe(Phen)_3]^{2+}$	12.774	7.269	-10.542	-8.594	-9.568(-10.021)	0.974(2.752)	46.995(18.242)	0.513(0.181)
Fe-PhenY	6.618	3.010	-5.022	-3.506	-4.264(-4.814)	0.758(3.608)	11.993(3.211)	0.659(0.138)
$[Cu(Phen)_3]^{2+}$	11.965	7.523	-9.747	-8.537	-9.142(-9.744)	0.605(2.221)	69.071(21.37)	0.826(0.225)
$[Cu(Phen)_3]^{2+}(\downarrow)$	-	-	-9.895	-9.320	-9.607	0.2875	160.529	1.740
$[Cu(Phen)_3]^{2+}(\uparrow)$	-	-	-10.259	-8.591	-9.425	0.834	53.255	0.560
Cu-PhenY	6.044	2.607	-4.406	-3.493	-3.949(-4.325)	0.456(1.718)	17.084(5.443)	1.095(0.290)
Cu-PhenY(↓)	-	-	-4.742	-4.094	-4.418	0.324	30.121	1.543
Cu-PhenY(↑)	-	-	-4.826	-3.531	-4.1785	0.647	13.482	0.772
$[Zn(Phen)_3]^{2+}$	13.072	6.372	-11.43	-8.496	-9.963(-9.722)	1.467(3.350)	33.831(14.107)	0.340(0.149)
Zn-PhenY	6.159	2.214	-5.651	-4.438	-5.044(-4.137)	0.606(1.972)	20.978(4.451)	0.824(0.260)

Table 3.6. Calculated first ionization energy (IP) and electron affinity (EA), HOMO and LUMO energies (in eV), hardness (η, in ev), chemical potential (μ, in eV), electrophilicity index (ω in eV) and global softness (S, in eV) of the encapsulated charged complexes. The values in parenthesis are obtained from finite difference approximation.

Complexes	IP	EA	E_{HOMO}	E_{LUMO}	μ	η	ω	S
$[Fe(Phen)_3\text{-}Y]^{2+}$	9.213	5.556	-7.824	-6.328	-7.076(-7.384)	0.748(1.828)	33.469(14.712)	0.668(0.273)
$[Cu(Phen)_3\text{-}Y]^{2+}$	8.786	7.002	-6.952	-6.069	-6.510(-7.894)	0.441(0.892)	48.002(34.930)	1.132(0.560)
$[Cu(Phen)_3\text{-}Y]^{2+}$ (↑)	-	-	-7.609	-6.608	-7.108	0.500	50.480	0.999
$[Cu(Phen)_3\text{-}Y]^{2+}$ (↓)	-	-	-7.475	-6.587	-7.031	0.444	55.67	1.126
$[Zn(Phen)_3\text{-}Y]^{2+}$	8.977	5.493	-9.164	-7.980	-8.572(-7.235)	0.592(1.742)	62.060(15.024)	0.844(0.287)

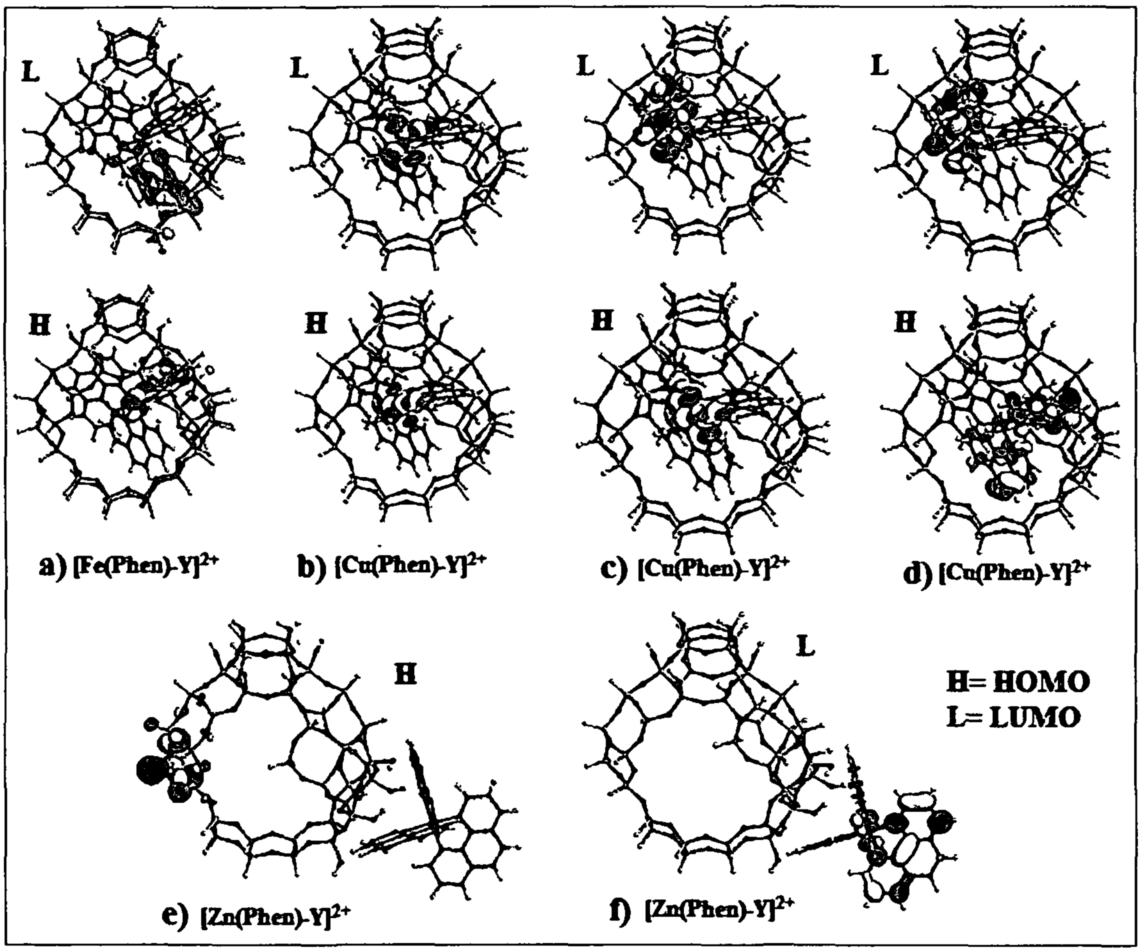

Figure 3.17. HOMO and LUMO orbitals of zeolite encapsulated charged complexes, $[M(Phen)_3\text{-}Y]^{2+}$ (M= Fe, Cu and Zn).

The interaction energies of the encapsulated iron and copper complexes and that of the surface adsorbed zinc complex are calculated as the energy differences between the optimized encapsulated complexes and the corresponding fragments (neat metal complex and the zeolite framework) optimized as isolated molecules. The calculated interaction energies are in the order of $[Cu(Phen)_3]^{2+}$(-52.97eV) > $[Zn(Phen)_3]^{2+}$(-50.48 eV) > $[Fe(Phen)_3]^{2+}$(-12.08eV). This result indicates that $[Cu(Phen)_3]^{2+}$-complex interacts more strongly and becomes more stabilized than the other two complexes. This difference in interaction energy can be attributed to change in the geometrical parameters and number of *d*-electrons in the central metal atom. As the number of the *d*-electrons increases, the metal-nitrogen bond (M-N) lengths vary significantly between 1.9 and 2.3 Å. It can be seen from Table 3.4 that the most stable complex i.e $[Cu(Phen)_3]^{2+}$ complex encapsulated in zeolite-Y has the longest M-N bond length. The interaction energy of $[Fe(Phen)_3]^{2+}$ complex is less incomparison to the other because of the high crystal field stabilization energy ($-2.4\Delta_0$) associated with this low spin complex. The $[Cu(Phen)_3]^{2+}$ complex encapsulated in zeolite undergoes *Jahn-Teller* distortion and the distortions undergone by the complex give the dominant contribution to interaction energy. These differences in the interaction energy bring a considerable change in the energies of the HOMO and the LUMO levels. This approach will further help to rationalize the observation made by Maruszewski et al. that the encapsulation entails an increase in energy of the excited d-d quencher state in $[Ru(bpy)_3]^{2+}$ but also in other Ru(II) polypyridine complexes of similar size[33]. More generally it can be used to address the prediction of the influence of the environments provided by different hosting cavities on the electronic and physicochemical properties of a given complex.[34]

3.2.2.3. Global Descriptors

Since the zeolite matrix influences the electronic as well as the chemical behavior of the transition metal complexes, the DFT-based global descriptors *viz* chemical hardness (η), chemical potential (μ), electrophilicity index (ω) and softness (S) are calculated using DN basis set and VWN functional for the neat, encapsulated (Fe and Cu) and tethered (Zn) complexes. The values for η, μ, ω and S given in Table 3.5 and Table 3.6 are calculated

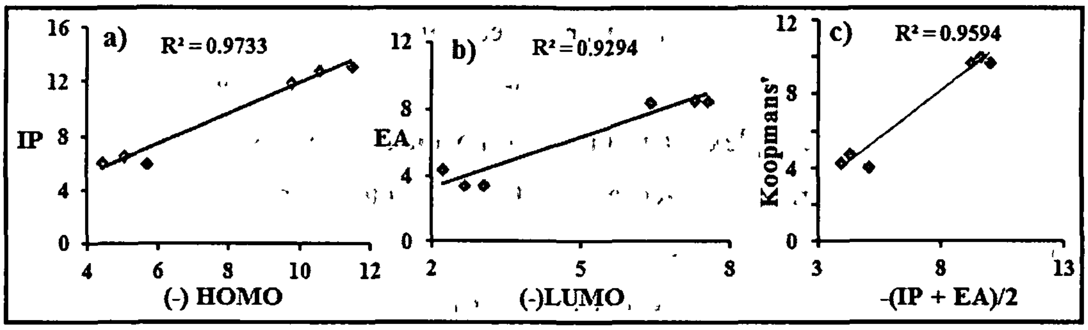

Figure 3.18. Plot showing the correlation between the A) IP and –ve of HOMO B) EA and –ve of LUMO C) chemical potential (μ) values calculated using Koopmans' approximation against those obtained in terms of IP and EA.

based on Koopmans' and finite difference approximations. According to Koopmans' approximation ionization potential is the negative of HOMO energy and electron affinity is the negative of LUMO energy. The plot of IP and EA against the HOMO and LUMO energies respectively shows a linear correlation with r^2 values of 0.973 and 0.929, Figure 3.18a and 3.18b. Similarly, the plot of chemical potential values obtained by Koopmans'approximation against those of IP and EA gives an r^2 value of 0.959, Figure 3.18c. Due to several limitations associated with Koopmans' approximation,[35-38] especially in case of transition metal complexes, numerical values of η, S and ω obtained from both the approximations are found to be different. But the trend in the change of global descriptors values predicted by both approximations for the considered systems follows the same order. For example the change in global hardness values predicted by equations (26) and (27) as well as by equations (30) and (31) [see Chapter 2] follows the same order i.e. $[Cu(Phen)_3]^{2+} < [Fe(Phen)_3]^{2+} < [Zn(Phen)_3]^{2+}$ for the neat complexes and Cu -PhenY < Zn-PhenY < Fe-PhenY for the hybrid complexes.

According to maximum hardness principle (MHP),[39,40] the most stable structure has the maximum hardness. Thus the neat complexes with maximum hardness are chemically more stable compared to the encapsulated ones. Further, it can be seen from the Table 3.5 and Table 3.6 that upon encapsulation the value of chemical potential (μ) increases whereas that of the electrophilicity index (ω) decreases. In this context, it is pertinent to mention that electrophilicity containing information for both electron transfer (chemical potential) and stability (hardness) is considered to be a better descriptor of global chemical reactivity. Moreover, ω includes a hardness term in the denominator which is a descriptor of stability. Electrophilicity is expected to exhibit an inverse linear relationship with hardness or in correlation with MHP it can be said that under the conditions for the existence of an MHP there will also be a *minimum electrophilicity principle*.[41] It can be observed from Table 3.5 and Table 3.6 that complex having the maximum hardness has the minimum electrophilicity i.e. in case of neat complexes $[Zn(Phen)_3]^{2+}$ with maximum hardness has minimum electrophilicity whereas in case of encapsulated systems Fe-PhenY or $[Fe(Phen)_3\text{-}Y]^{2+}$ with maximum hardness has minimum electrophilcity. Thus it is found that on encapsulation of the complexes into zeolite framework the chemical potential (μ) and the global softnees (S) values increase whereas that of η and ω decreases. This change in values of the global descriptors reflects the effect of zeolite matrix on the reactivity of the complexes and it can be said that complexes with high μ value can actively participate in electron transfer reactions. In our case the Cu-PhenY or $[Cu(Phen)_3\text{-}Y]^{2+}$ complex with maximum μ, minimum η and maximum S values will be the most reactive system.

3.2.2.4. Local Descriptors

Table 3.7 and Table 3.8 presents the Fukui functions (FFs, f_κ^+ and f_k^-) for the selected metal atoms and the coordinated nitrogen atoms calculated using Hirshfeld Population Analysis (HPA) scheme for the neat and encapsulated metal complexes. It is seen in Tables 3.7 and 3.8 that the values of the Fukui functions at the metal centers decrease upon encapsulation. In the context of Li and Evans rationalization,[42] a minimum Fukui function at the metal center would be an indicator for the nitrogen atoms of the phenanthroline ring to maximize the hardness of the metal atom. Some of the reported calculations have shown that a minimum Fukui function site is preferred for hard-hard interaction whereas a soft-soft interaction is preferred at the site with maximum Fukui function.[43-45] Thus the zeolite framework modifies the reactivity of the metal atom from a soft site in $[M(Phen)_3]^{2+}$ neat complexes to a hard site in M-PhenY. Among all the systems, the Zn-PhenY or $[Zn(Phen)_3\text{-}Y]^{2+}$ complex will have more preferential site for interacting with a hard species. As per the attack of nucleophile or electrophile at a particular site is concerned, the Cu-atom (in both neat and the encapsulated) possessing the higher value of Fukui functions ((FFs, f_κ^+ and f_k^-) in comparison to the other systems will be the most preferential site. However, the Fukui functions values (shown in parenthesis, Table 3.7) obtained by spin unrestricted calculations are found to be less in comparison to those obtained by spin restricted calculations. This further reflects the fact that the HOMO and LUMO energies for the spin up and spin down orbitals also influences the reactivity of the two complexes. In other words, if the unpaired electron of the Cu-atom uses a single molecular orbital twice, once multiplied by the α spin function and once multiplied by the β spin function, the metal centre becomes more susceptible for both nucleophillic as well as electrophillic attack. But if it uses different molecular orbitals for α and β electrons, it becomes less susceptible for those attacks.

Table 3.7. Fukui functions (FFs, f_κ^+ and f_k^-) for the selected atoms of neat [M(Phen)$_3$]$^{2+}$ and M-PhenY complexes (M = Fe, Cu and Zn). The values given in parenthesis are obtained by spin unrestricted calculation.

Selected Atoms	[Fe(Phen)$_3$]$^{2+}$		[Cu(Phen)$_3$]$^{2+}$		[Zn(Phen)$_3$]$^{2+}$		Fe-PhenY		Cu-PhenY		Zn-PhenY	
	f_κ^+	f_κ^-	f_κ^+	f_κ^-	f_κ^+	f_κ^-	f_κ^+	f_κ^-	f_κ^+	f_κ^-	f_κ^+	f_κ^-
N(1)	0.008	0.001	0.010 (0.008)	0.011 (0.009)	0.009	0.012	-0.003	0.001	0.011 (0.006)	0.010 (0.007)	-0.006	-0.001
N(2)	0.009	0.000	0.003 (0.003)	0.005 (0.010)	0.009	0.012	-0.005	-0.001	0.010 (0.005)	0.009 (0.006)	0.005	0.019
N(3)	0.007	0.001	0.009 (0.006)	0.011 (0.009)	0.009	0.012	-0.005	0.000	0.002 (0.002)	0.005 (0.008)	0.026	0.009
M	0.004	0.084	0.116 (0.074)	0.113 (0.109)	0.004	0.060	0.014	0.032	0.074 (0.053)	0.071 (0.063)	0.001	0.002
N(4)	0.007	0.000	0.003 (0.002)	0.005 (0.010)	0.009	0.012	-0.005	-0.001	0.010 (0.002)	0.012 (0.009)	0.026	0.009
N(5)	0.008	0.001	0.010 (0.012)	0.011 (0.009)	0.008	0.012	0.017	0.004	0.001 (0.012)	0.000 (0.006)	-0.005	-0.001
N(6)	0.008	0.001	0.011 (0.012)	0.012(0.010)	0.009	0.012	0.032	0.007	0.015 (0.016)	0.012 (0.011)	-0.007	-0.004

Table 3.8. Fukui functions (FFs, f_K^+ and f_k^-) for the selected atoms of $[M(Phen)_3\text{-}Y]^{2+}$ complexes (M = Fe, Cu and Zn). The values for Cu-complex are those obtained by spin unrestricted calculation.

Selected Atoms	$[Fe(Phen)_3\text{-}Y]^{2+}$		$[Cu(Phen)_3\text{-}Y]^{2+}$		$[Zn(Phen)_3\text{-}Y]^{2+}$	
	f_K^+	f_K^-	f_K^+	f_K^-	f_K^+	f_K^-
N	-0.002	-0.001	0.005	0.015	0.005	0.002
N	-0.004	0.005	0.008	0.005	-0.001	0.002
N	0.002	0.004	0.008	0.007	0.015	0.008
M	0.012	0.050	0.018	0.026	0.001	0.001
N	0.008	0.004	0.006	0.006	0.014	0.008
N	0.011	0.002	0.009	0.011	-0.005	-0.002
N	0.014	0.002	0.019	0.017	-0.003	-0.002

3.2.2.5. Absorption Spectra

Comparisons between the experimental and theoretical absorption spectra of all the three neat phenanthroline complexes in methanol are provided in Figure 3.19, Figure 3.20 and Figure 3.21. In all the three systems it is noticed that increasing the Gaussian width used for the simulation of the transitions leads to an improved overall shape. The HOMO (**153**), HOMO-1 (**152**) and HOMO-2 (**151**) of the Fe-phananthroline complex are metal based *d* orbitals. The HOMO corresponds to A_1, while the doubly degenerate HOMO-1 and HOMO-2 correspond to E in D_3 point group. The HOMO-3 (**150**) to HOMO-8 (**145**) are phenanthroline based π MOs while LUMO (**154**) to LUMO+10 (**164**) are phenanthroline based π* orbitals. TDDFT predicted vertical excitation energies for the neat Fe-phanathroline complex along with the experimental UV-vis spectra are shown in Figure 3.19. The TDDFT predicted band positions in methanol solution are found to be in good agreement with the experimentally observed ones with a minor error in their relative intensities. The most relevant transitions are discussed here which are labeled as I, II, III and IV in order of decreasing energy (detailed list of TDDFT data and orbitals are provided in Table 3.9). The most intense band I (highest energy) calculated at around 214 nm (5.7 eV, f = 0.057) is mainly due to $\pi \rightarrow \pi^*$ transition arising from transition of π symmetric phenanthroline based occupied MO (HOMO-3, **150**) to phenanthroline based unoccupied π* MO (LUMO+7, **161**) with an expansion coefficient of 0.454 for single electron transitions. The next lower energy band II is calculated at around 252 nm (4.9 eV, f = 0.694) arises due to two major transitions. One of them is a ligand based $\pi \rightarrow \pi^*$ transition

Table 3.9. Selected energies, oscillator strengths, and expansion coefficients for vertical transitions in $[M(Phen)_3]^{2+}$ (M = Fe, Cu and Zn) calculated using a TDDFT approach.

Complex	Transition	E, eV	E, nm	*f*	Predominant Character	Major expansion coefficients for single electron transitions
$[Fe(Phen)_3]^{2+}$	I	5.7837	214.37	0.057	$\pi \rightarrow \pi^*$	**150 → 154**, 0.45417, **150 → 162**, 0.141168
	II	4.9082	252.61	0.694	$\pi \rightarrow \pi^*$	**145→154**, 0.28003, **153→164**, 0.24685
	III	2.9690	417.59	0.064	$d\pi \rightarrow p\,\pi^*$	**153→159**, 0.4670, **153→158**, -0.39840
	IV	2.6721	464.00	0.061	$d\pi \rightarrow p\,\pi^*$	**152→154**, 0.52480, **153→159**, 0.26916
$[Cu(Phen)_3]^{2+}$	I	4.8986	253.10	0.309	$\pi \rightarrow \pi^*$	**150→164**,0.28576, **149→159**, 0.29966, **148→160**,0.28610
	II	4.7761	259.59	0.0793	$\pi \rightarrow \pi^*$	**148→159**, 0.60423, **148→155**, 0.1851
	III	4.1965	295.49	0.0072	$d\pi \rightarrow p\,\pi^*$	**154→164**, 052334, **151→157**, 0.34186
	IV	3.9555	313.45	0.0272	$\pi \rightarrow \pi^*$	**152→157**, 0.37377, **152→155**, 0.39093, **153→156**, 0.30348
$[Zn(Phen)_3]^{2+}$	I	4.9814	248.89	1.2749	$\pi \rightarrow \pi^*$	**148 →159**, 0.39931, **149 →156**, 0.18407, **150 →157**, 0.18308
	II	4.8082	257.86	0.1489	$\pi \rightarrow \pi^*$	**150 →161**, 0.29120, **150 →160**, 0.23318, **148 →160**, 0.24511
			257.97	0.1323	$\pi \rightarrow \pi^*$	**150→161**, 0.29777, **150→161**, 0.25655, **148→161**, 0.23433
	III	4.7035	263.60	0.1224	$\pi \rightarrow \pi^*$	**149→158**, 0.60424, **154→162**, 0.12984
		4.7021	263.68	0.1169		**150→158**, 0.60424, **155→159**, 011621
	IV	4.2655	290.67	0.0239	$\pi \rightarrow \pi^*$	**152→158**, 0.20539, **152→159**, 0.21171, **153→158**, 0.28347
	V	3.9740	311.99	0.0375	$\pi \rightarrow \pi^*$	**153→156**, 0.34262, **155→156**, 0.32913

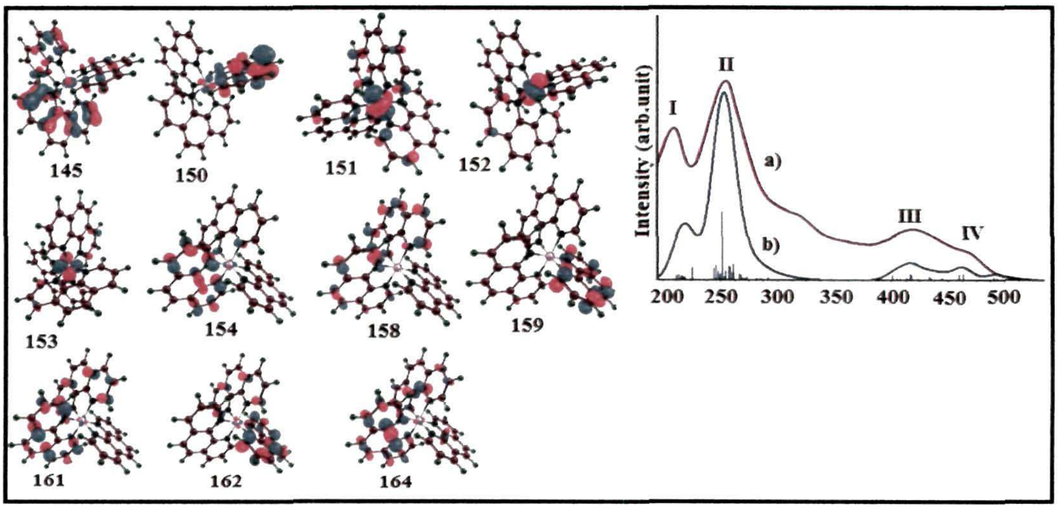

Figure 3.19. Important frontier orbital calculated for $[Fe(Phen)_3]^{2+}$ neat complex and simulation of a) experimental and b) theoretical absorption spectra.

from the π symmetric MO (**145**) centered at phenanthroline ligand to the π* symmetric ligand centered MO (**154**) with an expansion coefficient of 0.280. The other major transition calculated is from the metal and is a typical metal to ligand charge transfer, MLCT transition with an expansion coefficient of 0.246. This band is the most intense one observed both theoretically as well as experimentally. The next lower energy band, III, at around 417 nm (2.9 eV, $f = 0.064$) is due to predominant MLCT arising from the metal centered A_1 symmetric HOMO (**153**) to ligand based π* symmetric orbital (**158** and **159**) transition. The lowest energy band, IV, at around 464 nm (2.6 eV, $f = 0.062$) is again due to predominant MLCT from E symmetric metal based HOMO-1 (**152**) to ligand based π* symmetric LUMO (**154**) with an expansion coefficient of 0.524. Thus, the most relevant bands I and II calculated for neat $[Fe(Phen)_3]^{2+}$ complex using TDDFT method in methanol solution are due to ligand to ligand charge transfer (LL'CT), while the other two III and IV are mainly due to metal to ligand charge transfer (MLCT). The HOMO and LUMO orbital pictures of $[Cu(Phen)_3]^{2+}$ and $[Zn(Phen)_3]^{2+}$ have been shown in Figure 3.16. Other molecular orbitals relevant for UV-vis spectra analysis are shown in Figure 3.20 and 3.21.

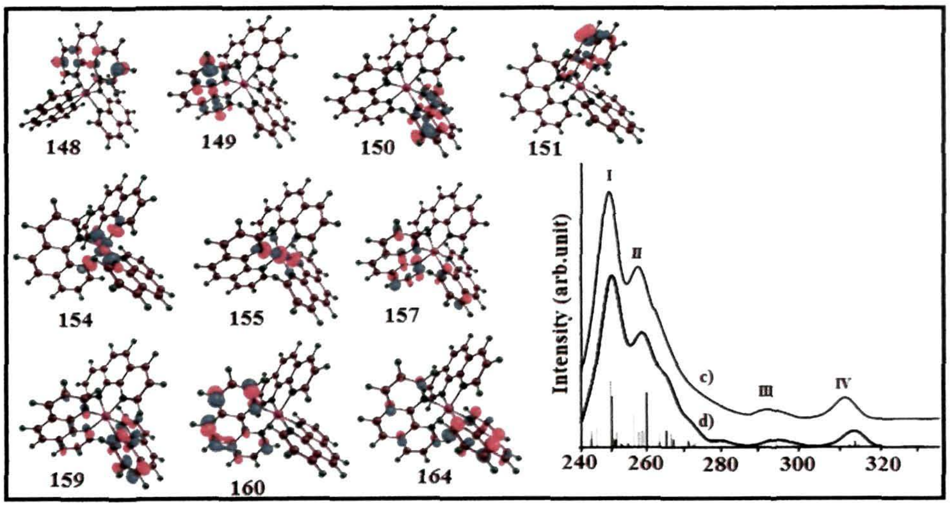

Figure 3.20. Important frontier orbital calculated for $[Cu(Phen)_3]^{2+}$ neat complex and simulation of c) experimental and d) theoretical absorption spectra.

The HOMO of $[Cu(Phen)_3]^{2+}$ complex has a significant metal *d* orbital contribution while there is no contribution of the metal *d* orbital in $[Zn(Phen)_3]^{2+}$ complex. The HOMO of $[Zn(Phen)_3]^{2+}$ is a pure ligand based π orbitals while HOMO – 4 (**148**) has some *d* orbital contribution, Figure 3.21. The LUMO of both these two complexes are essentially the same ligand based π* orbitals. TDDFT approach is undertaken to assign the vertical transitions. Figure 3.20 shows the experimental as well as TDDFT UV-vis spectra of $[Cu(Phen)_3]^{2+}$ complex. The electronic transitions from one electronic level to another are composed of several, often commensurable, orbital to orbital transitions which are represented by vertical lines. Four different transitions are assigned to this UV-vis spectrum. The first two transitions (I and II) at 253.10 and 259.59 nm with an oscillator strength of 0.309 and 0.079, respectively are due to the ligand based $\pi \rightarrow \pi^*$ transitions (details of the transitions are provided in Table 3.9). The third transition (III) at 295.45 nm is an admixture of metal based *d* orbitals and ligand based π molecular orbitals to the ligand based π* orbitals with an oscillator strength of 0.0072. The last transition identified at 313.45 nm is again mainly due to ligand based $\pi \rightarrow \pi^*$ transitions.

Like $[Cu(Phen)_3]^{2+}$ complex, five different transitions are assigned to the UV-vis spectra of $[Zn(Phen)_3]^{2+}$ complex, Figure 3.21. The first transition (I) at around 248.89 nm is the most intense one with oscillator strength of 1.274. This transition is mainly from the ligand-metal bonding orbital (MO number **148)** with a significant metal *d* orbital participation to the ligand based π* orbitals. The second one (II) at around 257 nm is attributed to two transitions: one at around 257.86 nm (*f* = 0.148) while the other at around 257.97 nm (*f* = 0.132). Both these transitions are due to ligand based π → π* transitions with a significant amount of metal to ligand charge transfer (MLCT) (from MO number **148** to **162**). The third transition (III) at around 263 nm is again attributed to two transitions: one at around 263.60 nm (*f* = 0.122) and the other around 263.63 nm (*f* = 0.116). Both these transitions are ligand based π → π* transitions. The fourth one (IV) at around 290.67 nm (*f* = 0.020) is attributed mainly due to ligand based π → π* transition and metal to ligand π* transition (MLCT). The last assigned band (V) at around 311-312 nm are slightly more intense (*f* = 0.037) than those obtained for band III (*f* = 0.023). This band (V) arises due to ligand based π → π* transition with significant metal to ligand π* transition (MLCT). Thus, in both $[Cu(Phen)_3]^{2+}$ and $[Zn(Phen)_3]^{2+}$ complexes, metal to ligand charge transfer (MLCT) is somewhat buried by accompanying ligand based π → π* transitions.

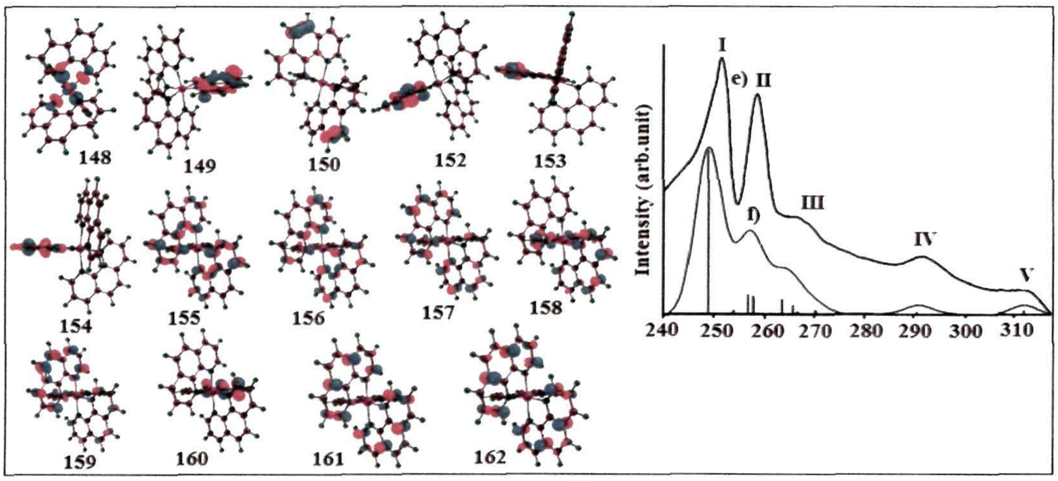

Figure 3.21. Important frontier orbital calculated for $[Zn(Phen)_3]^{2+}$ neat complex and simulation of e) experimental and f) theoretical absorption spectra.

3.3. Conclusion

Zeolite-Y encapsulated M (II) complexes of phenanthroline ligand (M= Fe, Cu and Zn) have been synthesized using flexible ligand method. The physiochemical and electrochemical behavior of the complexes confirm that the Fe-Phen and Cu-Phen complexes are formed inside zeolite supercage whereas the corresponding zinc complex is tethered via the formation of H-bond on the external surface of zeolite-Y. The results of the spectrochemical study show that encapsulation or tethering of the metal complexes lead to the red shifting of the MLCT as well as intraligand transitions. DFT-based calculations further support the lifting of the HOMO and LUMO levels under the influence of the space constrain as well as the Coulombic electrostatic field imposed by the zeolite mantle Evaluation of the DFT-based reactivity descriptors suggest for a hard-hard interaction in Zn-Phen-Y complex and for preferential soft-soft interaction in Cu-Phen-Y system. The absorption spectra obtained from TDDFT calculation for the homogeneous complexes in methanol solution are found to be in good agreement with the experimental results.

References

[1] Carter, M. T., et al. *J. Am. Chem. Soc.* **111**(24), 8901-8911, 1989.

[2] Labuda, J., et al. *Electroanalysis* **11**(2), 101-107, 1999.

[3] Barton, J. K., et al. *J. Am. Chem. Soc.* **104**(18), 4967-4969, 1982.

[4] Robertazzi, A., et al. *J. Phys. Chem. B* **113**(31), 10881–10890, 2009.

[5] Haq, I., et al. *J. Am. Chem. Soc.* **117**(17), 4788–4796, 1995.

[6] Munakata, H., et al. *J. Phys. Chem. B* **105**(17), 3493–3501, 2001.

[7] Sinclair, P. E., & Catlow, C. R. A. *J. Phys. Chem. B* **103**(7), 1084–1095, 1999.

[8] Jin, C., et al. *J. Mol. Catal. A: Chem.* **249**(1-2), 23-30. 2006.

[9] Zecchina, A., & Otero, A. C. *Chem. Soc. Rev.* **65**, 187–197, 1996.

[10] Armaroli, T., et al. *Phys. Chem. Chem. Phys.* **2**, 3341–3357, 2000.

[11].Bordiga, S., et al. *J. Chem. Soc., Dalton Trans.* 3921–3929, 2000.

[12] Delabie, A., et al. *Micropor. Mesopor. Mat.* **37**(1-2), 209–222, 2000.

[13] (a) Quayle, W. H., & Lunsford J. H. *Inorg. Chem.* **21**(1), 97-103, 1982, (b) Quayle, W. H., et al. *Inorg. Chem.* **21**(6), 2226-2231, 1982.

[14] Ames, W. M., & Larsen, S. C. *J. Phys. Chem. A* **113**(16), 4305–4312, 2009.

[15] Flentge, D. R., et al. *J. Phys. Chem.* **79**(4), 354-360, 1975.

[16] Herman, R. G., & Flentge, D. R. *J. Phys. Chem.* **82**(6), 720-729, 1978.

[17] Carl, P. J., & Larsen, S. C. *J. Phys. Chem. B* **104**(28), 6568-6575, 2000.

[18] Shaw, B. R., et al. *J. Electrochem. Soc.* **135**(4), 869-876, 1988.

[19] Zhang , R., et al. *J. Electroanal. Chem.* **643**(1-2), 31–38. 2010.

[20] Bedioui, F., et al. *J. Electroanal. Chem.* **373**(1-2), 19-29, 1994.

[21] Mesfar, K., et al. *J. Mater. Chem.* **3**(8), 873-876, 1993.

[22] Bedioui, F., et al. *J. Electroanal. Chem.* **315**(1-2), 313-318, 1991.

[23] Bedioui, F., et al. *J. Chem. Soc. Faraday Trans.* **87**, 3831-3834, 1991.

[24] Gaillon, L., et al. *J. Electroanal. Chem.* **345**(1-2), 157-167, 1993.

[25] Gemborys, H. A., & Shaw, B. R. *J. Electroanal. Chem.* **208**(1-2), 95-107, 1986.

[26] Gillard, R.D., & Williams, P. A. *Transit. Met.Chem.* **2**(1), 109-110, 1977.

[27] Ganesan, V., & Ramaraj, R. *Langmuir* **14**(9), 2497-2501, 1998.

[28] Shen, J. B., et al. *Acta Cryst.* **E67**, m186–m187, 2011.

[29] Youngme, S., et al. *Polyhedron* **26**(7), 1459–1468, 2007.

[30] Johansson, L., et al. *Inorg. Chim. Acta.* **31**, 117-123, 1978.

[31] Sauer, J. *Chem. Rev.* **89**(1), 199-255, 1989.

[32] Zicovich-Wilson, C. M., et al. *J. Phys. Chem.* **98**(42), 10863-10870, 1994.

[33] Maruszewski, K., et al. *J. Am. Chem. Soc.* **115**(18), 8345–8350. 1993.

[34] Vargas, A., et al. *J. Chem. Theory. Comput.* **5**(1), 97–115, 2009.

[35] Calabro, D. C., & Lichtenberger, D. L. *Inorg. Chem.* **19**(6), 1732-1734, 1980.

[36] Bally, T., et al. *J. Am. Chem. Soc.* **106**(14), 3927–3933, 1984.

[37] Jano, I. *J. Phys. Chem.* **95**(20), 7694–7699, 1991.

[38] Schildcrout, S. M., et al. *J. Am. Chem. Soc.* **90**(15), 4006–4010. 1968.

[39] Parr, R. G., & Chattaraj, P. K. *J. Am. Chem. Soc.* **113**(5), 1854-1855, 1991.

[40] Chattaraj, P. K., et al. *Chem. Phys. Let.* **237**(1-2), 171-176, 1995.

[41] Morell, G., et al. *Phys. Chem. Chem. Phys.* **11**, 3417–3423, 2009.

[42] Li, Y., & Evans, J. N. S. *J. Am. Chem. Soc.* **117**(29), 7756-7759, 1995.

[43] Nguyen, L. T., et al. *J. Am. Chem. Soc.* **121**(25), 5992-6001 1999 and references therein.

[44] Pal, S., & Chandrakumar, K. R. S. *J. Am. Chem. Soc.* **122**(17), 4145-4153, 2000 and references therein.

[45] Chattaraj, P. K. *J. Phys. Chem. A* **105**(2), 511-513. 2001.

Chapter 4

Encapsulation of Bis(Picolinato) Complexes of Co(II), Ni(II) and Cu(II) Inside Zeolite-Y and Their Application in Selective Oxidation of Phenol

4.1. Introduction

The contemporary interest in the selective oxidation of phenol to catechol, to a great extent, has been fuelled by its utility in nearly every sector of chemical industries including pharmaceuticals, agrochemicals, flavors, polymerization inhibitors and antioxidants.[1] Worldwide, the catechol production from phenol involves two procedures: (i) ortho-formylation of phenol followed by subsequent oxidation and (ii) oxidation of phenols to o-quinones and subsequent reduction of the latter into catechol. These multi step routes are often lengthy, energy-intensive and generate a large number of oxidized, coupling and polymerized products.[2] To meet the increasing demand for catechol and to satisfy environmental requirements, considerable efforts have been made for producing catechol by the one-step hydroxylation method using various homogeneous and heterogeneous transition metal complexes.[3-5] The utility of hydroxidation is mainly measured by several factors, including selectivity and ecological sustainability of the oxidation and the availability of the oxidant and catalyst. Among various oxidants, H_2O_2 of less than 60% concentration has been recognized as ideal, clean and green oxidizing agent.[6-8] In recent years, it has been established that zeolite encapsulated organometallic compounds and transition metal complexes, in addition to chiral metal complexes and biocatalysts, can be highly selective and efficient catalysts. As a consequence, the application of intrazeolite complexes is rapidly gaining importance in organic transformations, complementing bio and organometallic catalysis.[9] The steric constrain imposed by the walls of the zeolites plays a vital role in modifying the properties *viz.* magnetic, electronic and redox behavior of the encapsulated complexes.[10,11] These changes in the properties of the transition metal complexes upon encapsulation have led various researchers to develop newer heterogeneous catalyst and apply them in various organic transformations including the asymmetric synthesis. Besides having wide advantages of these heterogeneous catalysts over the homogeneous counterparts, the microwave assisted catalytic transformation in presence of these hybrid catalysts are now found to be most atom economic in comparison to the conventional methods.[12] In the context of the growing general interest in microwave-assisted organic synthesis, we plan here, to perform selective oxidation of phenol to catechol by few homogeneous and zeolite-Y encapsulated transition metal picolinato complexes under the influence of microwave irradiation.

The picolinato complexes of transitional metals have been determined to exhibit a broad spectrum of physiological effects on the activity functions of both animal and plants organisms.[13] And in recent years the complexes especially of vanadium,[14] zinc,[15] manganese,[16] copper,[17] chromium,[18] and tungsten[19] are known to have in vitro insulin mimetic activity and in vivo antidiabetic ability. However, these type of complexes as catalyst in organic transformations are less explored.[20] There are only few reports on the encapsulation of picolinato complexes into cavity of zeolite-Y and on their application as heterogeneous catalyst.[21] We report herein the first systematic experimental and theoretical studies on the selective oxidation of phenol under microwave irradiation by bis(Picolinato) complexes of cobalt, nickel, copper complexes and those encapsulated in zeolite-Y.

4.2. Results and Discussion

4.2.1. Experimental Section

4.2.1.1. XRD Study

The powder X-ray diffraction patterns of the zeolite NaY, metal exchanged zeolites and the encapsulated metal picolinato complexes are shown in Figure 4.1. Comparison of XRD pattern of the NaY, with the zeolite encapsulated complexes [M(Pic)$_2$]Y (M= Co, Cu and Ni) shows differences in the relative peak intensities of the 220 and 311 reflections appearing at 2θ = 10 and 12^0, respectively. For pure zeolite-Y and for M^{2+} -exchanged zeolite-Y $I_{220} > I_{311}$, but for the encapsulated complexes $I_{311} >$

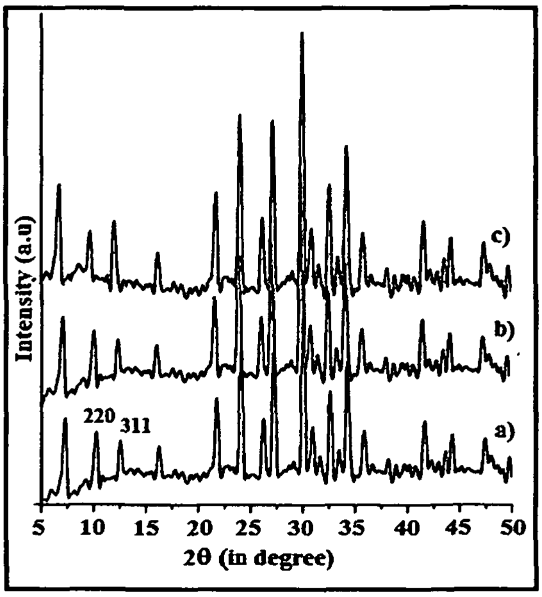

Figure 4.1. XRD pattern of a) Pure zeolite-Y, b) metal exchanged zeolite-Y, c) [M(Pic)$_2$]Y complexes (M = Co^{2+}, Ni^{2+} and Cu^{2+}).

I_{220}. This reversal in intensities has been empirically correlated with the presence of a large complex within the zeolite-Y supercage.[22] This change in the relative intensities may be associated with the redistribution of randomly coordinated free cations. in zeolite-Y at sites II and I. The above observation may therefore be construed as evidence for the successful encapsulation of metal picolinato complexes within the supercage of zeolite-Y.

4.2.1.2. FTIR Study

The FTIR spectra of neat and encapsulated picolinato complexes are shown in Figure 4.2. The FTIR spectra of metal exchanged zeolite-Y and NaY are almost same, hence herein their spectra are not presented as the FTIR spectra of NaY is already discussed in Chapter 1. The typical IR spectra of the neat metal picolinato complexes [Figure 4.2, curve (d)] shows major bands at 1642 (C=C), 1599 ($\nu_{C=O}$ carboxylate), 1445 (C=N), 1343, 1283 (C-O), 770 cm^{-1} (ν_{C-H} aromatic ring). Similar frequencies are also observed in the case of zeolite-Y encapsulated complexes with a little shift in the C=O, C=N and C-O bands to wave numbers 1565, 1480 and 1335 cm^{-1}, respectively indicating nitrogen and oxygen coordination inside the cavity of zeolite framework, Figure 4.2(a-c). In addition to these bands the encapsulated complexes also shows a band at 1403 cm^{-1} corresponding to C-H deformation. These results give information for the formation of metal picolinato complexes in zeolite-Y.

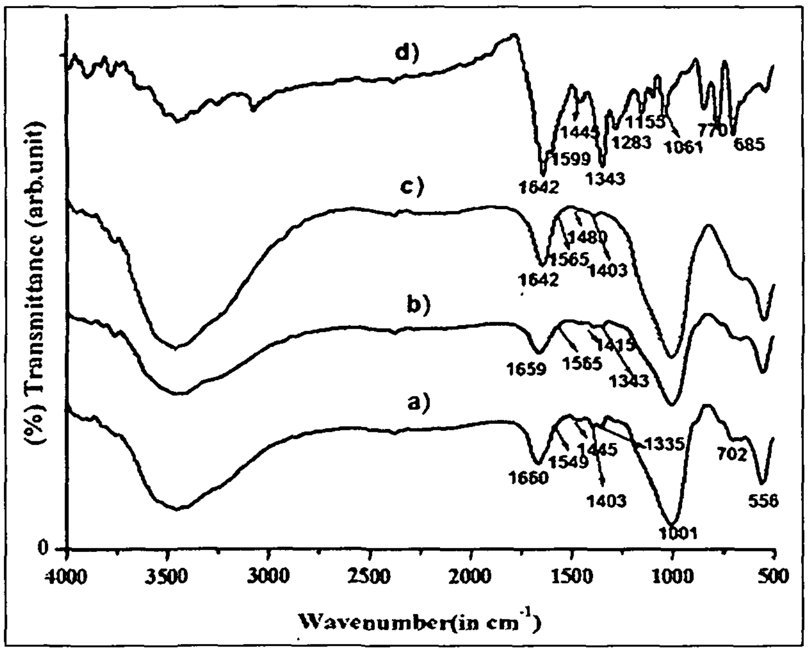

Figure 4.2. IR spectra of a) [Cu(Pic)$_2$]Y b) [Co(Pic)$_2$]Y c) [NI(Pic)$_2$]Y d) typical spectra for [M(Pic)$_2$] complexes [M = Cu^{2+}, Co^{2+} and Ni^{2+}].

4.2.1.4. UV-vis/DRS Study

The UV-vis spectrum of the neat picolinato complexes taken in methanol are shown in Figure 4.3. The UV-vis spectrum of bis (Picolinato) Co(II) complex, Figure 4.3a, shows two intense peak in the region 267 and 368 nm due to intraligand and metal to ligand charge transfer (MLCT) transitions i.e $\pi \rightarrow \pi^*$ and $d\pi \rightarrow p\pi^*$, respectively. The highest energy d–d transition from the lower-lying fully occupied $3d_{x2-y2}$ orbital to the upper empty $3d_{yz}$ orbital ($^2A_{1g} \rightarrow {}^2B_{1g}$, transition) at 432 nm is obscured by the above MLCT transitions. The peak at 574 nm is again mainly due to $^2A_{1g} \rightarrow {}^2B_{1g}$ transition supporting a square-planar geometry of the $[Co(Pic)_2]$ complex. The electronic spectra are clearly distinct from both the well-known tetrahedral and octahedral species. The tetrahedral $[CoCl_4]^{2-}$ has two features at around 650 (ε=550) and 675 nm (590 $m^{-1}cm^{-1}$) with a smaller feature at 600 nm (360 $m^{-1}cm^{-1}$). The octahedral $[M(H_2O)_6]^{2+}$ complexes have distinct absorbances at 560 nm for Co(II).[23] The corresponding Ni(II) complex (Figure 4.3c) shows five characteristic absorption bands at 257, 295, 331, 383 and 427 nm. The first two high energy bands are due to intraligand $\pi \rightarrow \pi^*(A_g \rightarrow B_{2u}, 3b_{1u} \rightarrow 4b_{3g})$ transition. The high intense band at 331and 383 nm are the MLCT transitions ($A_g \rightarrow B_{2u}$, $4b_{2g} \rightarrow 3a_u$) from the filled metal $3d_{yz}$ and $3d_{zx}$ orbital to the two lowest-energy ligand based π^* orbital. The lowest energy band at 427 nm is due to $A_{1g} \rightarrow B_{1g}$, suggesting the formation of a square planar $[Ni(Pic)_2]$ complex.[24] The copper (II) picolinato complex (Figure 4.3e) shows a sharp peak at 233 nm and two low intense peaks at 307 and 354 nm. The first highly intense peak can be attributed to intraligand $\pi \rightarrow \pi^*$ transition and the other two are due to ligand to metal charge transfer transition. In addition to these it shows MLCT at 434 nm and a broad d-d ($^2B_{1g} \rightarrow {}^2E_{2g}$) transition at 562nm.[25]

The diffuse reflectance spectra of the calcined metal exchanged zeolites and encapsulated complexes calcined at 550°C are represented in the form of Kubelka–Munk function $F(\alpha)$ in Figure 4.3 as inset. The DR-spectrum of dehydrated Co^{2+}-exchanged zeolite NaY, shows peak at 194 and 210 and 262 nm which can be assigned to ligand to metal charge transfer (MLCT) transition, in the present case from the oxygen atom of zeolite moiety to a tetra coordinated Co^{2+} ion. The DR spectrum of the Ni exchanged zeolite exhibits three bands at about 208, 288, 388 and 726 nm. The first two bands at 208 and 288 nm are due to charge transfer transition originated from a transition from oxygen-to Ni^{2+}. This indicates the presence of some tetrahedrally coordinated Ni^{2+} ions in the supercages. The band at about 388 and 725 nm is assigned to $^3A_{2g} \rightarrow {}^3T_{1g}$ (*F*), $^3A_{2g} \rightarrow {}^3T_{1g}$ (*P*) transitions related to the octahedrally coordinated Ni^{2+} ions mainly in the hexagonal prisms of the zeolite.[26] The dehydrated Cu^{2+}-Y sample exhibits absorption band at 578 nm, characteristic of the $e \rightarrow t_2$ transition of the Cu(II) ($3d^9$) ion in the trigonal site. The intense UV absorption component is attributed to charge transfer excitation. This spectral behaviour of the Cu^{2+} exchanged zeolites indicates that Cu^{2+} ion maintains a pseudo tetrahedral environment of the type $(O_l)_3$-Cu^{2+}-L (where O= oxygen of the supercage of zeolite-Y).[27]

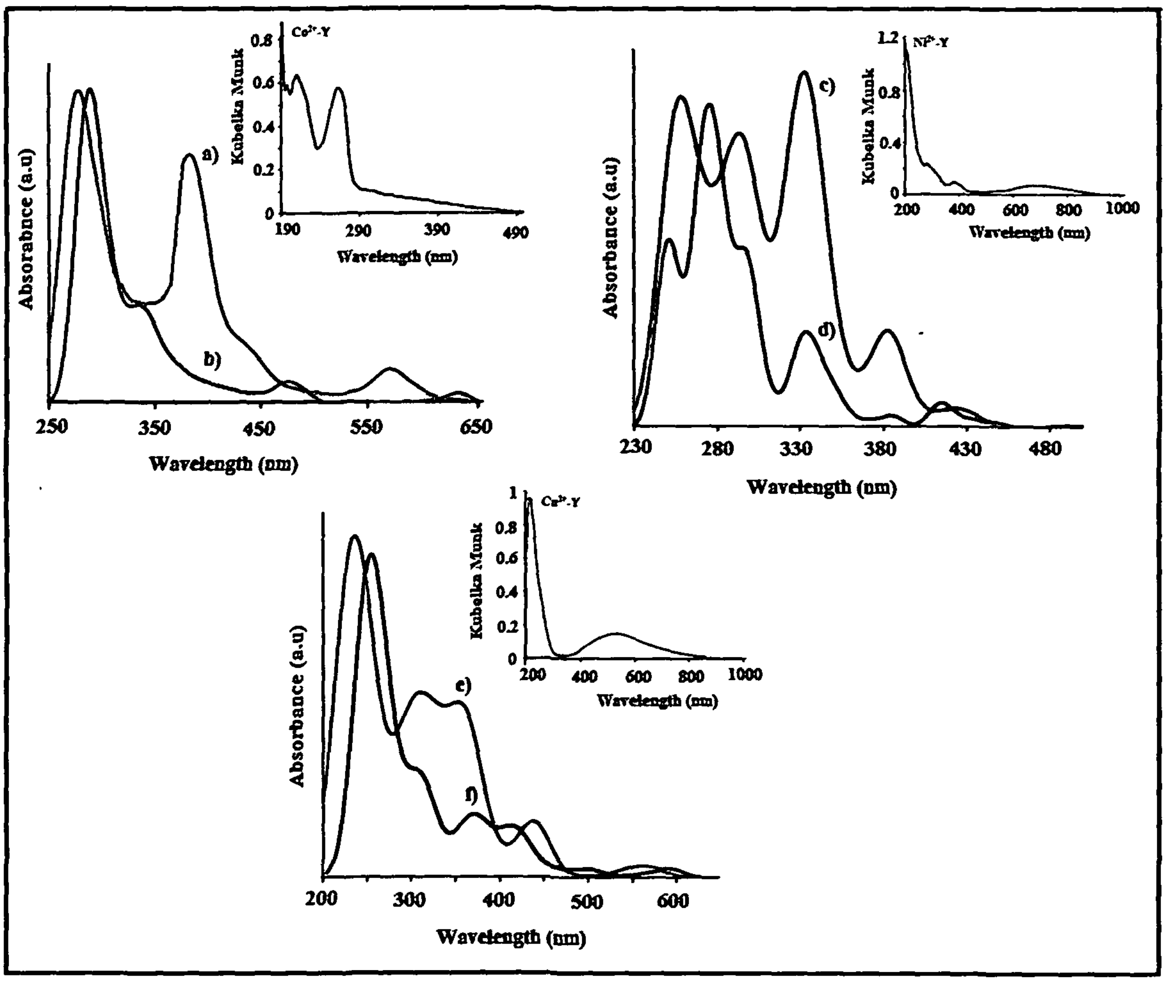

Figure 4.3. UV-vis /Diffuse reflectance spectra of a) $[Co(Pic)_2]$ b) $[Co(Pic)_2]Y$ c) $[Ni(Pic)_2]$ d) $[Ni(Pic)_2]Y$ e) $[Cu(Pic)_2]$ f) $[Cu(Pic)_2]Y$. The DRS spectra of metal exchanged zeolites are shown in the inset for the respective cases.

In Figure 4.3b the DR-spectrum of $[Co(Pic)_2]Y$ shows peak at 292, 344, 496 and 635 nm. The first intense peak is due to π→π* transition originated from the ligand system. The next two low intense bands are due to n→π* transitions associated with the ligand and are being veiled by the MLCT associated with Co^{2+}-exchanged zeolite.

The other two bands are mainly due to $d\pi \rightarrow p\pi^*$(MLCT) and d-d transition (${}^2A_{1g} \rightarrow {}^2B_{1g}$). The encapsulated Ni-picolinato complex gives a number of peaks, Figure 4.3d. The first three bands are due to ligand based $\pi \rightarrow \pi^*$ transition and the other two bands are due to MLCT and ${}^1A_{1g} \rightarrow {}^1B_{1g}$ transitions, respectively. The DRS-UV-vis spectrum of encapsulated copper complex is shown in Figure 4.3f. The absorption peaks in the range 280-308nm are due to intraligand transition. The bands at 366 and 426 nm are due to ligand to metal charge transfer transition. The peaks at 503 and 602 nm can be attributed to MLCT and d-d transitions, respectively.

The comparison of the absorption spectrum of the neat complexes with those of the encapsulated complexes demonstrates that encapsulation results in a blue shift in the electronic transitions associated with the nickel complex. In case of the corresponding cobalt and copper complex the peaks are found to be red shifted under the influence of the zeolite matrix. This further gives an idea that all the three complexes do not undergo similar kind structural change inside zeolite-Y. However, the presence of the similar electronic transitions in the encapsulated complexes in comparison to the neat complex in solution gives evidence for the formation of complexes inside the supercage of zeolite-Y.

4.2.1.5. Cyclic Volatmmetry Study

The cyclic voltammogram of neat complexes, metal exchanged zeolites and those of zeolite-Y encapsulated ones are depicted in Figure 4.4(a-i). The cyclic voltammogram of neat Cu(II) complex, Figure 4.4a shows two anodic peaks at -0.165V , -0.061V and a single cathodic peak at -0.266V. However, the first anodic peak vanishes during the second cycle. This indicates that both *cis* and *trans* isomers persist in solution for a smaller period of time. In the second cycle the *cis* Cu (II) complex undergoes a chemical isomerisation reaction to form the corresponding *trans* isomer. The peak potential obtained from the cyclic voltammogram of the encapsulated Cu(II) complex match almost with that of the *trans* isomer of the neat complex, Figure 4.4g. This further revealed the fact that *cis –trans* isomerism does not occur inside the zeolite cages. And these results are in accordance with our ESR analysis and theoretical studies (discussed latter). The cyclic voltammogram of the neat Co(II) complex, Figure 4.4b taken in solution mode at a scan rate of 0.1 Vs shows a redox couple with values of E_{pc} = -0.307V and E_{pa} = 1.14V, $E_{1/2}$ = 0.416V. At different scan rates, there is no major change in $E_{1/2}$ values, clearly indicating that $E_{1/2}$ is independent of scan rate. The corresponding zeoliteY encapsulated Co(II) complex gives a quasi reversible couple with E_{pc} = 0.322V and E_{pa} = 0.677V, $E_{1/2}$ = 0.499V, Figure 4.4h. The shifting of the peak potential toward more positive values on encapsulation indicates the stabilization of Co(II) oxidation state in zeolite cages. This may be attributed to axial interaction with the zeolite matrix.

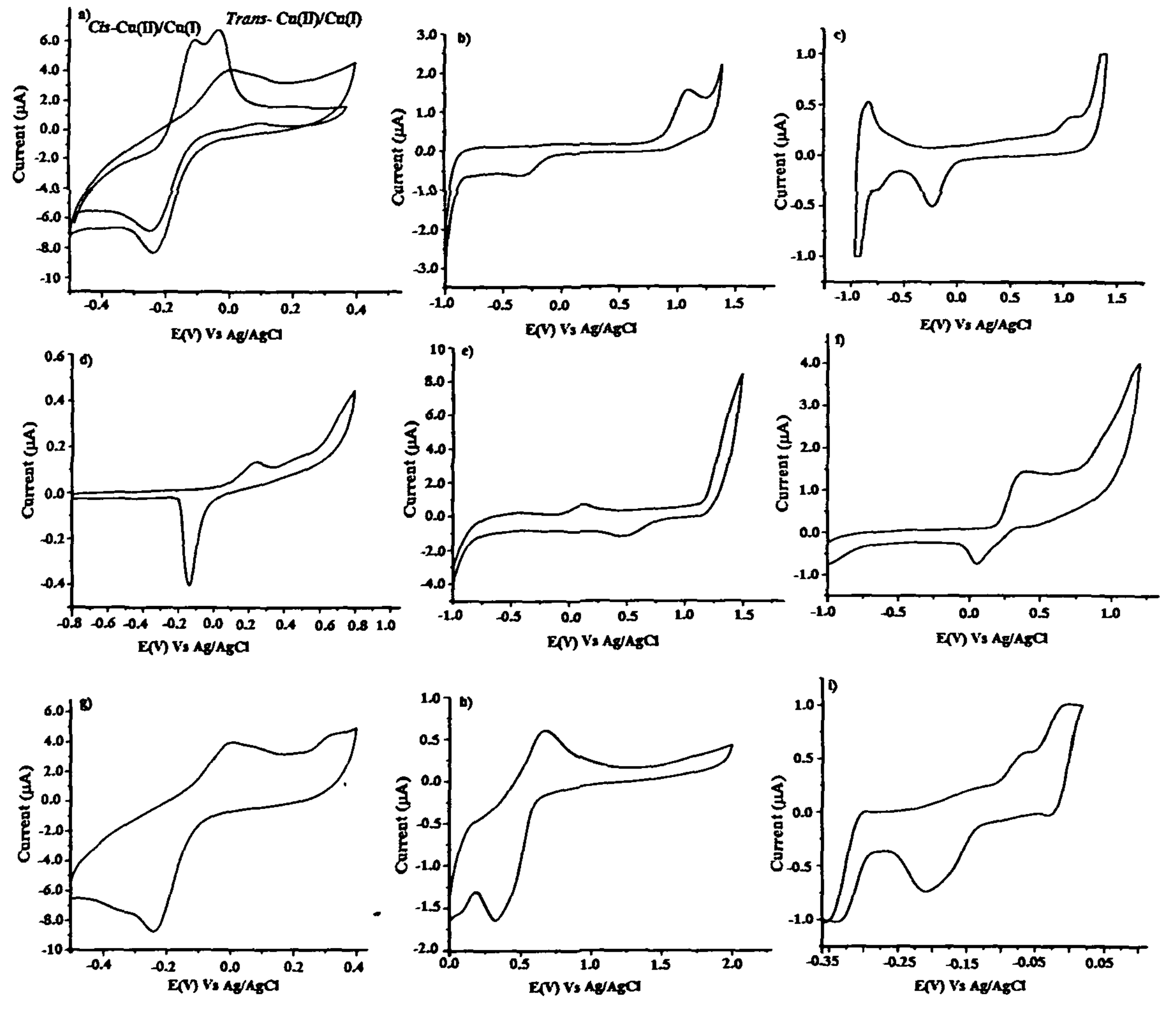

Figure 4.4. a), b) and c) are cyclic voltammograms for neat picolinato complexes of copper cobalt, and nickel respectively taken in DCM using 0.1M TBAP as supporting electrolyte. d), e) and f) are cyclic voltammograms of metal exchanged Cu^{2+}-Y, Co^{2+}-Y and Ni^{2+}-Y, respectively. g), h) and i) are for encapsulated complexes of copper, cobalt and nickel respectively. The cyclic voltammograms for metal exchanged zeolites and encapsulated complexes are taken as zeolite modified electrode.

The neat nickel complex undergoes a reversible and a quasi-reversible one-electron reductions process corresponding to Ni(II)/Ni(I) and Ni(I)/Ni(0) couples, respectively as shown in Figure 4.4c. The Ni(II/I) couple shows a cathodic reduction peak at -0.76V and the corresponding anodic peak at -0.82V. The Ni(I)/Ni(0) couple shows the cathodic peak at -0.23V and the anodic peak at 1.08V indicating a highly quasi reversible process. The corresponding zeolite encapsulated Ni(II) complex exhibits a broad cyclic voltammogram and the average $E_{1/2}$ are shifted to more negative values in comparison to the neat complex, Figure 4.4i. This indicates that on encapsulation Ni(I) oxidation state becomes more stabilized.

4.2.1.6. ESR study

The ESR spectrum of the metal exchanged zeolites, neat and the zeolite encapsulated transition metal complexes are shown in Figure 4.5(a-f). The ESR signals of neat Cu (II) complexes in the polycrystalline state are usually broadened due to dipolar and spin–spin exchange interactions. Consequently, structural information from the hyperfine and superhyperfine coupling interactions between the unpaired electron of copper and surrounding magnetic nuclei are lost and the *g* values are not that of the molecular values. Encapsulation of complexes in the supercages of zeolites results in isolation and dilution of the paramagnetic complex in a diamagnetic aluminosilicate matrix and, hence, is expected to yield resolved signals. For one copper (II) species, the typical ^{63,65}Cu hyperfine structure quartet is expected due to the interaction of the unpaired electron with the Cu nuclei (^{63,65}Cu, I = 3/2). However, in the spectrum represented in Figure 4.5b for neat Cu-picolinato complex in addition to an intense Cu hyperfine structure quartet in the high-field part there are further lines in the low field region which indicate the presence of a second copper (II) species with a lower concentration. The zeolite encapsulated Cu- complex however, shows well resolved hyperfine structure quartet, Figure 4.5c. Appearance of more number of peaks of lower intensity at low field region indicates the *cis-trans* equilibrium in neat Cu-picolinato and this result is in accordance with our cyclic voltametric study. The *g*-tensor values of Cu(II) complex can be used to derive the ground state. In square-planar complexes if the unpaired electrons lie in the $d_{x2}-d_{y2}$ orbital gives $^2B_{1g}$ as the ground state with g_{II} > $g_{\perp}$ and if it lies in the d_{z2} orbital gives $^2A_{1g}$ as the ground state and with g_{II}= 2.32 and $g_{\perp}$= 2.10 for encapsulated complex, it is clear that ground state is $^2B_{1g}$. The observed values g_{II}= 2.21 and $g_{\perp}$= 2.09 for neat complexes, indicates that the structure of the complex is square-planar and that the unpaired electron is predominantly in the $d_{x2}-d_{y2}$ orbital. The ESR spectrum of Co^{2+}-Y exchanged zeolite, recorded with the sample at 77 K shows a broad signal having a *g* value of 4.35, Figure 4.5d. This g value is consistent with a high-spin d^7 ion in the weak-field limit. The ESR spectrum of neat cobalt complex recorded at 77 K is depicted in Figure 4.5e. The spectrum exhibits axial symmetry with well-resolved eight line patterns characteristic of the ^{59}Co (I = 7/2) hyperfine interaction with $g_{\perp} = 2.95$, and $g_{II} = 2.02$, similar to those found for a variety of low-spin Co(II) complexes.[28] Identical spectrum is observed following the reaction of the Co^{2+}-Y with the picolinic acid. Since the spectra are not clearly separated into perpendicular and parallel components, it was not possible to determine directly the anisotropic *g* and *A* values. The absence of the broad signal at g = 4.35 in case of both the neat and the encapsulated complexes indicates the formation of low-spin square planar $[Co(Pic)_2]$.

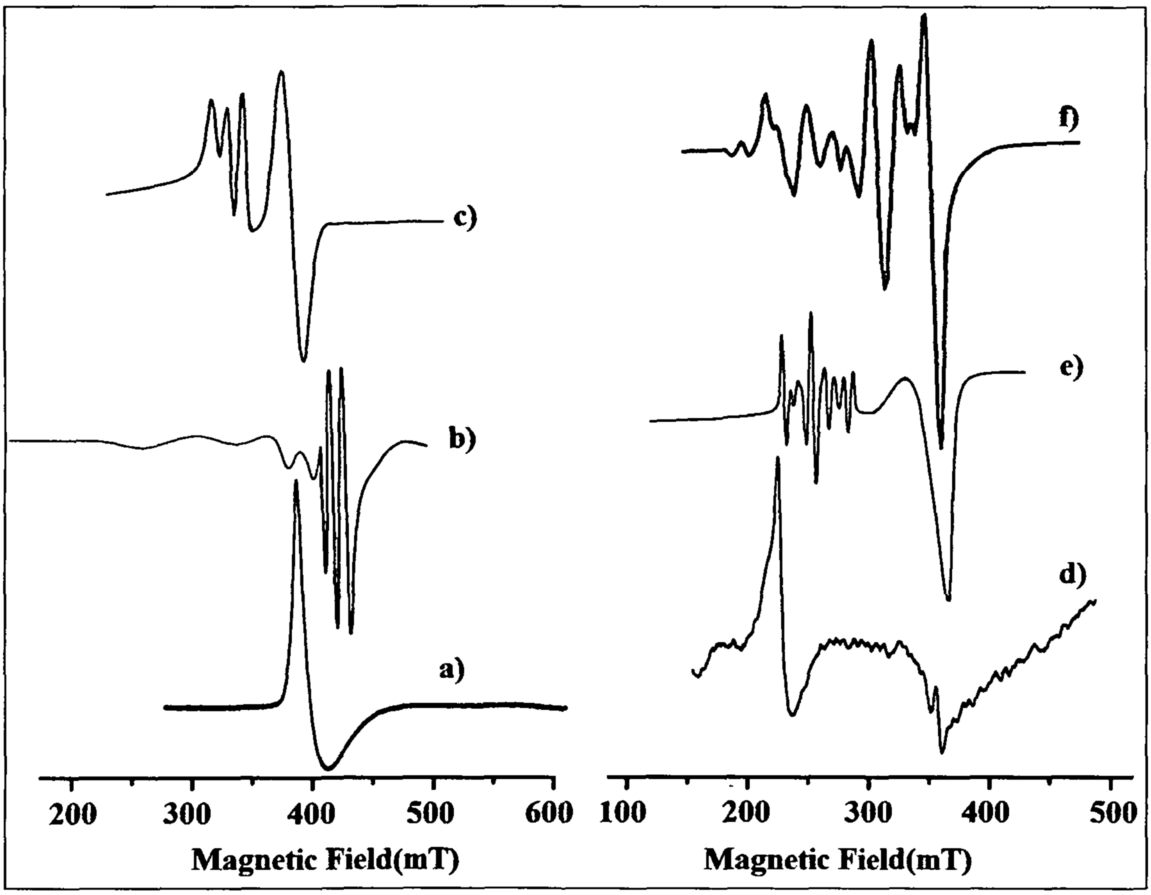

Figure 4.5. Powder ESR spectra of a) $Cu^{2+}Y$ b) $[Cu(Pic)_2]$ c) $[Cu(Pic)_2]Y$ d) $Co^{2+}Y$ e) $[Co(Pic)_2]$ f) $[Co(Pic)_2]Y$ taken at 77K.

Nickel (II) (d^8) ion being a non-Krammer's ion, ESR spectra is observable, generally at low temperatures. Most of the reported work concerns the study of this ion at 77 K or 4 K.[29,30] The *g* value is isotropic and close to 2.2. In general, if the zero-field splitting (*D*) is negligible, one would expect and observe a single ESR line. However, in most of the systems, *D* is non-zero and hence more than one line has been observed. Generally, when zero-field splitting is large, one would expect forbidden transitions.[31] This observation has been found in case of the Ni-exchanged zeolite-Y, Figure 4.6, but not in the neat and the encapsulated complexes. This further indicates the formation of low spin square-planar complex of Ni(II) inside zeoliteY.

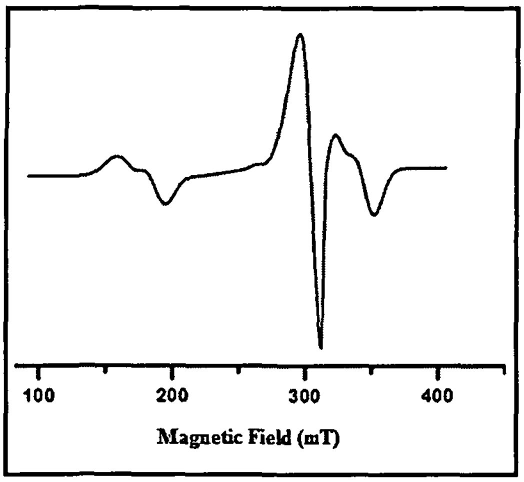

Figure 4.6. ESR spectrum of calcined Ni^{2+}-exchanged zeolite-Y at 77K.

4.2.1.6. XPS Study

The location of the complexes in the zeolite cages can also be confirmed by XPS as it provides information about the relative concentrations of elements in the surface ca. 40-50Å thick layers of the sample (ca. 1% of the crystal).[32] The XPS measurements are carried out for various metal-picolinato samples. It is found from comparison of the signal intensities of the M 2p level (M= Co, Ni and Cu) for the encapsulated samples and the metal exchanged samples that the encapsulated complexes contains less concentration of the metal ions than NaY metal exchanged samples. The results obtained are in accordance with our UV-vis study. The decrease in the metal content in the encapsulated metal complexes can be attributed to the migration of non-complexed metal ions under the high-temperature synthesis conditions used in the flexible ligand method. In addition to the information about location of the complexes, some preliminary information about the oxidation states of the metal ion in both the neat and the zeolite complexes can be obtained from the XPS data. Table 4.1 lists the binding energies for M_{2p}, O_{1s}, N_{1s}, C_{1s}, Si_{2s}, Si_{2p}, Al_{2p}, and Na_{1s} in various metal picolinato complexes. In all the picolninate complexes (both neat and encapsulated) two different

Table 4.1. Binding energy (in eV) for neat and the encapsulated complexes.

State	$[M(Pic)_2]$			$[M(Pic)_2]$-Y			M^{2+}-Y		
	Co	Ni	Cu	Co	Ni	Cu	Co	Ni	Cu
$M\,2p_{3/2}$	782.4	851.6	932.2	782.6	851.7	931.5	782.5	851.5	931.3
$M\,2p_{1/2}$	785.2	877.4	955.2	786.3	878.0	956.2	785.0	877.2	955.2
Satellite	-	-	941.3	-	-	943.1	-	-	942.1
O_{1s}	531.4	531.4	531.4	531.4	530.1	529.9	530.2	531.4	531.4
N_{1s}	400.2	400.2	400.2	399.2	399.6	399.4	-	-	-
C_{1s}(C-C)	284.6	284.6	284.6	284.6	284.6	284.6	-	-	-
(O-C=O)	287.2	287.2	287.2	287.2	287.2	287.2			
Si_{2s}	-	-	-	154.0	154.0	154.0	154.0	154.0	154.0
Al_{2p}	-	-	-	74.4	74.4	74.4	74.5	74.5	74.5
Na_{1s}	-	-	-	1073.2	1073.2	1073.1	1073.1	1073.0	1073.2

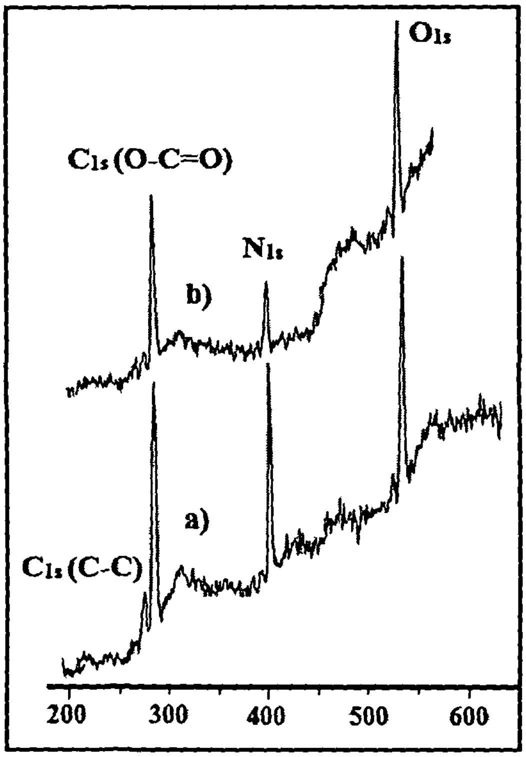

Figure 4.7. XPS spectra of N_{1s} C_{1s} and O_{1s} showing two different kind of carbon atom and only one kind of nitrogen in a) neat complexes b) zeolite encapsulated complexes

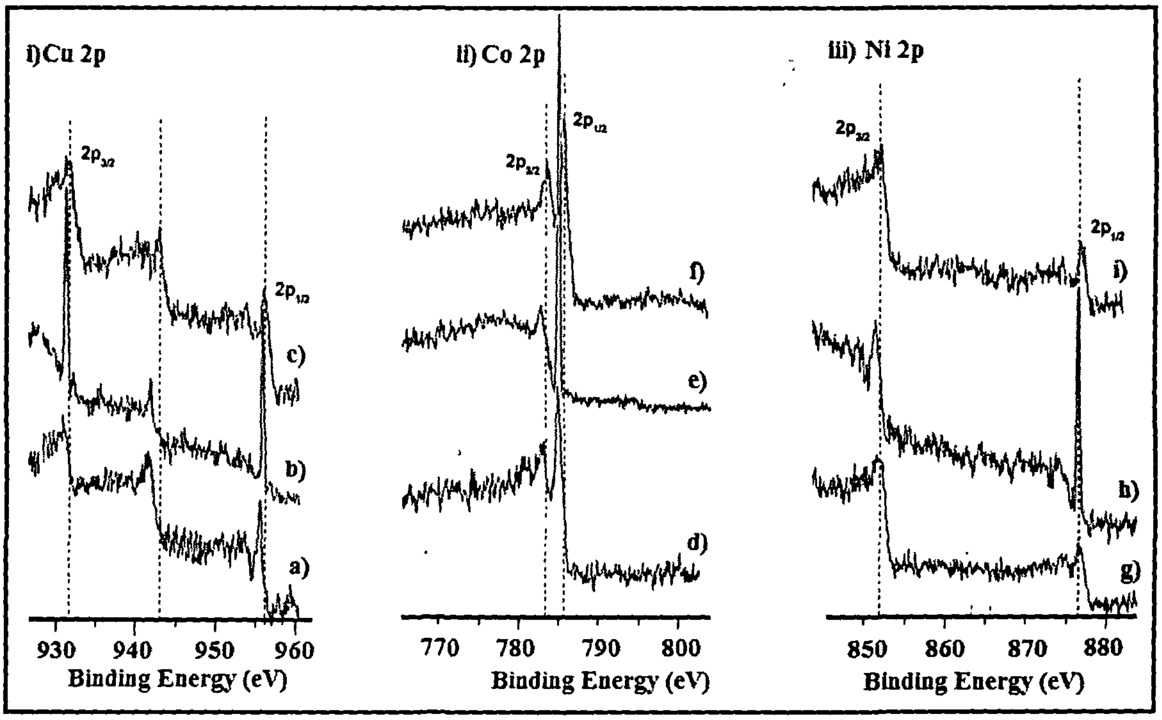

Figure 4.8. XPS of i) a) Cu^{2+}-Y b) $[Cu(Pic)_2]$ c) $[Cu(Pic)_2]Y$ ii) d) Co^{2+}-Y e) $[Co(Pic)_2]$ f) $[Co(Pic)_2]Y$ iii) g) Ni^{2+}-Y h) $[Ni(Pic)_2]$ i) $[Ni(Pic)_2]Y$.

kinds of carbon atoms (C-C 284.6 eV and O-C=O 287.2 eV) and the only kind of nitrogen atom (399.2 eV) are observed, Figure 4.7. The core level photoelectron peaks of neat and the encapsulated complexes as well as of the metal exchanged zeolites are assigned in Figure 4.8. The presence of Cu^{2+} is confirmed by the $Cu\,2p_{3/2}$ and $Cu\,2p_{1/2}$ peaks at 932.4eV and 955.2 eV, respectively accompanied by a relatively low intense satellite peak at 941.3eV. These values are in accordance with the previously reported binding energy value for Cu.[33] Similar to Cu-complexes the presence of Co^{2+} and Ni^{2+} is confirmed by XPS and the values are given in Table 4.1. It can be observed from Table 4.1, in all the samples the binding energy of Si_{2s}, Al_{2p} and Na_{1s} remain unchanged. However, small shifts towards higher energies for M_{2p} and towards lower energy for O_{1s} and N_{1s} are observed in all the encapsulated complexes. The high $M\,2p_{3/2}$ binding energy found in $[M(Pic)_2]Y$ indicates the presence of picolinato complexes inside zeoliteY. This is attributed to the fact that upon encapsulation the charge density on the metal centres decreases which could be due to the impairment of the delocalization of the π-electrons of the ring brought by the loss of planarity caused by the distortion of the complexes when confined in the zeolite cavity.[34]

4.2.1.7. SEM Study

SE micrographs of bis(Picolinato) complexes taken before and after Soxhlet extraction are shown in Figures 4.9 (a), (b) and (c), respectively as representative cases. The SEM taken before purification shows the presence of some unreacted or extraneous particles on the external surface. In the SEM of finished products, no surface complexes are seen and the particle boundaries on the external surface of zeolite are clearly distinguishable. This is much clearer from the surface plot shown in Figure 4.10 (a), (b) and (c). Homogeneous surface morphology observed for the neat NaY zeolite and the samples after Soxhlet extraction shown in Figure 4.10 a) and 4.10c). The surface plot for the samples before Soxhlet extraction however, are found to be non-homogeneous indicating the surface is being occupied by extraneous complexes or the uncomplexed ligands. The presence of similar surface morphology before and after encapsulation into zeolite-Y confirms that encapsulation has not affected the surface crystallinity. Further, it indicates the efficiency of purification procedure to effect complete removal of extraneous complexes, leading to well-defined encapsulation in the cavity.

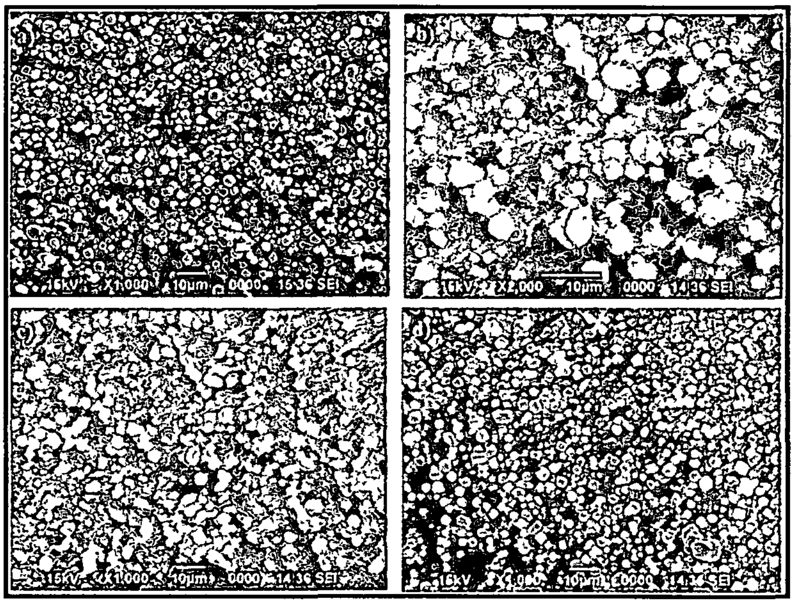

Figure 4.9. SE micrographs of a) NaY zeolite b) and c) Typical SE micrographs of $[M(Pic)_2]Y$ complexes ($M = Co^{2+}$, Ni^{2+} and Cu^{2+}) complexes before Soxhlet extraction. d) Typical SE micrographs of $[M(Pic)_2]Y$ complexes after Soxhlet extraction.

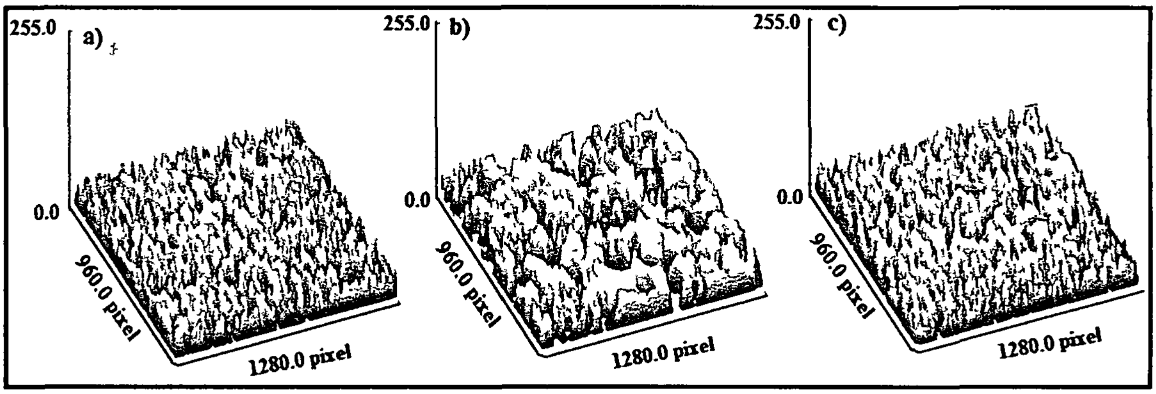

Figure 4.10. Surface plot of a) Pure NaY, b) Encapsulated $[M(Pic)_2]Y$ complexes ($M = Co^{2+}$, Ni^{2+} and Cu^{2+}) complexes before Soxhlet extraction, c) Encapsulated $[M(Pic)_2]Y$ complexes after Soxhlet extraction. X and Y axis represents width and height, respectively.

4.2.1.8. TGA Study

The TG patterns of metal exchanged zeoliteY, neat and the encapsulated complexes are shown in Figure 4.11 (a-i). All the three metal exchanged zeolite-Y shows only single degradation at 190 °C due to loss of surface hydroxyl group and shows no weight loss up to 700°C, Figure 4.11, g-i). The thermo-gravimetric analysis of the neat $[M(Pic)_2]$ [M = Co(II), Ni(II) and Cu(II)] complexes almost shows similar pattern. The neat complexes mainly show three weight losses at 82, 196 and 248 °C. The first weight loss corresponds to loss of water of crystallization and the other two weight losses are due to partial sublimation and pyrolitic decomposition of the sample. The comparison of thermo-gravimetric analysis for neat picolinato complexes with the encapsulated one shows that these complexes become more stable once they get embedded inside the cavity of zeolite-Y. In case of the encapsulated metal complexes the weight losses due to sublimation and pyrolytic decomposition of the complexes extends up to 427 °C. These indicate that on encapsulation the thermal stability of the complexes are greatly enhanced and hence can be thermally treated without any decomposition.

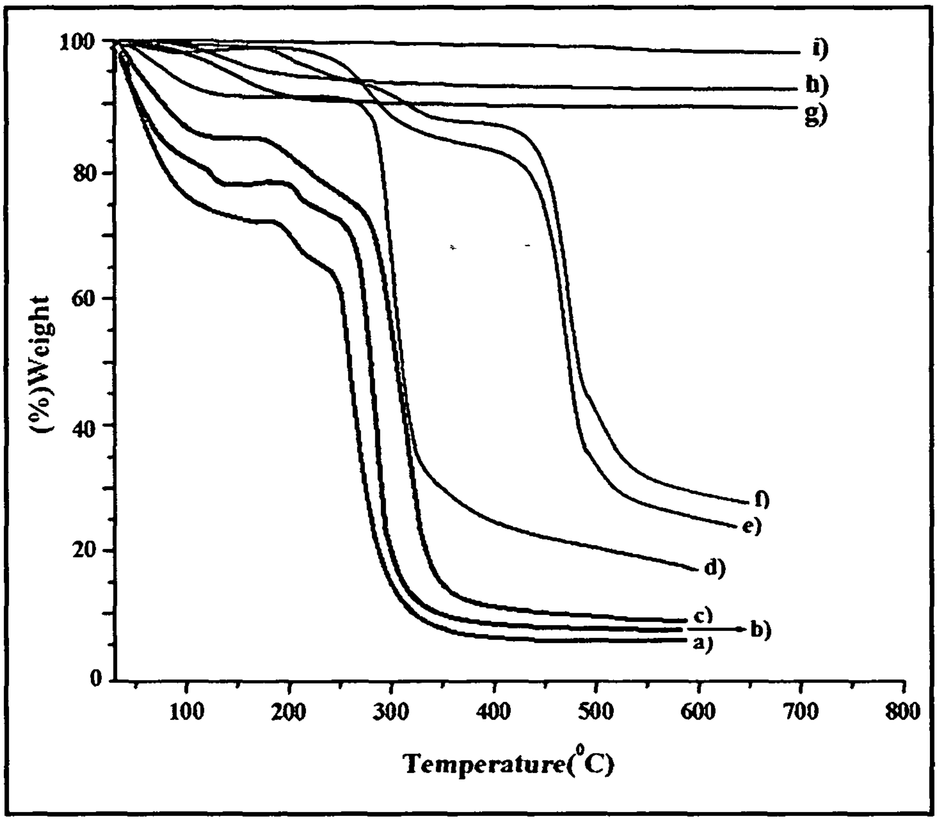

Figure 4.11. Thermogravimetric analysis (TGA) for a) $[Cu(Pic)_2]$ b) $[Co(Pic)_2]$ c) $[Ni(Pic)_2]$ d) $[Ni(Pic)_2]Y$ e) $[Co(Pic)_2]Y$ f) $[Cu(Pic)_2]Y$ g) Ni^{2+}-Y h) Co^{2+}-Y i) Cu^{2+}-Y.

4.2.2. Theoretical Study

From our experimental studies it is evident that cobalt and nickel complexes do not undergo *cis-trans* isomerization whereas the copper complex is found to undergo such kind of isomerization. Hence, to have an insight into such kind of isomerization process, we performed DFT calculation using *gaussian03* programm, at PBE1/SDD level. The isomerization process is shown in Figure 4.12b.

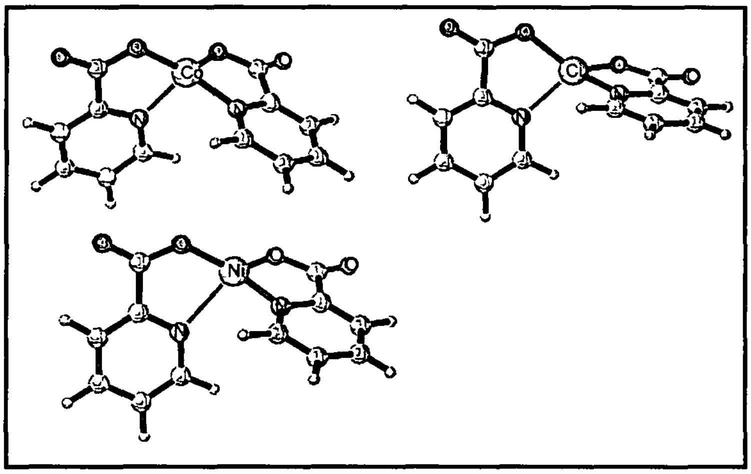

Figure 4.12 a) Transition state geometries involve in *cis-trans* isomerization

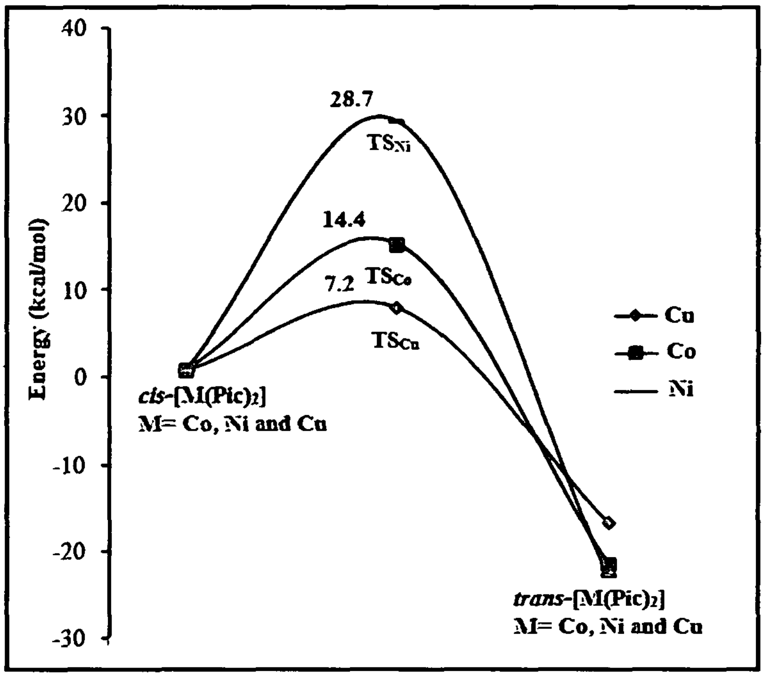

Figure 4.12 b) Energies (kcal mol^{-1}) for the *cis-trans* isomerization process for the picolonate complexes of Co, Ni and Cu. The low energy barrier between the *cis* and the *trans* isomers of Cu-complex favours the isomerization.

Starting bis(Picolinato) M(II) (M = Co, Ni, Cu) complexes has a distorted *cis* conformation where one of the phenyl, group is slightly twisted from the molecular plane. On the contrary, the *trans* conformation of the complexes have perfectly planar phenyl rings. The transition state geometries involved in this isomerization process resemble more towards the reactant (Figure 4.12a), the *cis* form, rather than the product, the *trans* form. The *trans* conformation of all the complexes are found to be energetically more preferable. The energy difference between the *cis* and *trans* conformers for the Cu(II) complex is found to be the least (17.4 kcal mol^{-1}), while that for Co(II) and Ni(II) complexes are found to be higher (23.6 and 22.3 kcal mol^{-1}, respectively). Interestingly, the transition state TS_{Cu} for the conversion of *cis*-bis(Picolinato) Cu(II) to the corresponding *trans*- geometry lies only 7.2 kcal mol^{-1}, while the transition state TS_{Co} and TS_{Ni} lie almost twice and thrice than that of TS_{Cu}, respectively, Figure 4.12b. Thus, it is evident from Figure 4.12b that the *cis*-*trans* isomerisation for the Cu(II) complex is energetically favorable. In other words, there might be a possible equilibrium between the *cis* and *trans* forms of copper complex while this possibility is less in case of Co and Ni complexes. This is in tune with cyclic voltammetry measurement as well as ESR spectra for the complexes.

Table 4.2. Selected bond distance (in Å) and bond angles (in degree) of the optimized neat complexes, $[M(Pic)_2]$ and zeolite encapsulated picolinato complexes, $[M(Pic)_2]Y$ (M = Co, Ni and Cu).

Bonds	$[Co(Pic)_2]$	$[Co(Pic)_2]Y$	$[Ni(Pic)_2]$	$[Ni(Pic)_2]Y$	$[Cu(Pic)_2]$	$[Cu(Pic)_2]Y$
$M\text{-}N_4$	1.906	1.860	1.870	1.851	1.954	1.911
$M\text{-}N_{15}$	1.905	1.848	1.870	1.853	1.955	1.904
$M\text{-}O_9$	1.864	1.840	1.844	1.833	1.923	1.929
$M\text{-}O_{22}$	1.864	1.845	1.844	1.833	1.923	1.926
Angles						
$\angle N_4\text{-}M\text{-}O_{22}$	94.510	95.699	93.780	95.752	95.468	98.552
$\angle N_4\text{-}M\text{-}N_{15}$	180.00	177.549	179.984	177.239	179.984	175.243
$\angle O_{22}\text{-}M\text{-}N_{15}$	85.490	86.206	86.220	86.369	84.532	85.226
$\angle N_{15}\text{-}M\text{-}O_9$	94.514	92.137	93.784	91.702	95.470	91.650
$\angle O_9\text{-}M\text{-}N_4$	85.487	86.055	86.216	86.290	84.530	84.890
$\angle O_9\text{-}M\text{-}O_{22}$	179.83	176.121	179.947	175.664	179.962	173.304

Our experimental studies suggest that the metal complexes do not maintain the same geometry on encapsulation into zeolite-Y; hence we have also performed all electron calculations on the encapsulated complexes. Herein, we have considered only the *trans* isomers for all the three complexes. The geometrical parameters obtained from VWN/DN level calculations for the neat and the encapsulated complexes are provided in Table 4.2. The geometrical parameters such as bond length and bond angles have been compared with the available crystal structures for bis(Picolinato) complexes of cobalt (II), nickel (II) and copper(II) and are found to be in good agreement. When these metal complexes with square planar geometry are encapsulated in zeolite-Y, the bond length and the bond angle between the metal and the ligand molecule slightly changes in comparison to those of the corresponding neat complexes. The pattern of the highest occupied molecular orbital (HOMO) and the lowest unoccupied molecular orbital for the neat and the encapsulated complexes are shown in Figure 4.13. It is observed from Figure 4.13 that encapsulation of the complexes into the zeolite framework increases the energies of the HOMO and the LUMO orbitals in comparison to the neat complexes. However, the HOMO-LUMO gap on encapsulation in copper and cobalt complexes is found to decrease whereas that of in nickel complex is found to increase in comparison to those for the free complexes. Among all the systems, the HOMO energies of zeolite-Y encapsulated [Co^{II}(Pic)$_2$] and [Cu^{II}((Pic)$_2$] complexes are higher in comparison to the other complexes. This indicates transfer of electrons from these two complexes becomes much more feasible. And this has been reflected in the catalytic ability of these two complexes towards the selective oxidation of phenol to catechol. Applying the Koopmans' theorem[35] global hardness and softness values of the neat and encapsulated complexes are calculated. The values are given in Table 4.3. According to the maximum hardness principle, the most stable structure has maximum hardness. So, the encapsulated complexes with minimum η values will be comparatively

Table 4.3. Calculated energy of HOMO and LUMO (in eV), hardness (η, in ev), chemical and global softness (S, in eV).

Complexes	HOMO	LUMO	η	S
[Cu(Pic)$_2$]	-4.919	-4.219	0.35	1.428
[Co(Pic)$_2$]	-5.355	-4.206	0.574	0.870
[Ni(Pic)$_2$]	-5.534	-3.739	0.897	0.557
[Cu(Pic)$_2$]Y	-3.429	-3.920	0.245	1.855
[Co(Pic)$_2$]Y	-3.761	-2.890	0.435	0.954
[Ni(Pic)$_2$]Y	-4.572	-2.466	1.053	0.4748

less stable and hence more reactive than the neat complexes. Further more on encapsulation the values of the Fukui functions[36] calculated using the Hirshfeld population analysis are also found to differ from those of the neat complexes. Table 4.4 presents the Fukui functions (FFs) for the selected metal atoms and the coordinated nitrogen and oxygen atoms. It is seen in Tables 4.4 that the values of the Fukui functions at the Cu center increases upon encapsulation. In case of cobalt complex the f^+ values remains approximately the same to that of the neat complex. However, the f^- value decreases at cobalt metal centered. In case of nickel complex the Fukui function values almost remain unchanged. These results further indicate that on encapsulation the copper centre becomes a favorable site either for a nucleophillic or electrophillic attack. This further reflects the difference in the catalytic behavior of the two complexes. And it has been found in our experimental studies that the encapsulated Cu-complex serves as better candidature for catalytic oxidation of phenol. The change in the energies of the frontier orbital as well as the chemical behavior of the complexes on encapsulation can be attributed to the influence of the zeolite matrix.

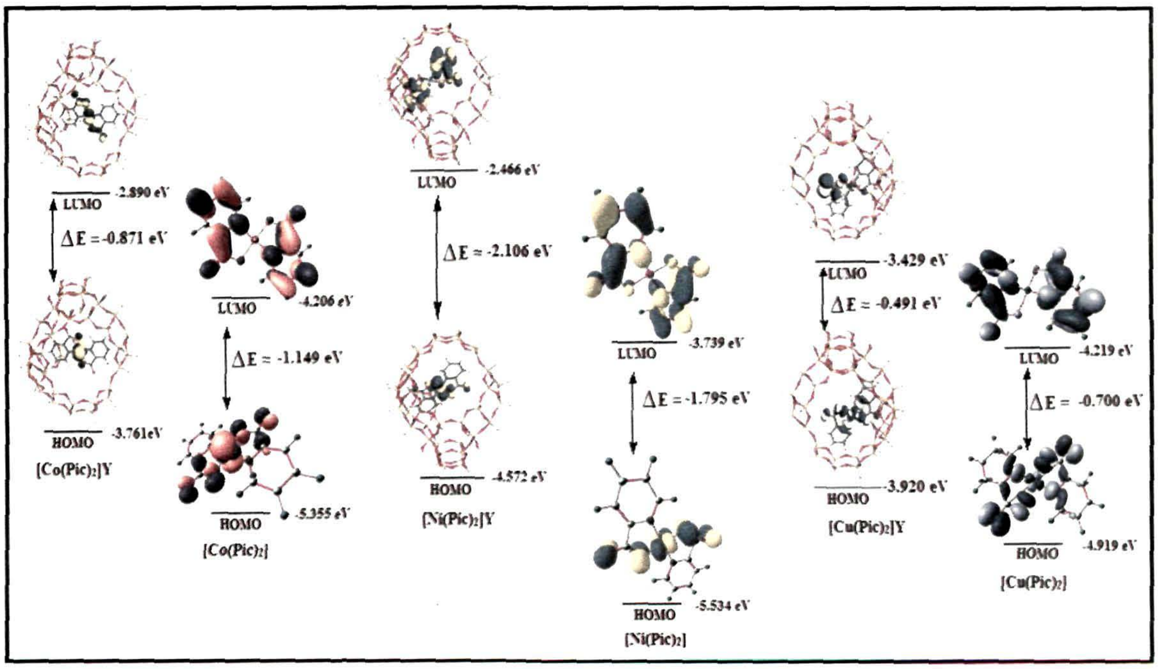

Figure 4.13. Schematic representation of the HOMO and LUMO level of the neat and the encapsulated phenanthroline complexes showing the change in the HOMO-LUMO gap between a) $[Co(Pic)_2]$ and $[Co(Pic)_2]Y$ b) $[Ni(Pic)_2]$ and $[Ni(Pic)_2]Y$ c) $[Cu(Pic)_2]$ and $[Cu(Pic)_2]Y$.

Table 4.4. Fukui function values for both neat and encapsulated complexes. M= Co, Ni and Cu in respective complexes.

Selected Atoms	$[Cu(Pic)_2]$		$[Co(Pic)_2]$		$[Ni(Pic)_2]$		$[Cu(Pic)_2]Y$		$[Co(Pic)_2]Y$		$[Ni(Pic)_2]Y$	
	f_K^+	f_K^-	f_K^+	f_K^-	f_K^+	f_K^-	f_K^+	f_K^-	f_K^+	f_K^-	f_K^+	f_K^-
M	0.101	0.082	0.121	0.144	0.146	0.219	0.144	0.146	0.123	0.146	0.04	0.224
N	0.025	0.014	0.019	0.015	0.016	0.004	0.015	0.016	0.01	0.007	0.022	0.001
N	0.025	0.014	0.019	0.02	0.02	0.004	0.02	0.02	0.014	0.01	0.034	0.064
O	0.083	0.06	0.024	0.065	0.069	0.087	0.065	0.069	0.028	0.039	0.051	0.025
O	0.042	0.135	0.077	0.049	0.054	0.035	0.049	0.054	0.071	0.086	0.014	0.224
O	0.042	0.06	0.024	0.058	0.063	0.087	0.058	0.063	0.054	0.063	0.023	0.037
O	0.083	0.135	0.077	0.090	0.095	0.035	0.090	0.095	0.022	0.030	0.070	0.085

4. 3. Catalytic Oxidation of Phenol

Selective oxidation of phenol is conducted to investigate the potential catalytic ability of neat and the encapsulated picolinato complexes. In contrast to the large number of publications dealing with the selective oxidation of phenol compounds in presence of molecular oxygen or hydrogen peroxide, the number of examples reporting the use of picolinato complexes of transition metals to synthesize selectively catechol as the desirable product is sparse.[37] To the best of our knowledge this is the first example for selective oxidation of phenol to catechol under microwave irradiation catalysed metal picolinato encapsulated in zeolite-Y. Microwave enabling selective organic transformations may have advantages over conventional thermal reactions as it avoids the use of acid, bases, and other toxic reagents. And in terms of greener context, such organic transformations are considered to be environmentally benign.

We found that in presence of hydrogen peroxide metal picolinato complexes of copper and cobalt can selectively oxidized phenol to catechol. Upon encapsulation of the complexes within zeolite-Y the catalytic activity of the complexes are found to enhance further. Nickel picolinato complexes are found to be inactive under identical condition. No significant reaction is observed either in absence of peroxide or in absence of the catalyst. The progress of the reaction is extremely slow in a nonpolar solvent, such as toluene and hexane. The reaction is found to proceeds well in acetonitrile, DMF and dichloromethane with maximum conversion in acetonitrile. Water and ammonia are not chosen for such catalytic conversion as they have strong tendency to form hydrogen bond with phenol or on the other hand they may block the vacant co-ordination site in the metal complexes.[38] So we carry out all the catalytic reaction in minimum amount of acetonitrile. Furthermore, catalytic oxidation did not occur to a significant extent in the presence of metal salts or in presence of metal exchanged zeolites under identical reaction conditions. However, the addition of stoichiometric amount of 30% H_2O_2 results in a mixture of products. The formation of the product is monitored through HPLC analysis and UV-vis spectroscopy. From the HPLC analysis it is found that in case of the reaction catalysed by $[Cu(pic)_2]Y$ and $[Co(Pic)_2]Y$ shows two peaks with a retention time 3.684 and 2.265 min corresponding to those of phenol and catechol, respectively (Figure 4.13a). In case of the reaction catalysed by neat complexes, other than phenol and catechol we observe one more additional peak with a retention time of 3.373 min corresponding to hydroquinone (Figure 4.13b). The reaction catalysed by metal-exchanged zeolites and metal salts in presence of peroxides results in a number of peaks indicating the mixture of products. The wt (%) value of the catechol is found to be highest in case of the reaction catalysed by [Cu(Pic)$_2$]Y

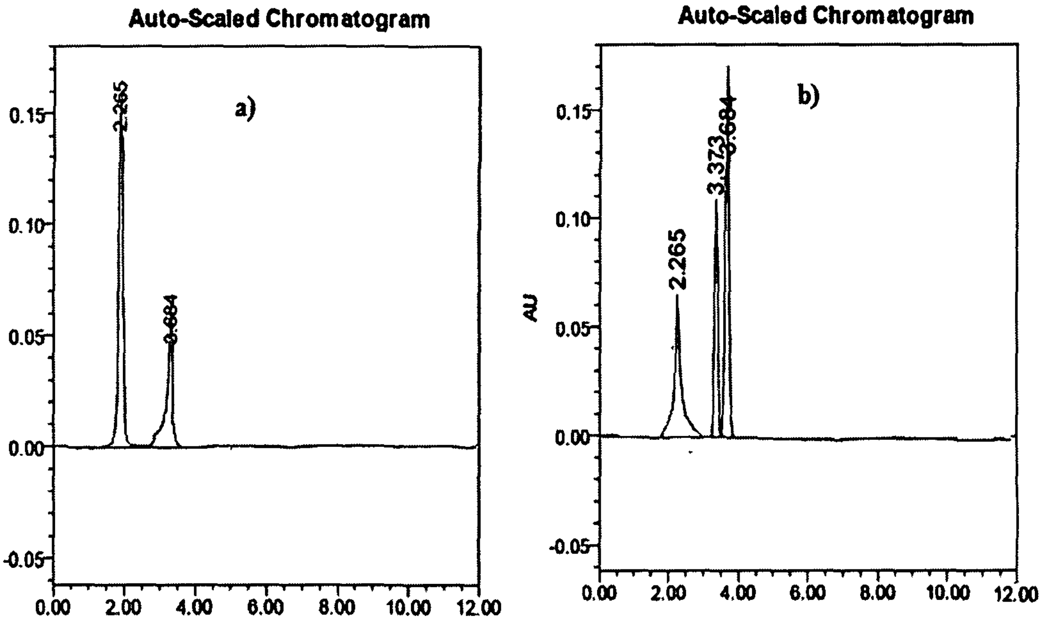

Peak Results

	Name	RT	Area	Height	Amount	Units
1		2.265	1263493	165189		
2		3.684	705862	104778		

Peak Results

	Name	RT	Area	Height	Amount	Units
1		3.684	1263493	165189		
2		3.373	705862	104778		
3		2.265	590263	56812		

Figure 4.13 a) HPLC analysis of the reaction catalyzed by encapsulated [Cu(Pic)$_2$]Y complex. b) Typical HPLC analysis of the reaction catalyzed by Cu and Co neat picolinato complexes.

and considered to be better catalyst. Depending on the HPLC analysis we have monitored the progress of the reaction catalysed by [Cu-(Pic)$_2$]Y catalyst after every 10 min *via* UV-vis spectroscopy. From the UV-vis spectrum shown in Figure 4.14 a) it is clearly visible that as the reaction precedes the absorption intensity of the peak at 254 nm corresponding to phenol[39] decreases whereas that at 285nm corresponding to that of catechol[40] increases. Moreover, we observe almost a symmetrical curve which indicates that almost all of the phenol that diffuses into the cavities of zeolites has been selectively converted to catechol.

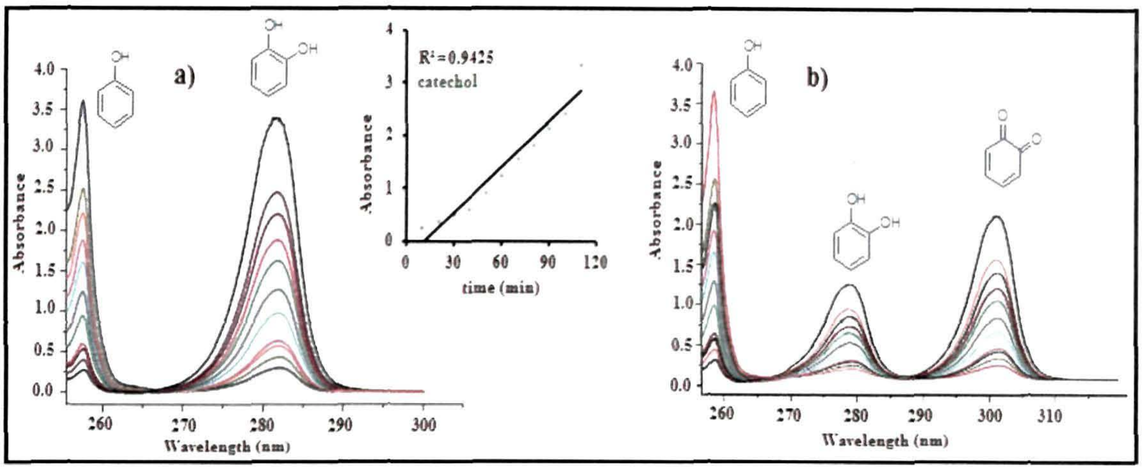

Figure 4.14. a) UV-vis spectrum showing the conversion of phenol to catechol after an interval of 10 min catalyzed by $[Cu(Pic)_2]Y$ in presence H_2O_2. b) Effect of peroxide amount on selective oxidation of phenol. Appearance of a second peak above 300nm indicates the further oxidation of catechol to benzoquinone.

Increase in the amount of catalysts (keeping the amount of substrate) does not affect the conversion to a greater extent. However, on increasing the amount of hydrogen peroxide results a new peak corresponding to that of benzoquinone as observed in the HPLC analysis. The UV-vis study also shows an additional peak above 300 nm and its absorption maxima is found to increase as the reaction proceeds, Figure 4.14b). In order to understand the effect of peroxide concentration on catechol formation we further chose three molar ratio of phenol: H_2O_2 viz 1:1, 1:2 and 1:3. The maximum yield is found when the molar ratio is 1:2. But increasing the molar ratio to 1:3 retards the catechol formation. The reason for decreasing % conversion of phenol might be due to dilution of the reaction mixture, since 30% H_2O_2 has considerable amount of water. Thus1:2 molar ratios are considered considered to be optimum. The material balance between phenol and the product after the reaction are of course, not in reasonable agreement. To understand this fact UV-vis absorption spectroscopy is applied to record the adsorption behavior of the phenol solution before and after treatment with the catalyst, Figure 4.15a-g. For this we treat 10mg of catalyst in 10ml of acetonitile containing 1mmol of phenol. The characteristic absorption of phenol at 254 nm is chosen for monitoring the adsorption process. It is found that some amount of phenol get adsorbed on the surface or remains bound to the metal centred via chelate formation. Among all the catalyst Ni-complex exhibited highest adsorption capability for phenol. This accounts for the mass imbalance and catalytic inactivity of nickel catalyst. The comparison of TON based on metal content is presented in Table 4.5. It is observed from Table 4.5 that although [Cu(Pic)$_2$]Y gives high yield, the [Co(Pic)$_2$]-Y will serve as better catalyst in terms of the TON.

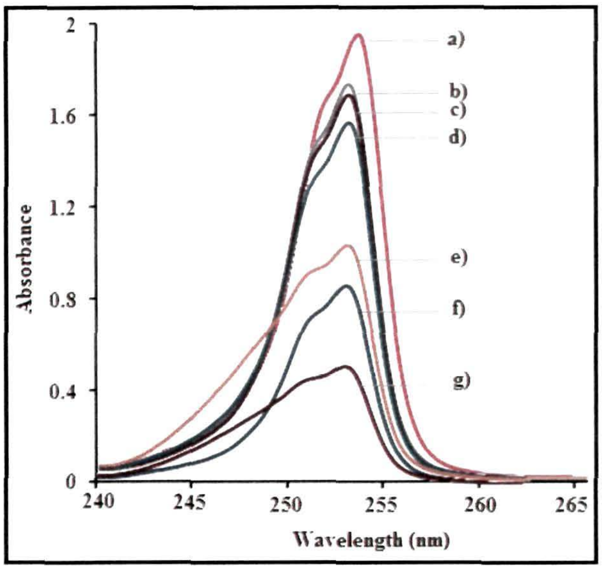

Figure 4.15. UV-vis absorption spectra of phenol. Curve a) corresponds to the spectrum of phenol in absence of catalyst. Curves (b-g), respectively correspond to the spectra of phenol after treated with [Cu(Pic)$_2$]Y, [Co(Pic)$_2$]Y, [Cu(Pic)$_2$], [Co(Pic)$_2$], [Ni(Pic)$_2$] and [Ni(Pic)$_2$]Y.

Table 4.5. Oxidation of Phenol by metal chlorides, metal exchanged zeolites, neat and encapsulated picolinato complexes under microwave irradiation in presence of H_2O_2.

Catalyst	M^{2+}in mmol[a]	Time (min)	Yield (mmol)[b]			TON[c]
			Catechol	HQ	BQ	
$CoCl_2.6H_2O$	0.063	70	0.20	0.15	0.10	3
$CuCl_2.2H_2O$	0.088	70	0.23	0.12	0.17	2.6
$NiCl_2.6H_2O$	0.063	70	-	-	-	
Co^{2+}-Y	0.054	70	0.21	0.20	0.30	3.8
Cu^{2+}-Y	0.067	70	0.23	0.18	0.32	3.4
Ni^{2+}-Y	0.047	70	-	-	-	
[Co(Pic)$_2$]	0.040	70	0.52	0.10	-	13
[Cu(Pic)$_2$]	0.044	70	0.54	0.12		12
[Ni(Pic)$_2$]	0.040	70	-	-	-	
[Co(Pic)$_2$]Y	0.028	70	0.70	-		25
[Cu(Pic)$_2$]Y	0.032	70	0.74	-		23
[Ni(Pic)$_2$]Y	0.027	70	-	-	-	

[a] Amount of metal content in 15mg of the catalyst. [b] Isolated yield obtained by chromatographic separation.[c] TON= [amount of catechol(mmol)/Metal atom(mmol) per 15 mg of catalyst]. HQ = hydroquinone, BQ = benzoquinone.

4.4. Mechanism of Phenol Oxidation

The mechanisms of the catalytic oxidation reaction have been the subject of intense research, since many reactive species are involved and their roles vary depending on the catalytic systems. A plausible mechanism for the conversion of phenol to catechol catalyzed by picolinato complexes of Co and Cu in presence of H_2O_2 has been proposed in Figure 4.16. An active species ML_2*(M= Co or Cu, L= 2-pyridine carboxylate) is first generated quickly in the ML_2–H_2O_2 buffer solution, then the intermediate ML_2*S is generated by coordination of phenol to M^{2+}. Finally the catechol is obtained by abstraction of oxygen with the simultaneous release of H_2O. In order to have an insight into the mechanism of phenol oxidation, we have further carried out DFT calculation on the probable transition (TS) intermediates (Int) states formed during the catalytic cycle. We examined relative energies for conversion of ML_2→TS1→ML_2*→TS2→ ML_2S*→TS3→ catechol.

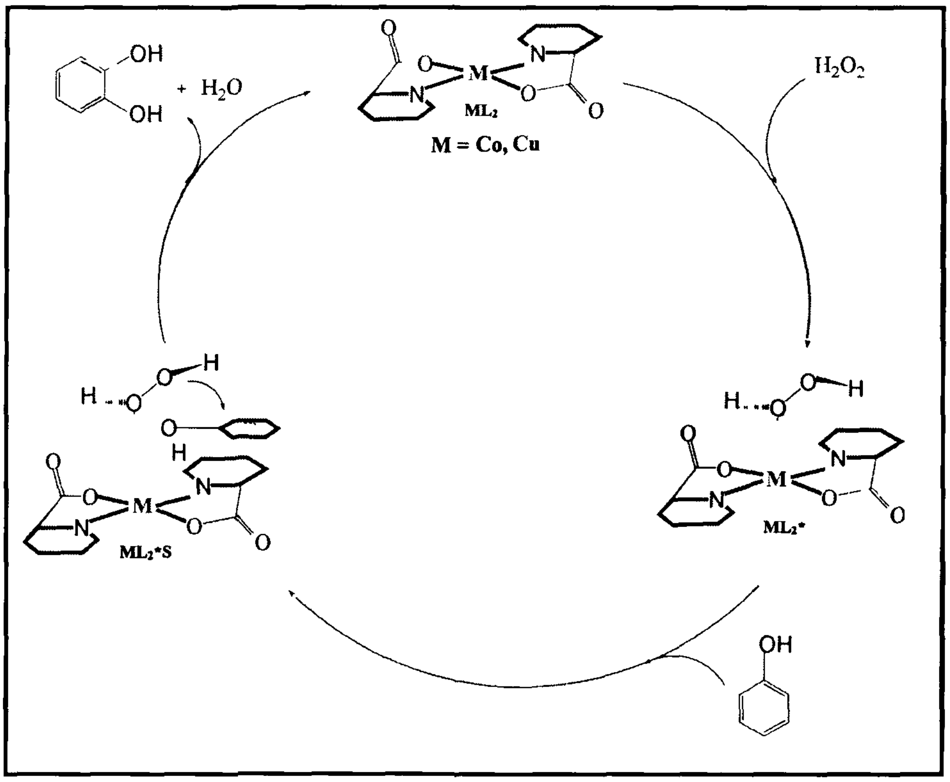

Figure 4.16. A plausible catalytic cycle for conversion of phenol to catechol in presnce of metal picolinato complex and H_2O_2.

Starting from the *trans* bis(Picolinao) M(II) [M= Co, Ni and Cu] complex, we introduced hydrogen peroxide which immediately leads to the formation of a weakly bound van der Waals complex [ML_2].H_2O_2 (ML_2*, Int-1) through TS1. This step has a barrier (ΔE) of 8.8 and 8.0 kcal/mol for Cu and Co complex, respectively (Figure 4.17). At the TS1, one of the hydrogen atom of H_2O_2 moves towards the oxygen atom of picolinato lignad and one of the oxygen towards the metal centre. The M...O and O...H distances are found to be 2.40 and 3.32Å, 2.91 and 1.73 Å, respectively in case of Cu-complex and Co-complex (Figure 4.18, c and d). The optimized geometries of the intermediate states of cobalt and copper shows that the weakly bound species complexes are formed *via* the interaction of the metal centre with one of the oxygen atom of the peroxide moiety. The M···O and O···H distances are found to be 2.22Å and 1.69Å, 2.36Å and 1.67Å in Co and Cu complexes, respectively (Figure 4.18, e and f). NBO analysis shows that in both the system there occurs a negligible electron transfer between the H_2O_2 and ML_2 complex. Unlike Co and Cu picolinato complexes, Ni failed to form ML_2* intermediates. This may be attributed to the special stability associated with square planar 16 electron metal complexes. However, addition of H_2O_2 to the square planar 15 and 17 electron picolinato complexes of Co and Cu are not prohibited and hence, they can easily react with H_2O_2 to form $[M(Pic)_2].H_2O_2$. The addition of H_2O_2 to ML_2 is calculated to be thermodynamically favorable by 14.5 and 13.3 kcal

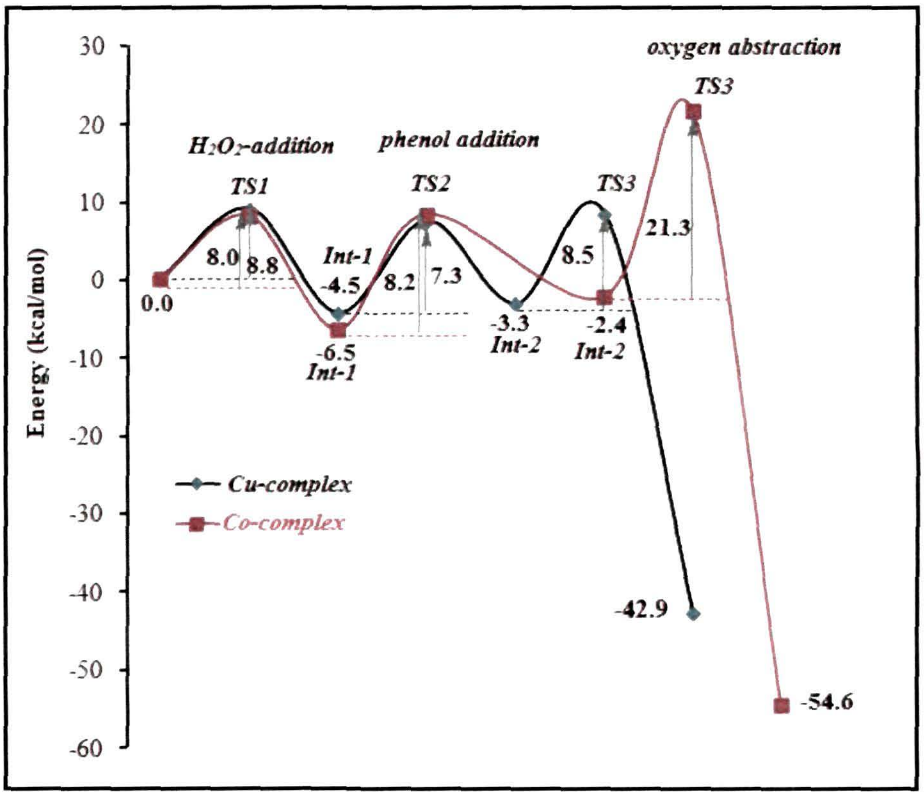

Figure 4.17. Simple energy profile plot for the catalytic cycle.

mol^{-1} for the Co and Cu complexes, respectively. On phenol insertion into the metal peroxide complex (ML_2*, Int-2), the H_2O_2 moves away out of the square plane towards the Pic ligand and facilitates the formation of M-O (phenyl) linkage. This step proceeds through TS2 and has a barrier of 7.3 and 8.5 kcal/mol for Cu and Co-complex respectively (Figure 4.17). However, the peroxide is bound to the O-atom of the picolinato ligand through one of the H- atom. At this stage O-H bond distance is found to decrease from 1.67 to 1.58 in case of copper complex and from 1.69 to 1.64 Å in case of cobalt complex (Figure 4.18, i and j). The formation of ML_2*S is found to be equally favorable for both the complexes. The last step of the mechanism involves the abstraction of oxygen (TS3) leading to the formation of catechol and liberation of water

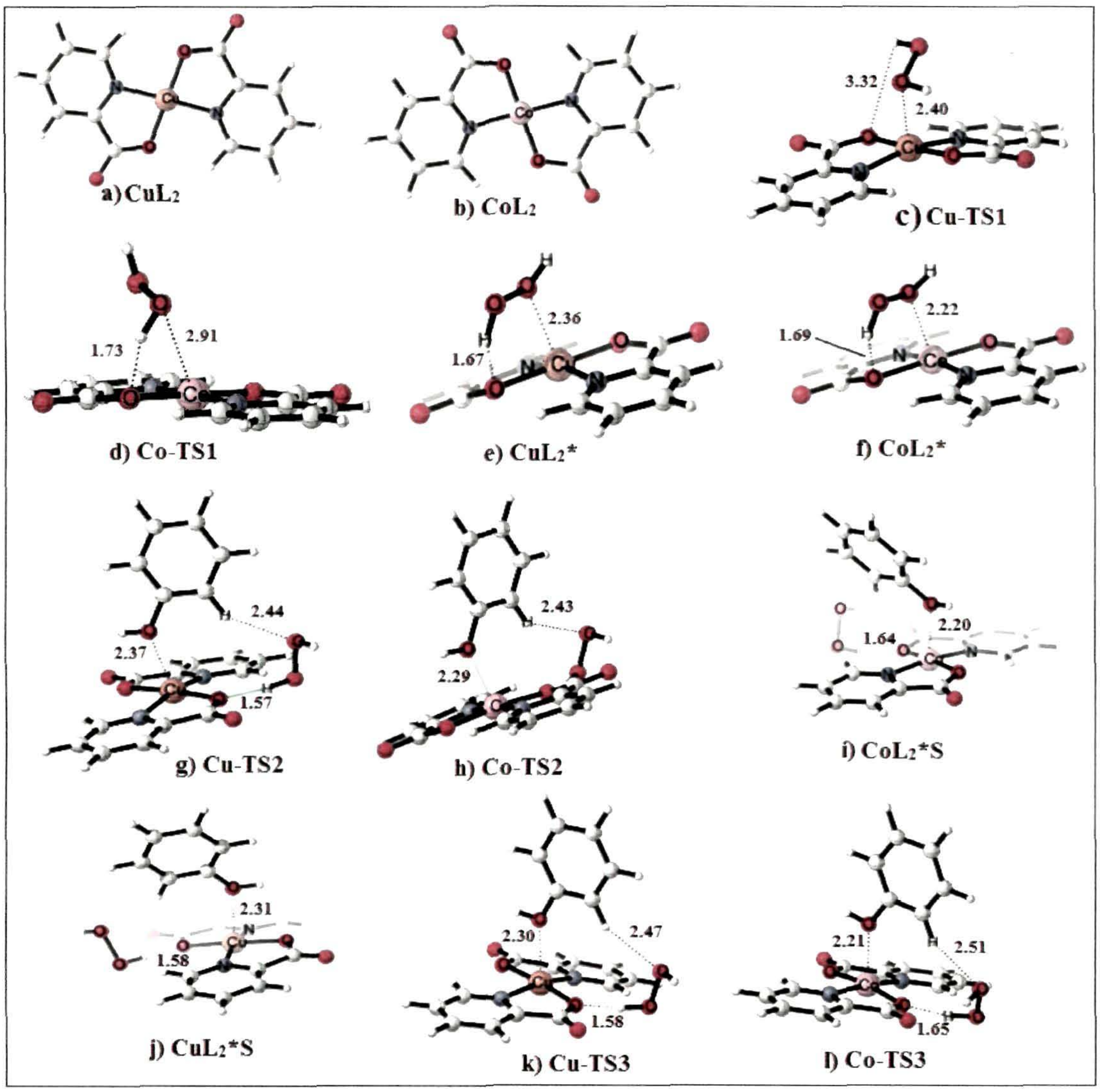

Figure 4.18. The optimized geometries of the possible transition and intermediate states involved in the conversion of phenol to catechol a) CuL_2 b) CoL_2 c) Cu-TS1 d) Co-TS1 e) CuL_2^* f) CoL_2^* g) Cu-TS2 h) Co-TS2 i) CoL_2^*S j) CuL_2^*S k) Cu-TS3 l) Co-TS3.

and subsequent regeneration of the square planar complex ML_2. This step has a barrier of 8.2 and 21.3kcal/mol for Cu and Co-complex respectively (Figure 4.17) and is found to be favorable by 33.3 and 34.4 kcal mol^{-1} for Co and Cu complexes, respectively. It can be observed from Figure 4.17 that formation of ML_2* and ML_2*S is not energetically costly in case of Cu-complex. However, in case of cobalt complex the last step i.e the migration of oxygen to phenol leading to catechol formation involves a high energy barrier. And this brings out a difference in the rate of the catalytic oxidation mediated by two complexes. In addition to the *trans* isomer, we also studied the catalytic cycle starting with the *cis* geometry of Cu-complex as it is likely that both *cis* and *trans* isomers of Cu-complex may co-exist in reaction mixture. However, addition of H_2O_2 to *cis* ML_2 complex results in a ML_2*, similar to that we obtained by starting with the *trans* geometry. This further revealed that even though both the isomer may exist in solution, after addition of peroxide the catalytic cycle will be governed by the stable *trans* Cu-complex.

4.5. Conclusion

In summary, three square planar picolinato complexes of Co (II), Ni(II) and Cu(II) are being synthesize inside zeolite-Y and their encapsulation is ensured by different studies. The spectroscopic and theoretical studies revealed that the walls of the zeolite framework imparts space constrain to the metal complexes which modifies their structural, electronic and catalytic behavior. Under microwave irradiation and in presence of hydrogen peroxide these metal complexes facilitate the selective oxidation of phenol to catechol with moderate to good yield. DFT based study allows us to conclude that the H_2O_2 interacts with the transition metal complexes *via* an electron transfer process occurring from the occupied metal *d*-orbital to the π^*-orbital of H_2O_2. Out of the three metal complexes, the bis(Picolinato) Cu(II) and Co(II) being 15 and 17 electron species, respectively participate actively in this electron back donation process and hence shows better catalytic activity in comparison to the corresponding 16-electron Ni(II) complex. In case of the reaction catalysed by neat metal complexes, catechol is found to be major oxidation product along with hydroquinone as the minor product. The selective oxidation of phenol to catechol is found to enhance in presence of the encapsulated complexes. The amount of H_2O_2 is found to affect the selectivity of the reaction. UV-vis and HPLC analyses suggest that increasing the concentration of hydrogen peroxide further oxidize the catechol to benzoquinone. A plausible catalytic cycle is proposed on the basis of DFT calculation. Both the studies suggest that the reaction precedes via the formation a $[M(Pic)_2].H_2O_2$ (M= Co and Cu) intermediate.

References

[1] a) Korkina, L. G., et al. *Curr.Med. Chem.* **16**(30), 3943-3965, 2009 and references cited therein b) Nemoto, H., et al. *Org. Lett.* **13**(10), 2714-2717, 2011, c) Abraham, I., et al. *J. Braz. Chem. Soc.* **22**(3), 385-421, 2011, d) Nohl, H., et al. *Adv. Free Radical Biol.* **2**(1), 211-279, 1986.

[2] (a) Capdevielle, P., & Maumy, M. *Tetrahedron Lett.* **23**(15), 1573-1576, 1982, (b) Re´glier, M., et al. *J. Chem. Soc., Chem. Commun.* 1752-1755, 1990, (c) Casella, L., et al. *J. Chem. Soc. Chem. Commun.* 1611-1612, 1991, (d) Sayre, L. M., & Nadkarni, D. V. *J. Am. Chem. Soc.* **116**(7), 3157-3158, 1994, (e) Casella, L., et al. *Inorg. Chem.* **35**(26), 7516-7525, 1996, (f) Mandal, S., et al. *J. Org. Chem.* **65**(16), 4804-4809, 2000.

[3] Rolff, M., et al. *Angew. Chem. Int. Ed.* **49**(36), 6438 -6442, 2010.

[4] a) Itoh, S., et al. *J. Am. Chem. Soc.* **123**(27), 6708-6709, 2001, b) Osako, T., et al. *J. Am. Chem. Soc.* **125**(36), 11027-11033, 2003.

[5] Deshpande, S., et al. *J. Catal.* **188**(2), 261-269, 1999

[6] Noyori, R., et al. *Chem. Commun.* 1977-1986, 2003.

[7] Jones, C. W. *Applications of Hydrogen Peroxide and Derivatives*, Royal Society of Chemistry, Cambridge, 1999.

[8] Lane, B. S., & Burgess, K. *Chem. Rev.* **103**(7), 2457-2473, 2003.

[9] (a) Stratakis, M., & Froudakis, G. *Org. Lett.* **2**(10), 1369-1372, 2000, (b) Stratakis, M., et al. *J. Org. Chem.* **68**(7), 2839-2843, 2003. (c) Stratakis, M., et al. *Org. Lett.* **5**(19), 3471-3474, 2003.

[10] Majetich, G. *J. Am. Chem. Soc.* **128**(40), 13314-13315, 2006.

[11] Corma, A., & Garcia, H. *Eur. J. Inorg. Chem.* **2004**(6), 1143-1164, 2004.

[12] Zovinka. P. E., & Stock. A. E. *J. Chem. Educ.* **87**(4), 350-352, 2010.

[13] Yasumatsu, N., et al. *Bioorg. Med. Chem.* **15**(14), 4917-4922, 2007.

[14] a) Shechter, Y., & Karlish, S. J. D. *Nature* **284**(5756), 556-558, 1980, b) Chruscinska, E. L., et al. *Inorg. Chem.* **50**(3), 883-899, 2011.

[15] Coulston, L., & Dandona, P. *Diabetes* **29**(8), 665-667, 1980.

[16] Fonteles, M. C., et al. *Horm. Metab. Res.* **32**(4), 129-13, 2000.

[17] Sorenson, J. R. *J. Prog. Med. Chem.* **26**, 437-568, 1989.

[18] Anderson, R. A., et al. *Diabetes* **46**(11), 1786-1791, 1997.

[19] Munoz, M. C., et al. *Diabetes*, **50**(1), 131-138, 2001.

[20] Bonchio, M., et al. *J. Org. Chem.* **59**(21), 6262-6267, 1994.

[21] Kozlov, A., et al. *J. Chem. Soc., Faraday Trans.* **94**, 809-816, 1998.

[22] (a) Quayle, W. H., & Lunsford, J. H. *Inorg. Chem.* **21**(1), 97-103, 1982, (b) Quayle, W. H., et al. *Inorg. Chem.* **21**(6), 2226-2231, 1982.

[23] Cantalupo, S. A., et al. *Angew. Chem. Int. Ed.* **51**(40), 1000 -1005, 2012.

[24] Carrasco, R., et al. *Dalton Trans.* 2527-2538, 2005.

[25] (a) Kosman, D. J., & Hassett, R. *J. Am. Chem. Soc.* **120**(16), 4037-4038, 1998, (b) Raman, N., et al. *Proc. Indian Acad. Sci. (Chem. Sci.)* **115**(3), 161-167, 2003.

[26] Zanjanchi, M. A., & Ebrahimian, A. *J. Mol. Struc.* **693**(1-3), 211-216, 2004.

[27] Delabie, A., et al. *Micropor. Mesopor. Mat.* **37**(1-2), 209-222, 2000.

[28] (a) Hoffman, B. M., et al. *J. Am. Chem. Soc.* **92**(1), 61-65, 1970, (b) Maki, A. H., et al. *J. Am. Chem. Soc.* **86**(21), 4580-4587, 1964.

[29] Kadish, K. M., et al. *Inorg. Chem.* **28**(13), 2542-2547, 1989.

[30] Bencini, A., et al. *Inorg. Chem.* **20**(8), 2544-2549, 1981.

[31] Griffith, J. H. E., & Owen. J. *Proc. R. Soc.* **A213**, 459-473, 1952.

[32] Bessel, C. A., & Rolison, D. R. *J. Phys. Chem. B* **101**(7), 1148-1157, 1997.

[33] Reddy, B. M., et al. *Ind. Eng. Chem. Res.* **48**(18), 8478-8486, 2009.

[34] Mozo, E .P., et al. *J. Phys Chem.* **97**(49), 12819-12827 , 1993.

[35] Koopmans, T. A. *Physica.* **1**(1-6), 104-113, 1933.

[36] Yang, W., & Mortier, W. J. *J. Am. Chem. Soc.* **108**(19), 5708-5711, 1986.

[37] Bonchio, M., et al. *J. Org. Chem.* **59**(21), 6262-6267, 1994.

[38]Feng, Y., et al. *J. Phys. Chem. A* **106**(47), 11518-11525, 2002.

[39] Alapi, T., & Dombi, A. *J. Photochem. Photobiol. A: Chemistry* **188**, 409-418, 2007.

[40] Wang, Y., et al. *J. Phys. Chem. B* **107**(35), 9434-9440, 2003.

Chapter 5

Effect of Alkali Metal Cations on Electronic, Redox and Catalytic Properties of Fe(III) Schiff Base Complexes Encapsulated in Zeolite -Y

5.1. Introduction

Zeolites are attractive materials for encapsulation of transition metal complexes, organometallics, organic dyes and polymers within their voids.[1-3] The topology of the voids, the steric and electrostatic constraints imposed by the walls of the zeolite framework can influence the geometry and hence changes magnetic, electronic and redox properties of the encapsulated complex leading to changes in the reactivity of the enclosed species.[4] Besides the space and steric constraints of the zeolite matrix, the cations in zeolites have been known to play an important role other than merely compensating the negative charge in the framework. It has been shown that the cations govern the donor strength of the zeolite framework and the strength increases with increasing electro positivity of the cations.[5,6] Physicochemical characteristics such as electrostatic potential and electric field within the cage, spin–orbit parameter and space available for guest molecules inside the supercage are known to be controlled by these exchangeable charge compensating alkali metal cations. Moreover, one can readily switch to a base catalyst by replacing Na^+ of zeolite-NaY with other large alkali metal cation such as Cs^+.[7,8] It has also been reported that these cations offer different reactive sites for the interaction of the incoming guest molecules.[9,10] However, only a limited number of studies have been addressed to examine the effect of alkali metal cations on the physicochemical, electronic, redox and catalytic behaviour of zeolite encapsulated transition metal complexes.[11,12]

The zeolite encapsulated transition metal complexes of Shiff-base ligands especially of Salen are well known to mimic the catalytic cycle of cytochrome P-450 and have attracted research interest in recent years.[13,14] They have been extensively used as biomimetic catalysts for hydrocarbon hydroxylation/epoxidation and alcohol carbonylation with a variety of oxidants including hydrogen peroxide,[15-19] tertbutylhydroperoxide (TBHP)[14,20,21] and iodosobenzenes (PhIO)[20,22] and with less frequent use of O_2 as oxidant.[23,24] Molecular oxygen is not considered to be a good oxidant as compared to other oxidants mentioned for oxidation reaction of organic substrates because of its higher chemical stability. So the search for a better catalyst which can reduce molecular oxygen and thus make use of it as oxidant in organic reaction is ongoing. It has been reported on the basis of electrochemical studies that Schiff-base complexes of Fe, Mn and Co encapsulated in zeolite-Y can reduce the molecular oxygen to water.[25]

Asymmetric aerobic oxidative coupling of 2-napthol to BINOL is now considered to be most atom economical method but limited success have been obtained by the extension of the known homo-coupling reaction. Since C_1 and C_2 –symmetric BINOL and its derivative are deemed to be efficient chiral auxiliaries, therefore designing of newer catalyst for such oxidative coupling reaction is now under development. And recent studies have shown that chiral iron(Salen) complex can act as a better catalyst for aerobic oxidative coupling of 2-napthol.[26,27] However, the catalytic activity of achiral Fe(Schiff) base complexes without any additive are less explored in such kind of oxidative coupling reaction since they are less facile in bringing out the enantioselectivity in the resultant BINOL.

Stemming from our interest on the effect of alkali metal cations on the physicochemical properties and reactivity of encapsulated transition metal complexes, in this work we have carried out a systematic study on the effect of counter cations of zeolite on the charge transfer bands of Fe-Schiff base complexes (Fe-Salen and Fe-Salophen) encapsulated in zeolite-Y and its synergistic effect on the redox potential of the encapsulated complexes and tried to shed light on dependency of the aerobic oxidative coupling of 2-napthol on the redox potential of the catalyst and rationalize how the size of the alkali metal cations controls the chirality inside the confined space of zeolite. Density functional theory (DFT) methods have been extensively used to understand the structure, electronic properties, and chemical reactivity of zeolitic materials.[28]

5.2. Results and Discussion

5.2.1 Experimental Section

5.2.1.1. Elemental Analysis

The results of the elemental analyses are given in Table 5.1 and gives Si/Al ratio of 2.64 which corresponds to a unit cell formula Na_{54} $[(AlO_2)_{54}(SiO_2)_{138}]$ for parent NaY. Despite repetition of the exchange procedure five times, elemental analysis of the final zeolites revealed incomplete exchange of alkali cations, as shown in Table 5.1. From Table 5.1 it can be seen that the metal content in the encapsulated complexes are less compared to the metal exchanged zeolites. This result gives a preliminary idea regarding the participation metal ions residing mostly in site-II of zeolite –Y cavity in the complex formation. Further, it is also eviedent that the Si/Al ratio in all the hybrid

Table 5.1. Elemental analyses for pure NaY, iron exchanged zeolites and zeolite encapsulated complexes.

Samples	Metal %	Si %	Al %	Alkali Metal Cation%	C %	H %	N%	Unit cell formula
Li Y	-	22.76	8.60	4.85(Li)	-	-	-	$Li_{34}Na_{18}[(AlO_2)_{52}(SiO_2)_{140}]$
Na Y	-	22.70	8.57	7.55(Na)	-	-	-	$Na_{54}[(AlO_2)_{54}(SiO_2)_{138}]$
K Y	-	22.53	8.52	4.56(K)				$K_{32.5}Na_{19.5}[(AlO_2)_{52}(SiO_2)_{140}]$
Li Fe Y	4.12	22.96	8.44	4.50 (Li)	-	-	-	$Li_{31.47}Na_{6.7}Fe_{13.8}[(AlO_2)_{52}(SiO_2)_{140}]$
Na Fe Y	4.12	22.96	8.44	5.64(Na)	-	-	-	$Na_{38.4}Fe_{13.6}[(SiO_2)_{52}(AlO_2)_{140}]$
K Fe Y	4.12	22.96	8.44	4.35 (K)	-	-	-	$K_{30.96}Na_{5.4}Fe_{15.7}[(SiO_2)_{52}(AlO_2)_{140}]$
Fe-Salen-Li Y	1.72	21.80	8.20	3.34 (Li)	2.86	1.40	1.68	
Fe-Salen-Na Y	1.68	20.40	7.80	3.63(Na)	2.62	1.61	1.76	
Fe-Salen-K Y	1.78	20.48	8.85	3.80 (K)	2.82	1.42	1.38	
Fe-Salophen-Li Y	1.74	21.75	8.35	3.25 (Li)	4.20	1.21	1.43	
Fe-Salophen-Na Y	1.65	21.25	8.80	3.29 (Na)	3.92	1.38	1.32	
Fe-Salophen-K Y	1.76	21.43	8.28	3.64 (K)	3.86	1.38	1.42	

system is almost same indicating the dealumination during complexation or else during the metal exchanged process.

5.2.1.2. XRD Study

The powder X-ray diffraction patterns of the zeolite NaY, Fe^{3+} exchanged zeolites and the encapsulated Fe-Schiff base complexes in various alkali exchanged zeolites are shown in Figure 5.1. Essentially similar diffraction patterns are noticed in the encapsulated Fe-Salen (or Fe-Salophen) and NaY, except the zeolite with encapsulated Fe-Salen (or Fe-Salophen) have slightly weaker intensity. These observations indicate that the framework of the zeolite does not suffer any significant structural changes during encapsulation. However, there are differences in the relative peak intensities of the 220 and 311 reflections appearing at $2\theta = 10$ and 12^0, respectively. For pure NaY and for Fe -exchanged zeolite-Y

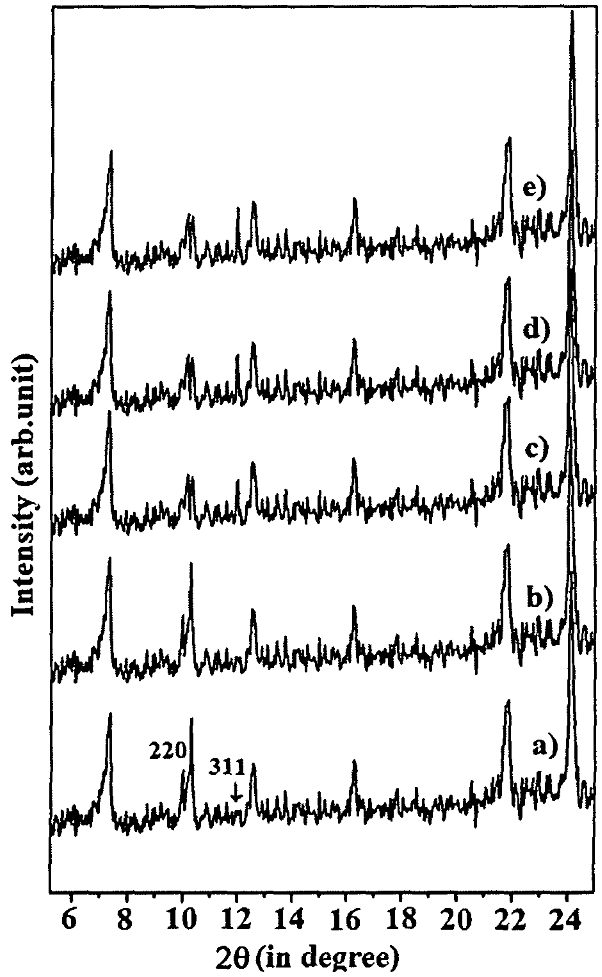

Figure 5.1. XRD pattern of a) Pure zeolite-Y, b) Fe exchanged zeolite-Y, c) Fe-Salen-LiY or Fe-Salophen-LiY d) Fe-Salen-NaY or Fe-SalophenNaY e) Fe-Salen-KY or Fe-Salophen-KY.

$I_{220} > I_{311}$, but for the encapsulated complex $I_{311} > I_{220}$. This reversal in intensities has been observed more as the size of the cations increases (Li<Na<K) in encapsulated complexes (Figure 5.2) and has been empirically correlated with the presence of a large complex within the zeolite-Y supercage.[29] This change in the relative intensities may be associated with the redistribution of randomly coordinated free cations in zeolite Y at sites II and I. The above observation may therefore be construed as evidence for the successful encapsulation of Fe-Salen or Fe-Salophen complex within the supercage of zeolite Y.

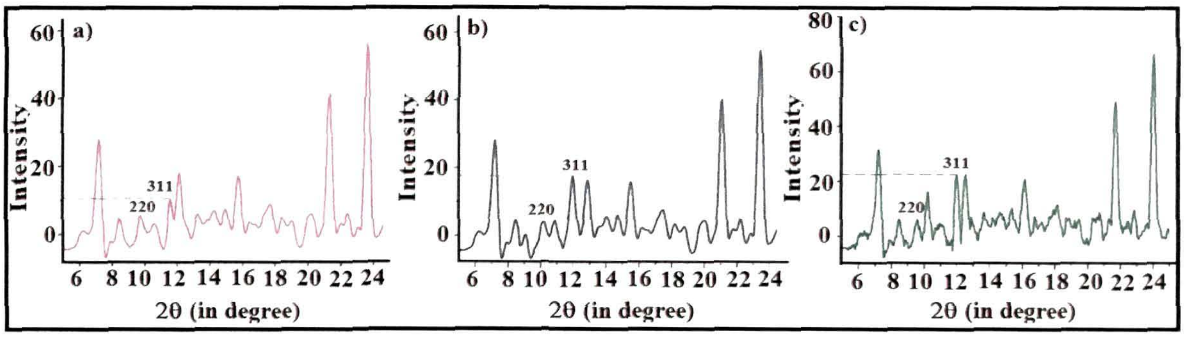

Figure 5.2. XRD pattern of a) Fe-Salen-LiY or Fe-Salophen-LiY b) Fe-Salen-NaY or Fe-SalophenNaY c) Fe-Salen-KY or Fe-Salophen-KY showing the change in intensities of 311 plane on increasing the size of alkali metal cations.

5.2.1.3. FTIR Study

The IR spectra of the neat Fe-Salen complex [Figure 5.3, curve (c)] shows major bands at 1626 (C=C), 1534, 1430, (C=N), 1288 (C-O), 1378, 767 cm^{-1} (ν_{C-H} aromatic ring) and IR spectra of the Fe-Salophen complex [Figure 3, curve (d)] shows major bands at 1632 (C=C), 1463, (C=N), 1302 (C-O), 1378, 751 (ν_{C-H} aromatic ring). Similar frequencies are also observed in the case of encapsulated complexes in various zeolites with a little shift in the C=N and C-O bands to wavenumbers 1522, 1450 and 1273 cm^{-1}, respectively indicating nitrogen and oxygen coordination inside the cavity of zeolite framework. The $\nu_{C-H\ def}$ band at 1378 cm^{-1} is shifted towards lower wavenumber as the size of the alkali cation increases. This shifting in $\nu_{C-H\ def}$ band on encapsulation has been reported for encapsulation of metal complexes in various zeolites.[30] The peak values in wavenumber of the selected IR-bands for the neat and the encapsulated complexes are given in Table 5.2.

Table 5.2. FTIR spectral data (in cm^{-1}) for the neat and the encapsulated Fe-Schiff base complexes.

Samples	$\nu_{C=C}$	$\nu_{C=N}$	$\nu_{C\text{-}H\ def}$	$\nu_{C\text{-}O}$
Na Y	-	-	-	-
Fe-Salen	1626	1534, 1430	1378, 767	1288
Fe-Salophen	1632	1463	1378, 751	1302
Fe-Salen-LiY	1645	1522,1450	1372	1273
Fe-Salen-NaY	1644	1522,1450	1367	1273
Fe-Salen-KY	1645	1522,1450	1362	1273
Fe-Salophen-LiY	1645	1476	1373	1282
Fe-Salophen-NaY	1645	1476	1361	1282
Fe-Salophen-KY	1645	1476	1358	1282

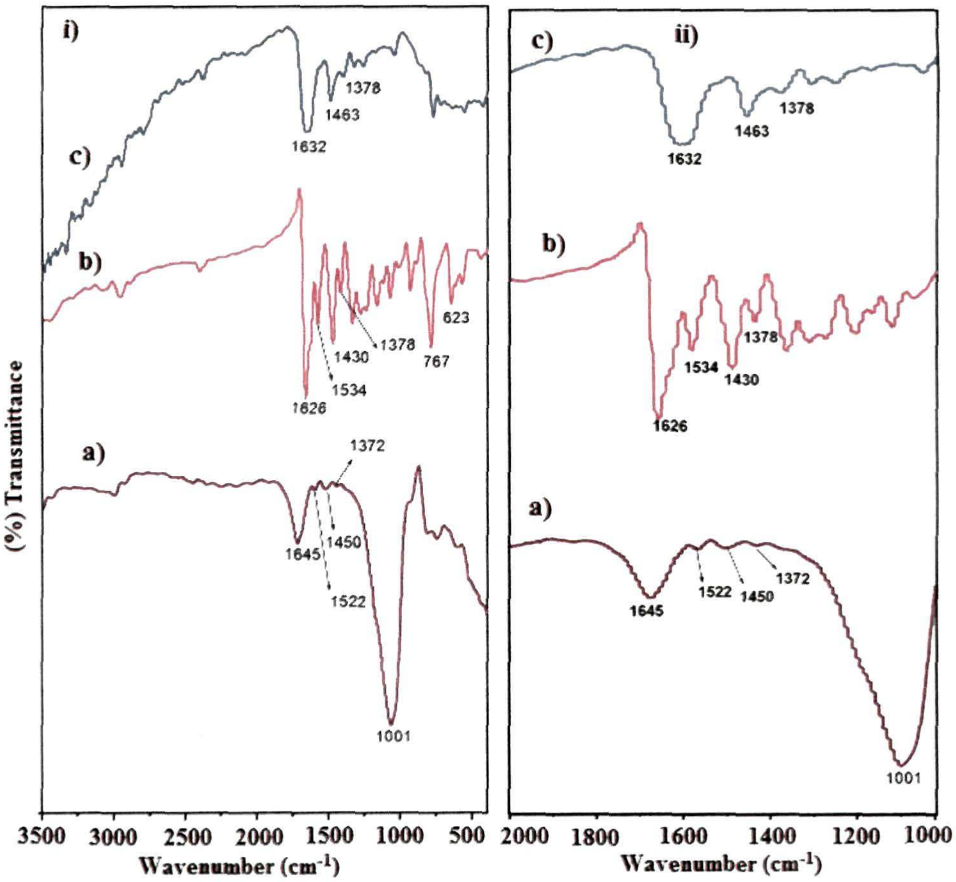

Figure 5.3. IR spectra of [i] a) Pure zeoliteY, b) typical FTIR spectra of encapsulated iron Schiff base complexes in various alkali exchanged zeolites c) Neat Fe-Salen complex d) Fe-Salophen complex [ii] Expanded IR-spectrum of a), b), c) and d) in between 2000 and 900 cm^{-1}.

5.2.1.4. UV-vis /DRS Study

The peak values for the electronic transitions observed in uncomplexed ligands, neat Fe-Schiff base complexes and encapsulated Fe-complexes in various alkali exchanged zeolites are given in Table 5.3. The absorption spectrum of uncomplexed Salen features two higher energy bands at 213 and 256 nm and two lower energy bands at 320 and 397 nm [Figure 5.4, (a)]. The bands at lower wavelength are attributable to π → π* transitions and the bands at higher wavelength arises from n → π* transitions. In the corresponding phenyl substituted ligand, Salophen, absorption bands are observed at 205 nm, 257 nm and 329 nm, Figure 5.4b. The first two bands are assigned to π → π* and the band at 329 nm is due to n → π* transition.

Table 5.3. UV-vis/DRS spectral data (λ_{max} in nm) for the uncomplexed ligands, neat and the encapsulated Fe-Schiff base complexes.

	Electronic transitions		
Samples	π→ π*	n→π*	pπ→dπ*
Salen	213, 256	320,397	-
Salophen	205, 257	329	-
Fe-Salen	215,231,257,299	317	505
Fe-Salophen	218,241,290	321	590
Fe-Salen-LiY	234, 290	427	489
Fe-Salen-NaY	237, 294	434	517
Fe-Salen-KY	239, 296	443	527
Fe-Salophen-LiY	217,285, 317	-	510
Fe-Salophen-NaY	219, 287, 319	-	523
Fe-Salophen- KY	223, 288, 321	-	574

The Fe(III) Salen complex in methanol solution exhibit four absorption peaks at 215, 231, 257 and 299 nm due to intraligand π → π* transitions. These bands are approximately shifted relative to those of the uncomplexed ligand, [Figure 5.4(c)]. In the corresponding Fe (III) - Salophen complex, three bands are observed at 218, 241 and 290 nm as shown in Figure 5.4(d). In addition to these π → π* transitions two additional bands are observed in both the complexes. The bands at 317 nm in case of Fe-Salen and bands at 321 nm in case of Fe-Salophen is attributable to n → π* intraligand transitions in the aromatic rings. The presence of an additional bands at about 300 nm in both the complexes may be due to the first allowed π → π* transition in the aromatic rings. The most important feature in the near UV-region of the Fe (III) Schiff-base complexes is a band at 505 nm in Fe-Salen and weak band at 590 nm in Fe-Salophen. These bands indicate the co-ordination of metal ion with the ligands and this can be assigned to a charge-transfer band, a transition from pπ orbitals on the phenolate oxygen atom to the half-filled dπ* orbitals of the Fe(III).[31]

The diffuse reflectance (DR) spectra of the dried cation exchange zeolites *viz* Fe-LiY, Fe-NaY and Fe-KY are shown in Figure 5.5. The DR-spectrum contains an intense band at 275 nm, a weak band at 340 nm and a broad band in the region 420-475 nm. The low intense broad peak below 500 nm can be attributed to ligand-to-metal charge transfer transition, in the present case from the oxygen ligand to a tetracoordinated Fe^{3+} ion. The weak bands between 300 and 400 nm may be due to formation of some iron oxide on the surface during calcination, while the peaks below 300 nm are due to isolated Fe^{3+} ions.[32-34] These results indicate that, in the dried sample, iron is mainly in the form of Fe^{3+} ion. It can be observed from Figure 5.5 that on increasing the size of the alkali cation the band below 300 nm shifted to lower wavelength while the lower energy band below 500 nm shifted to higher wavelength. This further indicates that the size of the alkali metal cation influences the charge transfer transitions.

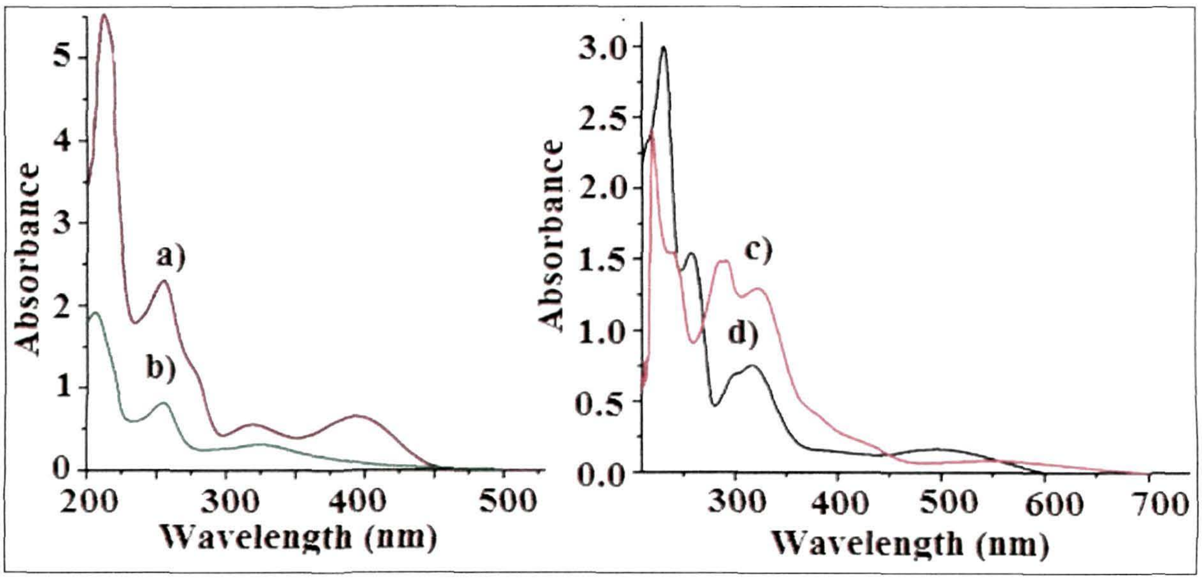

Figure 5.4. UV-vis spectra of (a) *N, N′*-bis(salicylidene)ethylenediamine (Salen) b) *N, N′*-disalicylidene-1,2-phenylendiamine (Salophen) (c) Neat Fe-Salen complex d) Neat Fe-Salophen complex.

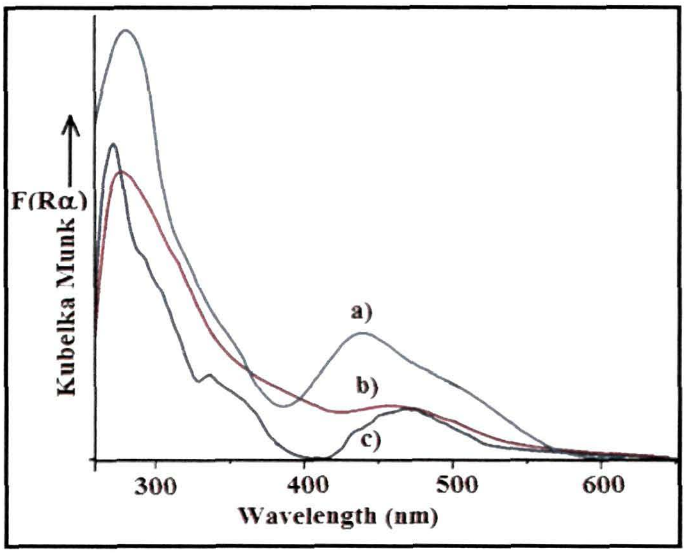

Figure 5.5. DR-spectra of ion exchanged zeolites a) Fe-LiY b) Fe-NaY c) Fe-KY

The diffuse reflectance UV-vis spectra (DRS) of the encapsulated complexes [Figure 5.6] show characteristic changes in electronic transitions. In case of the Fe (III)-Salen complex encapsulated in various ion–exchanged zeolites *viz.,* LiY, NaY and KY, the diffuse reflectance spectra show four major bands in the region 234, 290, 425-443 and 489-527 nm. The first two higher energy bands due to π → π* transitions gets blue shifted in comparison to the neat complex. The bands below and above 480 nm are due to n → π* and ligand to metal charge transfer (LMCT) transitions respectively. Most notably, both the n→ π* and the charge transfer transitions are progressively red shifted and the intensity of

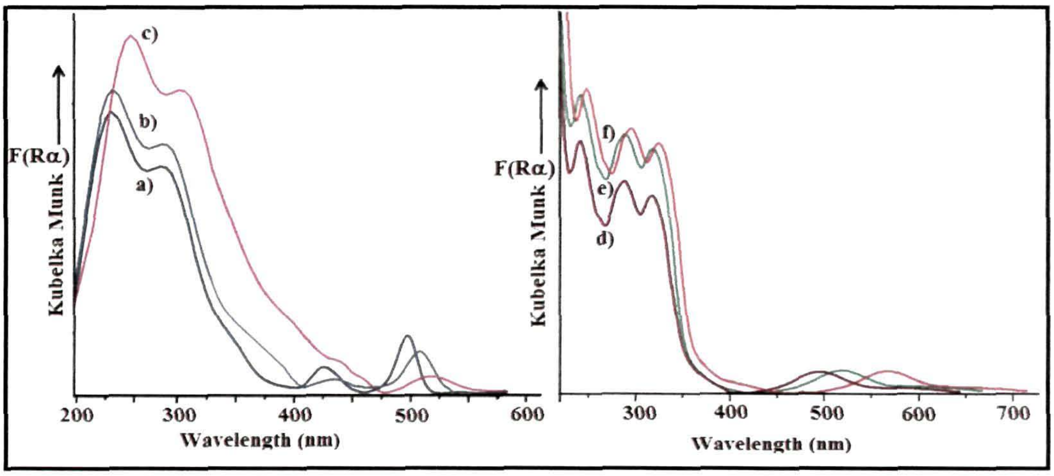

Figure 5.6. UV-vis/DRS spectra of a) Fe-Salen-LiY b) Fe-Salen-NaY c) Fe-Salen-KY d) Fe-Salophen-LiY e) Fe-Salophen-NaY f) Fe-Salophen-KY showing the red shift of the charge transfer bands with the progressive increase in size of the counterions.

the n → π* get diminished with increase in cationic size in the order Li < Na < K [Figure 5.6 (a), (b) and (c)]. Concomitantly, the width of the charge transfer bands increases with the increase in the size of the alkali metal cation, the order being Li< Na< K. The shifting of the peak to lower energy side in comparison to the neat complex suggest that after encapsulation the energy levels of the Fe-Salen complexes splits from its bary centre under the influences of the zeolite framework and changes crystal field stabilization energy and hence becomes less stable under the steric and space constraints imposed by the walls of the zeolite framework. Similar kind of influence of alkali metal cation on the charge transfer bands of methyl viologen, iron and ruthenium tris (bipyridyl) complex are reported by various authors and this type of shifting of lower and higher energy bands has been correlated with donor strength of the zeolite framework and Sanderson's electronegativity or partial charge of the framework oxygen.[11,12,35]

The DRS of Fe (III) Salophen complex encapsulated in various alkali metal cations exchanged zeolites also shows four characteristic bands at 219, 285, 317 and 510-574 nm. The bands due to π→ π* transitions are red shifted and the LMCT band above 500 nm is blue shifted corresponding to that of the neat complex. The shifting of peak to lower energy side when the Fe-Salophen complexes are encapsulated in zeolite-Y [Figure 5.6 (d), (e) and (f)] suggests a greater stability of the complexes on encapsulation inside the supercages of zeolite-Y. The possible explanations for the shifting of the peaks and significant broadening of the pπ → dπ* transition bands are (i) the ligands are distorted to some extent by the steric constrain imposed by the zeolite supercage, (ii) the ground and/or excited state of the LMCT transition is altered by encapsulation of Fe-Schiff base complexes (iii) the increase in size of alkali metal cation could masked the n → π* and pπ → dπ* transition, (iv) the increase in the electropositivity of the surrounding cation gives rise to changes in donor strength (basicity) i.e. the increase in negative charge density of the framework oxygen leading to the progressive red shift of the lower and higher energy bands .

The presence of the similar electronic transitions in the encapsulated complexes in comparison to the neat complex in solution gives evidence for the formation of complexes inside the supercage of zeolite Y. However, the shifting of peaks on encapsulation of the complexes into various cations exchanged zeolites implies that the electronic transitions are greatly influenced due to the interaction of the metal complexes with the walls of zeolite framework.

5.2.1.5. Relationship of the lower energy and higher energy band with the Framework Donor strength

Since the increase in the electropositivity of the counteraction give rise to the increase in the donor strength (basicity) of the framework, we examined the relationship between the spectral shift and the framework donor strength. For this purpose, in fact, it is necessary to get the ionization potentials of zeolite frameworks, $I_p(Z)$, as the direct measures of the framework donor strengths as in the case of small molecules. However, the corresponding values of $I_p(Z)$ are not available at this stage for zeolites Y, therefore, we used Sanderson's partial charges of the framework oxygen atoms. Sanderson's partial charges of the framework oxygen atoms for the zeolites are calculated on the basis of their chemical compositions listed in Table 5.4.

It can be seen from Figure 5.7 that for both the iron complexes encapsulated in various alkali exchange zeolites, red shift of the lower and the higher energy band indeed arises in response to the increase in the negative charge density of the framework oxygen, i.e., upon increasing the framework donor strength. The observed sharp increase in the LMCT bands upon increasing the size of the alkali cation indicates that the degree of red shift of the CT band are sensitive towards the donor strength of zeolite-Y.

Table 5.4. Type of zeolites, Sanderson's electronegativity and Sanderson's partial negative charge density on the framework oxygen ($-\delta_o$)[a]

Zeolite	Sandersons electronegativity	$-\delta_o$
Li^+-Y	2.67	0.24
Na^+-Y	2.60	0.26
K^+-Y	2.58	0.27

[a] The Sanderson's electronegativity of each M^+-exchanged zeolite S_Z was calculated according to the equation $S_Z = (S_M{}^p S_H{}^q S_{Al}{}^r S_{Si}{}^t S_o{}^u)^{1/(p+q+r+t+u)}$, where S_M, S_H, S_{Al}, S_{Si}, and S_O represent the Sanderson's electronegativities of the alkali metal, hydrogen, aluminum, silicon, and oxygen, respectively and p, q, r, t, u represent the number of the corresponding element in a unit cell, respectively. The Sanderson's partial charge of the framework oxygen (δ_o) was calculated using the equation $\delta_o = (S_Z - S_o)/(2.08\ S_o^{1/2})$. The values are taken from:J. E. Huheey, E. A. Keiter and R. L. Keiter, Inorganic Chemistry,Harper Collins College Publications, New York, 4th edn, 1993.

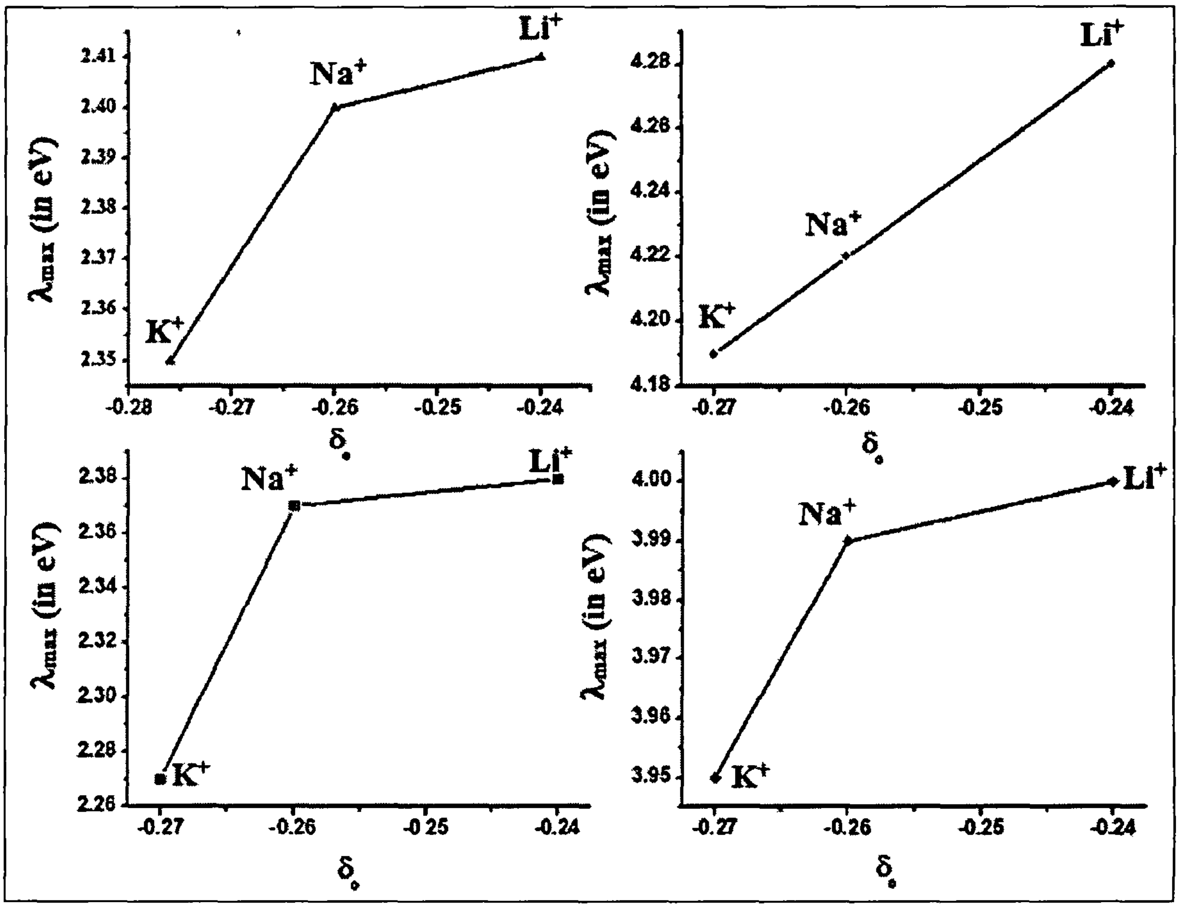

Figure 5.7. Relationship between the a) lower energy bands of encapsulated Fe-Salen b) higher energy bands of encapsulated Fe-Salen c) lower energy bands of encapsulated Fe-Salophen d) higher energy bands of encapsulated Fe-Salophen in various alkali exchanged zeolite with the calculated Sandersons partial charge of the framework oxygen of M^+Y.

5.2.1.6. ESR Study

Powder ESR spectra of neat Fe-Schiff base complexes and the encapsulated complexes are obtained with microwaves in the 9442-10000MHz region at 77 K with fields corresponding to about 50 to 500 mT. Figure 5.8 shows the ESR spectra of neat complexes and the encapsulated complexes in various alkali exchanged zeolite Y and the g-values for all the neat and encapsulated complexes are given in Table 5.5. As expected, for axially distorted octahedral Fe^{3+} ions, the broad single line having g_{II} value > 4.23 in all the cases corresponds to the low spin d^5 ion in the weak field region. Many monomeric iron (III) complexes show signal of this nature.[36,37] In case of the neat complex, the signals having $g_{II} = 2.03$ and $g_{\perp}$ value of 1.980 could probably arise from location of unpaired electrons in the organic ligands of the complex or due to the presence of impurity radicals. The hyperfine lines are not resolved in neat Fe-Salen complex even at 77 K. A similar broad signal at $g \approx 4.2$ prevails in the encapsulated complexes indicating the presence of low-spin

Table 5.5. ESR analysis of the neat and the encapsulated iron complexes.

Samples	g_{II}	$g_{\perp}$	g_{II}
Fe-Salen	4.24	2.03	1.986
Fe-Salophen	4.24	2.02	1.978
Fe-Salen-Li Y	4.22	2.147	2.110
Fe-Salen-Na Y	4.21	2.120	2.140
Fe-Salen-KY	4.20	2.107	2.180
Fe-Salophen-Li Y	4.23	2.148	2.122
Fe-Salophen-Na Y	4.22	2.132	2.150

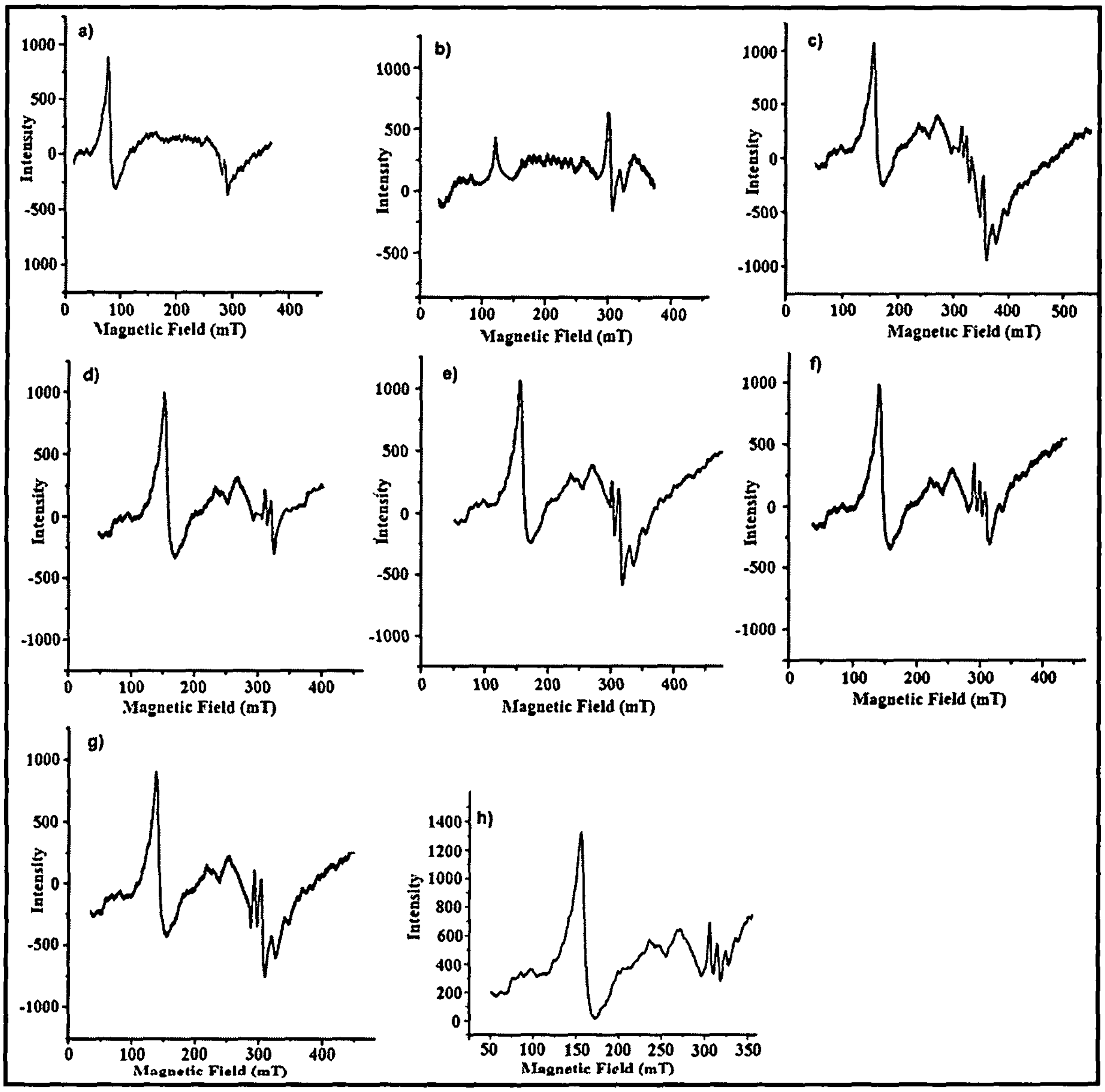

Figure 5.8. Powder ESR spectra of a) Neat Fe-Salen complex b) Neat Fe-Salophen complex c) Fe-Salen-LiY, d) Fe-Salen-NaY, e) Fe-Salen-KY, (f) Fe-Salophen-LiY, g) Fe-Salophen-NaY, h) Fe-Salophen-KY, at 77 K.

iron (III) configurations in them. In the case of encapsulated Fe-Schiff base complexes the hyperfine splitting are resolved and the number of hyperfine lines are more in case of the Shiff-base complexes encapsulated in Li^+ ion exchanged zeolites. The anisotropy in the g-values suggests that the Fe-complexes get rhombically distorted under the influence of zeolite matrix. It can be seen from Table 5 that the g_{II} values increases with the increase in the size of the alkali exchanged cations and $g_{\perp}$ values gradually decreases. The difference in the g-values between the neat and the encapsulated complexes gives a clear indication for formation of Fe-complexes inside zeolite.

5.2.1.7. Cyclic Voltammetry Study

Cyclic voltammetry provides information on the nature of intra-zeolite complexes that may not be readily apparent from spectroscopic studies. Zeolites are basically insulator, so the encapsulation of transition metal complexes makes these molecular sieves to show redox behaviour if they are encapsulated inside the cavities or bound to the surfaces within zeolite lattice. Shaw et al.[38] first proposed two possible mechanism – intrazeolite and extrazeolite mechanism for electron transfer associated with encapsulated transition metal complexes within the supercage of zeolite and surface bound metal complexes, respectively based on zeolite modified electrodes (ZMEs). Although, these mechanistic assignments are controversial, there are various reports demonstrating the redox behaviour of transition metal complexes encapsulated in zeolite cavities.[39-41]

Bedioui et al.[42,43] have synthesized metal Schiff base complexes inside the supercages of zeolite (ship-in-a-bottle). They have concluded that the electro active species are reduced or oxidized within the supercages of zeolite-Y (intrazeolite electron transfer). Shaw and co-workers[44,45] have studied the electron transfer mechanism of methyl viologen (MV^{2+}) exchanged zeolite-Y. Rolison[46] and Baker et al.[47] showed that the electron transfer takes place at the zeolite-solution interface (extrazeolite electron transfer). Calzaferri et al.[48] studied the potential for strong acidity. Very recently Zhang et al. studied the electrochemical behaviour of M (Co, Fe, Mn) (SALEN) complexes as a component of modified glassy carbon electrode.[25]

So relying on the ZMEs to obtain information for zeolite encapsulated transition metal complexes we have studied the redox activity of the Fe (III) Schiff base complexes and the effect of counterions on the redox behaviour of these complexes. Initially we study the electrochemical behaviour of the synthesized neat iron complexes using 0.1 M TBAP as supporting electrolyte in DCM solution and then compared these with the encapsulated complexes using modified glassy carbon electrode.

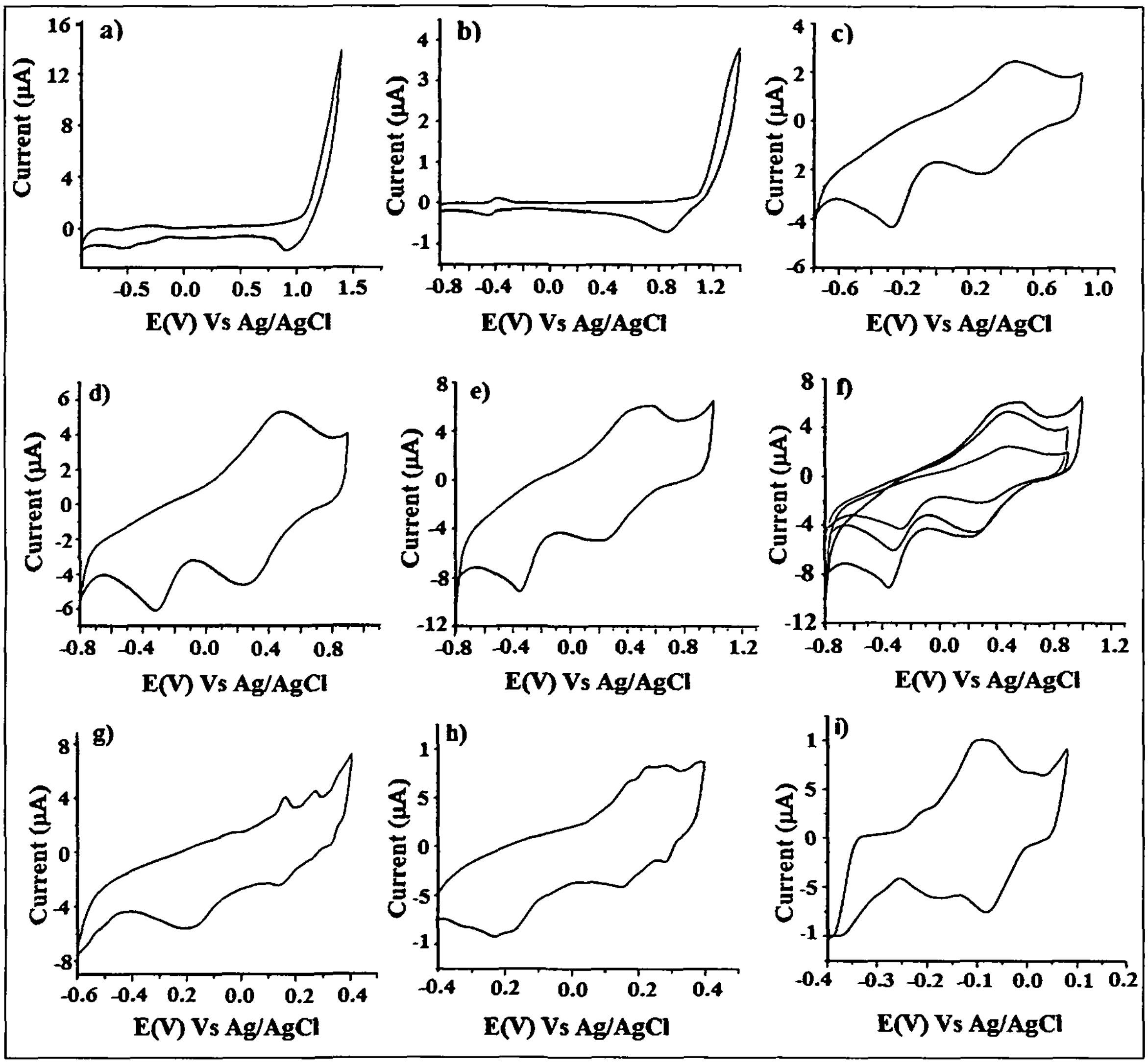

Figure 5.9. Cyclic Voltammograms of a) Neat Fe-Salen b) Neat Fe-Salophen complexes taken in DCM using 0.1M TBAP as supporting electrolyte, c) Fe-Salen-LiY, d) Fe-Salen-NaY, e) Fe-Salen-KY, f) Overlay of (c) (d) and (e) (g) Fe-Salophen-LiY, h) Fe-Salophen-NaY, i) Fe-Salophen-KY, taken as a component of ZME in DCM using 0.1M TBAP as supporting electrolyte.

5.2.1.7. a) Electrochemistry of the neat Fe (III) Schiff base (Salen, Salophen) complexes

A typical cyclic voltammogram of the Fe (III)-Salen and Salophen are shown in Figure 5.9 (a) and (b), respectively. The Fe (III)-Salen complex shows a quasi-reversible peaks with a cathodic reduction peak at -0.461V corresponding to the one electron reduction process represented as $[Fe^{III} (L)_2 X]^{2+} + e^- \rightarrow [Fe^{II} (L)_2]^{2+} + X^-$. The reduction of the Fe (III) complex results in the loss of its axial ligands, since the electron is added to the antibonding d_z^2-orbital. Upon reversal of the scan direction, the Fe (II) complex is re-oxidized at -0.411 V. In case of the Fe (III)-Salophen, the cathodic reduction peak occurs at -0.526 V and the corresponding anodic oxidation at -0.335 V. This shows that the redox behaviour of this complex is quasi-reversible. In addition to the redox couple both the Fe-Salen and Fe-Salophen complex shows an additional cathodic peak at 0.847 V and 0.898 V, respectively. The difference in the electrochemical behaviour of the two complexes indicates that the effect of ligand substitution on the redox potential of complexes.

5.2.1.7. b) Electrochemistry of the encapsulated Fe (III) Schiff base (Salen, Salophen) complexes in various zeolites

The cyclic voltammogram of the encapsulated complexes in various cation exchanged zeolites are shown in Figure 5.9 (c, d, e, g, h and i) and E° values are given in Table 5.6. Several interesting changes are found in the redox behaviour of the encapsulated complexes: i) the redox signals are broad and persist for an interval of 30-60 min ii) the peak potentials are shifted as compared to the neat complexes as can be seen from Table 5.6.

Table 5.6. Oxidation and reduction peak potential values (in V) for neat and the encapsulated Fe-Schiff base complexes.

Samples	E^1_{oxd}	E^2_{oxd}	E^1_{red}	E^2_{red}	E^{av}_{oxd}	E^{av}_{red}
Fe-Salen	-0.411	-	-0.461	0.847	-	0.193
Fe-Salophen	-0.335	-	-0.526	0.898	-	0.186
Fe-Salen-Li Y	0.471	-	0.301	-0.273		0.014
Fe-Salen-Na Y	0.465	-	0.237	-0.312		-0.037
Fe-Salen-KY	0.567	-	0.217	-0.352		-0.067
Fe-Salophen-Li Y	0.162	0.274	0.323	0.141	0.218	0.232
Fe-Salophen-Na Y	0.225	0.283	0.235	0.156	0.254	0.195
Fe-Salophen-K Y	-0.206	-0.087	-0.080	-0.176	-0.147	-0.128

In case of Fe-SalenY complex encapsulated in various zeolites show a reversible peaks and an additional irreversible cathodic peak. The reversible peaks are associated with the one electron $Fe^{III} \rightleftharpoons Fe^{II}$. The additional cathodic peak may be due to the partially associated Fe^{III} (Salen)-species. Bedioui et al.[43] also reported several additional peaks in the cyclic volltammogram of {Co (Salen)} NaY ZME in DMSO or CH_3CN when compared to homogeneous counterparst. It can be seen from Table 5.6 and Figure 5.9 that significant differences in the cyclic voltammograms (peak potential, peak shapes, and relative integrated current areas) occur as the size of alkali cations shifted the reduction potential to more negative values. One possible reason is that during the exchange process some of the alkali metal cations diffuse into the cavities and can reside in the channels that exist in the lattice of zeolites and influences the intra-zeolite electron transport.

In case of the iron (III) -Salophen complex encapsulated in various zeolites two quasi- reversible peaks are obtained. The first cathodic wave is due to the reduction of Fe (III) to Fe (II) and second cathodic peak is due to the reduction of Fe (II) to Fe (I). Upon reversal of the scan, it shows the corresponding oxidation peaks i.e. from Fe (I) to Fe (II) and Fe (II) to Fe (III). The peaks become broadened and yielded well defined cyclic voltammogram of the encapsulated complexes as the size of the cation increases. Most importantly the average E_{red}^{av} values are shifted to more negative values in both the encapsulated complexes as the counter cation size increases. The alternation of the redox potential and the shifting of the peak potential towards more negative values as size of the cation increases indicates that the iron becomes stabilized in its Fe^{3+} state when encapsulated into the zeolites i.e. zeolite-Y exchanged with large alkali metal cation favours the oxidation of Fe (I) to Fe (II) and Fe (II) to Fe(III).

The alternation in the redox potentials of iron Schiff base complexes encapsulated in various zeolites suggests that complex suffers space constraint imposed by the zeolite matrix leading to geometrical distortion thereby changing the crystal field stabilization energy and the peak potentials in comparison to the neat complexes.

5.2.1.8. SEM Study

SE micrographs of Fe-Salen-Y and Fe-Salophen-Y taken before Soxhlet extraction and that of Fe-Salophen-Y taken after Soxhlet extraction are shown in Figures 5.10 (a), (b) and (c), respectively as a representative case. In the SEM taken before purification, the complexes deposited on the external surface are visible. In the SEM of finished products, no surface complexes are seen and the particle boundaries on the external surface of zeolite are clearly distinguishable. This is much clearer from the surface plot shown in Figure 5.11 (a), (b) and (c), where the white portion in Figure 5.11(b) indicates the surface occupied by extraneous complexes or the uncomplexed ligands. The surface plot of SE-micrograph taken after Soxhlet extraction showed no such white portion indicating the efficiency of purification procedure to effect complete removal of extraneous complexes, leading to well-defined encapsulation in the cavity. Moreover, no crystalline patterns are seen for the encapsulated complexes: this might be due to their fine distribution in the lattice.

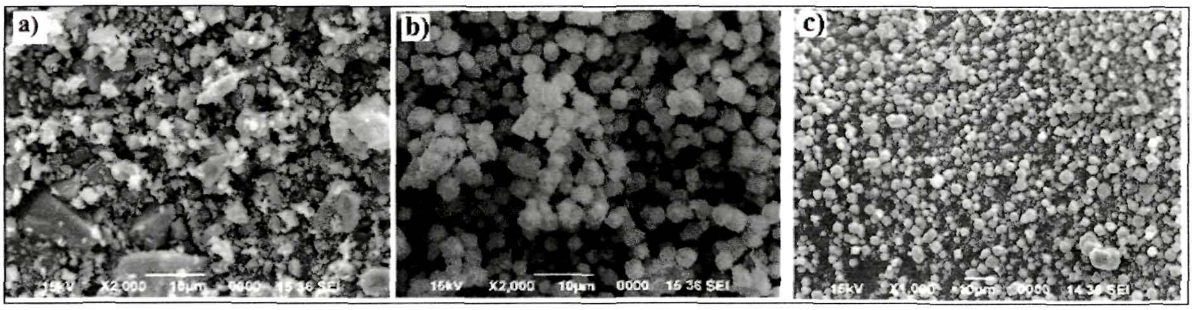

Figure 5.10. Typical SE micrographs of a) encapsulated Fe-Salen complex b) encapsulated Fe-Salophen complex before Soxhlet extraction c) encapsulated complexes after Soxhlet extraction.

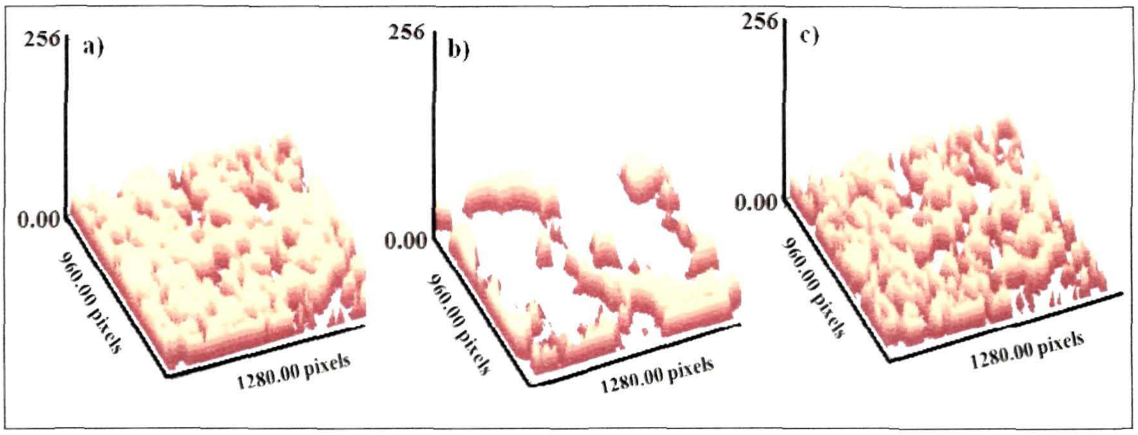

Figure 5.11. Surface plot of a) Pure NaY, b) Encapsulated Fe complexes before Soxhlet extraction, c) Encapsulated Fe complexes after Soxhlet extraction. X and Y axis represents width and height, respectively.

5.2.1.9. TGA Study

The TG patterns of neat Fe-Schiff complexes and encapsulated Fe Schiff base complexes (Salen and Salophen) are displayed in Figure 5.12. The comparison of thermo-gravimetric analysis for Fe-Schiff base complexes and encapsulated Fe-Schiff base shows that neat Fe-Salen complex has three weight loss steps at about 96, 322 and 448 °C while the Fe-Salophen complex shows four weight loss steps at about 116, 200, 402 and 500 °C. On the basis of the weight changes, the first weight-loss step in both neat complexes corresponds to the loss of water molecule as an endothermic phenomenon. The second weight loss at 200 in case of Fe-Salophen complex may be related to the loss of Cl_2. There is a sharp weight change at 322 °C and at 402 °C in case of Fe-Salen and Fe-Salophen which are attributed to loss of Salen and Salophen groups, respectively. There is weak peak at 448 °C and at 500 °C in case of both the complexes, which may be due to sublimation of part of Fe_2O_3. However, for the corresponding encapsulated complex the weight loss extend up to 560 °C, which indicates the thermal stability is greatly enhanced and there is no peak at 100-120 °C indicating the absence of water of crystallization. Further, it is observed that as the size of the alkali cation increases the thermal stability of the encapsulated complexes increases. This gives another piece of evidence for the inclusion of Fe Schiff base complexes in various alkali exchanged zeolite-Y. On the basis of thermal analysis data, we may conclude that zeolite encapsulated Fe-Schiff base complexes may be treated thermally without any significant decomposition.

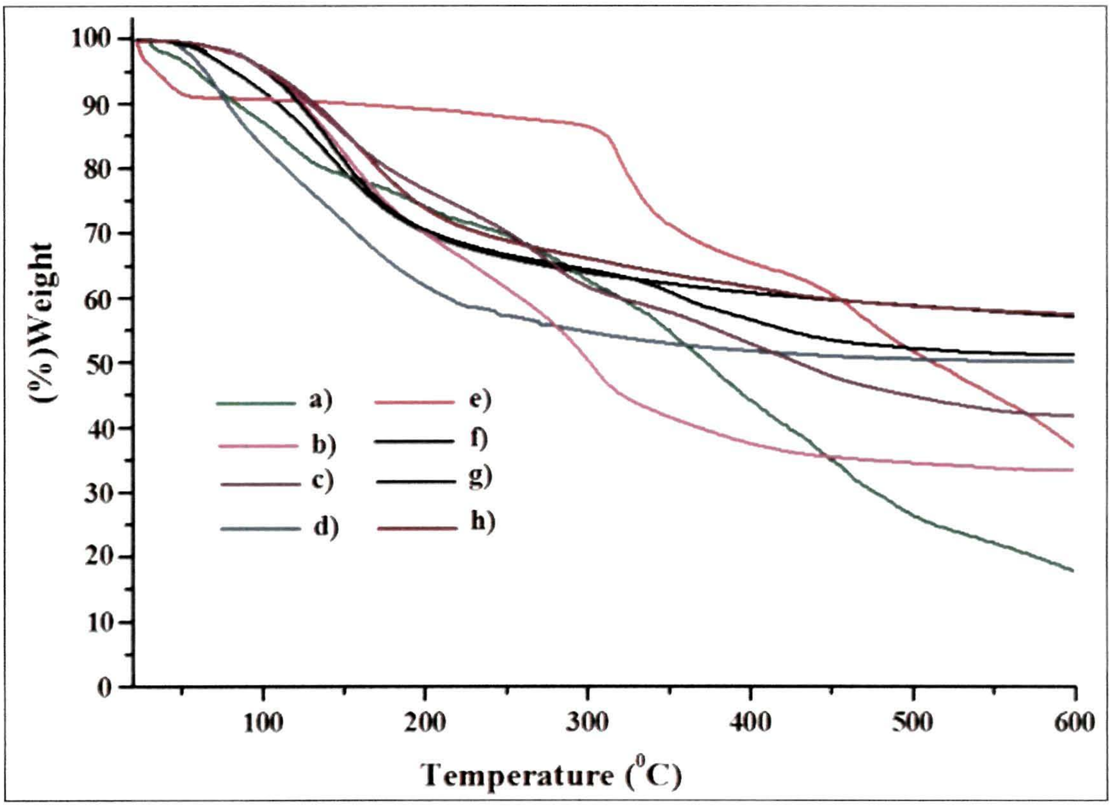

Figure 5.12. Thermogravimetric analysis (TGA) patterns of a) Neat Fe-Salen, b) Fe-Salen-LiY, complexes c) Fe-Salen-NaY, d) Fe-Salen-KY. e) Neat Fe-Salophen f) Fe-Salophen-LiY, (g) Fe-Salophen-NaY, h) Fe-Salophen-KY

5.2.2. Theoretical Calculation

The selected bond lengths and bond angles obtained from VWN/DN level calculations for the neat and the encapsulated complexes are presented in Table 5.7. The geometrical parameters are relatively in good agreement with the reported experimental values.[49,50] However, the geometrical parameters for the encapsulated complexes show slight deviations from those of the neat complexes. The change in the bond length and bond angle on encapsulation may be attributed to the influence of the zeolite framework. The valence electrons in zeolites are distributed all over the framework atoms as a partially delocalized electron cloud. At a relatively short distance between the complex and the walls of the zeolite cavities, the electron-electron repulsion will be operative, which will influence the structural and electronic properties of the encapsulated complexes. For all the considered complexes, the pattern of the occupied and the unoccupied orbitals are qualitatively similar. The energies of the HOMO and LUMO for the neat iron (III) Schiff base complexes and those encapsulated in zolite-NaY are represented as a comparative energy profile diagram in Figure 5.13.

Table 5.7. Selected bond length (in Å) and bond angles (in degree) of the optimized neat and encapsulated Fe-Schiff base complexes.

Bond length	$[Fe\text{-}SalenCl]^{2+}$	Fe-SalenY	$[Fe\text{-}SalophenCl]^{2+}$	Fe-SalophenY
Fe-O_1	1.79	1.776	1.80	1.840
Fe-O_2	1.81	1.839	1.79	1.858
Fe-N_1	1.89	1.920	1.87	1.950
Fe-N_2	1.84	1.830	1.89	1.970
Fe-Cl	2.09	-	2.11	-
Bond Angles				
$\angle O_1$-Fe-O_2	87.51	83.45	86.13	75.53
$\angle O_1$-Fe-N_1	88.77	89.28	92.51	86.44
$\angle O_1$-Fe-N_2	124.45	119.57	165.97	120.77
$\angle O_2$-Fe-N_1	173.41	169.74	157.42	145.43
$\angle O_2$-Fe-N_2	92.73	94.27	91.38	86.54
$\angle N_1$-Fe-N_2	84.88	82.98	84.48	77.62
$\angle O_1$-Fe-Cl	130.54	-	101.26	-
$\angle O_2$-Fe-Cl	95.65	-	105.41	-
$\angle N_1$-Fe-Cl	90.89	-	96.95	-
$\angle N_2$-Fe-Cl	104.72	-	92.69	-

It can be seen from Figure 5.13 that the energies of both the HOMO (-12.65eV) and the LUMO (-12.22eV) for the neat $[Fe(Salophen)_2]^{3+}$ complex lie higher in energy in comparison to the $[Fe(Salen)_2]^{3+}$ (E_{HOMO} = -12.97eV and E_{LUMO} = -12.489eV). Upon encapsulation, the HOMO and LUMO levels gets destabilized and the increasing order of

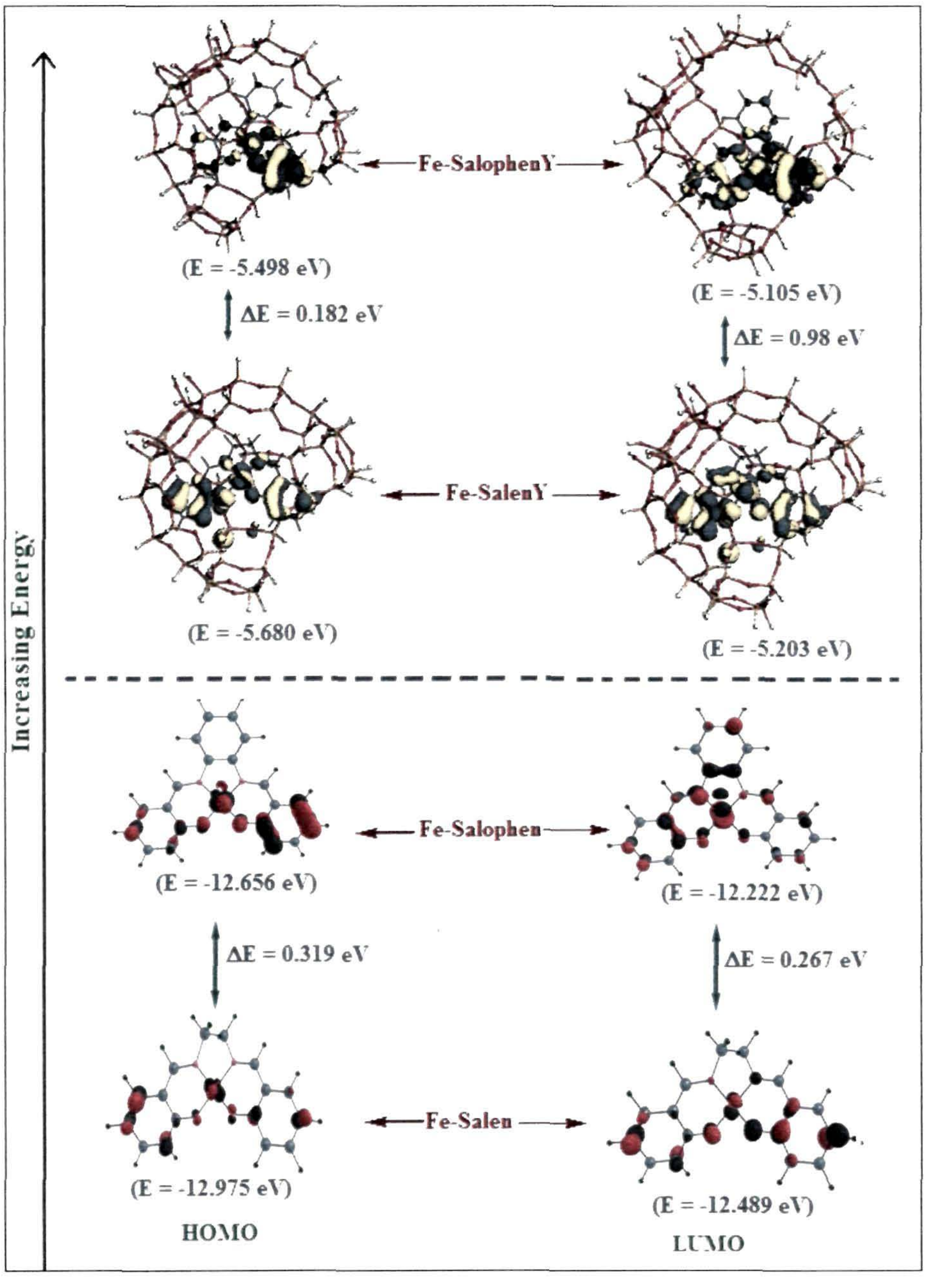

Figure 5.13. Schematic representation of the HOMO and LUMO level of the neat and the encapsulated Fe-Schiff base complexes. Orbitals below the dotted line represents the positions of the HOMO (left hand side) and LUMO (right hand side) of the neat complexes in increasing order of energy and above the dotted line represents the energies of the frontier orbitals of the corresponding encapsulated complexes.

energies (for both HOMOand LUMO level) is Fe-Salophen-NaY > Fe-Salen-NaY > Fe-Salophen > Fe-Salen. This change in the energies of the frontier orbital can be further correlated to the reducing ability Fe(III) or to the oxidation of Fe(III) to Fe(IV) by molecular oxygen which is reported to be the rate determining step in oxidative coupling reaction of 2-napthol to BINOL using molecular oxygen (discussed below). Since the

HOMO of the Fe-Salophen complexes comparatively lies higher in energy than Fe-Salen, it will have higher tendency to get oxidized. In contrast, since upon encapsulation the HOMO is much higher-lying in both the systems in comparison to the neat complexes, they will have higher tendency to get oxidized and enhances the rate of the reaction. And the reactivity of Fe-SalophenNaY will be more in comparison to Fe-SalenNaY system and this result is in accordance with our experimental results. Further, from Table 5.8 it can be seen that the global hardness of Fe-Salophen-NaY is less in comparison to its solution analogue and other complexes has higher value of global softness (S). According to maximum hardness principle[51,52] and minimum polarizability principle (MPP)[53], the hardness measures the stability and softness (polarizability) measures the reactivity. Thus, it can be said that among the four systems the Fe-Salophen complex encapsulated in NaY will show higher reactivity with minimum hardness and maximum softness.

Table 5.8. Calculated energies of HOMO and LUMO levels (in eV), global hardness (η, in eV) and softness (S, in eV)

Complexes	E_{LUMO}	E_{HOMO}	η	S
Fe-Salen	-12.489	-12.975	0.243	2.057613
Fe-SalenY	-5.203	-5.680	0.238	2.096436
Fe-Salophen	-12.222	-12.656	0.217	2.304147
Fe-SalophenY	-5.105	-5.498	0.196	2.544529

Table 5.9. Hirshfeld population analysis of Fukui functions for the neat and the encapsulated complexes.

Selected Atoms	$[\text{Fe-Salen}]^{3+}$		$[\text{Fe-Salophen}]^{3+}$		Fe-Salen-NaY		Fe-Salophen-NaY	
	f_K^+	f_K^-	f_K^+	f_K^-	f_K^+	f_K^-	f_K^+	f_K^-
O_1	0.032	0.031	0.026	0.025	0.011	0.010	0.018	0.017
O_2	0.030	0.029	0.024	0.024	0.016	0.016	0.012	0.012
Fe	0.032	0.031	0.020	0.019	0.012	0.012	0.008	0.007
N_1	0.013	0.013	0.010	0.010	0.008	0.008	0.010	0.009
N_2	0.014	0.014	0.012	0.012	0.007	0.007	0.007	0.007

The Hirshfeld population analysis (HPA) of the Fukui functions (f_K^+ and f_K^-) calculated at the same level of theory for the metal atom and those co-ordinated to it are given in Table

5.9. It can be seen that the values of the Fukui functions at the metal centre decreases in the order Fe-Salen> Fe-Salophen> Fe-SalenY> Fe-SalophenY. Some of the reported calculations have shown that a minimum Fukui function and maximum net charge site is preferred for hard-hard interaction whereas a soft-soft interaction is preferred at the site with maximum Fukui function.[54-56] Among our four systems, the central iron atom in Fe-SalophenY complex possesses maximum positive Mulliken and Hirshfeld charges calculated at VWN/DN level of theory and minimum value of the Fukui function. The order of positive Mulliken and Hirshfeld charges at the central atom are Fe-SalophenY (0.92) > Fe-SalenY (0.85) > Fe-Salophen (0.55) > Fe-Salen (0.53) and Fe-SalophenY (0.25) > Fe-SalenY(0.24) > Fe-Salen (0.20) > Fe-Salophen (0.19) respectively. Thus, it indicates that the central iron atom in Fe-SalophenY complex with maximum positive charge and minimum value of Fukui function is the most preferential site for interacting with hard species. This enhancement of hard-hard interaction on encapsulation into zeolite framework also reflects the higher catalytic activity. The catalytic conversion of 2-napthol to BINOL proceeds via the co-ordination of naptholate ion at the vacant site of Fe(III)-Schiff base complex and it involves a hard –hard interaction. Therefore, the first step i.e. the interaction of naptholate ion with the central metal atom to form a penta-cordinated iron complex is much more preferred in Fe-SalophenY.

5.3. Catalytic Activities

5.3.1. Oxidative Coupling of 2-napthol by neat and zeolite encapsulated Fe-Schiff base complexes

The oxidative coupling of 2-napthol is a representative reaction mode for direct synthesis of 1,1′-binapthol (BINOL) whose optically pure derivatives are regarded as versatile chiral auxiliaries and ligands in asymmetric synthesis. However, these substances remain largely unstudied because of their difficulties in synthesis. Most of the recently published highly enantioselective syntheses of BINOL and its derivatives are based on naphthol coupling catalyzed by chiral complexes containing one or two metal centre(s) *viz.*, vanadium, iron or copper.[26,57-60] The formation of a self dimerized chiral assembly of vanadium complexes on a SiO_2 surface is also reported to promote the enantioselective naphthol coupling. And the search continues for new heterogeneous catalyst capable of carrying out the selective oxidative coupling of 2-napthol.

We found that the encapsulated achiral iron Schiff base complex within zeolite-Y cages creates a catalyst that allows highly selective transformation of β-naphthol to BINOL under aerobic condition without any additive. The catalytic activities of the encapsulated Fe-complexes and their homogeneous analogues in the oxidative coupling of 2-napthol are shown in Table 5.10. The catalytic activities of the complexes are tested in different solvents like dichlromethane (DCM), dimethylformamide (DMF) and toluene refluxing at 30 °C. Most of the complexes showed very poor or no catalytic activity in these solvents at 30 °C. However, on increasing the temperature up to 60 °C in toluene, the neat complexes give the racemic mixture with moderate yield. The Fe -Salophen complex shows high selectivity and gives better yield compared to the Fe-Salen complex. Under the same conditions the catalytic activity of the encapsulated complexes are tested for oxidative coupling of 2-napthol. It can be seen from the data given in Table 10 that the encapsulated Fe-Schiff base complexes give high percentage yield and selectivity in comparison with the neat complexes. Increasing the amount of catalyst decreased the yield of the desired product with more by-products. Therefore, the reaction is performed with 10 mg of the catalysts. Among all the complexes, Fe-Salophen-KY shows good conversion of 2-napthol to BINOL. Blank experiments carried out without the catalyst under identical experimental conditions do not produce BINOL indicating the participation of the iron complex in the reaction path. The use of stoichiometric amount of complexes as oxidizing agent under nitrogen atmosphere do not yield the product indicating that oxygen is essential for the reaction. The time required for this catalytic conversion is found to be less in case of the encapsulated complexes in comparison to the corresponding neat complexes. The desired product is isolated by column chromatography, enatioselectivity are obtained by HPLC analysis on a chiral stationary phase column (Daisel Chiralcel AS-H) and the optical purity are determined by chiroptical comparison with the literature value. The iron –exchanged zeolites do not show any catalytic activity up to 6-days. Oxidative coupling of 2-napthol with the neat complexes resulted in the formation of racemic BINOL only. Further, we could isolate only 12% of the desired product in case of the reaction catalysed by Fe-salen complex. This may be due to chelate formation which remains bound with the catalyst (Fe-Salen) till the coupling reaction is completed. However, oxidative coupling of 2-napthol with Fe-Salophen and Fe-Salen complex encapsulated in potassium exchanged zeolite under similar conditions results 40% and 24% ee. This enhancement of selectivity towards the R-conformation on encapsulation of the complexes into various alkali exchanged zeolite may be due to the combined action of spatial confinement and metal-ion coordination of the substrate within the zeolite supercage both of which greatly reduce the freedom of the substrate and entropically manipulate the stereochemical outcome. It may be noted herein that during catalytic conversion of 2-napthol to BINOL, some mass losses have occurred. The high mass loss may be due to strong adsorption of the product i.e. BINOL on the metal complex and on the surface of the zeolite catalyst either through complexation with potential surface atoms like iron, since BINOL has a very strong affinity of chelate formation or through entrapment into the pores of the catalysts. The complexation of the substrate (naphthol) with the surface catalyst metal atoms also cannot be ruled out. Some unidentifiable products could have also been formed and held on the surface. This along with chelate formation[61,62] accounts for the mass imbalance that occurs during catalytic conversion of 2-napthol to BINOL.

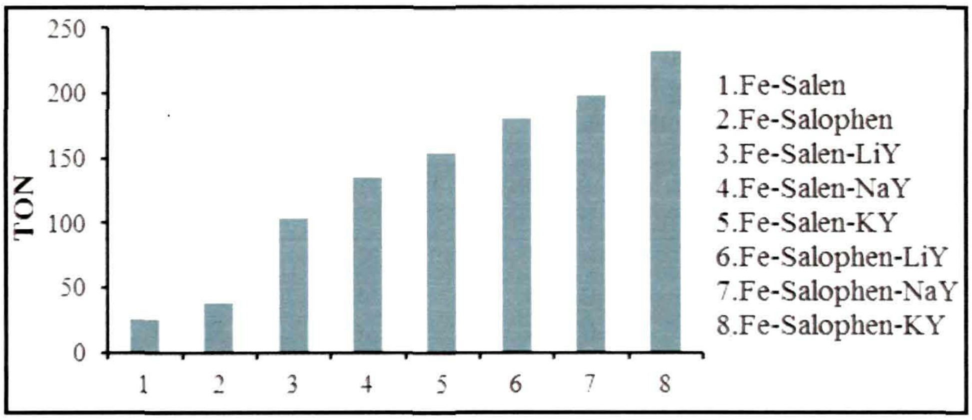

Figure 5.14. TON for the catalytic oxidative coupling of 2-napthol using various iron(III) Schiff-base complexes.

The turn over number (TON) increases on encapsulation of the iron Schiff base complexes into different cation exchanged zeolites. It can be seen from Figure 5.14 that the TON increases as the size of the alkali cation increases and has been found to be maximum in case of the coupling reaction catalysed by Fe-Salophen-KY (232), which is almost 6 and 9 times higher than the neat Fe-Salen and Fe-Salophen complexes, respectively (Table 5.10). This increase in the TON further reflects that the zeolite matrix provide an environment for achieving particular reactions by varying the exchangeable alkali metal cations.

Among the homogeneous catalysts, the complex bearing phenyl group shows the higher catalytic activity. This is in accordance with our cyclic voltametric study and theoretical study where we found that the second half –wave reduction potential of the Fe-Salophen complex to be more negative and higher lying HOMO than the Fe-Salen. In contrast to the neat complexes the catalytic conversion of the encapsulated complexes is found to be more and interestingly the activity increases with increase in size of the counter ion, as can be seen from the data in Table 5.10. This tendency is corroborated with shifting

Table 5.10. Results of the oxidative coupling of 2-naphthol in toluene at 60 °C under aerobic condition.

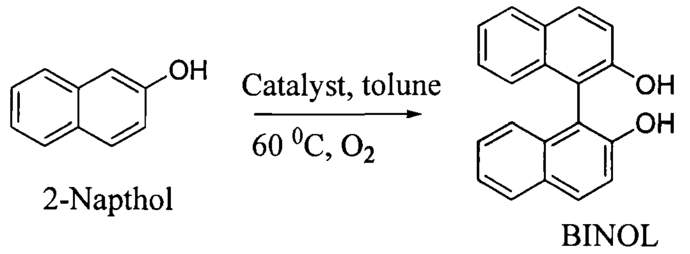

Catalysts 1. NaY 2. Fe-Salen 3. Fe-Salophen
4. Fe-Salen-LiY 5.Fe-Salen-NaY 6. Fe-Salen-KY
7. Fe-Salophen-LiY 8. Fe-Salophen-NaY
9. Fe-Salophen-KY

Catalyst	Time	% Yeild[a] in mmol	Amount of Fe in (mmol)[b]	% Conv.	R:S(%)[d]	TON
1	72	Nil	-	Nil	-	-
2	**72**	**0.6**	0.023	**50**	50:50	26
3	**66**	**0.9**	0.023	**56**	50:50	39
4	**28**	1.01	0.0097	**70**	50:50	104
5	**24**	1.32	0.0098	**84**	54:46	135
6	**21**	1.51	0.0098	**89**	62:38	154
7	**22**	1.77	0.0098	**86**	52:48	181
8	**20**	1.91	0.0096	**92**	56:44	199
9	17	2.26	0.0097	97	70:30	232

The reactions were carried out in toluene with catalyst (10 mg) on a 5 mmol scale under aerobic conditions. [a] Determined by chromatographic separation. [b] Amount of Fe-atom in mmol present per 10 mg of catalyst. [c] Conversion refers to fraction of starting material consumed in the reaction. [d] Determined by chiroptical comparison with the literature value and HPLC analysis on a chiral stationary phase column (Daisel Chiralcel AS-H).

of the E_{red}^{av} reduction potential towards more negative values. And it has been observed from voltammogram of the encapsulated complexes in various alkali exchanged zeolites that as the size of cation increases, electron flow is perturbed and influences the peak potential which in turn affects the catalytic activity of the encapsulated complexes. The values of the average reduction potential of the neat is close to that of the molecular oxygen. So the reduction of molecular oxygen and consequently the oxidation of Fe (III) to Fe (IV) which is considered to the rate determining step in oxidative coupling reaction of 2-napthol in presence Fe-Salen complex as catalyst is slow. Whereas in case of the encapsulated complexes the reduction potential lies below the reduction potential of molecular oxygen and it becomes more negative as the size of the alkali metal cation becomes more electropositive. Hence, the reduction of molecular oxygen in presence of Fe-Schiff base complex encapsulated in K^+ ion exchanged zeolite-Y becomes faster and shows better catalytic conversion in comparison to the neat complexes and its counter partners. So it can be said that the catalytic activity of the iron Schiff base complexes towards the oxidative coupling of 2-napthol can be affected by tuning the redox potential of the catalyst.

5.3.2. Influence of alkali metal cation on catalytic activity of encapsulated complexes

One of the main features of Faujasite-type Y zeolites is the charge-compensating alkali/alkaline-earth metal ions that occupy the three types of positions I, II and III (NaY with a Si/Al ratio of 2.4 has 55 metal ions per unit cell). Type I metal ions are generally too deeply buried within the sodalite cages to interact with the guest molecule, thus, only Type II and Type III metal ions are readily accessible. The metal ions are hydrated under ambient condition and the water molecules are generally located in the cages, cavities and channels of the zeolite. When the water is removed at elevated temperature, organic guest molecules may be caged within these voids and the metal ions abandon their original position to bind with the organic occupant. The binding interaction depends on the charge density of the metal ion (i.e. the higher its charge density, the stronger the binding).[63]

The size of the alkali metal cation influences the catalytic properties of the encapsulated complexes mainly in three ways: i) first, the interaction of the alkali metal cation with the phenyl ring of the 2-napthol. The ability of cations to interact with π-systems, especially phenyl rings, has been implicated in a number of important processes[64]and is recognized as a powerful conformation-controlling tool in synthetic organic chemistry (e.g., use of Na^+ cation in NaY zeolite as conformational recognition sites for chemoselective hydroperoxidation of alkenylarenes[65] or as activation sites for aldehyde derivatives[66]) due to its strength several times greater than other interactions, such as hydrogen bonding and van der Waals force. Very recently Kuwahara et al.[67] has reported for the predominance of cation-π interaction on the significant enhancement of catalytic oxidation of cyclohexene catalysed by various alkali metal cation functionalized titanosilicate molecular sieves. To clarify the intricate cation-guest interaction we carried out DFT calculation at VWN/DN level to find out the interaction energy. It has been found that the interaction energy decreases as the size of the cation increases i.e K^+-2napthol (-24.18 kcal/mol) < Na^+-2napthol (-31.93 kcal/mol) < Li^+-2napthol (-42.45 kcal/mol). Based

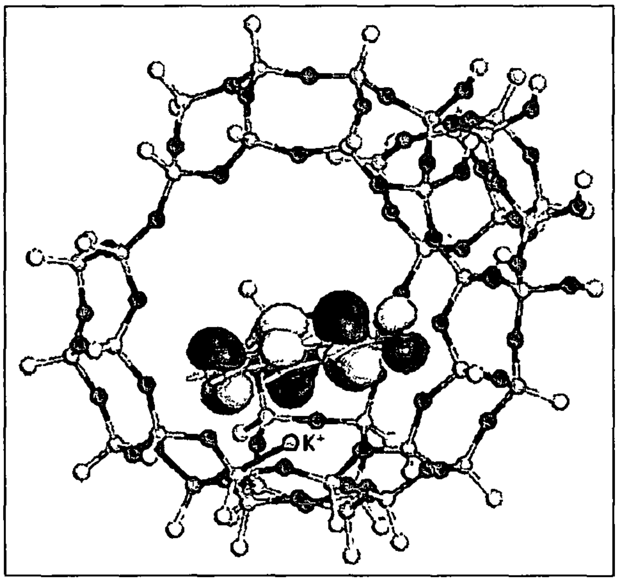

Figure 5.15. Positions of HOMO orbital in a supramolecular system consisting of a alkali metal cation (K^+), 2-napthol and the zeolite framework.

on this the adsorption energy (- ΔH_{ads}) are calculated from the total energy of a system consisting of 2-napthol, an alkali metal cation (herein we consider only Li^+ and K^+) and the zeolite framework. We found that the adsorption energy in case of K^+-exchanged zeoliteY (39.17 kcal/mol) is less in comparison to the Li^+-exchanged zeolite (42.35 kcal/mol). Moreover, it can be seen from Figure 5.15 that the HOMO is fully concentrated on the phenyl ring of 2-napthol and no overlapping occurs between orbital of the cation, K^+. This suggests that the 2-napthol is stabilized within the zeolite cages in presence of the alkali cation via the electrostatic interactions. On the basis of the experimental and computational results, we can attribute the enhancement of catalytic activity to weak cation-π interactions between heavier alkali metal cations and adjacent 2-napthol molecules which improve the diffusibility of napthol molecules within the micropores, contrarily, lighter alkali metal cations hinder the diffusion due to a strong cation-π interaction. ii) Secondly, it influences the redox properties of the encapsulated complexes which in turn influence the approach of molecular oxygen and consequently its reduction. iii) Lastly, the size of the metal cation influences the extent of asymmetric induction in the oxidative coupling of 2-napthol to BINOL and is found to be highest in the KY zeolite. This may be attributed to the available space in the zeolite supercage for the reactant molecule such that a smaller metal ion suffices. This stereoselectivity behaviour is a reflection of the spatial confinement imposed on the guest molecule within the zeolite supercage which forces the complexes to attain stepped conformation once the complex gets oxidized by molecular oxygen. On the other way one can say that larger the size of the alkali metal tighter the fit, the higher the asymmetric induction.

The encapsulated metal complexes show many advantages over their homogeneous counterparts. First, the catalytic activities of Fe-Schiff base complexes are found to be better than that of their respective non encapsulated complexes (Table 5.10). Secondly, the pure complexes dimerizes as it changes colour form dark brown to purple black. This may be attributed to the irreversible deactivation due to the formation of μ-oxo dimeric product, especially in presence of the oxidant. On the other hand, zeolite encapsulated metal complexes do not undergo any colour change during the reaction and could be easily separated and reused. Further the time required for the conversion of β-napthol to BINOL is significantly less in presence of the encapsulated metal complexes. And we have been successful in reducing the time consumed for such catalytic conversion in contrast to the recent publication dealing with oxidative coupling of 2-napthol.[26,,68] As illustrated in Table 5.10, the potassium exchanged zeolites shows better activity in comparison to the other catalysts.

5.4. Conclusion

Two monomeric iron(III) complexes of the ligands *N,N′*-bis(salicylidene) ethylenediamine, (Salen) and *N,N′*-disalicylidene-1, 2-phenylendiamine, (Salophen) with pseudo square pyramidal geometry are being synthesize inside the supercase of zeolite Y possessing various extraframework alkali metal cations (Li^+, Na^+ and K^+) *via* flexible ligand method. The influence of the alkali metal cations on the electronic transitions, redox and catalytic abilities of the guest Fe-(III) Schiff-base complexes in the restricted void space are investigated. The size of the exchangeable counter cation on zeolite framework is found to have profound influence on the LMCT and the average reduction potential of the encapsulated iron complexes. The increase in size of the alkali metal cation from Li^+ to K^+ dramatically red shifted the lower and the higher energy UV-vis bands. The smaller alkali metal cation interacts more strongly and hinders the passage of 2-napthol into the zeolite matrix. In contrast, presence of the larger cations with high electropositivity, less cation-π interaction energy and donor ability favours the high diffusibility of the incoming guest, influences the redox potential of the guest molecule and thereby enhances the rate of the catalytic conversion of 2-napthol to BINOL. The Fe-Schiff base complexes encapsulated in zeolite KY are found to have more negative reduction potential and hence varying the alkali metal cations from Li^+ to K^+ results in the enhancement of the catalytic ability of the encapsulated complexes for oxidative coupling of 2-napthol in presence of molecular oxygen as oxidant. DFT based calculation further supports the enhancement of reactivity on the basis of the change in the global hardness and softness of the systems on encapsulation into zeolite-Y. The catalytic conversion of 2-napthol to BINOL is found to be more in comparison to the neat complexes and most importantly the time required for such conversion is much less than those reported in literatures. Moreover, the selectivity towards R-configuration is found to be more in the catalytic conversion of 2-napthol to BINOL in presence of all the hybrid catalyst.

References

[1] (a) Balkus, K. J., Jr., & Gabrielov. A. G. *J. Incl. Phenom. Mol. Recognit. Chem.* **21**(1-4), 159-184, 1995, (b) De Vos, D. E., et al. *J. Incl. Phenom. Mol. Recognit. Chem.* **21**(1-4), 185-213, 1995, (c) Dutta, P. K. *J. Inclusion Phenom. Mol. Recognit. Chem.* **21**(1-4), 215-237, 1995, (d) Xuereb, D. J., & Raja, R. *Catal. Sci. Technol.* **1**, 517-534, 2011, (e) Jacob, C. R., et al. *Appl. Catal. A* **182**(1), 91-96, 1999.

[2] Cano, M. L., et al. *J. Am. Chem. Soc.* **118**(45), 11006-11013,1996.

[3] Álvaro, M., et al. *J. Am. Chem. Soc.* **129**(26), 8074-8075, 2007.

[4] Mizuno, K., & Lunsford, J. H. *Inorg. Chem.* **22**(23), 3484-3486, 1983.

[5] (a) Mortier, W. J., & Schoonheydt, R. A. *Prog. Solid State Chem.* **16**(1-2), 1-125, 1985, (b) Mortier,W. J. *J. Catal.* **55**(2), 138-145, 1978, (c) Heidler, R., et al. *J. Phys. Chem.* **100**(50), 19728-19734, 1996, (d) van Genechten, K. A., & Mortier, W. J. *Zeolites* **8**(4), 273-283,1988.

[6] No, K. T., et al. *J. Phys. Chem.* **85**(14), 2065-2070, 1981.

[7] Yashima, T., et al. *J. Catal.* **26**(1), 303-312, 1972.

[8] (a) Hattori, H. *Chem. Rev.* **95**(3), 537-550, 1995. (b) Tanabe, K., et al. *Stud. Surf. Sci. Catal.* **51**, 5-25, 1989.

[9] Deka, R. C., & Vetrivel, R. *J. Catal.* **174**(1), 88-97, 1998.

[10] Deka, R. C., et al. *Chem. Phys. Lett.* **389**(1-3), 186-190, 2004.

[11] Mori, K., et al. *J. Phys. Chem. C* **112**(49), 19449-19455, 2008.

[12] Mori, K., et al. *J. Phys. Chem. C* **112**(7), 2593-2600, 2008.

[13] Corrêa, R. J., et al. *Appl. Catal. A: Gen.* **336**(1-2), 35-39, 2008.

[14] Poltowicz, J., et al. *Appl. Catal. A: Gen.* **299**(1-2), 235-242, 2006.

[15] Sabater, M. J., et al. *Chem.Commun.* **14**, 1285-1286, 1997.

[16] Gigante, B., et al. *Catal. Lett.* **68**(1-2), 113-119, 2000.

[17] Jin, C., et al. *Mol. Catal. A: Chem.* **249**(1-2), 23-30. 2006.

[18] Saha, P. K., et al. *Polyhedron* **26**(3), 563-571, 2007.

[19] Knops-Gerrits, P., et al. *J. Mol. Catal. A: Chem.* **117**(1-3), 57-70, 1997.

[20] Mahdavi, V., et al. *Catal. Commun.* **9**(13), 2201-2204, 2008.

[21] Silva, M., et al. *J. Mol. Catal. A: Chem.* **258**(1-2), 327-333, 2006.

[22] Medina, J. C., et al. *J. Mol. Catal. A: Chem.* **115**(2), 233-239. 1997.

[23] Zsigmond, Á., et al. *J. Mol. Catal. A: Chem.* **171**(1-2), 95-102, 2001.

[24] Haber, J., et al. *J. Mol. Catal. A: Chem.* **224**(1-2), 153-159, 2004.

[25] Zhang , R., et al. *J. Electroanal. Chem.* **643**(1-2), 31-38. **2010**.

[26] Egami, H., & Katsuki, T. *J. Am. Chem. Soc.* **131**(17), 6082-6083, 2009.

[27] Egami, H., et al. *J. Am. Chem. Soc.* **132**(39), 13633-13635, 2010.

[28] Sinclair, P. E., & Catlow, C. R. A. *J. Phys. Chem. B* **103**(7), 1084-1095, 1999.

[29] (a) Quayle, W. H., & Lunsford, J. H. *Inorg. Chem.* **21**(1), 97-103, 1982. (b) Quayle, W. H., et al. *Inorg. Chem.* **21**(6), 2226-2231, 1982.

[30] Ganesan, R., & Viswanathan, B. *J. Phys. Chem. B* **108**(22), 7102-7114, 2004.

[31] Gaber, B. P., et al. *J. Am. Chem. Soc.* **96**(22), 6868-6873, 1974.

[32] Hensen, E. J. M., et al. *J. Catal.* **233**(1), 123-135, 2005.

[33] Kumar, S. M., et al. *J. Catal.* **239**(1), 173-186, 2006.

[34] Li, L., et al. *Appl. Catal. A* **344**(1-2), 131-141, 2008.

[35] Park, Y. S., et al. *J. Am. Chem. Soc.* **121**(13), 3193-3200. 1999.

[36] Webb, J. *In "Techniques and Topics in Bioinorganic Chemistry",* McAuliffe. C. A. Ed.Wiley, New York. 1975.

[37] Murray, K. S., et al. *Aust. J. Chem.* **31**(5), 983-992, 1978.

[38] Shaw, B. R., et al. *J. Electrochem. Soc.* **135**(4), 869-876, 1988.

[39] Bessel, C. A., & Rolison D. R. *Stud. Surf. Sci. Catal.* **98**, 114-115, 1995.

[40] Cassidy, J., et al. *Electrochim. Acta* **36**(2), 383-384, 1991.

[41] Bedioui, F., et al. *J. Electroanal. Chem.* **373**(1-2), 19-29, 1994.

[42] Mesfar, K., et al. *J. Mater. Chem.* **3**(8), 873-876, 1993.

[43] Bedioui, F., et al. *J. Electroanal. Chem.* **315**(1-2), 313-318, 1991.

[44] Gemborys, H. A., & Shaw, B. R. *J. Electroanal. Chem.* **208**(1), 95-107, 1986.

[45] Shaw, B. R., & Creasy, K. E., *J. Electroanal. Chem. Interfacial. Electrochem.* **243**(1), 209-217, 1988.

[46] Rolison, D. R., *Chem. Rev.* **90**(5), 867-878, 1990.

[47] Baker, M. D., et al. *J. Phys. Chem.* **98**(6), 1668-1673, 1994.

[48] Calzaferri, G., et al. *J. Chem. Soc., Chem. Commun.* **13**, 1313-1314. 1995.

[49] Gerloch, M., et al. *Nature* **212**(5064), 809-810,1996.

[50] Gerloch, M., & Mabbs, F. E. *J. Chem. Soc. A* **14**, 1900-1908, 1967.

[51] Parr, R. G., & Chattaraj, P. K. *J. Am. Chem. Soc.* **113**(5), 1854-1855, 1991.

[52] Chattaraj, P. K., et al. *Chem. Phys. Lett.* **237**(1),171-176, 1995.

[53] a) Pearson, R. G. *Chemical Hardness: Applications from Molecules to Solids,* Wiley-VCH Verlag GMBH: Weinheim, 1997. b) Pearson, R. G. *J. Chem. Educ.* **64**(7), 561-567, 1987, c) Chattaraj. P. K. *Proc. Indian Natl. Sci. Acad. Part A* **62**, 513-519, 1996, e) Chattaraj, P. K., et al. *Chem. Phys.* **204**(2-3), 429-437, 1996, e) Ayers, P. W., & Parr, R. G. *J. Am. Chem. Soc.* **122**(9), 2010-2018, 2000.

[54] Nguyen, L. T., et al. *J. Am. Chem. Soc.* **121**(25), 5992-6001, 1999, and references therein.

[55] Pal, S., & Chandrakumar, K. R. S. *J. Am. Chem. Soc.* **122**(17), 4145-4153, 2000, and references therein.

[56] Chattaraj, P. K. *J. Phys. Chem. A* **105**(2), 511-513, 2001.

[57] a) Luo, Z., et al. *Angew. Chem. Int. Ed.* **41**(23), 4532-4535, 2002, b) Guo, Q. X., et al. *J. Am. Chem. Soc.* **129**(45), 13927-13938, 2007.

[58] Somei, H., et al. *Tetrahedron Lett.* **45**(9), 1841-1844, 2004.

[59] Gao, J., et al. *Angew. Chem. Int. Ed.* **42**(48), 6008-6012, 2003.

[60] Tada, M., et al. *Chem. Commun.* **22**, 2542-2543, 2004.

[61] Li, X., et al. *J. Org. Chem.* **68**(14), 5500-5511, 2003.

[62] Sabarinathan, S., et al. *Euro. J. Chem.,* **1**(4), 360-367, 2010.

[63] Sivaguru, J., et al. *Photochem. Photobiol.* **82**(1), 123-131, 2006.

[64] (a) Ma, J. C., & Dougherty, D. A. *Chem. Rev.* **97**(5), 1303-1324, 1997, (b) Dougherty, D. A. *Science* **271**, 163-168, 1996, c) Lakshminarasimhan, P., et al. *J. Am. Chem. Soc.* **122**(19), 4815-4816, 2000.

[65] (a) Stratakis, M., & Froudakis, G. *Org. Lett.* **2**(10), 1369-1372, 2000.

[66] (a) Okachi, T., et al. *Org. Lett.* **4**(10), 1667-1669, 2002.

[67] Kuwahara, Y., et al. *J. Am. Chem. Soc.* **133**(32), 12462-12465, 2011.

[68] Guo, Q. X., et al. *J. Am. Chem. Soc.* **129**(45), 13927-13938, 2007.

Chapter 6

Asymmetric Henry Reaction by Chiral Cu(II) Schiff Base Complexes Encapsulated in Zeolite-Y

6.1. Introduction

Zeolite encapsulated transition metal complexes and organometallic complexes have now emerged as one of the potent competitors for the homogeneous counterpart, in terms of catalytic behaviour and stability.[1-3] There are several reports, in which zeolite encapsulated complexes found to exhibits better catalytic activity, high turn over number and high thermal stability in comparison to their homogeneous counterpart.[4-7]

Finding a commercially viable pathway for the stereoselective organic synthesis of biologically important chemicals may be considered as one of the major thrust area of chemistry today. Among the many routes attempted, those involving the use of chiral reagents and chiral catalysts are very important in the synthesis of effective drugs. Henry reaction commonly known as nitro-aldol condensation reaction is one of the important C-C bond formation reaction whose ultimate product has been used for various drug designing.[8] Apart from Shibasaki and Evans catalyst[9,10] various other chiral catalytic systems have been designed to bring out enantioselective Henry reaction. Still there remains a lot of scope to improvise this reaction.

Chiral Schiff bases and their complexes with transition metals are one of the most studied chiral catalysts. Starting from Jacobsen catalyst[11] to present date these type of catalyst has dominated a part of asymmetric catalysis.[12,13] Due to their ability to act as chiral catalyst or as co catalyst, Schiff base ligands as well as their complexes have been extensively applied either in homogeneous phase or by anchoring them in various inorganic support viz zeolite, clay, LDH etc.[15] However, to best of our knowledge, the enantioselective Henry reaction performed by incorporating such type of chiral catalyst in zeolite-Y is sparse. So considering the potentiality of chiral Schiff base complexes, advantages of heterogeneous catalytic system and importance of the enantioselective Henry reactions we have synthesized two Schiff base complexes of copper inside zeolite-Y and have been tested for enantioselective Henry reaction. Density functional theory (DFT) calculation has been applied to understand the nature of structural and electronic changes that occurs in the complexes under the influence of zeolite framework. Based on the theoretical and experimental evidences a plausible mechanism has been suggested for the reaction catalysed by such complexes.

6.2. Results and Discussion.

6.2.1. Experimental Section

6.2.1.1. Elemental Analysis

The elemental (Cu, C, N, O, Al, Na and Si) detection has been performed by EDX (Figure 6.1) and the amount of metal content in the synthesized complexes is determined by Vogel's method.[14] The Si/Al ratio in the virgin NaY is found to be 2.5. This ratio remain almost constant in all the prepared samples indicating the absence of dealumination either on metal exchange or on encapsulating the Cu-Schiff base complexes. The amount of metal content in the encapsulated complexes in comparison to the Cu^{2+}-exchanged NaY is found to be less. This implies that during complex formation some amount of metal cation are involved in the formation of the metal complex inside zeolite-Y.

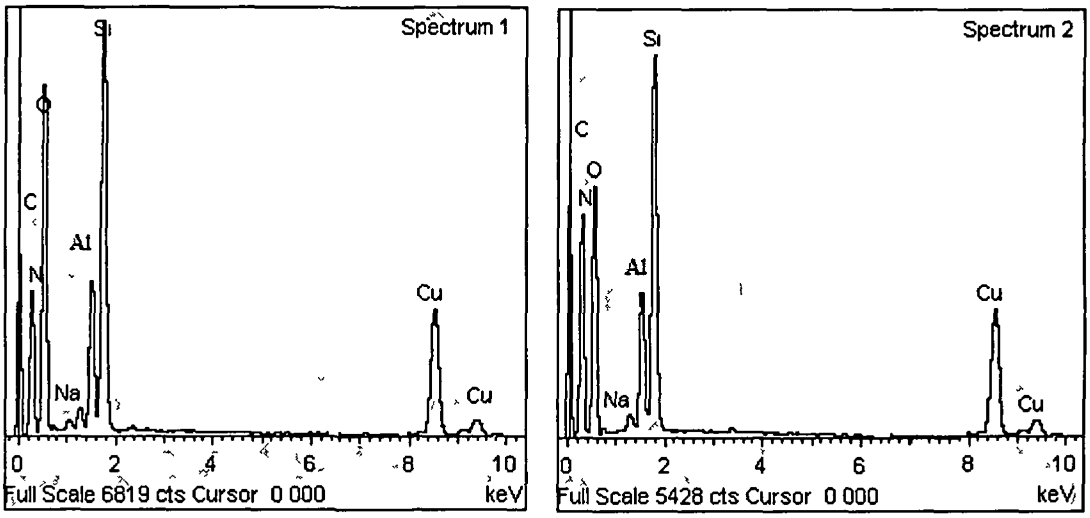

Figure 6.1. EDX analysis spectrum1 for $Cu(L1)_2$-Y-complex and spectrum 2 for $Cu(L2)_2$-Y.

6.2.1.2. XRD Study

The powder X-ray diffraction patterns of the zeolite-Y, metal exchanged zeolites and the encapsulated metal Schiff base complexes are shown in Figure 6.2. The diffraction pattern for the virgin zeolite-Y and encapsulated systems are found to be similar. The peak intensities of the encapsulated complexes are however, found to be less intense in comparison NaY and copper exchange-NaY. Besides this, there are also differences in the relative peak intensities of the 220 and 311 reflections appearing at $2\theta = 10$ and 12^0, respectively. For pure zeolite-Y and for M^{2+} -exchanged zeolite-Y the intensity of I_{220} plane is greater than that of I_{311}, but for the encapsulated complex the reverse is obtained i.e. $I_{311} > I_{220}$. This reversal in intensities gives a strong evidence for the successful encapsulation of Schiff base complexes of copper inside the cavity of zeolite-Y.[15]

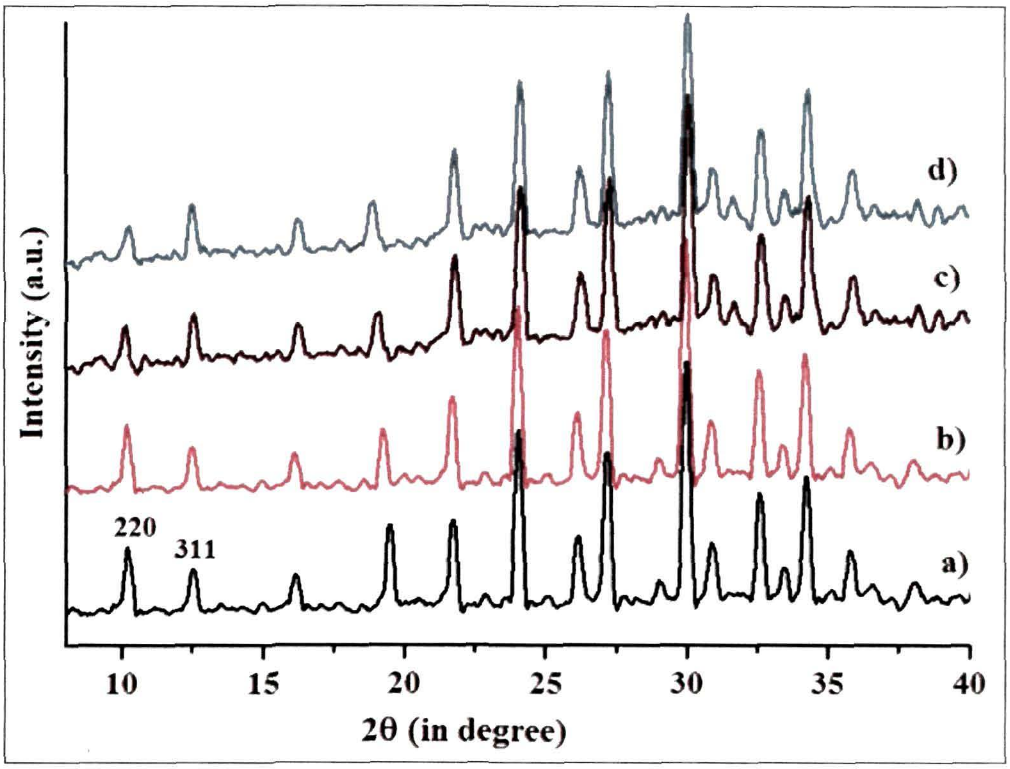

Figure 6.2. XRD pattern of a) Pure zeolite-NaY b) Cu^{2+}-Y c) $Cu(L1)_2$-Y d) $Cu(L2)_2$-Y.

6.2.1.3. FTIR Study

The FTIR spectra of Cu^{2+}-exchanged exchanged zeolite-Y, neat and encapsulated Schiff base complexes are shown in Figure 6.3. FTIR spectra of metal-exchanged zeolite shown in Figure 6.3a, shows a strong and broad band at 1009 cm^{-1} due to the asymmetric stretching vibrations of $(Si/Al)O_4$ units. The broad bands in the region 1650 and 3500 cm^{-1} are due to lattice water molecules and surface hydroxylic groups respectively. The IR spectra of the neat Schiff-base Cu(II) complexes [Figure 6.3 d and e] shows major bands at 1625 (C=C), 1600 ($\nu_{C=O}$ carboxylate), 1530 (C=N), 1450, 1325, (C-O), 753 cm^{-1} (ν_{C-H} aromatic ring). Similar frequencies are also observed in the case of zeolite-Yencapsulated complexes with a little shift in the C=O, C=N and C-O bands to wave numbers 1634, 1532, 1454 and 1335 cm^{-1}, respectively indicating nitrogen and oxygen coordination inside the cavity of zeolite framework, Figure 6.3 b and c. In addition to these bands the encapsulated complexes also shows a band at 1395 cm^{-1} corresponding to C-H deformation. These results give information for the formation of Cu-Schiff base complexes inside zeolite-Y.

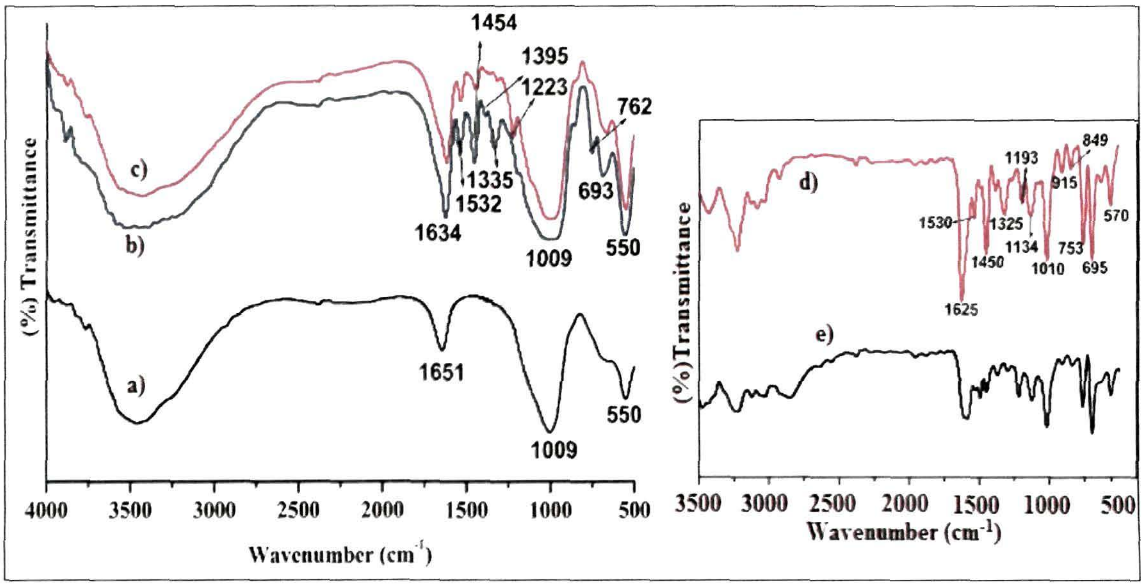

Figure 6.3. FTIR-spectrum of a) Cu^{2+}-exchanged zeolite-Y b) $Cu(L1)_2$-Y c) $Cu(L2)_2$-Y d) $Cu(L1)_2$ e) $Cu(L2)_2$.

6.2.1.4. Cyclic Voltammetry Study

Electrochemical study of the zeolite encapsulated complexes has recently gain considerable interest as it provides the information on the nature of intrazeolite complexes that may not be readily available from spectroscopic studies.[16] With the proposal of two redox mechanisms (intrazeolite and extrazeolite) by Shaw et al[17] associated with the chemically modified zeolites, there have been a lot of studies on the electroanalysis of redox active species present in the pores of zeolite. However, exact location of the electroactive sites in the voids of zeolite is controversial and still remains as an open question. In this study the cyclic voltammogram of zeolite encapsulated complexes are taken as a part of zeolite modified electrode in presence of 0.1M TBAP as supporting electrolyte. It has been reported that electrochemical analysis of chemically modified zeolite is much more reliable unless it rupture the crystallinity of the zeolites.[18] The cyclic voltammogram of the neat complexes $Cu(L1)_2$ and $Cu(L2)_2$ taken in solution mode are shown in Figure 6.4 a and 6.4b, respectively. It is observed that the $Cu(L1)_2$ shows two oxidation potential, Table 6.1. The first wave corresponds to the electrochemically quasi-reversible Cu(II)/Cu(I) transition, whereas the second one features a reduction of Cu(I) to the corresponding Cu(0) complex followed by the removal of the metal centre from the Schiff-base ligand. It also shows two oxidation peaks corresponding to Cu(0)/Cu(I) and Cu(I)/Cu(II) couples. Similar to the $Cu(L1)_2$, the $Cu(L2)_2$ complex also shows two reduction and two oxidation peak as shown in Figure 6.4b. The difference in redox potential values in the two complexes indicates

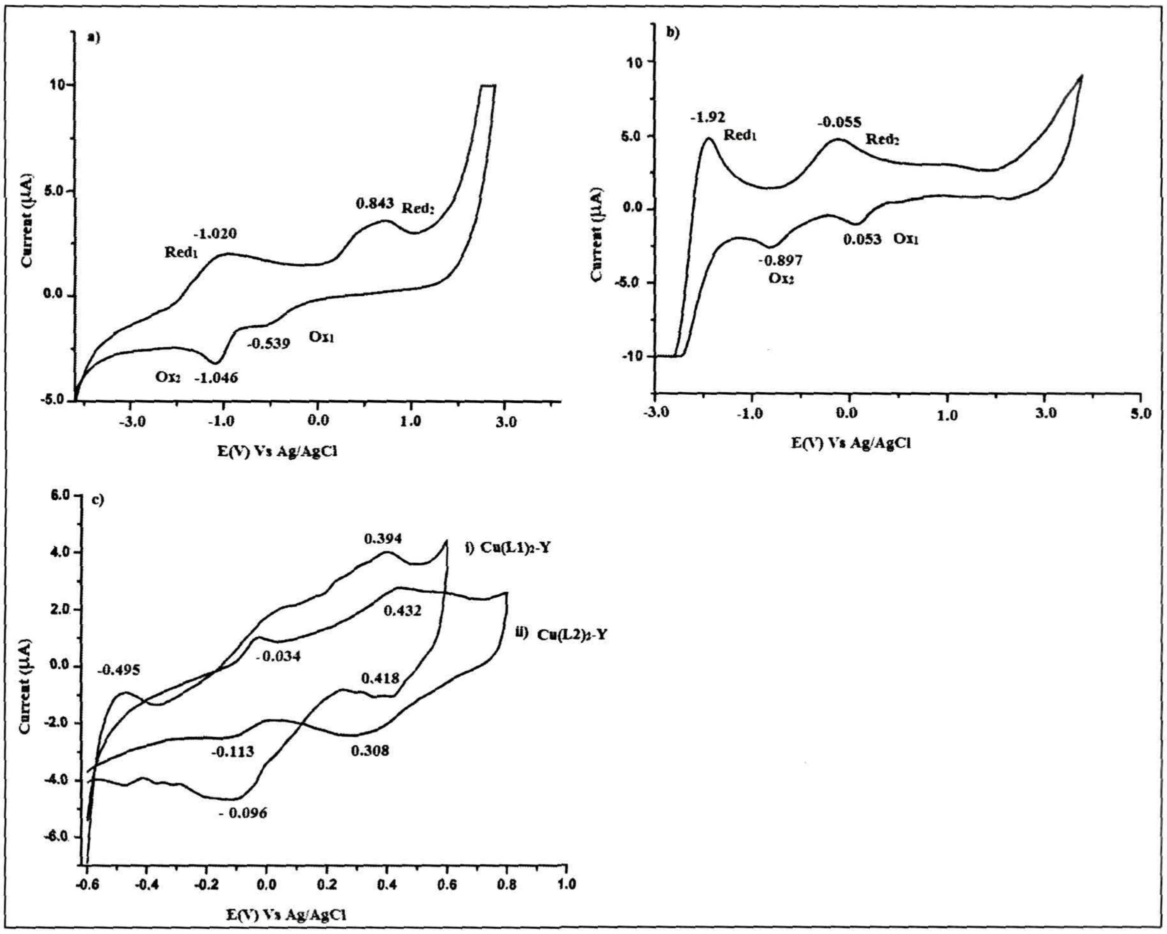

Figure 6.4. a) and b) are cyclic voltammograms for neat $Cu(L1)_2$ and $Cu(L2)_2$ complexes respectively taken in DCM using 0.1M TBAP as supporting electrolyte. c) i) and ii) are cyclic voltammograms of encapsulated $Cu(L1)_2$-Y and $Cu(L2)_2$-Y complexes, respectively taken as ZME in DCM using 0.1M TBAP as supporting electrolyte at a scan rate of 0.1V.

Table 6.1. Oxidation and reduction peak potential values (in V) for neat and encapsulated complexes.

Complex	E^1_{ox}	E^2_{ox}	E^1_{red}	E^2_{red}	E^{av}_{ox}	E^{av}_{red}
$Cu(L1)_2$	-0.539	-1.046	-1.02	0.843	-0.792	-0.088
$Cu(L2)_2$	0.053	-0.897	-1.92	-0.055	-0.422	-0.987
$Cu(L1)_2$-Y	0.418	-0.113	-0.495	0.394	0.152	-0.101
$Cu(L2)_2$-Y	0.398	-0.096	-0.034	0.432	0.151	0.199

that substitution at phenyl ring greatly influences the electrochemical behaviour. The cyclic voltammogram of encapsulated complexes as a part of ZME are shown in Figure 6.4c. The peak current remains stable for more than 6h indicating the stability of the complexes inside the cavity of zeolite. These redox potential values are completely different from that of the Cu^{2+}-exchanged zeolite-Y indicating the formation of Schiff-base complexes inside zeolite-Y. It can be observed from Figure 6.4c and Table 6.1 that on encapsulation the peaks are broadened and average reduction potential values of $Cu(L1)_2$-Y get shifted towards more negative values whereas that in case of $Cu(L2)_2$-Y it gets shifted to more positive values. The shifting of the reduction potential value towards more negative value in case of $Cu(L1)_2$-Y idicates the stabilization of Cu(II) oxidation state in zeolite cages.[19] The electrochemical analysis of zeolite encapsulated complexes based on ZME depends on the preparation of the modified electrode. It may so happen that during modification or pressing the sample the crystallinity of the zeolite may get ruptured and the voltammogram so obtained may not be apparently due to encapsulated complexes. It may be due to disintegration of the complexes over the zeolite surface. In order to confirm this we again perform the XRD and DRS analysis of the samples after performing the cyclic voltammrtic study. We obtain the same pattern of XRD and DRS-spectra as we obtain before it is subjected to ZME. So it can be concluded that during the preparation of ZME the zeolite structures are not ruptured and the redox behaviour is due to the presence of redox active Cu-Schiif base complex present in the cavities of zeolite-Y.

6.2.1.5. UV-vis/DRS Study

The UV-vis spectrum of the Schiff base ligands, their corresponding neat and the zeolite encapsulated copper complexes are depicted in Figure 6.5. The peaks are assigned in Table 6.2. It is observed that the Schiff base ligands give almost similar pattern of UV-vis peak in water, Figure 6.5 (spectrum a and b). Both the ligand system shows five peaks nearly at 232, 262, 340, 366 and 389 nm. The first two higher energy peaks are due to ligand based $\pi\rightarrow\pi^*$ and the three lower energy peaks are due $n\rightarrow\pi^*$ transitions. The neat Cu(II) complexes with ligand L1 and L2 shows peaks above and below 250 nm at due to $\pi\rightarrow\pi^*$ and $n\rightarrow\pi^*$ originated from ligand system, Table 6.2. Besides these it also shows a weak bands at 323, 377 and 384 which can be attributed to metal to ligand charge transfer (MLCT). The comparison of the UV-vis spectrum of the complexes (Figure 6.5, spectrum c and d) with those of the free ligands indicate a blue shifting in the π →π* and n →π* transitions. The shifting of the peaks towards higher energy value and appearance of MLCT transitions suggest the formation of the Cu-complexes.

Table 6.2. UV-vis/DRS spectral data (λ_{max} in nm) for the uncomplexed ligands, neat and the encapsulated Cu-Schiff base complexes.

Compounds	Wavelengths (nm)	Peak assignment
Ligand-1	233, 262	π→π*
	340,366,387	n→π*
Ligand-2	233,262	π→π*
	244,274,341,365,389	n→π*
Cu(L1)2	219,222	π→π*
	256,271	n→π*
	323,377	dπ→pπ
Cu(L2)2	213,230,	π→π*
	280, 306,	n→π*
	384	dπ→pπ
Cu(L1)2-Y	245, 285	π→π*
	343	n→π*
	575	dπ→pπ
Cu(L2)2-Y	217, 256	π→π*
	290, 335	n→π*
	617	dπ→pπ

The diffuse reflectance spectra of the encapsulated complexes are shown in Figure 6.5 (spectrum e and f) indicate that the peaks are less intense than the corresponding neat complex which may be due to the presence of low concentration of metal-complex inside the cavities. However, both the complexes retain the same spectral regions as in the neat complex. The only difference that can be observed from the peaks values that upon encapsulation the MLCT transitions significantly shifted to higher wavelengths. The shifting of the spectral region towards lower energy value may be due to the influence of the zeolite matrix on the electronic and structural properties of the encapsulated complex.

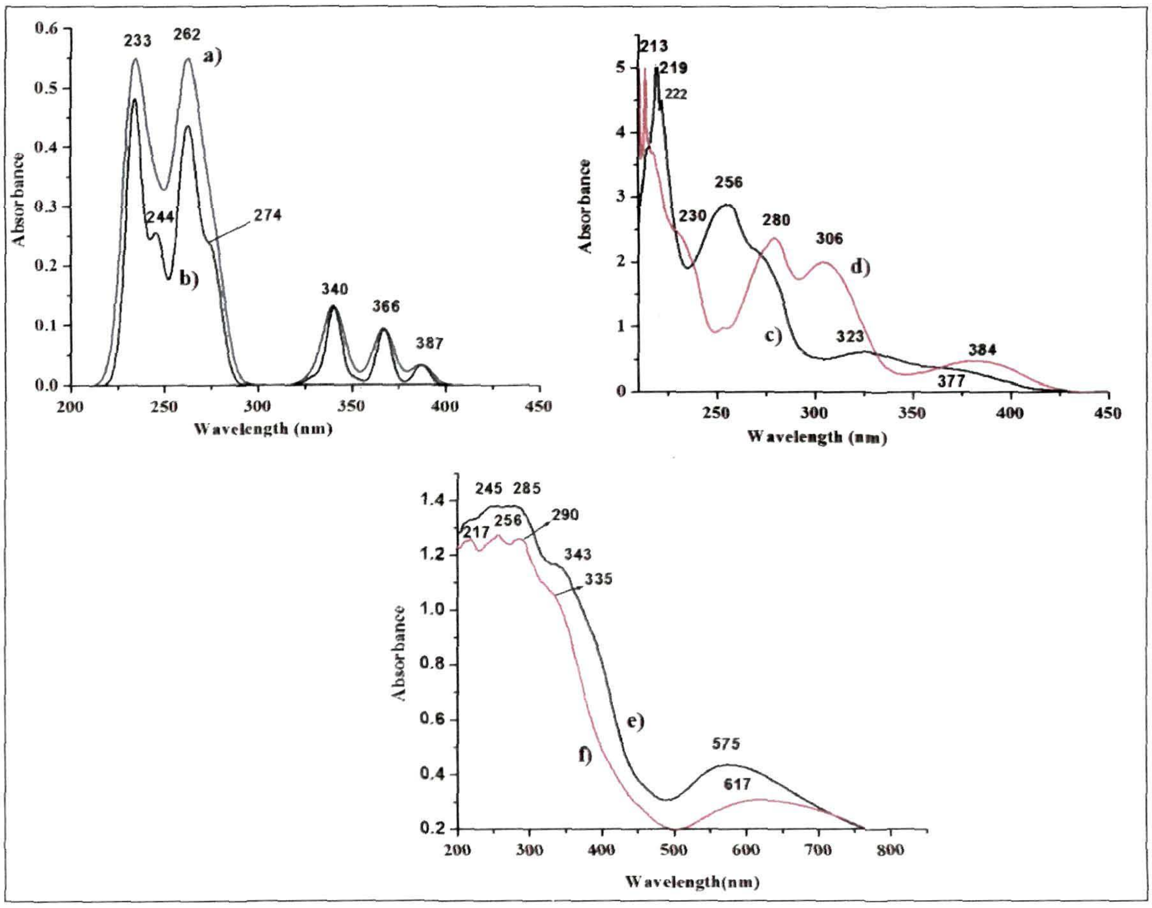

Figure 6.5. UV-vis/DRS spectra of a) ligand 1(L1) b) ligand 2(L2) c) $Cu(L1)_2$ d) $Cu(L2)_2$ e) $Cu(L1)_2$-Y f) $Cu(L2)_2$-Y.

6.2.1.6. ESR Study

ESR spectra of the Cu^{2+} exchanged zeolite, neat Schiff base complexes and the encapsulated Cu-Salen complexes are shown in Figure 6.6. ESR spectra for the neat complex as polycrystals are characterized by an axial g tensor. Hyperfine features for copper ($S = 1/2$ *and* $I = 3/2$) are observed at 77 K due to intermolecular spin–spin *coupling for both the neat and the encapsulated complexes.*

The ESR spectra of the neat Cu-Schiff base complexes show two g-values ($g_{//}$ = 2.450 and $g_{\perp}$ = 2.223 for $Cu(L1)_2$ and $g_{//}$ = 2.420 and $g_{\perp}$ = 2.218 for $Cu(L2)_2$ that are characteristics of a normal tetragonal environment. The $g_{//} > g_{\perp} > 2.0023$ indicates that the unpaired electron is present in the d_{x2-y2} orbital, which is characteristics of Cu^{2+} ions that undergoes tetragonal elongation. The encapsulated complexes show more than four hyperfine lines due to interaction between Cu nuclei and two equivalent ^{14}N-atoms indicating the presence of Cu (II) mononuclear complex inside zeolite. The $g_{//}$ value is found to be 2.227 for $Cu(L1)_2$-Y and 2.229 for $Cu(L2)_2$-Y and are less compared to the copper exchanged NaY (g_{II} = 2.397). It is known that when the symmetry of the ligand field of the copper complex changes from the octahedral via square pyramidal coordination to planar environment, the g_{II} value decreases. The decrease in g value suggests the formation of square planar copper complex within the framework of zeolite-Y.

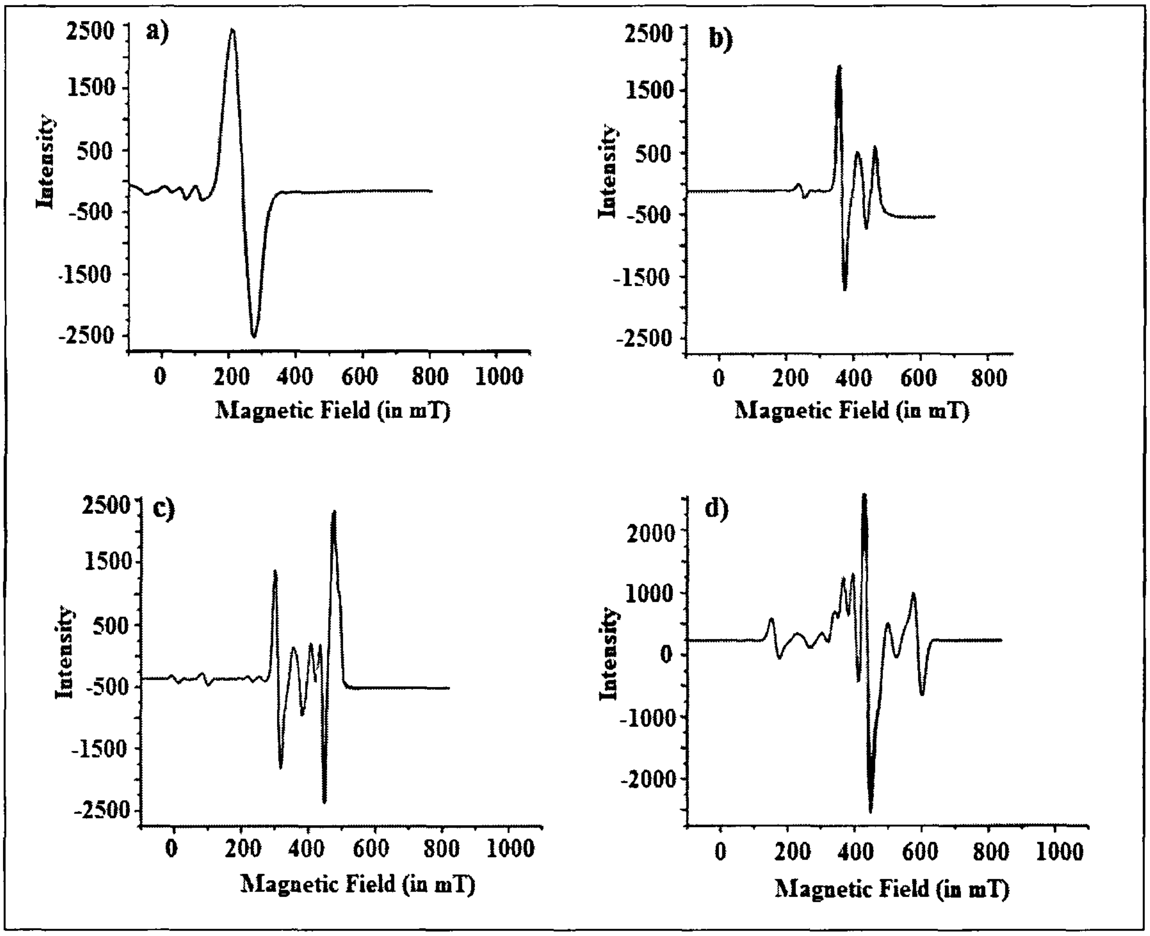

Figure 6.6. Powder ESR spectra of a) neat $Cu(L1)_2$ b) neat $Cu(L2)_2$ c) encapsulated $Cu(L1)_2$-Y and d) $Cu(L2)_2$-Y complexes.

6.2.1.7. SEM Study

SE micrographs of complexes taken before Soxhlet extraction and that taken after Soxhlet extraction are shown in Figures 6.7 (a), (b), (c) and (d). The SEM taken before purification shows the presence of some unreacted or extraneous particles on the external surface. In the SEM of finished products, no surface complexes are seen and the particle boundaries on the external surface of zeolite are clearly distinguishable. This is much clearer from the surface plot shown in Figure 6.8 (a), (b) and (c). Homogeneous surface morphology for the neat NaY zeolite and the samples after

Soxhlet extraction, respectively are observed in Figure 6.8a) and 6.8c). The surface plot for the samples before Soxhlet extraction however, are found to be non-homogeneous indicating the surface is being occupied by extraneous complexes or the uncomplexed ligands. The presence of similar surface morphology in before and after encapsulation into zeolite-Y confirms that encapsulation has not affected the surface crystallinity. Further, it also indicates the efficiency of purification procedure to effect complete removal of extraneous complexes, leading to well-defined encapsulation in the cavity.

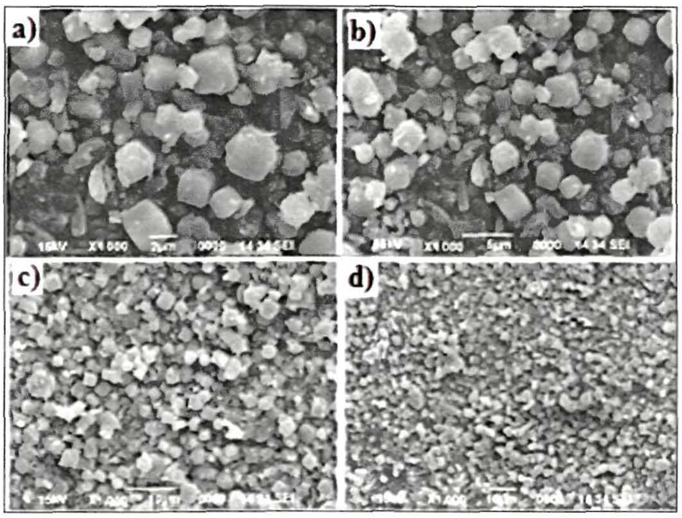

Figure 6.7. SE micrographs of a) Cu(L1)$_2$-Y b) Cu(L2)$_2$-Y before Soxhlet extraction d) &e) SE micrographs of Cu-Schiff base complexes after Soxhlet extraction

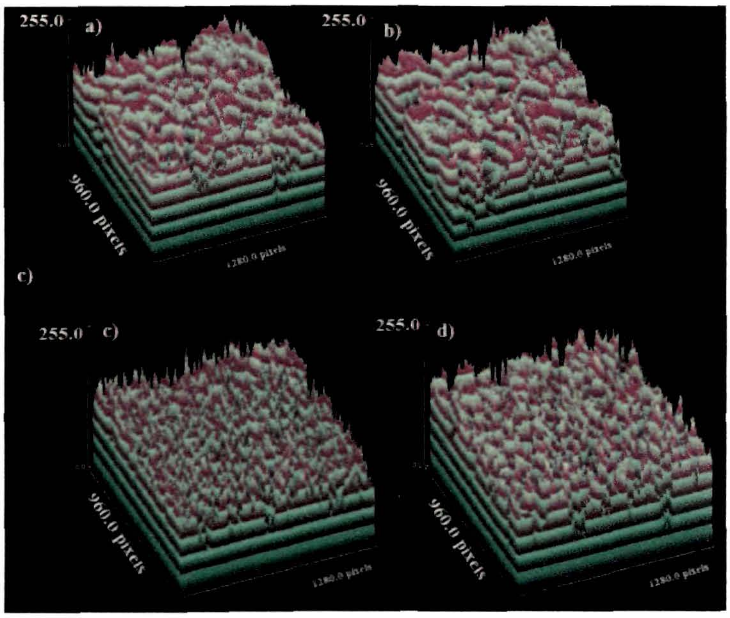

Figure 6.8. Surface plot of a) and b) Cu-Schiff base complexes before Soxhlet extraction c) and d) Cu-Schiff base complexes after Soxhlet extraction. X and Y axis represents width and height, respectively.

6.2.1.8. TGA Study

The thermo-gravimetric analysis of the neat Cu(II) Schiff-base and the encapsulated complexes are shown in Figure 6.9. The two neat complexes show peaks below 100 °C which is due to elimination of outer sphere water molecule, Figure 6.9 (curve a and b). The peaks above 300 °C are due to partial decomposition of the complexes. The weight losses at higher temperature range 350-550 °C are due to complete decomposition of the sample.[20] The comparison of thermo-gravimetric analysis for neat complexes with the encapsulated one shows that these complexes become more stable once they get embedded inside the cavity of zeolite-Y, Figure 6.9 (curve c and d). In case of the encapsulated metal complexes the weight losses due to partial decomposition occurs at lower temperature, however, they do not undergo complete decomposition upto 700°C. These indicate that the two chiral Cu(II) complexes become somewhat more stable on encapsulation.

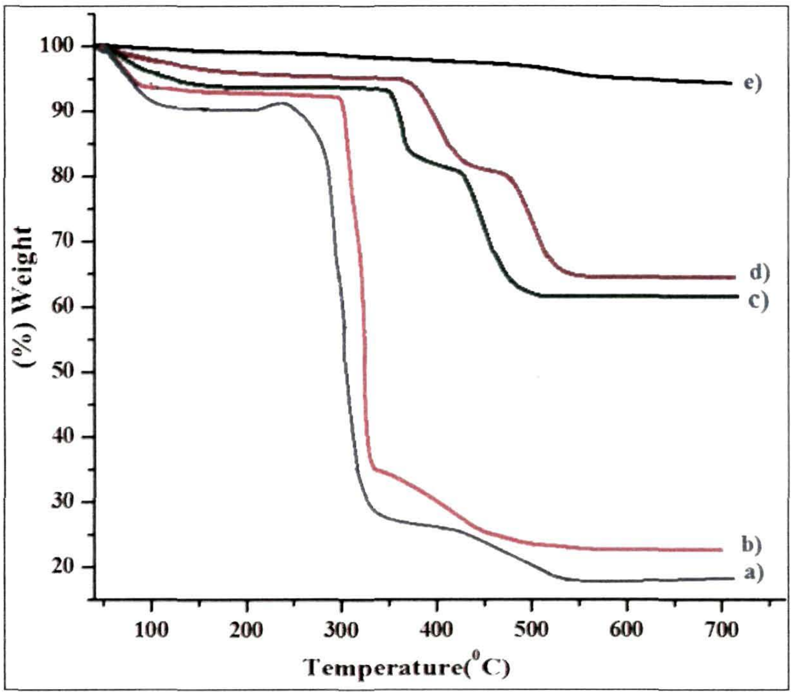

Figure 6.9. TGA of a) $Cu(L1)_2$ b) d) $Cu(L2)_2$ c) $Cu(L1)_2$-Y d) $Cu(L2)_2$-Y e) Cu^{2+}-Y.

6.2.2. Theoretical Calculation

6.2.2.1. Geometries

The geometrical parameters obtained from VWN/DN level calculations for the neat and the encapsulated complexes are provided in Table 6.3. The calculated bond lengths and bond angles for the neat complexes are found to be in good agreement with similar reported Schiff base complex of Cu. After encapsulation of the chelated Schiff base copper complexes the bond length and the bond angle are found to slightly differ in comparison to the neat complexes. This indicates, on encapsulation into zeolite framework, the complex has not undergone much more distortion which may change the active site in the complexes. Furthermore, we have also calculated the volume of the zeolite cluster model and the neat complexes using Hyperchem software.[21] It calculated volume of the zeolite framework (4014.8 Å^3) is found to be sufficient enough to hold the two Schiff base complexes having the volumes $Cu(L1)_2$=1212.71 Å^3, $Cu(L2)_2$= 1362.57 Å^3.

Table 6.3. Selected bond length (in Å) and bond angles (in deg) of the optimized neat and encapsulated Cu-Schiff base complexes.

Bond length	$Cu(L1)_2$	$Cu(L1)_2$-Y	$Cu(L2)_2$	$Cu(L2)_2$-Y
$Cu\text{-}O_1$	1.90	1.87	1.90	1.89
$Cu\text{-}O_2$	1.90	1.92	1.90	1.91
$Cu\text{-}N_1$	1.95	1.91	1.95	1.92
$Cu\text{-}N_2$	1.94	1.93	1.94	1.92
Bond Angles				
$<O_1\text{-}Cu\text{-}O_2$	91.6	90.3	91.6	89.9
$<O_1\text{-}Cu\text{-}N_1$	92.9	91.2	92.9	93.0
$<O_1\text{-}Cu\text{-}N_2$	169.6	167.9	169.5	177.4
$<O_2\text{-}Cu\text{-}N_1$	170.0	175.5	169.9	176.1
$<O_2\text{-}Cu\text{-}N_2$	92.3	93.9	92.4	92.1
$<N_1\text{-}Cu\text{-}N_2$	84.8	85.3	84.4	84.6

6.2.2.2. Electronic Structure, Ionization Potential, Electron Affinity and Binding Energy

A schematic representation of the frontier molecular orbital for the neat and the encapsulated complexes are shown in Figure 6.10. For all the complexes, the pattern of the occupied and the unoccupied orbitals are qualitatively similar. Copper (II) is an open shell system with d^9 configuration; hence we performed spin unrestricted calculations on all the systems. The energies of the HOMO and the LUMO orbitals corresponding to spin up and spin down state are found to be different in both the neat and the encapsulated systems. The energy values for the frontier orbital of all the four systems are given in Table 6.4. It can be seen from Table 6.4 that the HOMO and

LUMO orbitals of the encapsulated complexes lies higher in energy in comparison to neat complexes. The ionization potential (IP) and electron affinity (EA) values are also found to increase on encapsulation. However, the HOMO-LUMO gaps and the differences between IP and EA in the encapsulated complexes are found to decrease

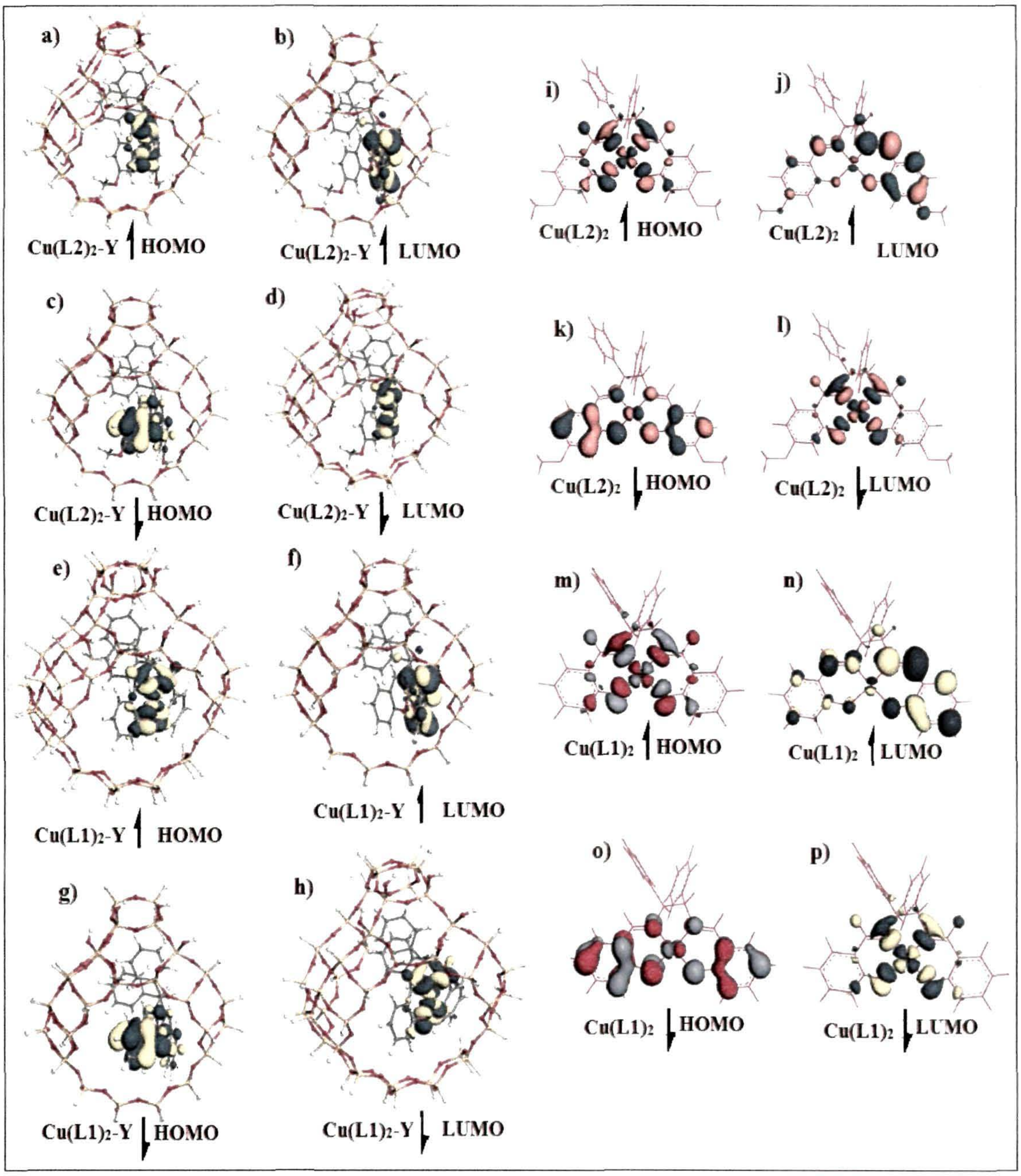

Figure 6.10. HOMO and LUMO orbitals of the neat and the encapsulated Cu(II) Schiff base complexes. The arrows in parenthesis indicates the HOMO and LUMO orbital with spin up (↓) and spin down state (↑).

Table 6. 4. Calculated energies of HOMO and LUMO levels (in eV), chemical potential (μ, in eV), global hardness (η, in eV), electrophilicity index (ω, in eV) and softness (S, in eV). The values given in parenthesis are those obtained by using IP and EA values.

Complex	IP	EA	HOMO	LUMO	μ	η	ω	S
Cu(L1)$_2$(↑)	2.419	1.221	-4.438	-2.341	-3.389	1.048	5.478	0.476
					(-1.820)	(0.599)	(2.764)	(0.834)
Cu(L1)$_2$(↓)			-4.478	-2.633	-3.555	0.9225	6.851	0.542
Cu(L2)$_2$(↑)	2.843	1.834	-4.171	-2.440	-3.305	0.865	6.312	0.577
					(-2.339)	(0.504)	(5.423)	(0.991)
Cu(L2)$_2$(↓)			-4.664	-3.052	-3.858	0.806	9.233	0.620
Cu(L1)$_2$-Y(↑)	**5.176**	**4.428**	-3.917	-2.440	-3.178	0.738	6.840	0.677
					(-4.802)	(0.374)	(30.838)	(1.336)
Cu(L1)$_2$-Y(↓)			-3.322	-2.118	-2.72	0.602	6.144	0.830
Cu(L2)$_2$-Y(↑)	**4.922**	**4.151**	-3.936	-2.416	-3.17	0.76	6.636	0.657
					(-4.537)	(0.385)	(26.690)	(1.296)
Cu(L2)$_2$-Y(↓)			-3.268	-1.963	-2.615	0.652	5.242	0.766

in comparison to those of the free complexes. Among encapsulated systems the HOMO energy of $Cu(L1)_2$-Y (with spin down state) is much higher lying and the LUMO of $Cu(L1)_2$-Y with spin up state is much lower lying . In the neat complexes, $Cu(L2)_2$ with spin up state has the higher lying HOMO whereas its down spin state has lower lying LUMO. This change in the HOMO and LUMO energies further signifies the effect of encapsulation on the orbital energies of the Cu-Schiff base complexes. We have also calculated the interaction energy of the encapsulated complexes as the energy differences between the optimized encapsulated complexes and the corresponding fragments (neat metal complex and the zeolite framework) optimized as isolated molecules. The calculation of the interaction energy at the same level of theory are found to be in the order of $Cu(L1)_2$-Y (32.02eV) < $Cu(L2)_2$-Y (36.83 eV). This result indicates that $Cu(L2)_2$-complex interacts more strongly and becomes more stabilized than the other two complexes. This difference in interaction energy can be attributed to change in the geometrical parameters and the presence of bulkier group in the phenyl ring. These differences in the interaction energy bring a considerable change in the energies of the HOMO and the LUMO levels.

6.2.2.3 Global Descriptors

Since the zeolite matrix influences the electronic as well as the chemical behavior of the transition metal complexes, we have calculated the DFT-based global descriptors *viz* chemical hardness (η), chemical potential (μ), electrophilicity index (ω) and softness (S) using DN basis set and VWN functional for the neat and the encapsulated complexes. The values for η, μ, ω and S given in Table 6.4 are calculated based on two approximations, Koopmans' and finite difference approximation. According to Koopmans' approximation ionization potential is the negative of HOMO energy and electron affinity is the negative of LUMO energy. The plot of IP and EA against the HOMO and LUMO energies of spin down state, respectively shows a linear correlation with regression r^2 values of 0.988 and 0.923, Figure 6.11. Due to several limitations associated with Koopmans' approximation,[22-25] especially in case of transition metal complexes, numerical values of η, S and ω obtained from both the approximation are found to be different. But the trend in the change of global descriptors values predicted by both approximations for the considered systems follows the same order. For example the change in global hardness values predicted by equation (27) as well as by equation (31) [see chapter 2] follows the same order i.e. $Cu(L2)_2 < Cu(L1)_2$ for the neat complexes and the reverse is for the encapsulated complexes.

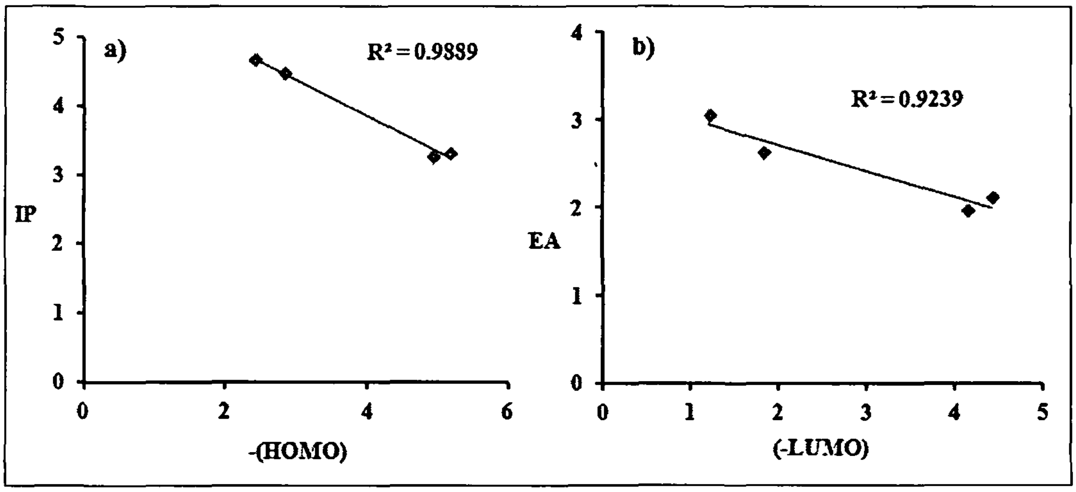

Figure 6.11: a) Correlation between the IP vs HOMO energies and b) EA vs LUMO energies for the systems.

According to maximum hardness principle (MHP),[26,27] the most stable structure has the maximum hardness. Thus the neat complexes with maximum hardness are chemically more stable compared to the encapsulated ones. Further, it can be seen from the Table 6.4 that upon encapsulation both the values of chemical potential (μ) increases whereas that of the electrophilicity index (ω) are found to increase in case of spin up state but it decreases in case of spin down state. This result suggest that occupancy of the electron i.e whether it involves a α-orbital or β-orbital will also brings out a considerable change in the reactivity of the system. In this context, it is pertinent to mention that electrophilicity containing information for both electron transfer (chemical potential) and stability (hardness) is considered to be a better descriptor of global chemical reactivity. Moreover, ω includes a hardness term in the denominator which is a descriptor of stability. Electrophilicity is expected to exhibit an inverse linear relationship with hardness or in correlation with MHP we can say that under the conditions for the existence of an MHP there will also be a *minimum electrophilicity principle*.[28] We have observed from our calculation that in case of neat complexes, $Cu(L1)_2$ complex with maximum hardness has minimum electrophilicity and the same is true in case of the encapsulated Cu(L2)$_2$-Y complex (Table 6.4). Thus it is found that on encapsulation of the complexes into zeolite framework the chemical potential (μ) and the global softnees (S) values increase whereas that of η decreases. This change in values of the global descriptors reflects the effect of zeolite matrix on the reactivity of the complexes and it can be said that complexes with high μ value can actively participate in electron transfer reactions. In our case the Cu(L1)$_2$-Y complex with minimum η and maximum S values will be the most reactive system.

6.2.2.4. Local Descriptors

Table 6.5 presents the Fukui functions (FFs, f_{κ}^{+} and f_{k}^{-}) for the selected metal atoms and the coordinated nitrogen atoms calculated using Hirshfeld Population Analysis (HPA) scheme for the neat and encapsulated metal complexes. It is seen in Tables 6.5 that the values of the Fukui functions at the metal centers increases upon encapsulation. Thus the zeolite framework modifies the reactivity of the metal atom from a less electrophilic or nucleophilic site in neat complexes to a higher site in encapsulated ones. As per the attack of nucleophile or electrophile at a particular site is concerned, the Cu-atom (in both neat and the encapsulated) possessing the higher value of Fukui functions ((FFs, f_{κ}^{+} and f_{k}^{-}) will be the most preferential site. Comparison of the Fukui function (at the metal centre) between the encapsulated and the neat complexes suggest that a nucleophile will preferentially attack the Cu-centre in the encapsulated complexes. This further indicates that encapsulated complexes can actively participate in a base catalyzed reaction.

Table 6.5. Hirshfeld population analysis of Fukui functions for the neat and the encapsulated complexes.

Selected Atoms	Cu(L1)$_2$		Cu(L2)$_2$		Cu(L1)$_2$-Y		Cu(L2)$_2$-Y	
	f_{κ}^{+}	f_{k}^{-}	f_{κ}^{+}	f_{k}^{-}	f_{κ}^{+}	f_{k}^{-}	f_{κ}^{+}	f_{k}^{-}
Cu	0.085	0.074	0.087	0.074	0.110	0.084	0.098	0.085
N	0.021	0.026	0.019	0.025	0.011	0.029	0.009	0.026
N	0.029	0.024	0.027	0.022	0.026	0.020	0.019	0.016
O	0.035	0.059	0.032	0.060	0.029	0.065	0.028	0.068
O	0.038	0.055	0.035	0.051	0.028	0.032	0.022	0.029

6.2.2.5. Spin Density Calculation

The considered Cu(II) complexes are open shell system with d^9 electronic configuration. The electronic configuration suggests that the excess spin density should be localized on the Cu-centre. The spin density calculation on the two neat complexes using DMOL^3 programme at VWN/DN level of theory, indicates that in both the complex the high percentage (more than 50% of the total Mullikan charge density), Figure 6.12 is concentrated on the central Cu-atom. A substantial minority spin density is located on co-ordinated nitrogen and oxygen atoms (10-11% of the total Mullikan charge density). This minority spin denisity results from the slight spatial offset between the α and β-spin forms of the $d_\pi - p_\pi$ MOs. The presence of the high spin density on the metallic centre implies that unpaired *d*-electron is mostly concentrated on the metallic centre and is not delocalized over the aromatic rings of the co-ordinating ligands.

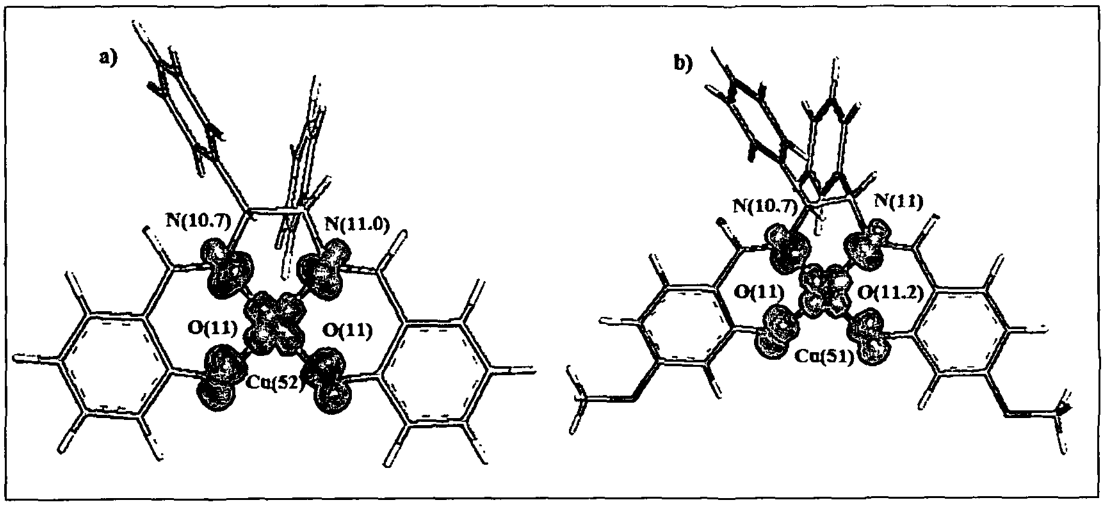

Figure 6.12. Representation of spin density distribution in a) $(CuL1)_2$ b) $(CuL2)_2$ complexes. The values in the parentheses are in percentage. The isovalues for these drawings are 0.02.

6.3. Catalytic Study

To test the catalytic efficiency of the synthesize complex, we choose *p*-nitrobenzaldehyde as a test substrate and compared with that of Cu(II) acetate. Since the Henry reaction is considered to employ basicity to generate the nitronate, acetic acid is added as base to the reaction system in order to increase the reactivity of the catalyst. It has been found that $Cu(L1)_2$-Schiff-base complexes encapsulated in zeolite-Y promote the reaction with 100% conversion and 96% yield (4°C, 16h) and is much better than those obtained in presence of $Cu(OAc)_2.2H_2O$ (58%). The complete conversion of the reaction is confirmed *via* UV-vis spectroscopy and HPLC analysis.

The reactivity and enantioselectivity of the nitroaldol reaction is strongly dependent upon the nature of the solvent used. Therefore, a catalytic enantioselective Henry reaction is conducted in different solvents, such as toluene, 1, 2-dichloroethane, THF, CH_3CN, ethanol, and methanol, with catalyst $Cu(L1)_2$-Y under identical reaction conditions. It can be seen from Table 6.6, that polar solvents give better yield and high enantioselectivity in comparison to the non –polar. In the present case, we found ethanol as the best solvent system; in term of productivity and enatioselectivity. Hence we performed all the reaction in ethanol by varying the catalyst. Temperature and catalytic amount also plays an important role in the yield and ee of the reaction.[29,30] We performed the nitroaldol reaction of *p*-nitro benzaldehyde as the model substrate at various temperature viz room temperature (rt), 0, -10 -20, -30 and -40°C.

Table 6.6. Henry reaction of *p*-nitro benzaldehyde under various solvent reaction conditions.

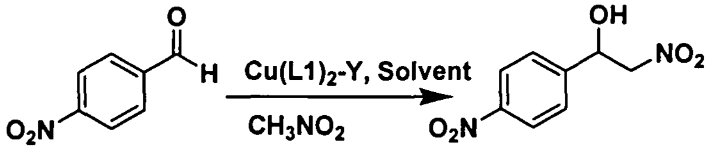

Entry	Catalyst amount (in mg)	Solvent	Time(h)	Yield	ee(%)
1	10	Tolune	48	72	54
2	10	CH_2Cl_2	40	74	63
3	10	CH_3CN	25	82	74
4	10	THF	22	88	78
5	10	CH_3OH	20	90	81
6	10	C_2H_5OH	16	96	84

Table 6.7. Effect of temperature on the Henry reaction of 4-nitro-benzaldehyde.

Entry	Temp(°C)	Solvent	Time(h)	Yield (%)	ee(%)
1	Rt	C_2H_5OH	34	78	70
2	0	C_2H_5OH	26	82	75
3	-10	C_2H_5OH	22	88	78
4	-20	C_2H_5OH	16	96	84
5	-30	C_2H_5OH	19	92	78
6	-40	C_2H_5OH	20	88	75

It can be observed from Table 6.7 that *p*-nitro benzaldehyde gives maximum yield and ee at -20°C. However, the enantioselectivity is found to decrease at -40°C. This may be due to the fact that below -20°C, the reaction intermediate gets stabilized and thereby affects the enantioselectivity. As we obtained better efficiency of the catalyst at -20°C so we performed all other reactions at this temperature using various Schiff base complexes, (Table 6.8). As per the catalytic amount is concerned we have varied the catalytic amount from 5mg to 25mg keeping the amount of the substrate constant. On increasing catalytic amount from 5 to10 mg, both the yield (above 90%) and ee (up to 84%) is found to enhance. However, no significant enhancement in the yield as well in enantioselectivity is observed on further increment of the catalytic amount. So we choose 10 mg of the catalyst to be the optimal.

Table 6.8 indicates that the zeolite encapsulated complexes shows better catalytic efficiency than their homologous analogue. The increase in catalytic ability of these catalysts can also be correlated to our theoretical results. Since our theoretical calculation suggests that on encapsulation the global hardness decreases, so according to Pearsons HSAB principle[31] they become more reactive in nature. Moreover, the f_K^+ value which indicate preferential site for a nucleophilic attack is mostly concentrated at Cu-centre in the encapsulated complexes (Figure 6.13). And as stated by Evan[10] after the generation of the nitronate ion, this nucleophile binds to the Cu-centre through one of the O-atom. So values of the Fukui function suggest that among our systems this step becomes more feasible in

Table 6.8. Results of the Henry reaction in presence of various catalysts. The values given in the parenthesis are time (in h) required for completion of the reaction. The (% ee) are calculated from HPLC analysis.

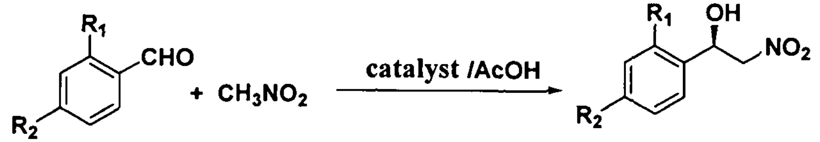

1a R_1= H, R_2 = H
1b R_1= H, R_2 = NO_2
1c, R_1= NO_2, R_2= H
1d, R_1= H, R_2= CH_3
1e, R_1=H R_2= OH
1f, Napthaldehyde

2a R_1= H, R_2 = H
2b R1= H, R_2 = NO_2
2c, R_1= NO_2, R_2= H
2d, R_1= H, R_2= CH_3
2e, R_1=H R_2= OH
2f, 1-(naphthalen-6-yl)-2-nitroethanol

Reactant	product	NaY		Cu^{2+}-Y		Cu(L1)$_2$		Cu(L2)$_2$		Cu(L1)$_2$-Y		Cu(L2)$_2$-Y	
		(%)Yield	(%)ee	(%)Yield	(%)ee	(%)Yield	(%)ee	(%)Yield	(%)ee	(%)Yield	(%)ee	(%)Yield	(%)ee
1a	2a	48(36)	-	63(28)	-	82(24)	62	80(24)	61	92(18)	82	90(18)	80
1b	2b	50(32)	-	66(22)	-	89(22	67	84(22)	72	94(17)	84	95(17)	82
1c	2c	54(32)	-	68(22)	-	87(21)	76	88(21)	74	96(16)	84	93(16)	83
1d	2d	53(34)	-	64(26)	-	78(25)	72	86(25)	66	93(19)	78	86(19)	79
1e	2e	49(38)	-	58(30)	-	82(24)	64	77(24)	60	88(20)	74	82(20)	76
1f	2f	47(38)	-	52(29)	-	83(26)	60	82(26)	68	82(22)	73	84(22)	74

case of Cu(L1)$_2$-Y encapsulated complex having maximum f_κ^+ value followed by Cu(L2)$_2$-Y, Cu(L2)$_2$ and Cu(L1)$_2$, respectively.

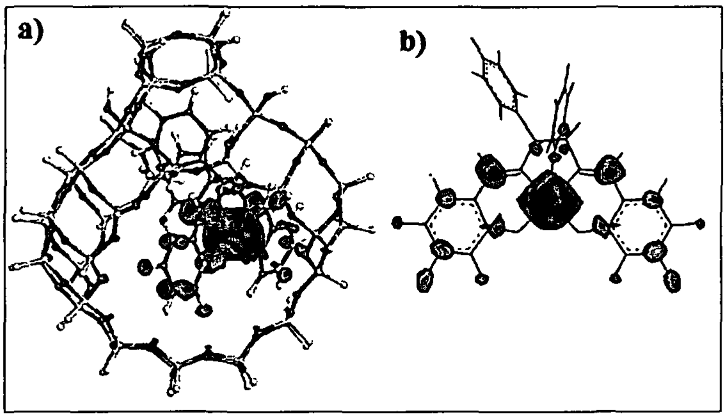

Figure 6.13. Fukui function corresponding to nucleophillic attack (f_κ^+) located at the Cu-centre of a) Cu(L1)$_2$-Y and b) neat Cu(L1)$_2$

In order to examine the roles of the Schiff base moiety of catalytic activity, we performed the nito-aldol reaction in presence of NaY and Schiff base ligands. Herein again we consider the reaction of *p*-nitro-benzaldehyde as model system. On addition of the chiral ligand system into the reaction media, the yield is found to increase from 50% to 60% and the ee is found to be 45%. This revealed that presence of chiral Schiff base ligand is critical for reaction efficiency and enantioselectivity.

6.4. Plausible Mechanism of Henry reaction catalysed by Cu(L1)$_2$complex

An attempt has been made to rationalize the plausible pathway involved in the catalytic conversion. The catalytic cycle is depicted in Scheme 6.1. Since Cu(L1)$_2$-Y is found to be better catalyst. Therefore, for the mechanistic study we choose neat Cu(L1)$_2$-complex. The catalytic cycle is supposed to involve three steps. The first step involves the abstraction of a methyl proton from nitromethane by acetate acting as base[14] generating nitronate ion. The second step involves the coordination of the nitronate to the Cu-centre *via* Cu-O-N linkage. Third step involves the simultaneous attack of the nucleophile to the incoming aldehyde and formation of activated complex followed by the release of the product. To support this mechanism we perform density function theory (DFT) calculation on the possible intermediate and transition state. The optimized geometry of Cu(L1)$_2$,

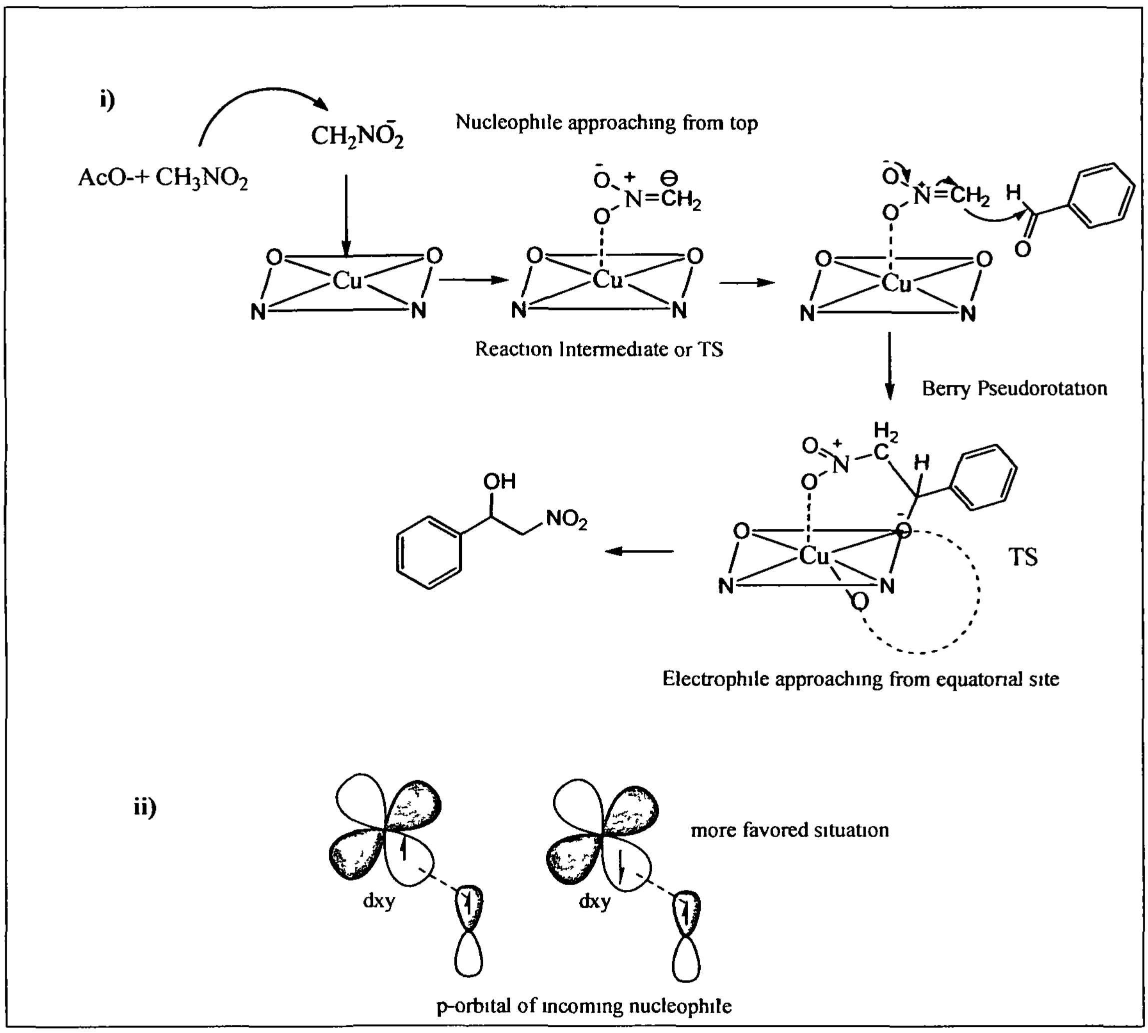

Scheme 6.1. Plausible reaction path for nitro-aldol formation

possible TS and reaction intermediates are shown in Figure 6.14. The energy profile for the three steps reaction is shown in Figure 6.15. It can be seen from Figure 6.14 that as the nitronate ion co-ordinates to the Cu-centre the square planar complex undergoes a *Jahn Teller* distortion with the compression of the Cu-O and Cu-N bonds. This step is endergonic in nature and has to cross an energy barrier of 15 kcal/mol to form the intermediate sate 1(Int-1) and is the rate determining step. In both the TS and intermediate state the incoming nucleophile is found to lie in the axial position with the Cu-O bond distances of 2.44 and 2.19 Å, respectivély. During this process the unpaired electron on the Cu-centre get coupled with the unpaired electron of O-atom of nitronate. This is in accordance with our ESR analysis and spin density calculation. Once the metal complex

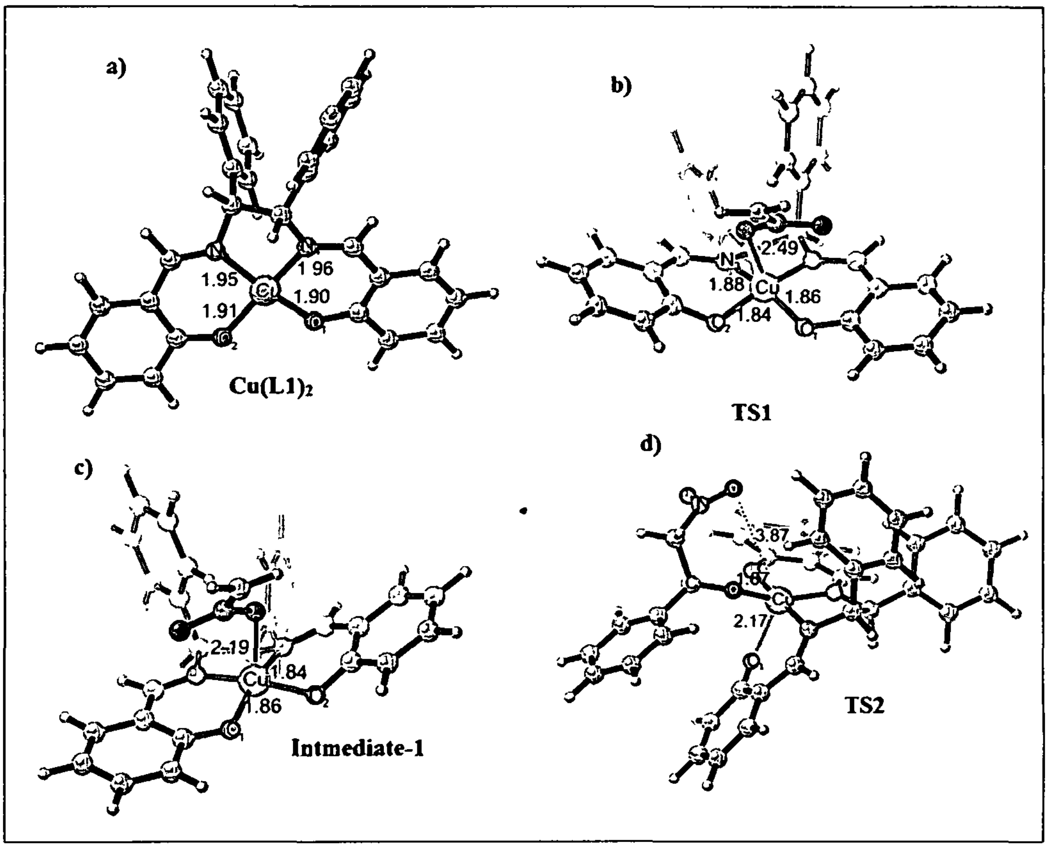

Figure 6.14. Optimized geometries of possible intermediates and transitions involved in the catalytic cycle.

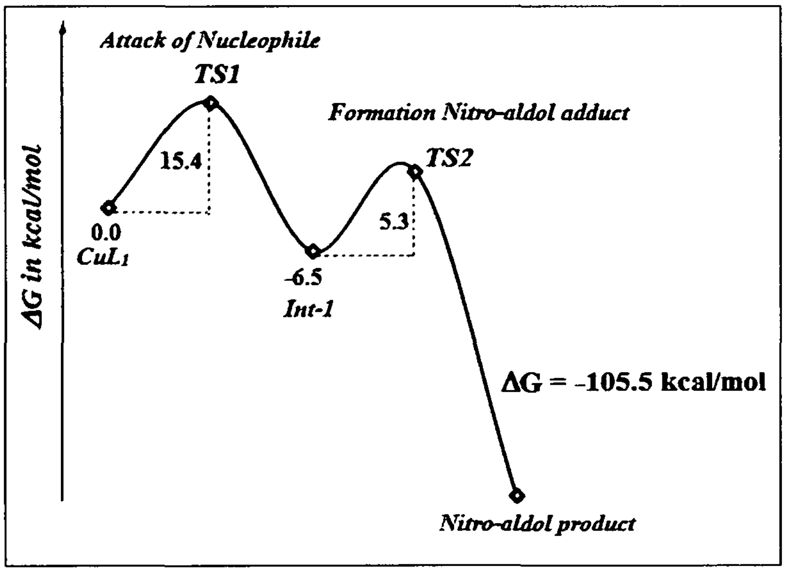

Figure 6.15. Simple energy profile diagram for catalytic conversion.

undergoes radical coupling it becomes ESR inactive. And since the spin density calculations predict that the unpaired electron is mostly located on the Cu-centre, so the incoming nucleophile will have higher tendency to get attached to the Cu-centre. Further, from our DFT calculation it is predicted that if the electron spin in d_{xy} orbital is in downward direction, the complex becomes more reactive. Therefore, the most favoured situation for *d-p* mixing between Cu-centre and nitronate in the TS1 or Int-1 will be the one in which the unpaired electron in d_{xy} allign in downward direction, Scheme 6.1 ii). On addition of the aldehydes, the nucleophile bonded to the Cu-centre attack the carbon atom of the aldehydic group and finally leads to the formation of product. On going from *Int-1* to the niro-aldol product, the intermediate complex-1 passes through a transition state (TS2) and has to cross an energy barrier of 5.3 kcal/mol. In the TS2, the square planar Cu-complex undergoes a Berry pseudo-rotation allowing the O-atom of the incoming aldehyde to bind from the equatorial position. At this stage there occurs a large elongation of the Cu-O_1 bond (due to *Jahn Teller* distortion), the nitronate moves away from the ligand plan and lies perpendicular to the ligand plan. The calculated transition state geometry is similar to the type proposed recently by Dhahagani et al.[12] It is evident that for those complexes that simultaneously bind both electrophile and nucleophile, the most reactive transition state is the one in which the nucleophile is lies perpendicular to the ligand plane, while the electrophile reside in the equatorial sites of the ligand plane.[10] This statement is in good agreement with our theoretical observation. By this argument it can be said that the TS2 will exhibit highest reactivity. After the formation of the reaction intermediate complex, the formation of the product is greatly favoured as indicated by high negative value of ΔG = -105.5 kcal/mol (Figure 6.15).

6.5. Conclusion

The chiral Schiff base complexes of copper encapsulated inside zeolite-Y found to be better catalyst in terms of thermal stability and catalytic efficiency. The catalytic ability of these complexes is found to depend on temperature, solvent system and catalytic amount. Lower the temperature (-20°C), higher the polarity of the solvent and lower the catalytic amount higher is the enantioselectivity. DFT theory predicts that encapsulation reduces the global hardness, increases the softness and Fukui function values of the complexes resulting in higher catalytic ability of the encapsulated complexes. Further it is revealed from our theoretical calculation that in the catalytic cycle (TS2) the nucleophile must reside in the axial position and the electrophile should positioned in the equatorial site of the ligand plane for better catalytic performance.

6.6. ^{1}H NMR, ^{13}NMR and HPLC Analysis of Nitro-Aldol Products

6.6.1. 2-nitro-1-phenylethanol

Determined by Chiral HPLC, acetonitrile:ethanol(70:30), 1 mL/min, minor enantiomer (*S*) *r.t* = 12.8, major enantiomer (*R*) *r.t* = 18.2), absolute stereochemistry assigned by comparison of the retention times in HPLC with the standard. ^{1}H NMR ($CDCl_3$, 400 MHz, ppm): δ = 7.46-7.36 (m, 5H), 5.42 (d,1 H), 4.63-4.43 (m, 2 H), 2.88(br, 1 H). ^{13}C NMR($CDCl_3$, 100 MHz, ppm): δ = 71.0, 81.2, 126.0, 129.0, 129.0, 138.3. IR (KBr film, cm-1): ν = 3535, 3032, 2920, 1554, 1495, 1453, 1418, 1379, 1290, 1212, 1066, 895, 764, 702, 608.

6.6.2. 2-nitro-1-(4-nitrophenyl) ethanol

Determined by Chiral HPLC, acetonitrile:ethanol(70:30), 1 mL/min, minor enantiomer (*S*) *r.t* = 33.21, major enantiomer (*R*) *r.t* = 28.24), absolute stereochemistry assigned by comparison of the retention times in HPLC with the standard. ^{1}H NMR (400 MHz, $CDCl_3$): δ = 8.25 (d, 2H), 7.63 (d, 2H), 5.62-5.52 (m, 1H), 4.61-4.54 (m, 2H), 3.25 ppm (br s, 1H). ^{13}C NMR ($CDCl_3$, 100 MHz, ppm): δ = 70.04, 80.12, 124.03, 127.01, 145.9, 147.9. IR (KBr film, cm^{-1}): ν = 3401, 2919, 1555, 1416, 1382, 1349, 1086, 856, 754, 727, 697.

6.6.3. 2-nitro-1-(2-nitrophenyl) ethanol

Determined by Chiral HPLC, (acetonitrile:ethanol(70:30), 1 mL/min, minor enantiomer (*S*) *r.t* = 18.50, major enantiomer (*R*) *r.t* = 19.23), absolute stereochemistry assigned by comparison of the retention times in HPLC with the standard. ^{1}H NMR (400 MHz, $CDCl_3$): δ = 8.08 (d, 1H), 7.96 (d, 1H), 7.77-7.73 (m, 1H), 7.57-7.53 (m, 1H) 6.05-6.03 (m, 1H), 4.89(dd, 1H), 4.59 (dd, 1H), 3.28 ppm (br s, 1H). ^{13}C NMR ($CDCl_3$, 100 MHz, ppm): δ = 66.7, 81.1, 126.7, 128.0, 129.7, 134.4, 134.5, 147.9. IR (KBr film, cm^{-1}): ν = 3537, 1587, 1533, 1422, 1380, 1365, 1091, 1071, 866.

6.6.4. 4-(1-hydroxy-2-nitroethyl) phenol

Determined by Chiral HPLC, acetonitrile:ethanol(70:30), 1 mL/min, minor enantiomer (*S*) *r.t* = 13.61, major enantiomer (*R*) *r.t* = 12.50), absolute stereochemistry assigned by comparison of the retention times in HPLC with the standard. ^{1}H NMR ($CDCl_3$, 400 MHz, ppm): δ = 7.53 (d, 2H), 6.41(dd, 2H), 5.3(m, 1H), 5.05 (br, 1H), 4.32-4.02 (m, 2H), 3.08 (br, 1H) ^{13}C NMR($CDCl_3$, 100 MHz, ppm): δ = 70.0, 81.1, 116.1, 129.1, 132.5, 156.5. IR (KBr film, cm-1): ν = 3348, 2923, 2852, 1675, 1601, 1553, 1515, 1495, 1449, 1378, 1261, 1219, 1157, 1108, 1042, 910, 838, 734, 698.

6.6.5. 2-nitro-1-p-tolyl ethanol

Determined by Chiral HPLC, acetonitrile:ethanol(70:30), 1 mL/min, minor enantiomer (*S*) *r.t* = 16.23, major enantiomer (*R*) *r.t* = 12.51), absolute stereochemistry assigned by comparison of the retention times in HPLC with the standard. ^{1}H NMR (400 MHz, CDCl3): δ = 7.29 (m, 2H), 7.24 (d, 2H), 5.45-5.33 (m, 1H), 4.59(dd, 2H), 2.88 (br s, 1H), 2.38 ppm (s, 3H). ^{13}C NMR(CDCl$_3$ 100 MHz, ppm): δ = 21.0, 71.0, 81.3, 126.0, 129.8, 135.3, 139.0. IR (KBr film, cm^{-1}): ν = 3548, 3028, 2924, 1555, 1516, 1418, 1378, 1287, 1208, 1077, 910, 819, 734.

6.6.6. 1-(naphthalen-6-yl)-2-nitroethanol

Determined by Chiral HPLC, acetonitrile:ethanol(70:30), 1 mL/min, minor enantiomer (*S*) *r.t* = 23.12, major enantiomer (*R*) *r.t* = 16.54), absolute stereochemistry assigned by comparison of the retention times in HPLC with the standard. ^{1}H NMR (400 MHz, CDCl$_3$) δ = 8.35 (d, 1H) 7.73-7.64 (m. 2H) , 7.51-7.54 (d, 1H) 7.50-7.27 (m, 3H) 6.92- 6.58 (m, 1H), 4.54-4.11 (m, 2H), 2.78 (br, 1H). ^{13}C NMR (CDCl$_3$, 100 MHz, ppm): δ = 67.3, 81.1, 122.2, 123.8, 125.5, 126.05, 126.09, 128.2, 128.3, 128.5, 131.6, 133.7. IR (KBr film, cm^{-1}): ν = 3558, 3062, 2922, 1552, 1513, 1418, 1378, 1277, 1204, 1097, 911, 802, 780, 738, 650, 622.

6.7. ^{1}H NMR, ^{13}NMR Analysis of Ligands L1 and L2

6.7.1. Ligand, L1

^{1}H NMR (500MHz, CDCl$_3$) δ 13.26 (s, 1H), 8.30 (s, 1H), 7.11-7.28 (m, 7H), 7.13 (d, J = 7.35Hz, 1H), 6.94 (d, 1H), 6.79 (t, J = 7.35Hz, 1H), 4.73 (s, 1H)

^{13}C NMR (75 MHz, CDCl$_3$) δ 166.06, 160.82, 139.27, 132.45, 131.63, 128.25, 127.74, 127.51, 118.62, 118.46, 116.78, 80.04.

6.7.2. Ligand, L2

^{1}H NMR (300MHz, CDCl$_3$) δ 13.83 (s, 1H), 8.17 (s, 1H), 7.19 (m, 5H), 7.01(d, J = 9.06Hz, 1H), 6.45(d,J = 2.26Hz, 1H), 6.35(dd, J = 2.26, 9.06Hz, 1H), 4.65 (s, 1H), 3.78 (s, 3H)

^{13}C NMR (75 MHz, CDCl$_3$) δ 165.06, 163.60, 163.28, 139.60, 132.81, 128.19, 127.72, 127.38, 112.36, 106.28, 100.96, 79.55, 55.15

References.

[1] Kervinen, K., et al. *J. Am. Chem. Soc.* **128**(10), 3208-3217, 2006.

[2] Modi, C. K., et al. *J. Incl. Phenom. Macrocycl. Chem.* **74**(1-4), 117–127, 2012.

[3] Zhu, D., et al. *Energy & Fuels* **23**(5), 2359–2363, 2009.

[4] Mori, K., et al. *J. Phys. Chem. C* **112**(49), 19449–19455, 2008.

[5] Mori, K., et al. *J. Phys. Chem. C* **112**(7), 2593-2600, 2008.

[6] Corrêa, R. J., et al. *Appl. Catal. A: Gen.* **336**(1-2), 35–39, 2008.

[7] Poltowicz, J., et al. *Appl. Catal. A: Gen.* **299**, 235–242, 2006.

[8] (a) Rosini, G. *In Comprehensive Organic Synthesis*, Vol. 2 (Ed.: B. M. Trost), Pergamon, Oxford, 1996, 321. b) Luzzio, F. A. *Tetrahedron* **57**(6), 915-945, 2001, c) Ono, N. *The Nitro group in Organic Synthesis*, Wiley-VCH, 2001, 30.

[9] (a) Sasai, H., et al. *J. Am. Chem. Soc.* **114**(11), 4418-4420, 1992, (b) Shibasaki, M., & Yoshikawa, N. *Chem. Rev.* **102**(6), 2187-2209, 2002, and references therein.

[10] Evans, D. A., et al. *J. Am. Chem. Soc.* **125**(42), 12692–12693, 2003.

[11] Jacobsen, E. N., et al. *J. Am. Chem. Soc.* **113**(18), 7063-7064, 1991.

[12] Dhahagani, K., et al. *Tetrahedron: Asymmetry* **22**(8), 857–865, 2011.

[13] Cheng,H. G., et al. *Chem. Commun.* **48**, 5596–5598, 2012.

[14] Vógel, A. I. *Textbook* of *Quantitative Chemical Analysis*, Pearson Education Asia, 2002, 6th Edn, p 393.

[15] (a) Quayle, W. H., & Lunsford, J. H. *Inorg. Chem.* **21**(1), 97-103, 1982, (b) Quayle, W. H., et al. *Inorg. Chem.* **21**(6), 2226-2231, 1982.

[16] Ganesan, R., & Viswanathan, B. *J. Mol. Catal. A: Chemical* **223**(1-2), 21–29, 2004.

[17] Shaw, B. R., et al. *J. Electrochem. Soc.* **135**(4), 869-876, 1988.

[18] a) Jafarian. M., et al. *J. Phys. Chem. C* **116**(34), 18518–18532, 2012, b) Dutta, P. K., & Ledney, M. *Prog. Inorg. Chem.* **44**, 209–271, 1997.

[19] Viswanathan, B., & Ganesan, R. *J. Phys. Chem. B* **108**(22), 7102-7114, 2004.

[20] Singh, K., et al. *Eur. J. Med. Chem.* **52**, 313-321, 2012.

[21] Hyper Chem (TM) Professional 7.51, Hypercube, Inc., 1115 NW 4th Street, Gainesville, Florida 32601, USA

[22] Calabro, D. C., & Lichtenberger, D. L. *Inorg. Chem.* **19**(6), 1732-1734, 1980.

[23] Bally, T., et al. *J. Am. Chem. Soc.* **106**(14), 3927–3933, 1984.

[24] Jano, I. *J. Phys. Chem.* **95**(20), 7694–7699, 1991.

[25] Schildcrout, S. M., et al. *J. Am. Chem. Soc.* **90**(15), 4006–4010, 1968.

[26] Parr, R. G., & Chattaraj, P. K. *J. Am. Chem. Soc.* **113**(5), 1854-1855, 1991.

[27] Chattaraj, P. K., et al. *Chem. Phys. Let.* **237**(1-2), 171-176, 1995.

[28] Morell, G., et al. *Phys. Chem. Chem. Phys.* **11**, 3417–3423, 2009.

[29] Park, J., et al. *J. Am. Chem. Soc.* **130**(49), 16484–16485, 2008.

[30] Trost, B. M., & Yeh, V.S. C. *Angew. Chem. Int. Ed.* **41**(5), 861-863, 2002.

[31] Pearson, R. G. *Chemical Hardness: Applications from Molecules to Solids,* Wiley-VCH Verlag GMBH: Weinheim, 1997.

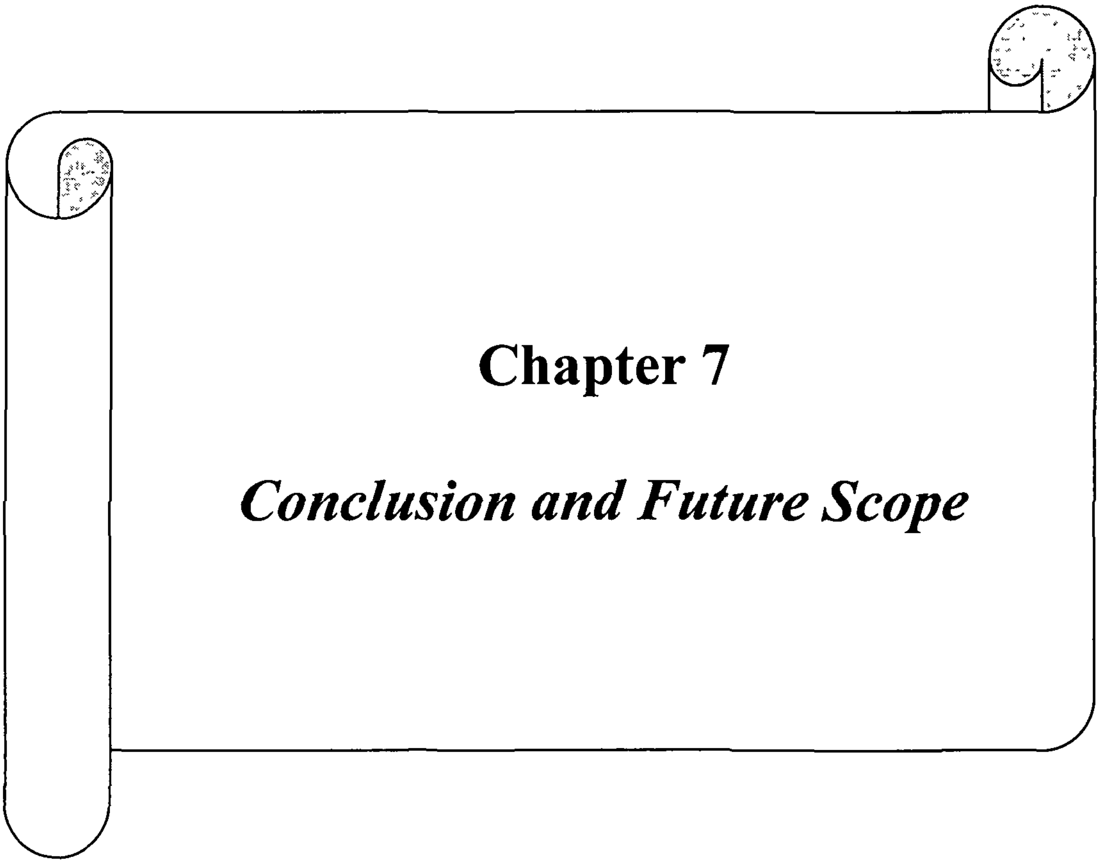

Chapter 7

Conclusion and Future Scope

7.1. Overall Conclusion of the Present Work

Due to several advantages of the heterogeneous catalyst over the homogeneous counterpart, in recent years much emphasis has been given in the designing of newer heterogeneous transition metal catalyst. Zeolite-Y owing to its high pore dimension acts as suitable host for various transition metal complexes and hence, provides a viable path for synthesizing of newer hybrid materials. Besides acting as scavenger for the organic substrates or for the inorganic metal complexes, zeolite-Y too can provide an environment similar to those of protein mantles and hence can act as inorganic protein mantle. Therefore, one can mimic the bio-system simply by incorporating similar kind of metal complexes (found in metalloenzymes) inside the cavity of zeolite-Y. So with an objective to add something in the field of heterogenisation of homogeneous transition metal complexes, in this thesis we provide an insight into the synthesis, characterization and catalytic application of some the zeolite-Y encapsulated transition metal complexes. Till now less importance has been paid to understand the structural and reactivity of the zeolite-Y encapsulated metal complexes. Herein, in the present work we have brought out the effect of the zeolite matrix on the structural and reactivity properties of the encapsulated metal complexes using density functional theory (DFT) calculation. A considerable effort has also been given to comprehend the effect of zeolite matrix on the electronic, redox and catalytic behaviour of encapsulated complexes via various experimental tools.

The findings of the thesis are summarized below.

We have successfully synthesized and characterized the tris(1,10 phenanthroline) complexes of Fe (II), Cu(II) and Zn(II) complexes inside the cavity of zeolite-Y. The spectroscopic and DFT calculation suggest that the iron and copper complexes are formed inside the cavity of zeolite Y and are hold together by Coulombic force of interaction. Whereas the zinc(II) complex is formed over the zeolite surface and is tethered via the H-bond formation. The changes in the electronic and electrochemical behaviour of the encapsulated phenanthroline complexes are comparable with those of the similar metal complexes interacted with DNA. This further indicates that these types of zeolite encapsulated systems can be considered to mimic the interaction of transition metal complexes with DNA. The calculation of the global and local descriptor values suggest that on encapsulation the phenathroline complexes becomes more reactive in comparison to the neat complexes and there occurs a hard-hard interaction between the metal atoms and the co-ordinated nitrogen atom of the phenanthroline ligand.

Similar to the phenanthroline complexes of transition metals, bis(Picolinato) complexes of Co(II), Ni(II) and Cu(II) are also synthesized inside the cavity of the zeolite-Y. The cyclic voltammetry, EPR and DFT study suggest that the neat Cu(II) picolinato complexes undergoes *cis-trans* isomerization. However, such geometrical isomeization is not observed in case of the encapsulated Cu(II) complex. The zeolite encapsulated complexes of copper and cobalt are found to active towards the selective oxidation of phenol to catechol in presence of H_2O_2. These two complexes selectively convert phenol to catechol with 70-74% yield in comparison to the neat complexes. The experimental and DFT study on the mechanism of the phenol oxidation suggest that the reaction proceeds via the interaction of the peroxide with the metal centre.

Following the similar methodology, two achiral Schiff base complexes of Fe(III) viz Fe(III) Salen and Fe(III) Salophen has also been synthesized inside the cavity of various alkali exchanged zeolite-Y viz LiY, NaY and KY. The synthesize complexes are found to be active for catalytic oxidation of 2-napthol to BINOL. The size and electronegativity of the alkali cations are found to have immense influence on the structural, electronic, electrochemical and catalytic behaviour of the encapsulated Fe-Schiff base complexes. It has been observed that as the size of the alkali cations increases the charge transfer transitions shifted to higher wavelength and redox potential values becomes more negative. This in turn also influences the C-C coupling reaction of 2-napthol. It has been found that as the size of the alkali metal cation increases the activity of the catalyst for the selective oxidation of the 2-napthol to BINOL also enhances. The cation-π interaction i.e the interaction of the alkali metal cation of the zeolite framework with the aromatic ring of 2-napthol plays a vital role in bringing out the enantioselectivity in the catalytic process in presence of the achiral catalysts. And it is found that larger the size of the alkali cation, tighter the fit, lesser the cation –π interaction, hence, higher is the asymmetric induction.

Finally, we have also been successful in synthesizing two chiral Cu(II) Schiff base complexes inside the cavity of zeolite-Y via "*ship in a bottle*" synthesis method. The two chiral complexes acts as active catalyst in the enantioselective Henry reaction and are found to be superior in comparison to the neat complexes. The asymmetric Henry reactions in presence of these chiral catalysts are found to depend on temperature and solvent system. At -20 °C and in ethanolic solution it gives high yield and 84% of the *S*-product. The DFT calculation suggest that in the transition state the nucleophile must reside in the axial position whereas the electrophile should lie in the equatorial position of the ligand plane for better catalytic activity.

7.2. Future Scope

After carrying out the experimental and theoretical studies on some zeolite-Y encapsulated transition metal we feel that these hybrid materials can pave a vast area in the field of heterogenisation of homogeneous catalyst. So the present work can be further extended in the following aspects

- Designing of newer heterogeneous catalyst by encapsulation of various other transition metal complexes inside zeolite-Y.
- Encapsulation of bio-inspired transition metal complexes inside zeolite-Y can provide a viable alternative path for sustainable development and mimicking the bio-system.
- Asymmetric catalysis by zeolite-Y encapsulated chiral transition metal complexes can be one of the vast areas to explore the heterogeneous catalyst.
- DFT calculation on such encapsulated complexes can bring out some of the vital aspects of these hybrid systems.

List of Publications

1. Influence of Zeolite Framework on the Structure, Properties, andReactivity of Cobalt Phenanthroline Complex: A Combined Experimental and Computational Study,
Kusum K. Bania *and Ramesh C. Deka** ***J. Phys. Chem. C***, 2011, *115*, 9601–9607

2. Experimental and Theoretical Evidence for Encapsulation andTethering of 1,10-Phenanthroline Complexes of Fe, Cu, and Zn inZeolite−Y
Kusum K. Bania *and Ramesh C. Deka** ***J. Phys. Chem. C*** *2012, 116, 14295−14310*

3. Enhanced Catalytic Activity of Zeolite Encapsulated Fe(III)-Schiff-Base Complexes for Oxidative Coupling of 2-Napthol
Kusum K. Bania, *† Dipsikha Bharali,† B. Viswanathan,‡ and Ramesh C. Deka*,†*
Inorg. Chem. *2012, 51, 1657−1674*

4. Zeolite Encapsulated Metal Picolinato Complexes as Catalyst for Oxidation of Phenol with Hydrogen Peroxide
Kusum K. Bania, Ramesh *C. Deka** ***Inorg. Chem.*** *ID: ic-2013-00169r (under review)*

5. Enantioselective Henry Reaction by Chiral Schiff base Cu(II) Complexes Encapsulated in Zeolite-Y
Kusum K. Bania,[†] *Galla V. Karunakar,*[#] *Kommuru Goutham,* [#] *Ramesh C. Deka*[†]** J. Phys. Chem ID: jp-2013-00351p (Revision Submitted)*

6. Enantioselective Henry Reaction via CH/π and H-bonding interaction
Kusum K. Bania*, Choitanya Dev. Pegu and Ramesh C. Deka* (Communicated to Inorg. Chem.)*

Conferences/ Seminar/workshop

1. National Seminar on Recent Advances in Synthessis and Catalysis, RASC -2011, Dibrugarh University, Assam.
2. National Conference On Chemistry, Chemical Technology and Society, 2011, Tezpur University, Assam.
3. Instructional School On Quntum Mechanics and Group Theory, JIST, Jorhat, Assam, 2010
4. 14th National Workshop On Catalysis, 2009, Tezpur University, Assam.
5. Frontier Lecture Series, 2009, Tezpur University, Assam.
6. Summer School On Green Chemistry, 2009, Tezpur University, Assam